Mathematical Modelling of Oxygen Transport in Skeletal and Cardiac Muscles

Abdullah A. Al-Shammari

Linacre College

University of Oxford

A thesis submitted for the degree of

Doctor of Philosophy

Trinity Term 2014

To my Mother

for her unending support and encouragement

Acknowledgements

I am deeply indebted to my supervisor, Prof Eamonn Gaffney, for his tireless academic supervision, tenacious encouragement and unwavering support and guidance, personal and professional, throughout the years leading to this dissertation. I am also grateful to our lead physiology collaborator, Prof Stuart Egginton, for his insightful discussions, valuable collaboration and support through generous lab invitations and provision of biological datasets, and for profoundly influencing my way of thinking about oxygen transport and angiogenesis. I would also like to thank Dr David Hauton for valuable academic and research collaboration that led to new avenues of physiological research for applying the modelling framework presented in this work.

This work was generously funded by Kuwait University (KU) via a comprehensive postgraduate scholarship. Within KU, I am sincerely grateful to Dr Haidar Khajah for his engaging conversations, genuine interest, guidance, faith and encouragement. I also wish to thank Prof Ismail Taqi and Prof Salem Al-Yaqoob for their support and encouragement, as well as Dr Mansour Al-Zanaidi for a valuable assistance, and Mrs Nouf Al-Faddagh for expediting the administrative aspects of my scholarship.

Within the Wolfson Centre for Mathematical Biology, I am grateful to Gabriel Rosser, Aaron Lim, Alhaji Cherif and Jochen Kursawe for brightening up my days at the office and for sparing a few doses of healthy chatter. Outside the world of mathematical biology, I wish to express my warmest gratitude to Meshal Al-Daalah, Jad Assi, Lucia Galli, Shams Ur Rahman, Nassir Ali, Octavian Antony, and Malek Al-Chalabi for being such good friends and keeping my sanity at bay.

I am grateful to my family for their patience, encouragement and faith. In particular, I am deeply indebted to my precious mother for instilling in me a passion for science and learning and for her unmatched support, encouragement and faith.

Abstract

Understanding and characterising the diffusive transport of capillary oxygen and nutrients in striated muscles is key to assessing angiogenesis and investigating the efficacy of experimental and therapeutic interventions for numerous pathological conditions, such as chronic ischaemia. In particular, the influence of both muscle tissue and microvascular heterogeneities on capillary oxygen supply is poorly understood. The objective of this thesis is to develop mathematical and computational modelling frameworks for the purpose of extending and generalising the current use of histology in estimating the regions of tissue supplied by individual capillaries to facilitate the exploration of functional capillary oxygen supply in striated muscles. In particular, we aim to investigate the balance between local capillary supply of oxygen and oxygen demand in the presence of various anatomical and functional heterogeneities, by capturing tissue details from histological imaging and estimating or predicting regions of capillary supply. Our computational method throughout is based on a finite element framework that captures the anatomical details of tissue cross sections. In Chapter 1 we introduce the problem. In Chapter 2 we develop a theoretical model to describe oxygen transport from capillaries to uniform muscle tissues (e.g. cardiac muscle). Transport is then explored in terms of oxygen levels and capillary supply regions. In Chapter 3 we extend this modelling framework to explore the influence of the surrounding tissue by accounting for the spatial anisotropies of fibre oxygen demand and diffusivity and the heterogeneity in fibre size and shape, as exemplified by mixed muscle tissues (e.g. skeletal muscle). We additionally explore the effects of diffusion through the interstitium, facilitated–diffusion by myoglobin, and Michaelis–Menten kinetics of tissue oxygen consumption. In Chapter 4, a further extension is pursued to account for intracellular heterogeneities in mitochondrial distribution and diffusive parameters. As a demonstration of the potential of the models derived in Chapters 2–4, in Chapter 5 we simulate oxygen transport in myocardial tissue biopsies from rats with either impaired angiogenesis or impaired arteriolar perfusion. Quantitative predictions are made to help explain and support experimental measurements of cardiac performance and metabolism. In the final chapter we summarize the main results and indicate directions for further work.

Contents

List of Figures

List of Tables

Chapter 1

Introduction

Oxygen is a vital element for consuming biological fuel and producing energy. Without adequate quantities of oxygen (O_2, henceforth) a biological cell is unable to drive most of its important biochemical processes, which in turn hinders it from carrying out its biological functions properly. Consequently, a shortage in O_2 supply to cells may destine them to die. Thus, it is no surprise that sustaining a healthy functioning of cells and body tissues requires a continuous supply of O_2.

1.1 Biological background

The delivery of O_2 to tissues is made possible via a cascade of convective and diffusive transport processes within the cardiovascular system [148]. The design of this vascular system accommodates these transport processes by supporting O_2/nutrient supply to, and metabolic waste removal from, tissue cells [151]. On one hand, convection mainly occurs by means of blood flow through vascular networks, where about 98% of O_2 is reversibly bound to haemoglobin within red blood cells (RBCs) and 2% is dissolved in *plasma* [148]. When the oxygenated blood is convected to the heart, it is pumped to the rest of the body via major vessels. Through terminal branches of the cardiovascular system, convection delivers the bulk of O_2 to and carries away metabolite waste from the vessels within tissues [148]. On the other hand, diffusive aspects of transport are driven by a partial pressure gradient from atmosphere down to micro-vessels in the lungs, across the walls of micro-vessels surrounding tissues, through interstitium and tissue cells, down to mitochondria [148, 150].

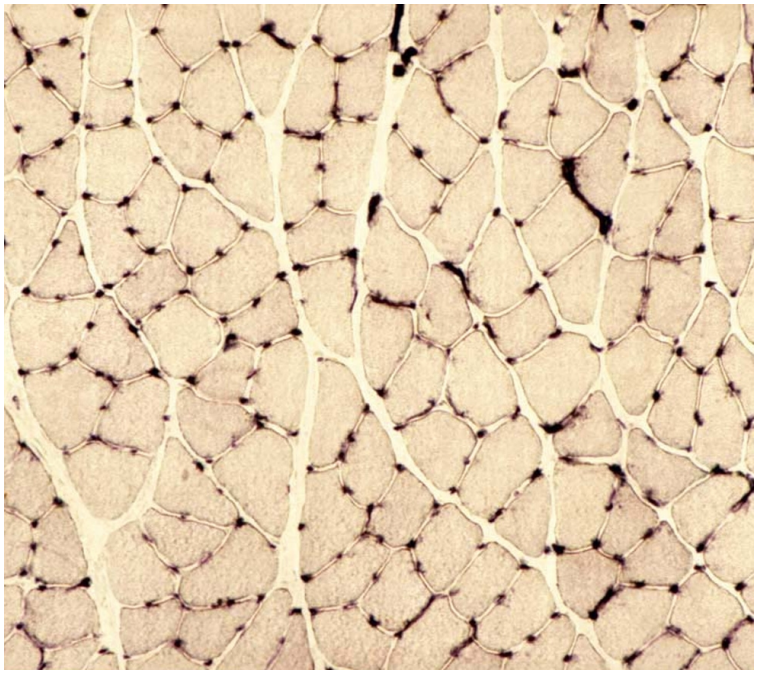

Figure 1.1: A typical tissue cross–section of rat skeletal muscle (*m. extensor digitorum longus*) with capillary location identified by alkaline phosphatase staining (*black*).

1.1.1 Oxygen transport in striated muscles

The transport of O_2 in tissues has received considerable attention, both experimentally and theoretically (see [62, 69, 92, 117, 119, 150, 152, 155] and references therein). In particular, physiologically important tissues that have undergone extensive experimentation and modelling are cardiac and skeletal muscles [13, 71, 117, 125, 152]. These muscles comprise a large fraction of body mass in mammals [148] and possess a simple geometrical structure with capillaries typically running approximately in parallel to fibre axis ([45]; see Fig. 1.1).

In addition, there are numerous histological data available from experimental and clinical studies on cardiac and skeletal muscles (e.g. [41, 137]), which are relatively straightforward to analyse through image processing and within mathematical models due to the simple geometry of cardiac and skeletal muscles [51], thus becoming suitable for studying the effects of physiological complications associated with serious disease (e.g. [42, 74, 153]). For example, in addition to an increased O_2 demand to compensate tissue pathology, there are a number of physiological complications that are directly linked with poor O_2 transport and microcirculation pathology (e.g. ischaemia; [37]).

1.1.2 Biological significance

1.1.2.1 Ischaemia

Ischaemia, a drop in blood supply to organs, tissues, or localised tissue part, is a serious medical condition caused by the constriction or obstruction of blood vessels. It induces local tissue complications due to poor O_2 supply [37], such as *hypoxia* and *anoxia*. Hypoxia is an insufficient tissue O_2 supply, whereas anoxia is a complete deprivation of tissue O_2 supply. Additionally, long-term ischaemia can potentially lead to serious tissue degeneration as seen in:

— gangrene [66], where a considerable mass of body tissue undergoes necrosis (cell death);

— bone necrosis [38], cellular death of bone components due to interruption of O_2 supply;

— angina pectoris [30], severe chest pain due to ischaemia of the heart muscle;

— brain ischaemia [157], insufficient blood flow to the brain (and thus poor oxygenation) leading to the death of brain tissue or cerebral infarction.

The study of O_2 transport in muscles plays a key role in investigating therapeutic interventions for numerous other pathologies, such as chronically ischaemic skeletal or cardiac muscle and cancer [17, 37, 70, 75, 106, 175]. For example, investigating O_2 distribution in tumour cells has led to advances in therapeutic and pharmacological treatments for cancer patients [18]. It was found that hypoxic tumour cells, which are usually resistant to radiotherapy and chemotherapy, can be made more susceptible to treatment by increasing their oxygenation [17]. Indeed, such studies require an objective assessment of functional capillary supply of O_2, thus highlighting the important role capillaries play in O_2 transport at the micro level.

1.1.2.2 Microcirculation

The smaller vessels of the cardiovascular system form the *microcirculation*, which is the part of the cardiovascular system that is composed of an intricate network of arterioles, capillaries, and venules [62]. Due to direct contact with parenchymal (tissue) cells, the microcirculation is known to play a critical role in transporting O_2 to tissues: it ensures adequate O_2 delivery to meet local tissue demand through a local

capillary bed [62, 69, 120]. Core features of this intricate and delicately–balanced delivery system include [62, 149, 155]:

- microvessels and the capillary bed are in very close proximity to parenchymal cells, providing small diffusion distances;
- microvessel walls are highly permeable to O_2;
- complex spatial relationships exist among various microvessels, such as heterogeneity, anastomoses, tortuosity, leading to diffusive interactions between them.

Of key interest in this thesis are capillaries, the terminal delivery conduits in the microcirculation, whose distribution is necessarily vital for healthy O_2 transport. Furthermore, their core properties for O_2 transport are observed to be that [149, 150, 152]:

- the velocity of red blood cells is slowest in capillaries which, leading to largest transient times, allows larger O_2 quantities to dissociate and diffuse away from haemoglobin;
- capillaries have thin walls (a single layer of smooth muscle) which only consume a small fraction of the O_2 destined for tissue cells;
- O_2 diffusion across capillary walls is passive;
- capillaries possess the largest *surface area to volume* ratio among microvessels;
- capillaries are the closest among all microvessels to tissue cells, allowing the shortest diffusion distances.

1.2 Theoretical development

Understanding O_2 transport at the microcirculatory level still faces outstanding challenges [92, 150, 152, 155], most notably the difficulty in quantifying how well a certain tissue is served with O_2. At such scales, experimentally measuring gradients of oxygen partial pressure (PO_2, henceforth) in muscle fibres is technically challenging, and even unachievable in many cases of interest [150, 152]. This has necessitated exploring oxygen transport in tissue using theoretical modelling.

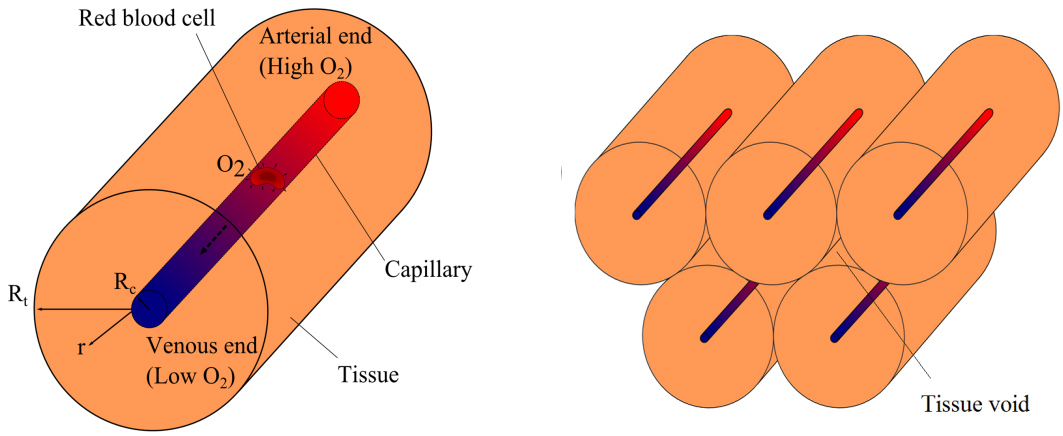

(A) Krogh cylinder (B) Tissue cylinder stacking

Figure 1.2: (A) Traditional view of tissue oxygenation in a Krogh cylinder. Estimation of PO_2 within a circular cylinder of tissue surrounding a capillary of radius R_c; r is the distance from the capillary centre; R_t denotes the cylinder radius where oxygen flux becomes zero [120]. (B) Krogh's view of circular tissue cylinder stacking, where tissue supply voids are inevitable.

1.2.1 Single capillary models

1.2.1.1 Krogh-Erlang model

The earliest attempt in the direction of theoretical modelling was made by the Noble Laureate August Krogh in collaboration with a mathematician named Agner Erlang, with a theoretical analysis of O_2 diffusion into muscle tissue in 1919 [120]. Their analysis was based on the idea that, via a capillary bed, such transport can be represented by a single tissue cylinder of circular cross–section which is supplied solely by a central capillary running parallel to it (i.e. an axisymmetric geometry; Fig. 1.2A). They considered this tissue cylinder to be the region of functional O_2 supply for the central capillary. In deriving the governing equation for O_2 transport in this tissue cylinder, they assumed that tissue O_2 consumption is uniform and constant, tissue PO_2 at the capillary wall equals the average capillary PO_2, tissue O_2 solubility and diffusivity are uniform, axial diffusion of O_2 is negligible in tissue, O_2 microvascular transport is in a steady state, capillaries are parallel and equally–spaced, capillaries receive equal convective O_2 supply, there is no O_2 exchange with adjacent cylinders (i.e. no-flux boundary condition), and capillaries are the only microvessels playing a role in O_2 transport to tissue. Together, these assumptions led to a simple 1D steady–state diffusion problem for oxygen tension, p,

$$K\frac{1}{r}\frac{\partial}{\partial r}\left(r\frac{\partial p}{\partial r}\right) = \mathcal{M}_0,$$
$$\left.\frac{\partial p}{\partial r}\right|_{r=R_t} = 0,$$
$$p(R_c) = p_{\text{cap}},$$

with an analytical solution (the Krogh–Erlang formula)

$$p(r) = p_{\text{cap}} - \frac{\mathcal{M}_0}{4K}\left[R_t^2 \log\left(\frac{r^2}{R_c^2}\right) - (r^2 - R_c^2)\right], \tag{1.1}$$

where R_t and R_c are the tissue and capillary radii with $R_c \leq r \leq R_t$, K is Krogh's diffusion coefficient of oxygen in tissue ($K = \alpha D$; α = oxygen solubility; D = oxygen diffusion coefficient), and $\mathcal{M}_0$ is a constant tissue demand for O_2. For detailed model formulation see reviews by [62, 69, 155]. Combining experimental measurements and geometrical observations of the microvasculature with this formula has led to estimates of the minimum tissue oxygen tension and capillary density [72, 120].

1.2.1.2 Extensions and limitations

Despite the conclusion that the Krogh–Erlang model works in the case of perfectly homogeneous O_2 transport, it does have many limitations that rendered it unable to accommodate a number of important physiological observations (see [119] for details).

Using a similar geometry, subsequent modelling efforts sought to match experimental results and incorporate more physiological details into the Krogh–Erlang model by relaxing its original assumptions (see reviews by [62, 69, 155] for a comprehensive list). Some researchers (e.g. [64, 67, 146, 170, 189]) have relaxed the assumptions pertaining to tissue functional properties to investigate their potential effects on O_2 transport. Others (e.g. [11, 71, 125, 165, 169]) have attempted to incorporate more structural heterogeneities that, in some cases, lead to the consideration of larger systems.

In devising such theoretical models to explore factors affecting O_2 transport in tissue, investigators have used Krogh–like geometries (i.e. based on circular cylinders) which, in most cases, can be deceptively simple. For example, when attempting to close pack (or stack) circular tissue cylinders to form a two-dimensional array of capillaries, non-physiological tissue voids or overlaps in supply from adjacent capillaries are inevitably present (Figs. 1.2B and 1.3). Here, the existence of tissue voids implies an inherent assumption that some parts of muscle fibres do not receive oxygen at all (anoxic regions), while tissue overlaps reflect possible interaction between adjacent capillaries. When a large number of capillaries are present, significant fluxes due to surrounding capillaries dictate the feedback between local tissue oxygenation and any given capillary, thus the effect of capillary interaction should be significant. Single Krogh–cylinder models do not capture this feature. Moreover, such models assume global features only by incorporating average values of physiological parameters. However, local variations in fibre size and metabolic demand are apparent in tissues possessing a heterogeneous capillary distribution [49].

In order to avoid tissue voids and overlaps, other researchers generalised Krogh's cylindrical tissue geometry by considering evenly–stacked cylindrical alternatives to approximate the tissue regions supplied by individual capillaries (*capillary supply regions*), but only found minor differences in comparison to studies based on Krogh cylinders. For example, Thews [178] and Hudson and Cater [107] considered hexagonal cylinders, Popel [154] considered square cylinders, and more generally Gonzalez-Fernandez and Atta [72] considered these alternatives in addition to equilateral triangular cylinders. Imposing functional and structural homogeneity assumptions in these models has simplified their study by considering only one such representative cylinder. However, in addition to following the classical route of using global tissue features and neglecting intercapillary interaction, their models still failed to explore the effects of tissue heterogeneities.

The need to capture the influence of heterogeneous tissue properties (spatial and functional) on O_2 supply has led to further generalisations of the Krogh model: (1) Multi-cylindrical systems and (2) Multi-capillary systems.

1.2.2 Multicylindrical models

As the name implies, multi-cylindrical models consider an array of Krogh cylinders. To accommodate spatial heterogeneities, Hoofd and co-workers [97] generalised the

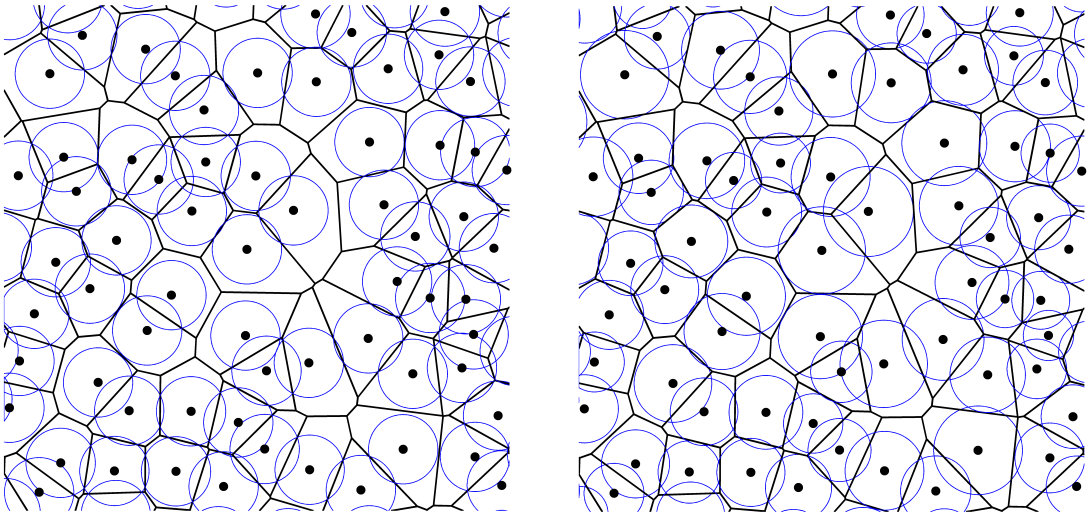

(A) Uniform radii (B) Non-uniform radii

Figure 1.3: A sample of random capillaries (dots) and the Voronoi polygon approximation of their capillary supply regions (heavy polygons; see text) and Krogh cylinders (light circles). (A) The radius of Krogh cylinders is derived by taking the cylindrical cross–section to have an area equal to the average area of capillary domains. (B) Each Krogh cylinder has a cross–sectional area equal to that of the Voronoi polygon enclosing its central capillary. In this case the total area of the circles is equal to the total area of the polygons. Note how some tissue areas are not covered by circles, while some are covered several times.

aforementioned evenly–stacked and symmetrical tissue cylinders to allow for asymmetrical space–filling cylinders via using Voronoi polygons (also termed *capillary domains*, DOM; [51, 97]) to approximate capillary supply regions. A Voronoi polygon enclosing a capillary is made up of all the tissue points that are closer to this capillary than all other capillaries. The fact that heterogeneities in capillary arrangements could lead to heterogeneities in areas of Voronoi polygons led Hoofd to suggest using distributions of these areas to obtain a heterogeneous array of Krogh cylinders of matching areas, from which cylindrical radii were easily calculated (Fig. 1.3A). Using these ideas, Turek and colleagues [183] obtained various arrays of Krogh tissue cylinders (Fig. 1.3B). Unfortunately, these efforts did not succeed in eliminating the aforementioned voids and overlaps in tissue domain [51], nor did they allow for capillary interactions [49].

1.2.3 Multicapillary models

Conversely, in multi-capillary systems, researchers abandoned the geometry of Krogh cylinders and attempted to either extend the Krogh–Erlang solution formula by as-

suming that capillaries can be approximated by point–like sources in sufficiently large tissue cross–sections [26, 93, 94, 98, 154, 186], or by attempting semi-analytical and computational methods. We remark here that the point–source approximation of capillaries ignores two factors influencing tissue O_2 levels: (1) the shape of the capillary cross–section and (2) capillary interactions.

1.2.3.1 Point–source approximations

In the limit of vanishing capillary radius, the Krogh–Erlang formula, Eq. (1.1), can be thought of as a generalised solution to the problem where an oxygen point source supplies a concentric circular tissue region consuming oxygen at a rate $\mathcal{M}_0$. In particular, the form of the solution is

$$p = \text{Constant} \; + \; \text{Source} \; + \; \text{Consumption field},$$

where the constant term represents the capillary oxygen supply, the source term is the fundamental solution to Laplace's equation in 2D with source at $r = 0$, and the consumption field is a particular solution to the non-homogeneous problem (Poisson's equation with consumption term), which depends on the geometry of the tissue field.

Some researchers used this observation in an attempt to develop a generalised solution for the transport equation given multiple capillary sources embedded in the cross–sectional tissue plane [92]. The solution has the form

$$p(r) = C_p - \frac{\mathcal{M}_0}{4K}\left\{ \sum_{i=1}^{N_c} \left[\frac{A_i}{\pi} \log\left(\frac{|r - r_i|^2}{r_{ci}} \right) \right] - \Phi(r) \right\}, \tag{1.2}$$

where N_c is the number of capillary sources, r_i is the centroid of the i^{th} capillary, r_{ci} is the radius of the i^{th} capillary, $\Phi(r)$ is the consumption field obtained from solving for the non-homogeneous solution of Poisson's equation over a predefined tissue field ($K\Delta p = \mathcal{M}_0$), and A_i is the tissue area exclusively supplied by individual capillaries.

Using the method of images, Clark and co-workers [26] were able to numerically

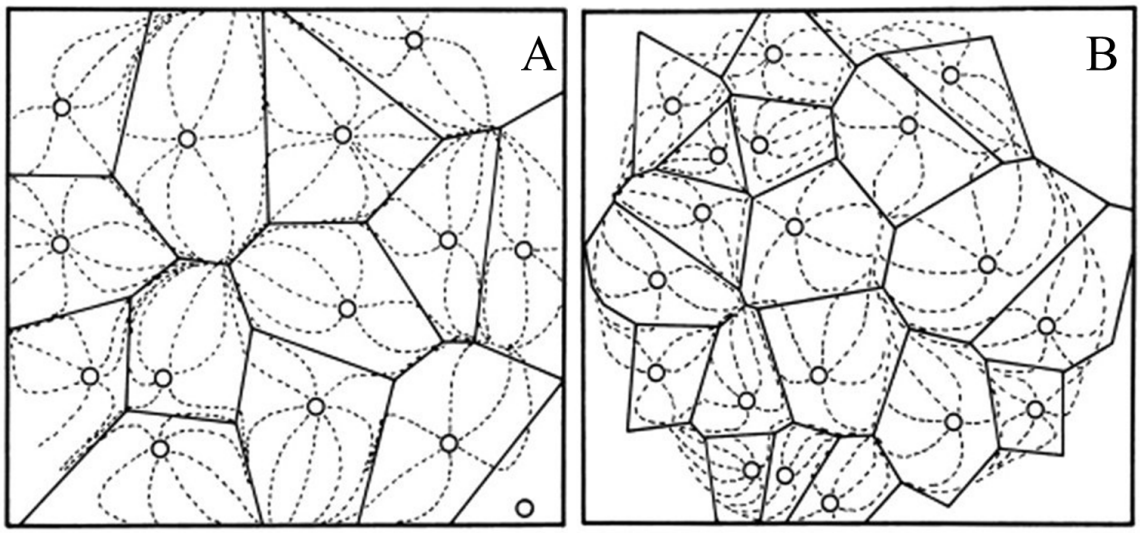

Figure 1.4: (A) If capillaries (open circles) have identical transport capacity, the predicted O_2 flux lines (dotted lines) coalesce at a no-flux points that match capillary domain boundaries (solid lines). (B) Given any capillary may be surrounded by distinct fibres, the heterogeneity in fibre composition and oxygen consumption reduces the fit between no-flux and capillary domain boundaries for mixed muscles. From [51, 98], with permission.

compute PO_2 distributions, but did not consider capillary supply regions. On the other hand, Hoofd and colleagues [96, 98] and Hoofd [93, 94] considered these supply regions by deriving analytical approximations for tissue PO_2 that are valid in the vanishing limit of the ratio of capillary diameter to domain size, ϵ. However, in solving their capillary sources equation, the requirement that flux integrals around boundaries of capillary supply regions must be zero led to a non-unique solution, as illustrated in [186]. Additionally, using weakly heterogeneous tissue properties, Hoofd and collaborators [96] concluded that capillary supply areas should be similar to Voronoi polygons (Fig. 1.4).

1.2.3.2 Spectral methods

Another notable contribution was made by Wang and Bassingthwaighte [186]. Similarly, they treated capillaries as point sources, but they also considered heterogeneous capillary distributions and non-uniform perfusion to test the degree of qualitative agreement between capillary supply regions and Voronoi polygons, and concluded that such equality was not feasible in general. This, however, was based on unrealistically low capillary densities. From a physiological viewpoint, these systems are not representative tissue regions and are subject to substantially exaggerated influences of

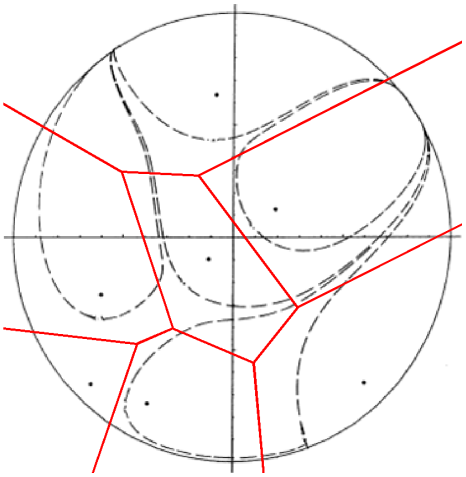

Figure 1.5: Under very low capillary densities, most capillaries (dots) would have supply regions in direct contact with the external modelling boundaries (black circle). In such cases, capillary supply regions (dashed) are greatly affected by the external boundary conditions imposed by the modeller. Red = Voronoi polygons. Modified from [186], with permission.

the domain boundary (Fig. 1.5). Nonetheless, this still leaves the question of whether Voronoi polygons are appropriate in the physiological setting. It is worth noting that the analytical solution obtained by Wang and Bassingthwaighte gives similar results to Clark and colleagues [26], but it differs from Hoofd's solution [94] by one term, namely, the solution to the homogeneous problem. In particular, Hoofd obtained a constant term whereas Wang and Bassingthwaighte derived an infinite Fourier expansion, thus contributing an additional computational complexity (refer to Eq. (1.2)). We note here that the analytical solvability of the Wang–Bassingthwaighte model is due to the use of a capillary–tissue boundary condition which is essentially based on angular averages of O_2 fluxes across capillary walls. In fact, up until this point, all efforts seeking to derive analytical approximations in the limit of point–like sources employ integral averages for boundary conditions at capillary walls. Such boundary conditions impose an averaged capillary O_2 flux which, in turn, implies that local O_2 flux variations are not accounted for.

1.2.3.3 Singular perturbation methods

To avoid the obvious weaknesses inherent in point–source approximations, such as the difficulties of representing PO_2 near a source in a complex system of capillaries, Titcombe and Ward [179] treated capillaries as having arbitrary areas and shapes when studying the steady–state diffusion problem in an analytical study. Although

they did not consider capillary supply domains, their study has cautioned against using point–source approximations to compute PO_2 without proper justification. In particular, they showed that the approximations in [26, 93, 94, 96, 98, 186] represent only the leading term in an infinite asymptotic expansion of the PO_2 in powers of $-1/\log(\epsilon)$, where ϵ is the ratio of capillary diameter to domain size. As such, relative errors in point–source approximations will scale with this term, which is negligible for sufficiently small ϵ. However, achieving a reasonable accuracy of 10% requires $\epsilon = 4.5 \times 10^{-5}$; this would impose domain sizes that are impractically large (for capillary radius 4 μm, the domain size is 15 cm). Thus, this could affect the validity of certain modelling assumptions pertaining to the original tissue scales considered (for instance, constant parameters). Interestingly, the alternative analytical expansion of Titcombe and Ward is expected to simplify when uniform circular shapes are assumed for capillaries, though this is unexplored.

1.2.3.4 Homogenisation methods

The nature of oxygen transport in striated muscle follows a multiple–scales description (intracellular, intercellular, capillary bed, tissue and organ scales). A few attempts have been made to develop a macroscale description of oxygen transport to striated muscle organs by homogenising fine-scale variations. Salathé [164] developed the earliest model of homogenised oxygen transport in uniform muscle by smoothing intercapillary variations using a volume–averaging over the tissue–capillary space. He derived a single PDE describing a volume–averaged oxygen transport that accounts for capillary convection, tissue diffusion, and tissue consumption:

$$\frac{\partial}{\partial t}\Big[c + \Psi CS(c)\Big] + \frac{\partial}{\partial q}\Psi v_c\Big[c + CS(c)\Big] = D\Delta c - (1-\Psi)M,$$

where Ψ is the volume fraction of capillary space, C is the O_2 content at 100% haemoglobin saturation, S is the haemoglobin O_2–saturation relationship ($0 < S < 1$), v_c is the velocity of blood within capillaries, q is coordinate along capillary axis, D is the O_2 diffusivity, and M is the tissue O_2 consumption rate. This formulation allowed an investigation of large scale oxygen gradients within tissue, thus permitting *macro* diffusional interactions of adjacent tissue regions to be explored. Nonetheless, the contribution of fine–scale variations was not accounted for by Salathé's *macro*

diffusion and oxygen consumption rates, nor was the average extent of capillary supply regions explored. In addition, the model could not resolve potential significant fluctuations in local oxygen tension at the level of a few capillaries, though heterogeneities in intercapillary separation are known to impact global tissue PO_2. Indeed, such factors may also influence the extent of capillary supply regions.

1.2.3.5 Computational methods

A major part of our current state of knowledge is due to the development of sophisticated computational models of oxygen transport in muscle striated tissues [11, 13, 71, 125, 154, 156, 169]. These models explored the spatial distribution of oxygen tension under different capillary and/or fibre arrangements and parameter regimes. Nonetheless, solving such models still consumes a large amount of computer memory and time at the expense of restricted tissue and capillary bed sizes and smoothed-out histological details. This imposes prohibitive limitations especially when high–throughput processing of data from biological experiments is demanded to establish statistical significance. In addition, the nature of these models permits no investigation of any influence that individual capillaries and/or fibres may have on oxygen transport. In particular, the spatial limitations inherent in exploring average values for PO_2 do no permit an exploration of the local balance between capillary supply and oxygen demand, thus potentially missing important regulatory mechanisms in tissue.

1.2.3.6 Green's function methods

Hsu and Secomb [105] developed a modelling framework for steady–state oxygen delivery from vascular networks to tissue regions based on a Green's function approach. Intravascular oxygen transport was described in terms of a distribution of oxygen sources along the capillary axis (i.e. a line source). Assuming a constant (and uniform) tissue oxygen consumption, this led to a Green's function solution (an integral solution) for tissue oxygen distribution which, when combined with a local transport equation (Krogh–type), permitted an efficient iterative numerical computation of the source strengths along the capillary. However, this efficiency is lost when considering nonlinearities in oxygen consumption (Michaelis–Menten kinetics) and oxygen diffusive flux (facilitated–diffusion by myoglobin) for cases of low oxygen tension [168]. Nonetheless, this framework allowed for arteriole–capillary interactions to be explored theoretically, regardless of the spatial arrangement of capillaries and arterioles, leading to important contributions to our understanding of the influence of microvascular

spatial arrangements and the relative importance of diffusive and advective supply from arterioles to capillaries.

Currently, however, this framework is restricted to uniform tissues (i.e. tissues with spatially uniform oxygen demand). In contrast, skeletal muscles exhibit local variations in muscle fibre phenotype (e.g. metabolic demand), a heterogeneity that may have a significant influence on both global oxygen levels [125] and local capillary supply, particularly capillary supply regions (though this has not been considered in detail in the literature). In addition, given local capillary supply is significantly influenced by capillary–capillary interactions, line–source approximations may suffer from a large domain–size restriction for higher order errors to be negligible, as has been demonstrated in 2D [49, 179]. It is interesting to note here that, to our knowledge, the accuracy of such approximations has not been confirmed yet against computational models of 3D cylindrical capillaries (e.g. [13, 71]) where finite–element or finite–difference methods are used. Indeed, in the latter models, capillaries possess a volume with a wall dictating an oxygen flux that is proportional to the oxygen tension difference across the capillary (i.e. Robin–type boundary conditions), thus automatically accounting for capillary–capillary interactions.

1.3 Theoretical critique

1.3.1 Limitations of current tissue frameworks

In experimental biology, in order to understand the system under consideration it is vital to determine the functional consequences of interventions or pathologies. In particular, experimental investigations of microvascular remodelling (angiogenesis) in striated muscles [49, 106] have demonstrated that it is a highly coordinated physiological process that appears to compensate for potential losses of the local oxygen demand–supply equilibrium. How this process is assessed in functional terms is still a topic of extensive undergoing research.

Theoretical advances in the field of microvascular oxygen transport have led to a profound understanding of some of the major biophysical processes governing oxygen delivery to tissue. A major consequence of this was the appreciation of intravascular resistance to oxygen transport (blood flow re-distribution and rate, the role of haematocrit, haemoglobin kinetics, oxygen extraction pressure, capillary network structure, and microvascular shunting). Functional consequences of pathologies or structural

network adaptation can be theoretically explored, but are usually based on predicting the average spatial distribution of oxygen in idealised tissue and capillary network realisations. While such predictions have led to profound insight into the physiology of oxygen delivery and demand, the current theoretical approaches still lack a number of important considerations:

1. since capillaries are embedded in a contiguous tissue region, simply assuming each capillary supplies a pre-defined tissue region (e.g. Krogh cylinder) implies that there is no significant exchange between neighbouring capillaries, and that capillary shunting is not feasible;

2. while PO_2 predictions are informative for comparative studies, they give no information whatsoever about the spatial extent of individual capillary supply. This, in turn, implies that any potential *local* regulation between capillary supply and fibre demand and/or size may be missed. Moreover, such predictions are mainly based on large scale and "idealised" tissue geometries rather than histological ones, thus implicitly assuming that histological scales have negligible effect on tissue oxygenation;

3. individual capillary supply, if delimited spatially, will give rise to a space–filling generalisation of Krogh cylinders. Each such tissue cylinder is predicted to be supplied by the individual capillary enclosed within. The spatial extent of these cylinders as well as the average PO_2 within them may give insight into the regulation of individual capillary growth and the local balance between supply and demand in mixed muscles, potentially allowing for a theoretical measure of localised angiogenic signals;

4. since capillaries can be embedded in a tissue where oxygen extraction is spatially heterogeneous, one may be able to better understand the interplay between fibre and capillary physiology with the aid of generalised Krogh cylinders;

5. the nature of physiological research typically demands experimental designs and methodologies that aim to produce large datasets with statistically significant results. In terms of functional consequences, a side-by-side *in silico* experimentation will inevitably inherit the burden of processing such large data sets. Apparent issues with this are: (a) current medical imaging technology is unable to construct sufficiently 3D tissue slabs (fibres and capillary network)

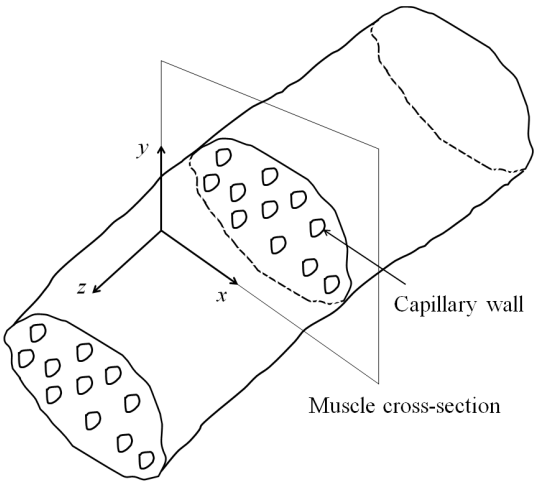

Figure 1.6: A schematic illustration showing a planar cross–section perpendicular to muscle fibre axis. Reproduced and modified from [179], with permission.

with reasonable accuracy to allow for statistically significant results, (b) even with accurate 3D imaging, computational O_2 transport modelling is still limited by computer capabilities, (c) current 3D *in silico* modelling is memory hungry and time consuming even for an idealised tissue of 30 fibres and 50 capillaries (18 hour/run; [71, 125]) (d) high resolution anatomical and histological details will have to be smoothed out, although as of yet no theoretical work has ever attempted to justify or explore such an assumption;

6. in contrast, it is relatively easy to extract two-dimensional (2D) sections perpendicular to fibre orientation from muscle biopsies (see Fig. 1.6), perform histochemical staining to resolve micro-anatomical and functional details, and export digital images of these for theoretical investigations of oxygen transport.

1.3.2 Current planar frameworks

From the previous review of theoretical modelling, there is a clear disagreement as to whether Voronoi polygons can accurately represent capillary supply regions. For example, with homogeneous and some heterogeneous (yet symmetrical) capillary arrangements, Voronoi polygons match the biophysical predictions of capillary supply regions perfectly [96, 186]. However, Voronoi polygons still pose many issues as possible representatives of functional capillary supply regions. In particular, Wang and

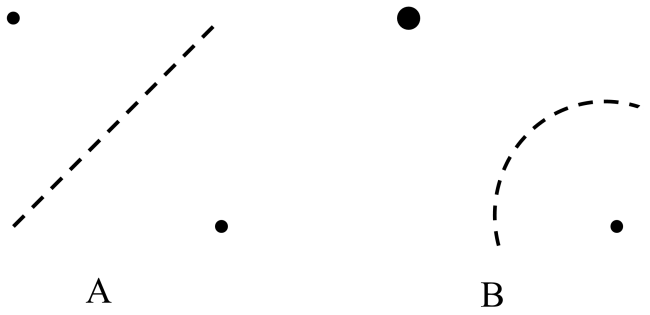

Figure 1.7: A geometrical argument demonstrating the potential effect of different relative strengths of adjacent capillary sources. (A) Voronoi polygon boundary. (B) Capillary supply region boundary. Relative dot size reflects the relative source strengths. Reproduced from [186], with permission.

Bassingthwaighte [186] presented a geometrical argument showing that this agreement is bound to worsen if the strength of adjacent capillaries varies extensively (Fig. 1.7). Similarly, Egginton and Gaffney [49] have recently shown that breaking the symmetry in capillary distribution can lead to deterioration of the representation of capillary supply regions by Voronoi polygons. However, it is still unknown to what extent the introduction of asymmetry in capillary distribution has an effect on the ability of Voronoi polygons to capture functional capillary supply. More so, it is as yet unclear whether Voronoi polygons can be a reliable candidate for capillary supply regions and, therefore, it is apt to investigate how well Voronoi polygons represent areas of capillary supply. Such investigations necessitate a consideration of the fundamental biophysical processes underlying O_2 transport as well as geometries that are faithful to the histological details of muscle tissue cross–sections.

1.4 Capillary oxygen supply

As detailed previously, the capillary supply of oxygen was originally conceived as being restricted to a pre-defined area of the respiring tissue (e.g. Krogh cylinders and capillary domains), which allowed the influence of the surrounding tissue to be explored via models of tissue oxygenation. In particular, it was realised that a balance must exist between the extent of this area of supply and the metabolic demand of the surrounding tissue in order for muscle fibres to sustain healthy function. Despite this insight into local oxygen regulation, these anatomical constructions proved to have inherited artefactual spatial limitations that are dictated by idealised capillary and tissue geometries. We devote this section to addressing this problem by detailing the

current physiological use of capillary supply regions and deriving a realistic framework on which mathematical models of oxygen transport can be based.

1.4.1 Local environment

In the previous section we emphasised the anatomical relevance of capillary supply regions for applications of oxygen diffusion theory. Here, we discuss the physiological importance of the natural partitioning of capillary supply regions by muscle tissue fibres as dictated by the local heterogeneity in anatomy and metabolic demand surrounding capillaries.

In early models of striated muscles, interstitial spaces are formed by close–packing Krogh cylinders (Fig. 1.2B), though *in vivo* observations reveal much more local heterogeneity of muscle fibre cross–section, size and the associated capillary distributions and interstitial regions (Fig. 1.1). Given the growth of capillaries is predominantly restricted to interstitial spaces, capillary distributions (and thus spacing) is heavily influenced by fibre size and shape [50, 53]. Therefore, to objectively analyse the growth process in tissue, capillary supply of oxygen needs to be explored in relation to the natural heterogeneous features of muscle fibres. The local nature of these features dictates that objective measures of local capillary supply should incorporate the cross–sectional heterogeneities of individual fibres and the capillary bed.

Exploring the extent of capillary interaction with the surrounding fibres is currently quantified in terms of the overlap between the planar capillary supply region and the surrounding muscle fibres (Fig. 1.8; [51]). In tessellating a muscle tissue cross–section by regions of individual capillary oxygen supply, muscle fibres are unambiguously partitioned in such a manner as to account for both the proximity of neighbouring capillaries and the heterogeneity in their spacing. In particular, the capillary contribution to an individual fibre is proportional to the fraction of its oxygen supply region that overlaps the fibre. Hence, regardless of type, each fibre is effectively supplied by a "number" of capillaries that is equal to the sum of fractional contributions from all overlapping capillary supply areas. This definition characterises a local capillary supply to individual fibres that is flexible enough as to account for (1) the heterogeneity in local capillary spacing, (2) the influence of neighbouring fibres, (3) the heterogeneity of fibre size, and (4) the influence of neighbouring capillaries. If further refined by normalising by fibre area, this measure can provide direct information about the balance between local capillary supply to and oxygen demand of

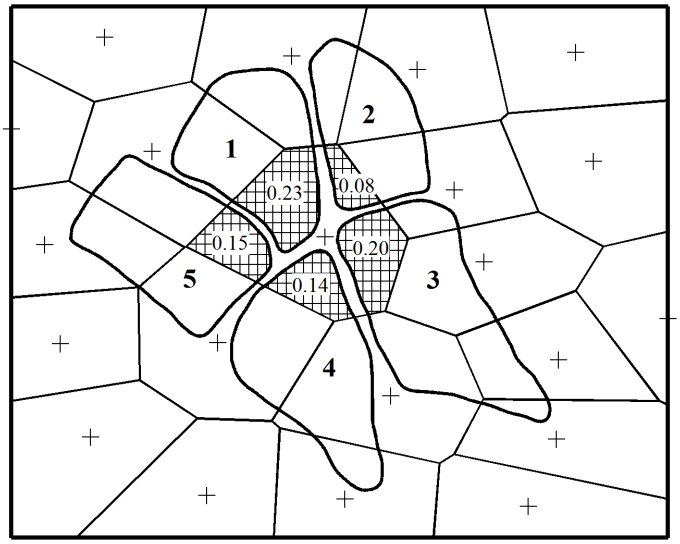

Figure 1.8: Muscle fibres partition capillary supply unambiguously by overlapping capillary domains. The central domain (shaded) overlaps five neighbouring fibres (bold polygons indicated by the numbers 1–5) in proportion to its proximity. Here, the physiological premise is that capillary supply of the central capillary is divided among adjacent, and metabolically similar, fibres in proportion to the overlapping domain fraction. The effective local capillary supply to each such fibre is the sum of the fractional contribution from all overlapping domains (capillary domain centroids are indicated by a + sign). Note that this method allows capillary supply to fibres with no direct contact (e.g. fibre #5). Reproduced from [51], with permission.

metabolically distinct fibres in mixed muscles. Indeed, not only have distributions of idealised supply areas demonstrated a great sensitivity to adaptive microvascular remodelling (angiogenesis) in skeletal and cardiac muscles [106], but also their derived local supply indices have highlighted the importance of factors other than fibre size in determining capillary oxygen supply (e.g. oxidative capacity; [1, 50, 193]).

1.4.2 Morphometric analysis

Morphometric analyses of striated muscles are quantitative analyses that seek to adequately describe the anatomical (or histological) distribution of capillaries and their interaction with muscle fibres to derive estimates of functional capillary supply of oxygen (and other nutrients) [51], where 'functional' refers to the maximal allowable capillary supply to meet maximum tissue oxygen uptake. Furthermore, it is important to note here that the structural indices describing a capillary bed represent a limiting factor only during the relatively infrequent bouts of maximal activity, thus they can

only estimate the maximal capacity of a system [51]. However, this may be feasibly extended to assess the functional characteristics of a normal physiological state by estimating capillary supply of oxygen from mathematical models of oxygen transport that are based on representative images of histological muscle sections. There are currently numerous indices estimating capillary oxygen supply to tissue, and these can be generally categorised into two: global and local indices.

1.4.2.1 Global indices

Many measures have been developed to estimate functional capillary supply of oxygen, see for example [50, 51]. Some of these measures are 'scalar' such as the *capillary–to–fibre ratio* (C:F), the *intercapillary distance* (ICD), and the *capillary density* (CD). These measures represent global averages of tissue properties, rendering them scale–dependent as they can be greatly affected by fibre growth (or shrinkage) when the tissue is subjected to local remodelling. Hence, such indices cannot account for the local geometry of the underlying capillary distribution and instead only resolve global details, neglecting potentially important cellular level details such as local pockets of ischaemia [82].

1.4.2.2 Local indices

Measures based on distributions of capillary functional supply areas are far more informative as physiological changes tend to occur locally (Fig. 1.9; [51]), and thus averages do not capture relevant information. In contrast to scalar measures, these are typically scale–independent by definition and account for both local area and capillary count variations. Further examples that are currently used by physiologists include the *local capillary–to–fibre ratio* (LCFR) and the *local capillary density* (LCD; also known as the capillary fibre density, CFD), which will be detailed below.

1.4.3 Capillary supply regions

In an effort to develop a histological framework on which we can base mathematical models of oxygen diffusion in tissue, we present two approximations for the capillary supply region. Essentially, these are geometrical constructions that can be used as basis for the extraction of functional capillary supply areas from a muscle cross–section (Fig. 1.1), hence generalising the concept of a Krogh cylinder. The first is called a *capillary domain* (mathematically equivalent to a Voronoi polygon; Fig. 1.10A),

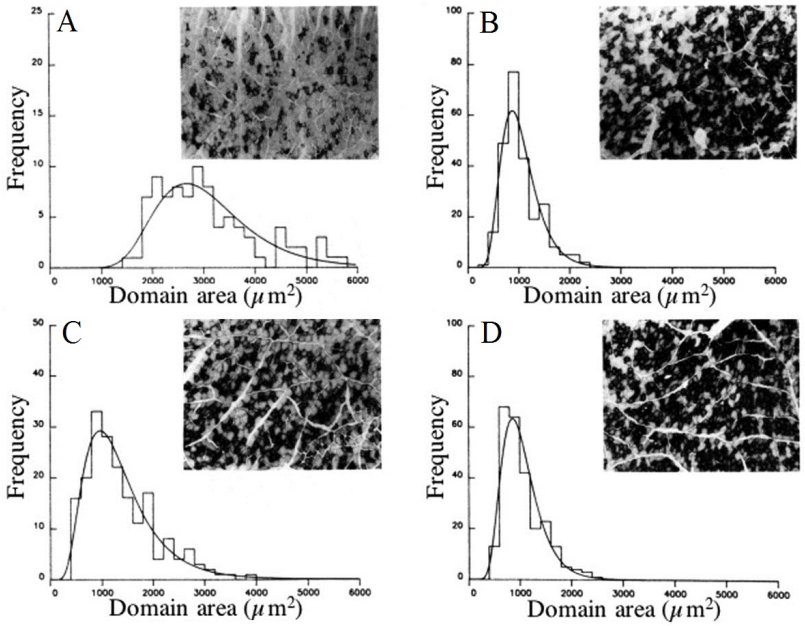

Figure 1.9: Indices of local capillary supply show distinctive lognormal distributions, demonstrating that capillary supply is qualitatively the same across different skeletal muscles. (A-D) Cross sections from muscles with different fibre–type compositions are inset against the frequency distribution of their capillary domain areas. Though the scale of the images of tissue sections is not provided in the original publication [45], all muscle images have the same scale. From [45], with permission.

which is a geometrical representation of capillary supply area that is based solely on the spatial distribution of capillary locations. The second is called a *flux trapping region*, which is the region predicted to be diffusively supplied with O_2 from individual capillaries in biophysical models of oxygen transport and thus is influenced by parameter estimates for biophysical tissue properties as well as the observed geometry of the capillary bed. However, trapping regions are not simple to calculate and, currently, physiologists use Voronoi polygons (defined in Section 1.4.3.1 below), as a convenient measure since all information is known only from the planar distribution of capillaries in a muscle tissue cross–section [50, 82].

Indices derived from Voronoi polygons have become very useful for highly homogeneous tissues, such as the cardiac muscle (myocardium) [51]. For example, using theoretical modelling based on the assumption of identical capillaries supplying tissue with uniform O_2 consumption, Hoofd and co-workers [96] demonstrated that Voronoi polygons closely match capillary supply regions in rat myocardium (Fig. 1.4A), although this match may be weaker in mixed muscles (Fig. 1.4B). Note, however,

despite their success, the idea behind Voronoi polygons is still based on a naïve rationale, namely, that the muscle tissue should be served by its nearest capillary, regardless of the metabolic surrounding. As we discussed before, in the presence of structural and functional heterogeneity within tissue such an assumption should be questioned.

1.4.3.1 Voronoi polygons

The Voronoi polygon (VP) of a capillary is a polygonal section of a muscle tissue cross–section that encompasses this capillary. In particular, this domain is made up of all points in a muscle cross–section that are closer to this capillary than to any other. An example of Voronoi polygons is shown in Fig. 1.10A.

We begin by assuming that in a muscle tissue cross–section, as in Fig. 1.1, capillary locations are represented by a single point, say the centroid of each capillary in the transverse image plane. Let N_c denote the number of capillaries, $\mathbf{x}_i$ denote the position of the i^{th} capillary, and Ω represent the global domain. Then the Voronoi polygon containing the i^{th} capillary is defined as the set

$$V_i \stackrel{\text{def}}{=} \left\{ \mathbf{x} \;\middle|\; \mathbf{x} \in \Omega;\ |\mathbf{x} - \mathbf{x}_i| \leq |\mathbf{x} - \mathbf{x}_k|,\ k \neq i \right\}. \tag{1.3}$$

This definition states that the Voronoi polygon associated with the i^{th} capillary is the closure of the set of points which are closer to capillary i than any other capillary. Note that Voronoi polygons tessellate Ω.

Voronoi polygons are easily determined from tissue cross–sections and very convenient to work with; thus they are used by physiologists to quantify capillary supply of oxygen in muscle with the assumption that they are considered to represent the area of muscle that receives O_2 from the capillary inside it. This appears reasonable at first sight as it assumes that every tissue point should receive O_2 from its nearest capillary. We know, however, that this is not always true; some capillaries further away may supply a given area of muscle if they produce higher gradients of PO_2. Nonetheless, Voronoi polygons may still provide a good approximation to the area of muscle receiving O_2 from a capillary, and this will be investigated in later chapters.

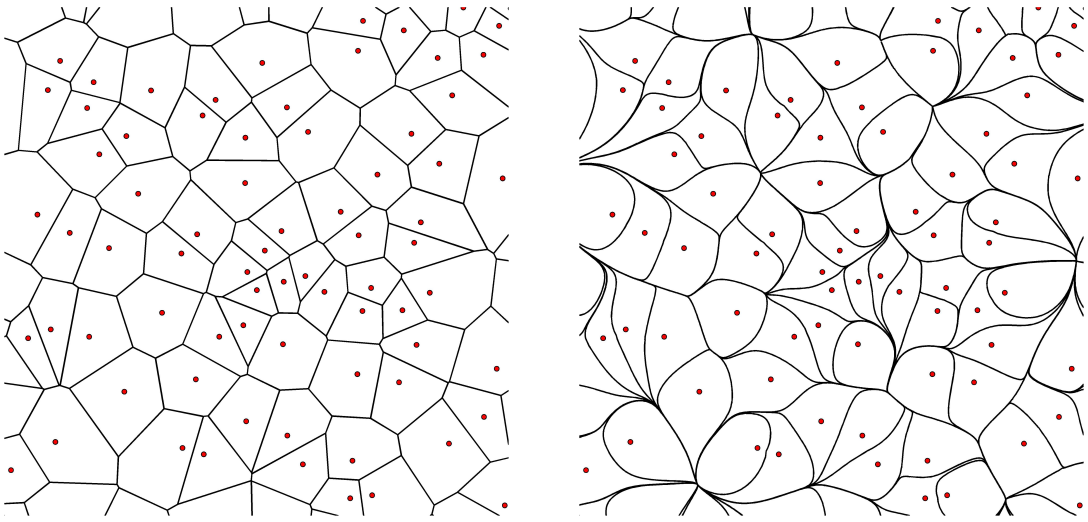

(A) Voronoi polygons (B) Flux trapping regions

Figure 1.10: Examples of Voronoi polygons and trapping regions tessellating the same plane. (A) Voronoi polygons tessellating the plane. (B) Typical flux trapping regions tessellating the same plane (i.e. the same planar capillary distribution). Capillaries are represented by red discs.

It is also worth noting that every point in the muscle is either on or inside a Voronoi polygon. Biologically, this implicitly implies that the entire muscle tissue receives at least some O_2. This is, again, something that does not hold in all cases; indeed this study is motivated by diseases resulting from insufficient O_2 delivery to muscle, though anoxia is only relevant to the severe pathologies of cancer tissue, where such approaches are not relevant due to the complexity of the vascular network geometry.

Derivative indices of the functional capillary supply for maximal activity are the local capillary–to–fibre ratio ($LCFR$) and the local capillary density (LCD). To define these, let Ω_j denote the region of the j^{th} fibre and let $A(\cdot)$ denote the two-dimensional Euclidean measure. Then the $LCFR$ and LCD of the j^{th} muscle fibre are mathematically defined as

$$LCFR_j \stackrel{\text{def}}{=} \sum_i \frac{A(\Omega_j \cap V_i)}{A(V_i)}, \qquad LCD_j \stackrel{\text{def}}{=} \frac{1}{A(\Omega_j)} \sum_i \frac{A(\Omega_j \cap V_i)}{A(V_i)}.$$

The meaning of these definitions is clear given a Voronoi polygon represents the

region of a capillary supply (Fig. 1.8). $LCFR_j$ denotes the sum of the fractional areas of all the Voronoi polygons intersecting the j^{th} fibre. Thus, it is taken to represent the fractional number of capillaries supplying the j^{th} muscle fibre with O_2, i.e. the number of capillary equivalents of supply at maximum supply capacity. Similarly, LCD_j is the number of capillaries supplying the j^{th} muscle fibre per unit area of muscle fibre.

In particular, under the assumption that Voronoi polygon areas accurately represent the regions of capillary supply, the distribution of Voronoi polygon areas and the distributions of their derivative indices can be used to estimate capillary supply capacity [50, 82], following microvascular remodelling or disruptions in the regulation between angiogenesis and oxygen demand [10, 31, 48, 112, 167, 194]. This is especially pertinent in the context of ischaemia due to disease and associated therapeutic interventions, which include strength training [37, 175], endurance exercise [1, 167], electrical stimulation [43] and alterations in temperature [47, 48].

1.4.3.2 Flux trapping regions

The second capillary supply region we are interested in is the *flux trapping region* of a capillary (Fig. 1.10B), sometimes referred to as a trapping region (TR) for brevity. This is a collection of all points that 'functionally' receive O_2 from a given capillary, at least according to the biophysical model under consideration. Here, *functional* signifies the diffusive transport of O_2 which depends on the properties of tissue as well as capillary locations and intravascular capacity. Thus, for a given capillary, this region is the smallest domain enclosing the capillary, with zero flux conditions on its boundary. Put mathematically, given a PO_2 solution to the model equations of O_2 transport in tissue, p, the TR $D_i \subseteq \Omega$, with outward pointing normal $\mathbf{n}_i$ is defined to be the smallest domain satisfying

$$D_i \stackrel{\text{def}}{=} \left\{ \mathbf{x} \in \Omega \;\middle|\; \mathbf{n}_i \cdot \nabla p = 0,\ \mathbf{x} \in \partial D_i \right\}. \tag{1.4}$$

Note that this is a model–dependent definition. In particular, TRs take into account some functional and structural physiologic parameters, depending on the model assumptions. Each D_i yields the region surrounding a capillary where the flux

out due to the i^{th} capillary is balanced by the flux due to all the other capillaries put together. In contrast to Voronoi polygons, the sets D_i need not tessellate Ω; if they do not, then there is at least one region in Ω which does not receive O_2 from any capillary.

Although TRs provide a more physiologically representative measure of how the muscle partitions capillary oxygen supply, they are more challenging to work with than Voronoi polygons. The exact position and size of Voronoi polygons are known just from the position of capillaries. For physiologists, this is important as it requires no experimental parameter estimation, mathematics or numerics to find the predicted area of O_2 supply. To know the area or position of TRs not only do we need to know where the capillaries are, but also the PO_2 at every point in the muscle, which is inferred from modelling.

The analogous derivative indices, local capillary–fibre ratio ($\mathcal{LCFR}$) and the local capillary density ($\mathcal{LCD}$), are defined by

$$\mathcal{LCFR}_j \stackrel{\text{def}}{=} \sum_i \frac{A(\Omega_j \cap D_i)}{A(D_i)}, \qquad \mathcal{LCD}_j \stackrel{\text{def}}{=} \frac{1}{A(\Omega_j)} \sum_i \frac{A(\Omega_j \cap D_i)}{A(D_i)}.$$

By construction, the D_i represent the region of supply of the i^{th} capillary, at least according to the model used to predict tissue PO_2. In the physiological literature [50, 51], however, Voronoi polygons are employed as representatives of this region (capillary domains), and the validity of this assumption or otherwise dictates the validity of the indices LCFR and LCD. Thus it is of particular interest to delimit when the i^{th} Voronoi polygon, V_i, yields a good approximation to the i^{th} TR, D_i, to support physiological studies exploring functional capillary supply, its regulation and disruption.

1.5 Dissertation objectives and plan

In an effort to address Krogh's original plea for incorporating the influence of the surrounding tissue in theoretical frameworks, a number of researchers over the last three decades have emphasised capillary domains as useful histological conduits for

exploring the supply–demand balance at the scale of a single capillary. Although such a histological framework provides a geometrical means for developing mathematical models of oxygen transport that allows an exploration of the functional capacity of the microcirculation in striated muscles, there is yet to be a theoretical approach that can systematically extend this framework to the normal physiological state.

Our general objective in this dissertation is concerned with exploring the transport of oxygen in cardiac and skeletal muscle 2D sections via developing mathematical and computational frameworks that can account for the anatomical and histological details of tissue sections. Ultimately, we seek to build a theoretical framework of oxygen diffusion that parallels the current morphological framework of capillary domains and extends it to more usual physiological states given the complex geometries of, and functional variability in, histological tissue sections. In particular, we wish to develop research tools to assess and improve the current measures of local capillary supply of oxygen.

Given the current application of capillary domains in the physiological literature exploring capillary oxygen supply, it is of particular interest to explicitly assess, qualitative and quantitatively, the accuracy of capillary domains in approximating the capillary supply regions of our biophysical models. This entails delimiting when and where capillary domains may be expected to fail and to what quantitative extent this failure might be. With this, it becomes feasible to characterise when and where capillary domain–based indices of local capillary supply are in fact likely to be an accurate representation of the underlying transport processes. In addition, it is desirable to correlate and interpret differences between capillary domains and their biophysical counterparts with the underlying physiological state of the system.

To this end, we develop general transport models for sections from cardiac and skeletal muscle biopsies, build a finite element computational framework, predict spatial distributions of oxygen tension and consumption rates in tissue section and, subsequently, derive a more realistic alternative to capillary domains, namely the flux trapping regions. This allows for more sophisticated measures of capillary supply capacity and is robust to the heterogeneities of the underlying transport process in striated muscle tissues. This can potentially provide experimental physiologists with a more robust tool for analysing the functional capillary supply of oxygen in muscle tissues from animal models and, conceivably, human biopsies. Further, this tool may reconcile previously conflicting analyses by improving interpretations of the local

angiogenic response to tissue pathologies (e.g. ischaemia) and associated therapies, potentially improving the current understanding of the therapeutic repair process of pathologically damaged microvasculature.

In Chapter 2 we develop a theoretical model to describe oxygen transport from capillaries to uniform muscle tissues (e.g. cardiac muscle). We systematically explore the influence of increased heterogeneities in capillary distributions on tissue oxygen levels and the quality of capillary domains in representing the underlying transport process. Particular attention is given to the case of capillary rarefaction. This work has been published in the Bulletin of Mathematical Biology, A. A. Al-Shammari et al. [3].

In Chapter 3 we extend the previous modelling framework to explore the influence of the surrounding tissue by accounting for the spatial anisotropies of the oxidative capacity and diffusivity of muscle fibres as well as the heterogeneity in fibre size and shape, as exemplified by mixed muscle tissues (e.g. skeletal muscle). We additionally explore the effects of diffusion through the interstitium, facilitated–diffusion by myoglobin, and Michaelis–Menten kinetics of tissue oxygen consumption. This work has been published in the Journal of Theoretical Biology, A. A. Al-Shammari et al. [4].

In Chapter 4 we extend the model in Chapter 3 to explore the influences of intracellular heterogeneities in mitochondrial distribution and diffusive parameters on fibre and tissue oxygen levels as well as the capillary supply indices. This work is being prepared for publication at the time of writing this dissertation with A. A. Al-Shammari as lead author.

In Chapter 5 we demonstrate the potential of the models developed in the previous chapters by predicting oxygen tension and consumption distributions in sections from myocardial tissue biopsies of rats with either impaired angiogenesis or impaired arteriolar perfusion. Our quantitative predictions are used to help interpret experimental measurements of cardiac performance and metabolism. Elements of these applications have been submitted for publication:

- D. Hauton, J. Winter, **A. A. Al-Shammari**, E. A. Gaffney, R. D. Evans, S. Egginton (2014), *Changes to both cardiac metabolism and performance accompany acute reductions in functional capillary supply*, BBA General Subjects,

and a further publication is planned:

- Hauton D, **A. A. Al-Shammari**, E. A. Gaffney, S. Egginton, *Maternal hypoxia decreases capillary supply and increases metabolic inefficiency leading to mismatch between oxygen supply and demand.*

Finally, in Chapter 6, we conclude with a summary of the main results of this dissertation and their biological implications, and indicate directions for further work.

We additionally supply Appendices A and B to provide details concerning the computational aspects underlying this work with particular focus on the algorithmic computation of trapping regions. Elements from these appendices and Chapters 1–3 have been published in the Springer Proceedings in Mathematics & Statistics 87, Advances in Applied Mathematics, A. A. Al-Shammari et al. [5].

Chapter 2

Oxygen Supply in Uniform Muscles

2.1 Summary

The ability to characterise capillary supply of O_2 in muscles plays a key role in developing effective therapeutic interventions for numerous pathological conditions, such as *capillary loss* in skeletal or cardiac muscle. However quantifying capillary supply is fraught with difficulties. Averaged measures such as capillary density or mean intercapillary distance cannot account for the local geometry of the underlying capillary distribution and thus can only highlight a tissue wide, global *hypoxia*. Detailed tissue geometry, such as muscle fibre size, has been incorporated into indices of capillary supply by considering the distribution of Voronoi tessellations generated from capillary locations in a plane perpendicular to muscle fibre orientation, implicitly assuming that each Voronoi polygon represents the area of supply of its enclosed capillary. Using a modelling framework to assess the *capillary supply capacity* under maximal sustainable conditions in muscle, we theoretically demonstrate that Voronoi tessellations often provide an accurate representation of the regions supplied by each capillary. However, we highlight that this use of Voronoi tessellations is inappropriate and inaccurate in the presence of extensive capillary rarefaction and especially non-uniform capillary perfusion resulting from variations in O_2 tension of different capillaries. In such cases, O_2 flux trapping regions are developed to provide a more general representation of the capillary supply regions, in particular incorporating the additional influences of heterogeneity that are absent in the consideration of Voronoi tessellations.

2.2 Introduction

Aerobic respiration for virtually all mammalian cells is contingent on a local capillary bed establishing an adequate partial pressure gradient for O_2 diffusion to drive its transport. This in turn depends on numerous factors including the distribution, perfusion and tortuosity of capillaries; mitochondrial locations; variations in the capillary blood flow and haematocrit; the interstitial and cellular geometry; the levels of facilitated diffusion; the interaction of haemoglobin and oxygen; tissue temperature and intracellular composition [106].

Understanding O_2 transport at the cellular level poses outstanding difficulties, for instance quantifying the link between cellular demand and capillary supply, whilst current experimental interrogations at the scale of several microns are laborious with limited resolution. However, skeletal and cardiac muscles exhibit a relatively simple histological structure, with capillaries typically parallel to muscle fibres, as illustrated in Fig. 2.1. Consequently, numerous theoretical models have been developed to give insight into microvascular O_2 transport in muscle, as initiated by Krogh and Erlang's 1919 cylindrical model [120], and culminating in relatively recent 3D microvascular oxygen transport modelling studies [12, 71, 169] as overviewed in Chapter 1. There we have also seen how Krogh's influential ideas have been used to characterise muscle tissue capillary supply and that the inability to tessellate tissue space with Krogh cylinders has motivated more sophisticated, space–filling, approaches. In particular, in the cross section of the muscle, as illustrated in Fig. 2.1, Voronoi polygon representations for the regions of capillary oxygen supply have often been considered [10, 31, 88, 112, 118, 158, 167, 180–182, 193] and derivative indices are also of key interest [50] in classifying, exploring and detecting the (dys)regulation of functional capillary supply capacity.

In detail, a Voronoi polygon is an area within a tissue cross–section that encloses a capillary whereby every tissue point is closer to this capillary than to any other, as illustrated in Fig. 2.2. Its adoption as a representation of capillary supply region can be attributed to its ease of use and the absence of detailed parameter estimation, and the first to effectively explore Voronoi polygons were Gonzalez-Fernandez and Atta [72]. They considered capillary geometries that led to various regular tessellations of the plane, including hexagonal tessellations. While Voronoi polygons will represent capillary supply regions for perfectly symmetric capillary distributions within tissue of homogeneous oxygen consumption, a sufficiently pronounced asymmetry will, in

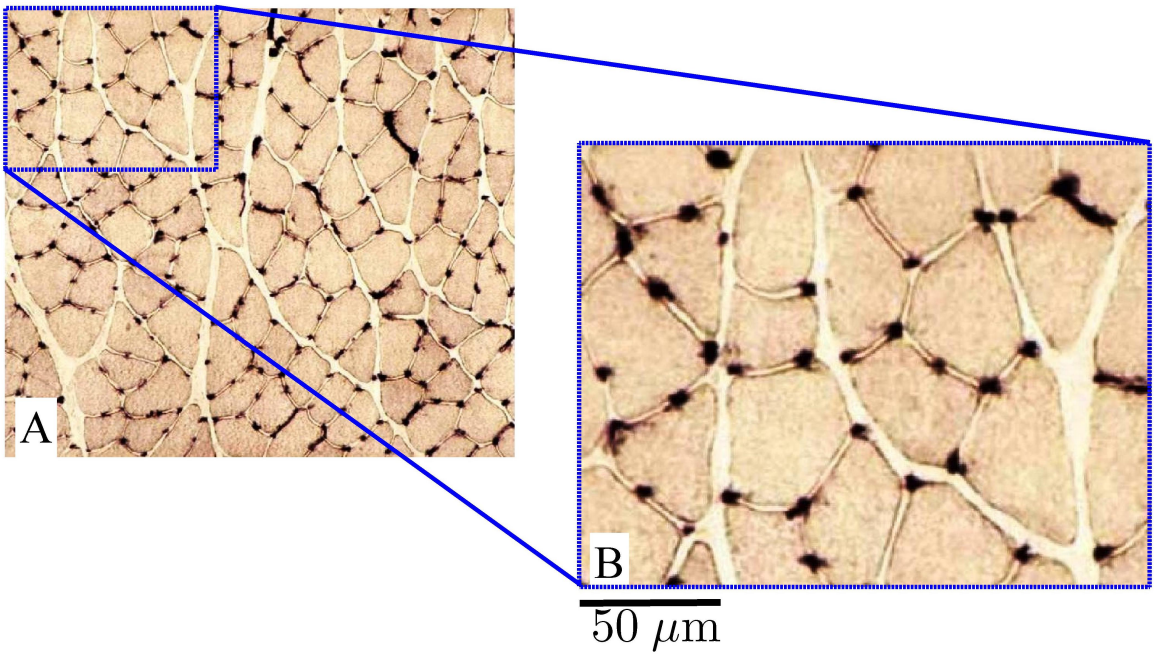

Figure 2.1: (A) typical tissue cross–section of rat skeletal muscle (*m. extensor digitorum longus*) with capillary location identified by alkaline phosphatase staining. (B) On the right is an expanded region of the left hand image. The dark structures are capillaries, the lighter objects are muscle fibres, and the lightest region is the interstitial space. Note the heterogeneity of intercapillary distances between adjacent vessels, in part reflecting heterogeneity of cell size in the host tissue [50, 53].

general, lead to a breakdown in the correlation between Voronoi polygon and capillary supply regions [49]. However, it is still unknown to what extent introducing physiologically representative asymmetries in capillary distribution influence the quality of Voronoi polygons in capturing capillary supply capacity. As we have already noted, Wang and Bassingthwaighte [186] criticised the use of Voronoi polygons for asymmetrical capillary arrangements, concluding that they are inappropriate. However, the study was based upon a mathematical analysis that necessitated the consideration of unphysiologically low capillary densities. Hence, this still leaves the question of whether Voronoi polygon indices are appropriate in the physiological setting. Therefore, our objective has been to explore a general model of oxygen transport under maximal sustainable conditions in tissue, characterising where and when Voronoi polygon indices are likely to accurately represent the underlying transport processes, while also characterising an alternative index of capillary supply capacity in muscle.

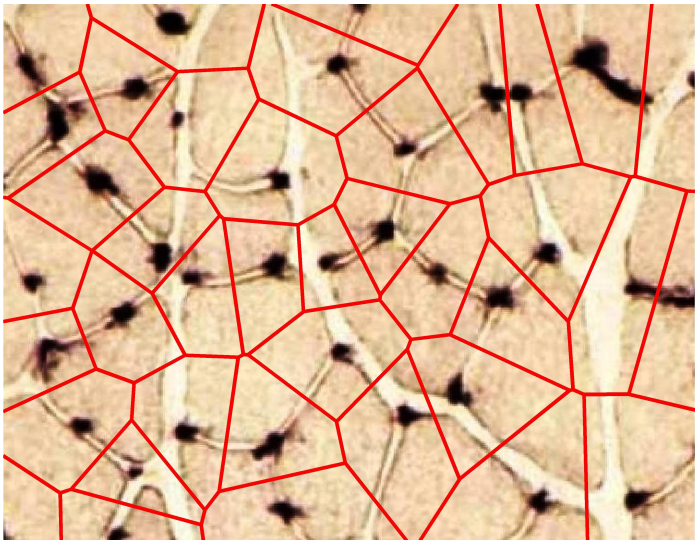

Figure 2.2: The Voronoi polygon tessellation superimposed on the magnified tissue cross–section from Fig. 2.1.

2.3 Methods

The cross sections in Figs. 2.1-2.2 are microscopy images of rat skeletal muscle, *m. extensor digitorum longus*, prepared via flash freezing in liquid nitrogen-cooled isopentane and cryostat sectioned at -20 °C with the capillary location identified using alkaline phosphatase staining [48].

2.3.1 Key definitions

We consider a cross section of tissue, as in Fig. 2.2 where the capillary locations are represented by a single point, e.g. the centroid of each capillary in the image plane of the muscle cross–section. Let N_c denote the number of capillaries, and $\mathbf{x}_i$ denote the position of the i^{th} capillary with Ω representing the global domain.

2.3.1.1 Voronoi polygons

Recall from Chapter 1 that the Voronoi polygon (VP) containing the i^{th} capillary with centre $\mathbf{x}_i$ is the set

$$V_i = \left\{ \mathbf{x} \;\middle|\; \mathbf{x} \in \Omega;\ \|\mathbf{x} - \mathbf{x}_i\| \leq \|\mathbf{x} - \mathbf{x}_k\|,\ k \neq i \right\}. \tag{2.1}$$

2.3.1.2 Trapping regions

For a given capillary with a positive oxygen flux at its boundary (vessel wall), we recall that the *trapping region* is the smallest domain which contains the capillary, with zero flux conditions on its boundary. Thus, as previously defined, for a solution of the model equations for tissue O_2 partial pressure p, the trapping region $D_i \subseteq \Omega$ of a capillary with centre $\mathbf{x}_i$, with outward pointing normal $\mathbf{n}_i$ is defined to be the smallest domain within a closed boundary containing $\mathbf{x}_i$ and satisfying

$$\partial D_i = \left\{ \mathbf{x} \;\middle|\; \mathbf{x} \in \Omega;\ \mathbf{n}_i \cdot \nabla p = 0 \right\}. \tag{2.2}$$

In addition, when the model prediction for O_2 flux at the capillary wall is negative, the trapping region is empty. Finally, when a mixture of positive and negative O_2 fluxes is present at the capillary wall, the boundary of the trapping region can also consist of the capillary boundaries so that each trapping region gives the predicted region of O_2 supply for each capillary.

Clearly, the above is a model–dependent definition. Each D_i yields the area surrounding a capillary where the outward flux due to the i^{th} capillary is balanced by inward flux due to all the neighbouring capillaries of contiguous supply regions. In particular, the regions D_i need not tessellate Ω; if they do not, then there is at least one region in Ω which does not receive any oxygen from any capillary. Therefore, by construction, D_i represents the region of supply of each capillary, according to the model used to determine the O_2 partial pressure, p, in tissue. When Voronoi polygons are used to represent the region of capillary supply, the validity of this assumption dictates the validity of capillary supply capacity indices. Thus we are interested in delimiting when the i^{th} Voronoi polygon, V_i, yields a good approximation to the i^{th} TR, D_i.

2.3.1.3 The Region of Interest

Motivated by experimental practice, we introduce the *region of interest*, a square box within the disc and concentric with it, which is used to select capillaries for consideration. The edges of this region are further from the edge of the domain than

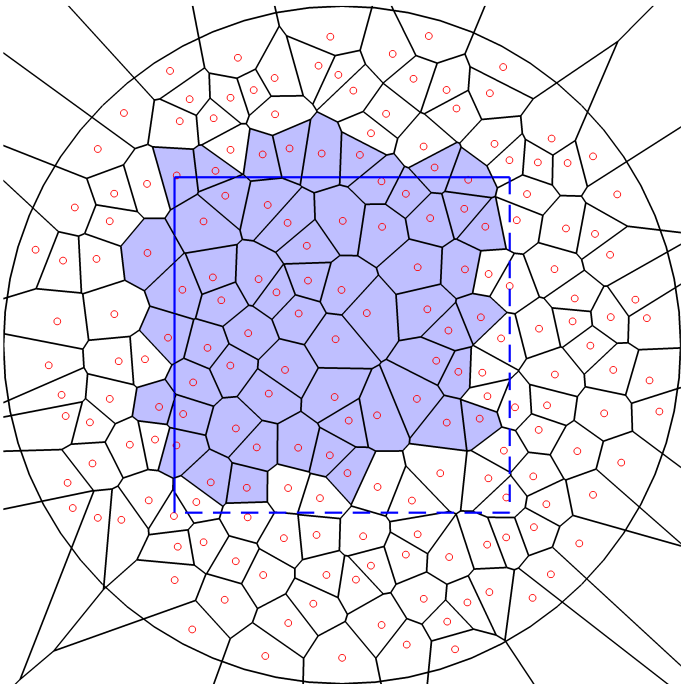

Figure 2.3: A graphical illustration of the inclusion criteria for the region of interest. *Black lines* = edges of Voronoi polygons, *Blue shading* = included Voronoi polygons, *Blue lines* = the region of interest (Solid = inclusion lines; Dashed = exclusion lines), *Red open circles* = capillary rims, and *Black circle* = domain boundary.

the intercapillary distance as the objective is to remove domain boundary artefacts, as can be confirmed *a posteriori*. The upper and left-hand sides of the square are identified as *inclusion lines*, and the lower and right-hand sides are, in contrast, *exclusion lines* [46]. A capillary domain of influence is counted as within the region of interest if it falls entirely within the box, or if it falls partly within the box and overlaps inclusion lines *only* (see Fig. 2.3). To ensure robust statistical measures we consider identical populations of capillaries, using Voronoi polygons *only* to represent the capillary domain of influence when considering the inclusion criteria for the region of interest. Furthermore, these criteria allow the tessellation of multiple regions of interest without double counting artefacts, so that it may represent the basis for considering transport processes at higher scales.

2.3.2 Statistical analysis

In Table 2.1 we define the statistical measures that will be used. These utilise D_i and V_i, the i^{th} trapping region and Voronoi polygon, as 2D domains, respectively

Statistic			Definition
μ_Δ	=	normalised mean of difference	$\frac{\text{mean}[\lvert A(D_i)-A(V_i)\rvert]}{\text{mean}[A(D_i)]}$
σ_Δ	=	normalised standard deviation of difference	$\frac{\text{std}[\lvert A(D_i)-A(V_i)\rvert]}{\text{mean}[A(D_i)]}$
$\mu_\cap$	=	normalised mean of intersection	$\frac{\text{mean}[A(D_i\cap V_i)]}{\text{mean}[A(D_i)]}$
$\sigma_\cap$	=	normalised standard deviation of intersection	$\frac{\text{std}[A(D_i\cap V_i)]}{\text{mean}[A(D_i)]}$
σ_{VP}	=	normalised standard deviation of Voronoi polygons	$\frac{\text{std}[A(V_i)]}{\text{mean}[A(V_i)]}$
σ_{TR}	=	normalised standard deviation of trapping regions	$\frac{\text{std}[A(D_i)]}{\text{mean}[A(D_i)]}$
μ_{R}	=	mean ratio	$\text{mean}[\frac{A(V_i)}{A(D_i)}]$
σ_{R}	=	standard deviation of mean ratio	$\text{std}[\frac{A(V_i)}{A(D_i)}]$

Table 2.1: Statistical measures for all capillaries i in the region of interest. These are used to evaluate the quality of Voronoi polygons. Here, D_i and V_i are the i^{th} TR and VP respectively, and $\cap$ denotes their spatial intersection. Here, *std* refers to the standard deviation, *mean* denotes the arithmetic mean, $|\cdot|$ denotes the absolute value, and $A(\cdot)$ is the non-dimensional area. See section 2.9.3 for a discussion of these measures in the context of our O_2 transport simulations.

within the region of interest and $D_i \cap V_i$, their intersection. For a tissue cross–section containing 204 capillaries, the region of interest typically includes about 50 capillaries which are used to generate statistics, though we can obtain a smaller sample in the case of rarefaction. In Table 2.4, we present the statistics defined in Table 2.1 together with area correlation coefficients, $\mathcal{CC}$, for various capillary arrangements. The correlation coefficient between TR and VP areas is defined as their covariance divided by the product of their standard deviations:

$$\mathcal{CC} = \frac{\sum_i \left(X_i - \bar{X}\right)\left(Y_i - \bar{Y}\right)}{\sqrt{\sum_i \left(X_i - \bar{X}\right)^2}\sqrt{\sum_i \left(Y_i - \bar{Y}\right)^2}}, \tag{2.3}$$

where X_i is the area of the i^{th} Voronoi polygon, Y_i is the area of the i^{th} trapping region, and $\bar{X}$, $\bar{Y}$ are the arithmetic means of these areas.

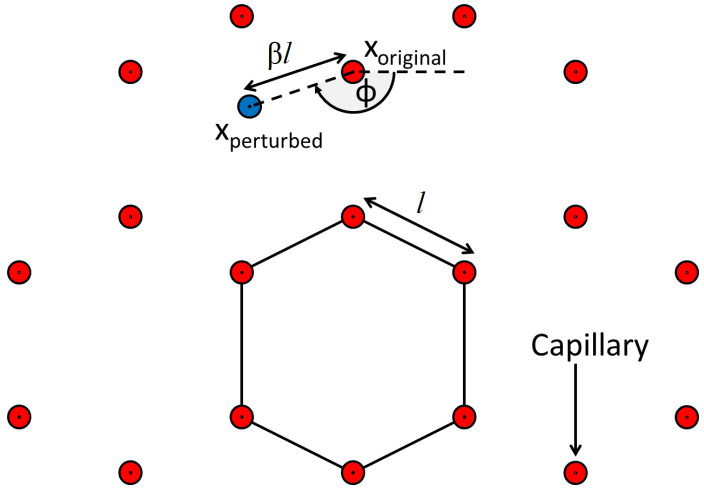

Figure 2.4: A diagram illustrating the perturbative method we use for generating heterogeneous capillary arrangements from a hexagonal array of capillaries. l = side length, β = side length fraction (our perturbative parameter), ϕ is a uniformly distributed angle in $[-\pi, \pi)$, and $\mathbf{x}$ denotes a capillary centroid.

2.4 Domain geometry

For our model, capillaries are initially placed based on a hexagonal array to mimic the approximate distribution of capillaries in select oxidative muscles. The heterogeneity in capillary placement is introduced by a *perturbative* method, with the addition of a random vector to the position of each capillary (an illustration of this method is presented in Fig. 2.4). The random vector has a magnitude that is a fraction of the hexagonal array side length, l, while its direction is based on an angle, ϕ, that is uniformly distributed on $[-\pi, \pi)$. We refer to perturbations via the parameter β defined by the relative magnitude of the random vector to the hexagonal array side length, and consider it as a measure of heterogeneity, with larger values indicating more heterogeneous arrangements. Hence we take

$$\mathbf{x}_{\text{perturbed}} = \mathbf{x}_{\text{original}} + \beta l(\cos\phi, \sin\phi), \quad \phi \in [-\pi, \pi). \tag{2.4}$$

We consider regular, perturbed, random and real distributions of capillary arrangements (Fig. 2.5). For regular and perturbed distributions, we initially place N_c capillaries on a hexagonal array. For regular distributions the capillaries are not perturbed, while for *small*, *medium* and *large* perturbations we then generate the capillary locations using Eq. (2.4), respectively taking $\beta = 0.25, 0.50, 1.00$. In addition,

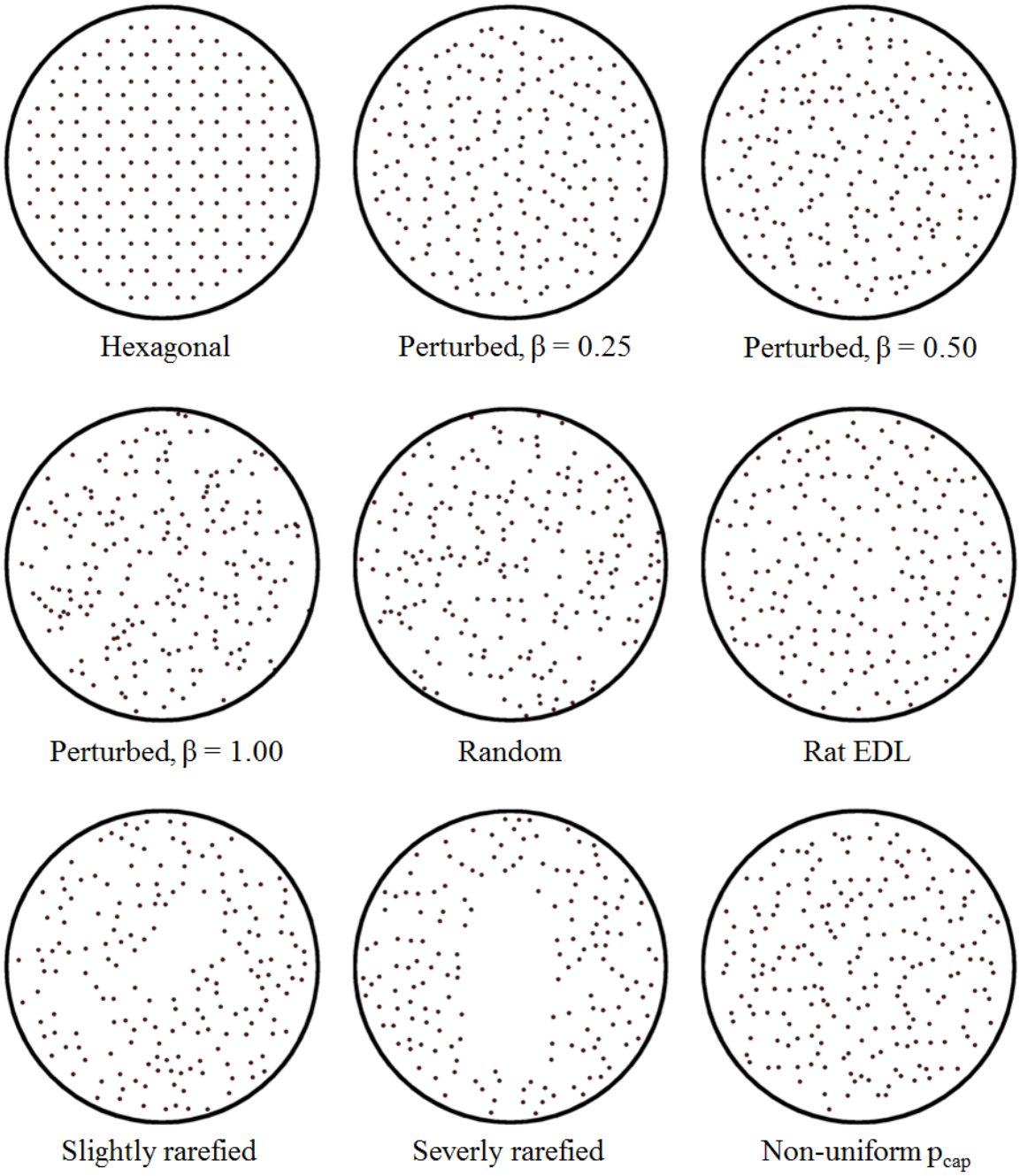

Figure 2.5: The geometries used for our model. Perturbed capillary arrangements are based on Eq. (2.4).

random distributions are generated with a uniform probability per unit area; in contrast, *real* distributions are based on a muscle image cross–section where the capillary arrangement is taken from a rat *extensor digitorum longus* muscle image rescaled onto the unit disc. Finally, we consider three rarefied capillary arrangements: *slight*, *se-*

vere and *rarefied muscle*. To generate the rarefied distributions, capillaries are simply removed from a capillary arrangement that is either randomly generated or extracted from a rat EDL muscle.

2.5 Mathematical formulation of the model

In the following we develop a detailed model for O_2 transport under maximal sustainable conditions in muscle tissue, as exemplified by the typical tissue cross–section presented in Fig. 2.1, where the lengthscale of a capillary cross–section is of order $2-4$ μm.

2.5.1 Modelling assumptions

We examine O_2 transport in a two-dimensional domain representing a cross–section of skeletal muscle tissue. Perpendicular to this domain, an array of small capillaries of circular cross–sectional shape supply the tissue with O_2 through passive diffusion [155]. Axial diffusion of O_2 in tissue can be neglected as long as the ratio of characteristic intercapillary distance ($\mathcal{O}(10)$ μm) to capillary length ($\mathcal{O}(10^3)$ μm) is sufficiently small, an assumption that is supported experimentally when myoglobin-facilitated diffusion is limited [68, 119]. In turn, myoglobin facilitation can be neglected when the tissue PO_2 is well above $p_{\mathrm{Mb},50} = 2-5$ mmHg [71, 155], where $p_{\mathrm{Mb},50}$ is the tissue PO_2 at 50% O_2 saturation of myoglobin.

2.5.1.1 Governing equations

Excluding unphysiologically high O_2 concentrations, the oxygen flux, $\mathbf{J}$, can be assumed to be proportional to the gradient of O_2 concentration, c, via Fick's first law

$$\mathbf{J} = -\mathcal{D}\nabla c,$$

where $\mathcal{D}$ is the O_2 diffusion coefficient in muscle tissue. By Henry's law we have $c = \alpha p$, where p is the tissue PO_2 and α is the coefficient of tissue O_2 solubility. Thus, in the absence of axial and myoglobin-facilitated diffusion, conservation principles give

$$\frac{\partial(\alpha p)}{dt} = \nabla \cdot [\alpha \mathcal{D} \nabla p] - \mathcal{M}(p), \tag{2.5}$$

where $\mathcal{M}$ is the rate of O_2 consumption in tissue. Note that, for a timescale of hours, this process is in *quasi-steady state* (see Table 2.2). Moreover, we assume that $\mathcal{M}$ is constant and uniform, and thus we implicitly assume that oxygen supply is sufficient to ensure that uptake is at saturation levels. As detailed by Wilson et al. [190], this necessitates that tissue PO_2 is above a critical value, denoted p_{critical}, which is approximately $0.5 - 1.0$ mmHg [69, 190]. Thus, for model consistency with the assumption of limited myoglobin facilitation, we only consider parameter scenarios with $p > p_{\text{Mb},50} > p_{\text{critical}}$ [162, 163] and hence $\mathcal{M}(p) = \mathcal{M}_0$, a constant metabolic demand. This likely pertains to a range of tissue activity from rest to sustainable aerobic activity in muscle, i.e. endurance exercise.

The domain geometry is typically obtained by considering a circular tissue cross–section and then rescaling onto the unit disc, $\mathbb{D}^1$. Capillaries are assumed to possess a circular area, C_i, and a boundary, ∂C_i. Therefore, we seek to investigate PO_2 in a region of the unit disc that excludes the capillary *lumina*, $\Omega := \mathbb{D}^1 \backslash \bigcup_i C_i$. Thus, our model oxygen transport equation is reduced to

$$\alpha \mathcal{D} \nabla^2 p - \mathcal{M}_0 = 0, \qquad \mathbf{x} \in \Omega. \tag{2.6}$$

2.5.1.2 Boundary conditions

We consider the partial pressure and flux of O_2 at the blood–tissue interface of the capillary wall. Since it is well known that there is a finite intracapillary resistance to blood–tissue O_2 transport [55], we can utilise the *mass transfer coefficient* [62, 71], k, which gives a quantitative measure for mass O_2 transport from haemoglobin and through the capillary–tissue interface. Letting each capillary have an *inward* normal, $\mathbf{n}_i$, such that $\mathbf{n}_i$ is outward to the region Ω, conservation of mass at the capillary wall requires

$$k(p_{\text{cap}} - p) = \mathbf{J}_{\text{wall}} = -\alpha \mathcal{D} \frac{\partial p}{\partial r} = \mathbf{n}_i \cdot \alpha \mathcal{D} \nabla p, \quad \mathbf{x} \in \partial C_i, \tag{2.7}$$

where p_{cap} is the transversally–averaged partial pressure of O_2 in blood (intracapillary), $\mathbf{J}_{\text{wall}}$ is the capillary–tissue O_2 flux, p is PO_2 at the external capillary wall, and

r is the radial coordinate. Additionally, a no-flux boundary condition is imposed at the outer boundary of the tissue, effectively the muscle fascicle, to signify no exchange across it

$$\left.\frac{\partial p}{\partial r}\right|_{r=1} = 0. \tag{2.8}$$

Even when the domain boundary within the model does not represent a physiological fascicle, the use of this no-flux boundary condition is still justifiable within the context of our study, as we justify *a posteriori* that perturbing this condition does not influence the system behaviour away from the boundary. In particular, our investigation will be based on a representative internal region of the tissue cross–section in which boundary effects become practically negligible, as described in Section 2.8.3.1.

2.5.2 Non-dimensionalisation

We nondimensionalise the spatial scales and partial pressure. With N_c capillaries in a disc of diameter L and an average density of ρ, we have $\pi(L/2)^2 = N_c/\rho$, i.e. $L = \sqrt{4N_c/\pi\rho}$. This is used along with p_{cap} to non-dimensionalise our model equation and boundary conditions. Hence, the non-dimensional problem to solve is

$$\nabla^2 p - \mu = 0, \qquad \mathbf{x} \in \Omega, \tag{2.9a}$$

$$\left.\frac{\partial p}{\partial r}\right|_{r=1} = 0, \qquad \mathbf{n}_i \cdot \nabla p\Big|_{\partial C_i} = \kappa(\eta_i - p), \tag{2.9b}$$

$$\mu = \frac{L^2 \mathcal{M}_0}{\mathcal{D}\alpha p_{\text{cap}}}, \qquad \kappa = \frac{Lk}{\alpha\mathcal{D}}. \tag{2.9c}$$

Here Ω is the unit disc excluding capillaries, C_i is the i^{th} circular capillary with non-dimensional radius $\epsilon = r_{\text{cap}}/L$, $\mathbf{n}_i$ is the normal *inward* to the i^{th} capillary and outward to Ω, $\mu > 0$ is the non-dimensional metabolic demand, $\kappa > 0$ is the nondimensional transfer coefficient (capillary permeability), and η_i is the non-dimensional PO_2 at the i^{th} capillary wall. Note that p is non-dimensionalised by the maximum p_{cap} such that the i^{th} capillary has a unit non-dimensional partial pressure when perfusion is uniform or a value $\eta_i \leq 1$ otherwise.

2.6 Model properties and parameters

2.6.1 Uniqueness of solution

Given the PDE problem (2.9) describes the distribution of PO_2 in tissue (p), for every $i \in \{1, \ldots, N_c\}$, the boundary condition on ∂C_i is $\mathbf{n}_i \cdot \nabla p = \kappa(\eta_i - p)$. When the O_2 tension is higher inside capillaries ($p < \eta_i$) the flux is then outward to the capillary ($-\partial_r p > 0$), so that κ is positive. The solution is unique, as we now demonstrate.

Let $q := p - \tilde{p}$ for two possibly different solutions $p, \tilde{p}$ which satisfy Eq. (2.9a). Thus $\nabla^2 q = 0$ with boundary conditions $\mathbf{n}_i \cdot \nabla q = -\kappa q$ on capillaries and $\mathbf{n}_i \cdot \nabla q = 0$ on the unit circle. By Green's identity, we employ these boundary conditions to get

$$0 \leq \int_\Omega (\nabla q)^2 \, dA = \oint_{\partial\Omega} q(\mathbf{n}_i \cdot \nabla q) \, ds - \int_\Omega q \nabla^2 q \, dA = -\kappa \sum_i \oint_{\partial C_i} q^2 \, ds \leq 0,$$

and therefore

$$\int_\Omega (\nabla q)^2 \, dA = 0,$$

which implies q is constant on Ω. Consequently,

$$\oint_{\partial C_i} q^2 \, ds = 0,$$

which further implies $q = 0$ on all ∂C_i. Thus $p - \tilde{p} = q = 0$ on Ω and the solution is unique.

2.6.2 Nature of trapping regions

The streamlines associated with the gradient of PO_2, ∇p, are the integral paths of the dynamical system

$$\frac{d\mathbf{x}}{ds} = -\nabla p, \tag{2.10}$$

where s parametrises the integral path. We note here that the TR associated with a capillary is the area of the muscle reached by streamlines emerging from the boundary of this capillary. Below we assume that all capillaries act as O_2 sources with no regions on their boundaries where O_2 flux is from the tissue into the blood compartment, unless explicitly stated otherwise. This is valid for all examples considered here except for non-uniform perfusion. In addition, note that the TRs considered below will tessellate the domain, requiring that O_2 supply is sufficient to prevent anoxia; the latter is highly pathological and the required parameter regimes are not considered in this study.

2.6.2.1 Area of trapping regions

Recall the TR $D_i \subseteq \Omega$ of a capillary with centre $\mathbf{x}_i$, with outward pointing normal $\mathbf{n}_i$ is defined to be the union of the smallest domain satisfying

$$D_i = \left\{ \mathbf{x} \in \Omega \middle| \ \mathbf{n}_i \cdot \nabla p = 0, \ \mathbf{x} \in \partial D_i \right\}. \tag{2.11}$$

Using by A_i to denote the area of the i^{th} TR, D_i, we integrate Eq. (2.9a) over this region to obtain

$$A_i = \frac{\kappa}{\mu} \oint_{\partial C_i} (\eta_i - p)\, ds, \tag{2.12}$$

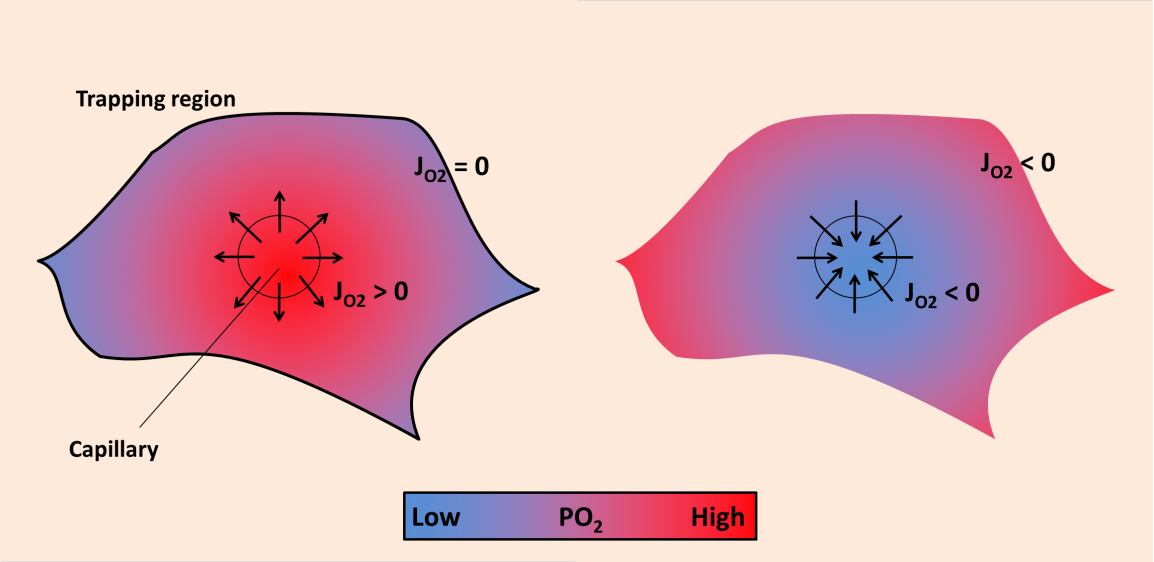

Figure 2.6: A diagram illustrating how a negative PO_2 flux at the capillary wall would lead to a zero–area trapping region. Left, in the case of postive capillary PO_2 flux, formula (2.13) is valid and the TR area is positive. Right, when the capillary wall has a negative PO_2 flux, formula (2.13) is no longer valid and the TR area is zero. Note that when part of the capllary wall has a negative PO_2 flux a valid formula should have the integrand of formula (2.13) multiplied by an indicator function for positive PO_2 flux.

where ds is the *anti-clockwise* parametrisation element around the capillary and the trapping region. Note that, for a fixed capillary radius ϵ, this further simplifies to

$$A_i = \frac{\epsilon\kappa}{\mu}\int_0^{2\pi}\Big(\eta_i - p_\epsilon(\theta)\Big)\,d\theta. \tag{2.13}$$

When any region of a capillary boundary acts as a sink, with an oxygen flux from the tissue into the blood compartment, the above equation for trapping region areas is not valid. This only occurs in our study for the case of non-uniform perfusion, and then we observe that all such cases have *all* streamlines at the capillary boundary pointing away from the tissue and into the capillary interior (see Fig. 2.6). In this instance, the trapping region is of zero area, allowing the evaluation of numerous statistics even in the case of a non-uniform perfusion.

We note that this provides the simplest and most accurate means to calculate trapping region areas from the numerical solution of the partial pressure. While the

resulting area does not require the geometric determination of the trapping region, the trapping region geometries are also determined as described in Section 2.8.2.

Central to the numerical computation of trapping regions of oxygen partial pressure, PO_2, is the concept of a *streamline*. A streamline for a vector field is a curve, the direction of which coincides at each point with the direction of the vector field; that is, at all locations it is tangent to the vector field. We consider the streamlines associated with the gradient of PO_2, ∇p, and note that these are the trajectories (integral paths) given by Eq. (2.10). Therefore, a trapping region is an area of the muscle reached by streamlines emerging from a given capillary and hence streamlines can be used to determine trapping region boundaries from modelling predictions of oxygen partial pressures, as detailed in Sections 2.6.2.2 and 2.8.

2.6.2.2 General properties of the trapping regions

When $\nabla p = \mathbf{0}$, we have a stationary point in the phase plane diagram associated with Eq. (2.10). Given the above is a gradient dynamical system, the Jacobian matrix must be symmetric. In particular, a nondegenerate stationary point of this system is restricted to a dynamical system sink, source, or saddle [78] and neither periodic streamlines (limit cycles) nor homoclinic connections can exist in a gradient dynamical system [78, 90].

Furthermore, no source exists other than possibly on capillary boundaries: at an interior source point, both p_{xx} and p_{yy} are negative or zero, giving the contradiction $0 \geq \nabla^2 p = \mu > 0$. Similarly, maxima may not occur on the domain boundary (the unit circle). In polar coordinates, a maximum on the domain boundary satisfies $p_\theta = 0$ and $p_{\theta\theta} \leq 0$. The boundary condition is $p_r = 0$ which, by Taylor expansion about $r = 1$, gives $p_{rr} \leq 0$. Then, as above, we have the contradiction $0 \geq \nabla^2 p = \mu > 0$. In addition, when no region of a capillary boundary acts as a sink, with instead the oxygen flux always from the capillary into the tissue, or vice-versa, no point on a capillary is a stationary point as $p_r \neq 0$, where the subscript r denotes the derivative of p in the normal direction pointing away from the capillary.

Hence, when streamlines emanate from capillary boundaries, the fact there are no sources in the tissue implies, from the Poincaré–Bendixson theorem [90], that a streamline within a trapping region can only approach a closed loop that is made up by heteroclinic connections of dynamical system stationary points. In principle

these stationary points may be degenerate, and thus non-hyperbolic, but this is not observed in practice (and the appearance of non-hyperbolic stationary points would require mathematical precision in parameter values, with a concomitant sensitivity in model behaviour). Hence we have that the trapping region boundaries are connections between the allowed hyperbolic stationary points, i.e. saddles to saddles or saddles to sinks, noting that sink–sink connections are inconsistent with Eq. (2.10). Furthermore, Wang and Bassingthwaighte [186] have shown that only saddle–minimum heteroclinic connections are possible on the boundary of a trapping region. This latter property, combined with stationary point hyperbolicity (and that stationary points are finite in number), as observed in practice, implies that Eq. (2.10) is a Morse–Smale gradient field [78], and thus the dynamical system is structurally stable [140].

The above properties of gradient dynamical systems are used below for a numerical algorithm that calculates the trapping region boundary given that all capillaries act as oxygen sources with no regions on their boundaries where the oxygen flux is from the tissue into the blood compartment.

2.6.3 Parameter values

Our parameter values are given in Table 2.2 and based upon those presented by Goldman et al. [71], which in turn are based on numerous experiments [8, 15, 23, 40, 58, 91, 110, 111, 127, 134, 174]. The lengthscale, L, can be derived by assuming the 612 capillaries in the unit disc have a dimensional density of 1400 mm^{-2} [71]. Although rat EDL muscle (*m. extensor digitorum longus*) has generally lower capillary density values that depend on animal mass and adaptation, the capillary density we use is typical for a heart muscle. The use of such scalings is justified in the sensitivity analysis we present in Section 2.6.4. In addition, we briefly consider variations in p_{cap} within a tissue for one of the simulations below. Due to possible experimental errors in estimating these parameters and natural variations, we also explore the influence of parameter variations in detail below.

2.6.4 Dependence on parameters

In the non-dimensionalised model there are $N_c + 3$ parameters: κ, μ, ϵ and η_i for $i = 1, \ldots, N_c$. The non-dimensional metabolic demand, μ, determines how much O_2 is absorbed by the tissue, and the non-dimensional mass transfer coefficient or

Parameter	Symbol	Value	Unit
Tissue O_2 solubility	α	3.89×10^{-5}	ml O_2 ml^{-1} mmHg^{-1}
Tissue O_2 diffusivity	$\mathcal{D}$	2.41×10^{-5}	cm^2 s^{-1}
Tissue O_2 uptake	$\mathcal{M}_0$	1.57×10^{-4}	ml O_2 ml^{-1} s^{-1}
Mass transfer coefficient	k	4.00×10^{-6}	ml O_2 s^{-1} cm^{-2} mmHg^{-1}
Average intracapillary PO_2	p_{cap}	20	mmHg
Capillary radius	r	1.8	μm
Capillary density	ρ	1400	mm^{-2}
Number of capillaries	N_c	612	
Lengthscale	L	7.46×10^{-2}	cm
Capillary permeability	κ	318.32	non-dimensionalised
O_2 uptake	μ	18.64	non-dimensionalised

Table 2.2: Except for number of capillaries, parameter values *above the line* are taken from [71], while those *below the line* are derived values. The number of capillaries is estimated from the capillary density. Note that $\rho\mathcal{D} \sim 3\text{s}^{-1}$ indicating that the transport equation, Eq. (2.5), is in quasi-steady state for timescales of hours and longer, as the evolution of the system towards the steady state is driven by the timescale emerging from diffusion and the intercapillary distance $\sim 1/\rho^{1/2}$.

capillary permeability, κ, is a measure of the O_2 flux leaving the capillary. The areas of the trapping regions are given by Eq. (2.13) and so are ostensibly dependent on κ, μ, the non-dimensional capillary radius ϵ, the i^{th} capillary non-dimensionalised partial pressure, η_i, and the solution p. Below, we consider uniform perfusion so that all the η_i are equal and denoted by η. For non-uniform capillary supply, there are no analogous simplifications in the parameter dependencies of the trapping regions; however studying such complications is not our focus.

2.6.4.1 Independence of p_{cap} and μ

We consider a rescaling of the equations to show that trapping region areas and shapes are independent of μ, η, and a rescaling of p.

Fixing κ, η and ϵ, we rescale $\mu \mapsto \xi\mu$. Then, let $\tilde{p}$ denote the solution of Eqs. (2.9a)–(2.9b) with parameters κ, $\eta_i = \eta$, ϵ, and $(\xi\mu)$. By uniqueness, the solution $\tilde{p}$ must satisfy $\tilde{p} = \xi p - \xi\eta + \eta$. This clearly satisfies Eq. (2.9a) for the given parameter values, while direct differentiation gives $\nabla\tilde{p} = \xi\nabla p$. Thus, all no-flux boundary conditions and stationary points are unchanged because $\nabla p = \mathbf{0} \implies \nabla\tilde{p} = \mathbf{0}$ provided $\xi \neq 0$. In addition, the streamlines and trapping regions, are unchanged as the streamline parameter may be rescaled to give

$$\nabla\tilde{p} = \xi\nabla p = -\xi\frac{d\mathbf{x}}{ds} = -\frac{d\mathbf{x}}{dt}, \quad \frac{ds}{dt} := \xi.$$

Integrating Eq. (2.9a) over the trapping region gives

$$\tilde{A}_i = \frac{\kappa}{\xi\mu}\int_{\partial D_i} \mathbf{n}_i \cdot \nabla\tilde{p}\, ds = \frac{\kappa}{\xi\mu}\int_{\partial D_i} \mathbf{n}_i \cdot \nabla\left(\xi p\right)\, ds = A_i,$$

where the ξ cancel to give the same expression as Eq. (2.12). Thus the modelling predictions do not depend on changes in μ, while holding other parameters fixed.

Instead, fix κ, ϵ and μ, and rescale $\eta \mapsto \zeta\eta$. Then $\tilde{p} = p - \eta + \zeta\eta$ satisfies Eqs. (2.9a)–(2.9b) with the rescaled value of the nondimensional capillary partial pressure, $\zeta\eta$. By analogous reasoning to the above, we have that the streamlines and trapping regions are unchanged.

2.6.4.2 Insensitivity to κ and ρ

Table 2.3 presents statistical measures for the geometry of rat EDL muscle (see Fig. 2.5), but with the non-dimensional capillary permeability, κ, reduced by factors of two and four, reducing oxygen supply into the tissue. Note that there is not an extensive difference on comparison with the unperturbed case, highlighting an insensitivity to κ, though the agreement between the Voronoi polygons and trapping regions is slightly reduced. This trend holds given the permeability is sufficient that oxygen levels are adequate for maximal uptake; analogous comments hold for variations in the dimensional capillary density ρ.

Note that the non-dimensional capillary radius, ϵ, depends on the dimensional value and the scaling (see Table 2.2). Recall that the latter is $L = \sqrt{4N_c/\pi\rho}$, where N_c is the number of capillaries in the non-dimensional unit disc and ρ is the dimensional capillary density. Thus, assuming the dimensional capillary radius does not vary between capillaries in the cross-section, varying ϵ is equivalent to varying ρ. Thus, the above observations of insensitivity also apply and more generally we have that the trapping region statistics used in the main text are robust to variations in the model parameters, at least in the case of uniform capillary O_2.

	μ_Δ	σ_Δ	$\mu_\cap$	$\sigma_\cap$	$\mathcal{CC}$	$\sigma_\cap$	μ_{R}
Unperturbed	0.1501	0.1548	0.9297	0.1764	0.9483	0.2529	0.9241
$\frac{\kappa}{4}$	0.1517	0.1551	0.9296	0.1768	0.9470	0.2529	0.9242
$\frac{\kappa}{2}$	0.1528	0.1553	0.9294	0.1770	0.9464	0.2529	0.9239
4ρ	0.1516	0.1553	0.9296	0.1768	0.9471	0.2529	0.9242
16ρ	0.1526	0.1551	0.9295	0.1771	0.9466	0.2529	0.9238

Table 2.3: Statistics determined from areas of VPs and TRs for the geometry of rat EDL muscle cross–section as in Fig. 2.8. Results for unperturbed and perturbed parameters are presented. We consider reducing the non-dimensional capillary permeability, κ, by factors of two and four, and increasing the dimensional capillary density, ρ, by factors of four and 16. Refer to Table 2.1 and Eq. (2.3) for definitions of these statistical measures.

2.7 Model limitations

It is assumed in the model that oxygen partial pressures in the capillaries are constant and equal. This is likely to be the case under maximal aerobic capacity in muscle, whereby all capillaries are perfused. In contrast, under sub-maximal work only a fraction of the capillaries are perfused. In addition, assuming a constant metabolic demand entails the implicit hypothesis that the tissue is never subjected to sufficiently low O_2 levels (hypoxia) such that its mitochondria would be unable to extract O_2 at the maximal rate [166, 190]. In particular, in the case of a uniform capillary supply, p_{cap} can be chosen in our model such that the tissue PO_2 values do not fall below 5 mmHg, thus giving a maximal O_2 uptake and minimal myoglobin facilitation. Indeed, in the presence of very low O_2 levels ($p < 0.50$ mmHg), metabolic demand may have a partial pressure dependence in accordance with Michaelis–Menten kinetics [155, 190] and the influence of myoglobin facilitated–diffusion may become significant. Further, we have assumed that the muscle fibre uptake of O_2, $\mathcal{M}_0$, is uniform, although adjacent muscle fibres may have varying oxidative demands; this additional source of heterogeneity is neglected here and will be explored in a subsequent chapter. Finally, since our model predicts the behaviour of this system within the limits of capillary supply capacity and no-axial convection and diffusion, its results are currently restricted to 2D muscle cross–sections, but in principle extendible to 3D image stacks.

2.8 Numerical solution

We solve Eqs. (2.9a)-(2.9b) to determine the oxygen partial pressure. This is accomplished by using the finite element method (see Appendix A). The mesh used was

generated by the PDE toolbox provided by Matlab [132] (see Appendix B). To resolve areas of rapid change in oxygen partial pressure gradients, and thus improve the accuracy of the computed solution around capillaries, an adaptive meshing technique was used.

2.8.1 Streamlines

Streamlines were computed by numerically solving Eq. (2.10) via Heun's method (see Appendix A). As frequent numerical evaluations of ∇p are required by this numerical solver, linear interpolation is called upon to provide approximate values within elements of the finite element solution.

2.8.2 Trapping regions

As above, in discussing trapping region properties, we assume that the flux of oxygen on capillary boundaries always points into the tissue compartment. We have that each trapping region is delimited by a collection of heteroclinic connections of type saddle–minimum. Such orbits of Eq. (2.10) are estimated numerically using the methodologies described in Appendix A. Here we describe these briefly:

(1) the unstable manifolds emerging from each saddle point are determined within machine level tolerances exploiting the local Hartman–Grobman theorem for hyperbolic equilibrium points of dynamical systems [78];

(2) integration proceeds until ending at a dynamical system sink, thus giving the saddle–sink connection;

(3) all these connections are determined and the resulting tessellation of the domain gives the trapping regions, each of which is identified with the capillary it encloses.

2.8.3 Accuracy

Given the complexity of our model geometry and boundary conditions we resort to checking the accuracy of our numerical solutions against cases where a tractable analytical solution is feasible. It is not surprising to find that highly symmetrical capillary arrangements yield such tractable solutions. For example, given a single

capillary centred at the origin, $(0, 0)$, we obtain the following radially symmetric solution for Eq. (2.9a)–(2.9b)

$$p(r) = \eta + \frac{\mu}{2}\left[\frac{r^2 - \epsilon^2}{2} + \frac{\epsilon^2 - 1}{\epsilon\kappa} + \ln\frac{\epsilon}{r}\right],$$

where $r = \|\mathbf{x}\|$, η is the non-dimensional capillary PO_2, μ is the non-dimensional uptake, κ is the non-dimensional permeability of the capillary, and ϵ is the non-dimensional capillary radius. Upon comparison with the finite element solution of the same problem the computational error is

$$\|p_{\text{exact}} - p_{\text{numerical}}\|_\infty = \mathcal{O}(10^{-3}).$$

2.8.3.1 Finite domain vs. zero-flux boundary condition

Given our domain is finite in size, it is important to recognise any potential influences that may be caused by imposing an 'artificial' external boundary condition. We remark here that imposing a no-flux boundary condition at the external boundary is observed to have a negligible effect on our modelling predictions, particularly within the *region of interest*. This has been checked by perturbing the exterior no-flux boundary condition to incorporate a small sinusoidal flux of the form

$$\frac{\partial p}{\partial r} = \varepsilon\cos\theta,$$

where $|\varepsilon| \leq 0.1$ to confirm that the trapping regions within the region of interest did not differ to any significant extent. Additionally, since for uniform perfusion and oxygen demand the trapping regions underlying a symmetric capillary distribution must match the corresponding Voronoi polygons, comparing our numerical predictions of trapping regions with Voronoi polygons in this case will give an estimate of the error incurred by both our calculations and the no-flux boundary condition (see Table 2.4). These confirm that the modelling predictions are insensitive to details of the boundary condition at the domain's external perimeter.

2.9 Results

We solve Eqs. (2.9a)–(2.9b) for the PO_2, enabling a derivation of the streamlines via Eq. (2.10), and a subsequent determination of TR areas using Eq. (2.13) and the TR geometries using the numerical methodologies in Section 2.8.

2.9.1 Simulations and qualitative correlation

2.9.1.1 Spatial profile of PO_2

The range of PO_2 is an increasing function of heterogeneity, with the widest range and lowest PO_2 found in severe rarefaction and heterogeneous capillary perfusion (Figs. 2.7 and 2.10A). Some capillaries act like sinks for oxygen when the local O_2 levels are higher than the capillary supply, even though the range of capillary partial pressures was restricted to $10 - 20$ mmHg (non-dimensional range $= 0.5 - 1.0$; Fig. 2.8I).

2.9.1.2 Comparison of predicted supply domains

The boundaries of the Voronoi polygons are indistinguishable from those of trapping regions in the case of perfectly symmetrical capillary arrangement (Fig. 2.8A). This is not the case for the other arrangements where boundary deviations become more pronounced with increasing heterogeneity (Figs. 2.8B-H and 2.10B). In the case of non-uniform capillary perfusion (Fig. 2.8I), such boundary deviations are much more pronounced, despite the fact the range of capillary partial pressures was limited.

2.9.1.3 Variability in predicted supply domain areas

Frequency histograms for the areas of the trapping regions and Voronoi polygons confirm that distributions are narrower for more homogeneous capillary arrangements. In all cases, trapping regions show narrower distributions and higher peaks than Voronoi polygons. In particular, the cases of capillary rarefaction exhibit the fattest tails with distinctive left–skewed distributions (Figs. 2.9 and 2.10C).

2.9.2 Qualitative observations

Voronoi polygons describe the behaviour of trapping regions with an identical agreement for a hexagonal array of capillaries (Fig. 2.8A). In this case, boundaries of Voronoi polygons coincide with trapping regions. In particular, given the fact that Voronoi polygons should perfectly match capillary supply regions when O_2 uptake is saturated and the capillary arrangement is symmetric, this agreement further confirms that domain boundary effects can be neglected within a region of interest. However, as the heterogeneity in capillary distribution is increased, the boundaries of trapping regions are seen to deviate slightly from Voronoi polygons (Figs. 2.8B-F). Despite this, Voronoi polygons provide a reasonable qualitative approximation to trapping regions in all cases of non-rarefied capillary distributions. Most of the area

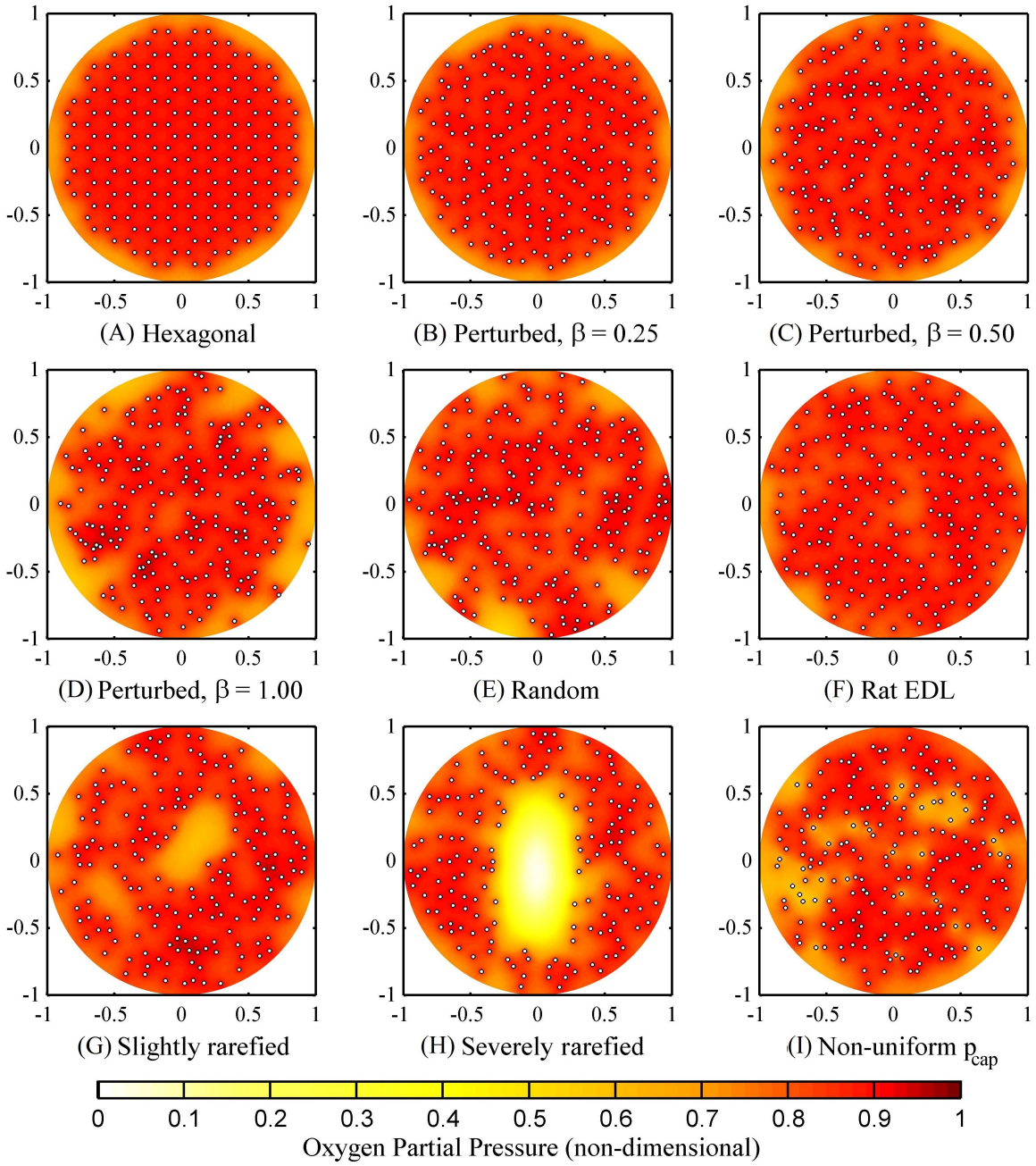

Figure 2.7: Spatial distribution of oxygen partial pressure (non-dimensional units), with capillaries as small open circles.

histograms of Voronoi polygons coincide with those of trapping region. However, as heterogeneity is increased, an extended (fat) tail begins to emerge for the Voronoi polygons histogram, whereas the histograms of the trapping regions remain relatively centralised, thus Voronoi polygons can exaggerate the extremes of the capillary supply areas.

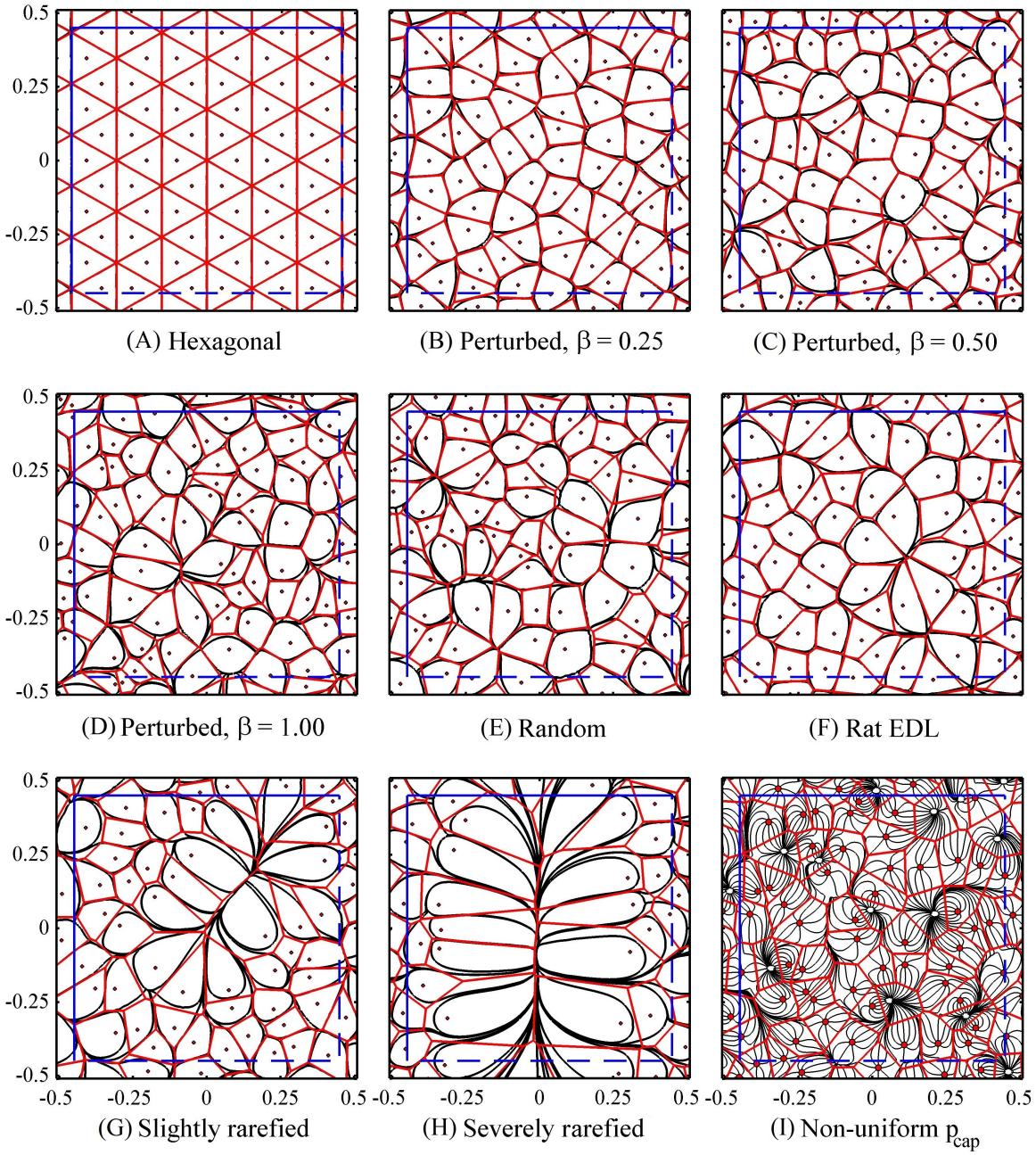

Figure 2.8: (A)-(H) Trapping region boundaries (black/dark) and Voronoi polygons (red/light) in the region of interest (blue/dark square: solid left/top edges and dashed right/bottom edges) for various capillary distributions. (I) This plot represents a 50% perturbed distribution of capillaries with heterogeneous capillary perfusion, p_{cap}. We have used two different p_{cap} values: $p_{\text{cap}} = 10$ mmHg for 30 randomly chosen capillaries, and $p_{\text{cap}} = 20$ mmHg for the rest. Streamlines (black/dark) emanate from capillaries acting as O_2 sources (*red–filled discs*), whereas the remaining capillaries (*white discs*) act entirely as receiving ends of PO_2 flux lines, thus possessing a zero area for O_2 supply.

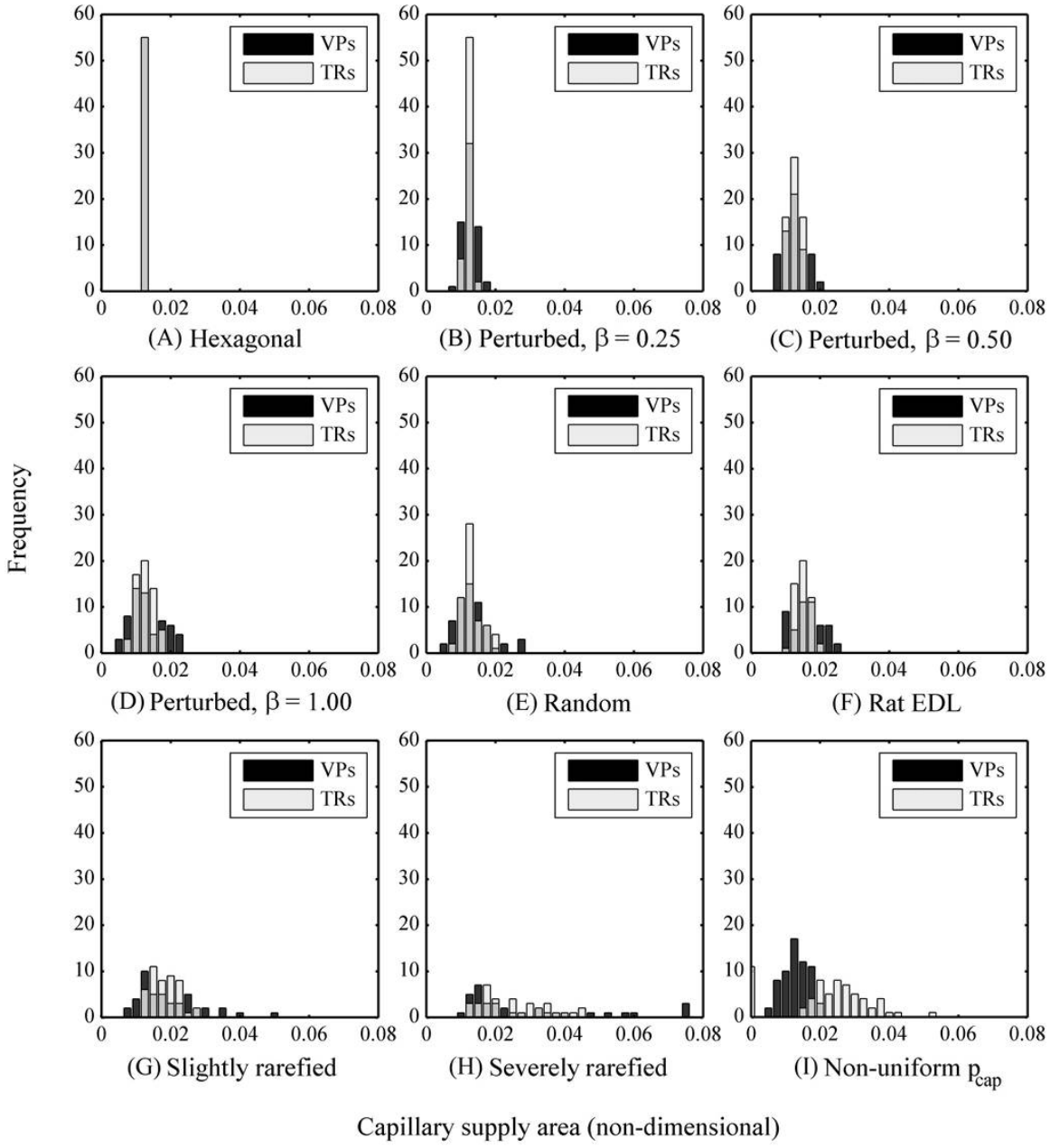

Figure 2.9: Frequency distributions of areas for VPs and TRs within the region of interest. Histograms of the areas of Voronoi polygons are given by black/dark bars and trapping regions by light grey bars. Overlapping histograms are of intermediate shading. The horizontal axis represents non-dimensional areas and the vertical axis shows frequency of occurrence, where the heights of the bars sum to the number of capillary domains included in the region of interest.

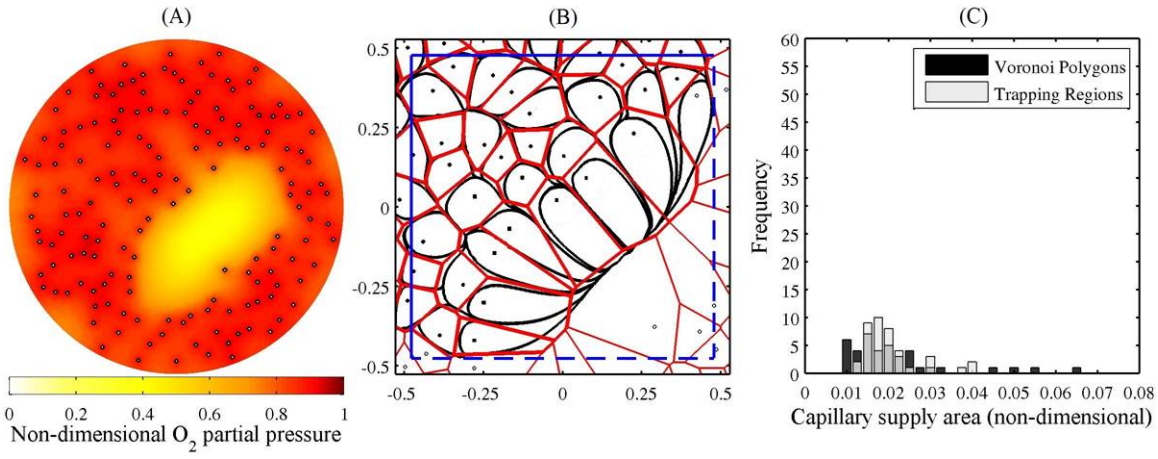

Figure 2.10: Simulations for rarefied rat EDL muscle: (A) Spatial distribution of oxygen partial pressure (non-dimensional units), with capillaries as small dark circles. (B) Trapping region boundaries (black/dark) and Voronoi polygons (red/light) in the region of interest (blue/dark square: solid left/top edges and dashed right/bottom edges). (C) Frequency distributions of areas for VPs and TRs within the region of interest. Histograms of the areas of Voronoi polygons are given by black/dark bars and trapping regions by light grey bars. Overlapping histograms are of intermediate shading. The horizontal axis represents non-dimensional areas and the vertical axis shows frequency of occurrence, where the heights of the bars sum to the number of capillary domains included in the region of interest.

With capillary rarefaction, Voronoi polygon boundaries show larger deviations from trapping regions (Figs. 2.8G-H and 2.10B), in addition to a more pronounced deviation in shape and distribution of the Voronoi polygon areas (Figs. 2.9G-H and 2.10C). These polygons deviate ever more extensively from their associated trapping regions as the severity of rarefaction is increased. In addition, a simple comparison reveals that higher degrees of rarefaction severity are accompanied by a smaller number of oxygen minima (Fig. 2.7C, F vs. Figs. 2.7G-H and 2.10A). Finally, the influence of rarefaction on distant capillaries reveals that both non-neighbouring and nearest trapping regions expand further in the direction of rarefaction while, in contrast, only the nearest Voronoi polygon neighbours compensate for rarefaction (Figs. 2.8C, F-H and 2.10B).

In the case of heterogeneous capillary perfusion, a complete breakdown in qualitative agreement between Voronoi polygons and some trapping regions is seen (Fig. 2.8I), despite the range of capillary partial pressures being restricted ($20-30$ mmHg) such that the variation in capillary oxygen levels was less than an order of magnitude. Nonetheless, many capillaries fail to supply any oxygen, implying null trapping region areas, while the corresponding Voronoi polygons remain unaffected.

		μ_Δ	σ_Δ	$\mu_\cap$	$\sigma_\cap$	$\mathcal{CC}$	σ_{VP}	σ_{TR}	μ_{R}
Perturbed	$\beta = 0\%$	0.0448	0.0093	0.9991	0.0084	$*$	0	0.0113	0.9991
	$\beta = 25\%$	0.0805	0.0940	0.9498	0.1026	0.9508	0.1504	0.0678	0.9474
	$\beta = 50\%$	0.1140	0.1495	0.9073	0.1880	0.9503	0.2609	0.1267	0.8988
	$\beta = 100\%$	0.1690	0.2034	0.8841	0.2502	0.9530	0.3574	0.1895	0.8689
Rarefied	Slight	0.2094	0.3071	0.8426	0.2816	0.9322	0.4714	0.2193	0.8247
	Severe	0.2919	0.4451	0.8104	0.4303	0.9399	0.6853	0.3820	0.7844
	EDL	0.1973	0.3057	0.8336	0.3594	0.9527	0.58	0.346	0.8223
EDL Image		0.1501	0.1548	0.9297	0.1764	0.9483	0.2529	0.1411	0.9241
Random		0.1631	0.2093	0.8803	0.2638	0.9180	0.3785	0.2164	0.8680
Varying p_{cap}		0.6215	0.5682	#	#	0.1047	0.2791	0.5615	$*$

Table 2.4: Statistics determined from areas of Voronoi VPs and TRs for different capillary arrangements and parameter regimes (leftmost column). μ = normalised mean; σ = normalised standard deviation (normalisation by the mean TR area). Δ = absolute difference of TR and VP areas, $\cap$ = area of overlap between TR and VP, and R = ratio of VP to TR areas. An entry denoted by * denotes cases where statistics are not applicable. The area correlation coefficient, $\mathcal{CC}$, is ill-defined for hexagonal arrays since all areas are the same and hence their standard deviation is null. Nonetheless, it is clear that VP areas provide exceedingly good estimates of TR areas in this case. Similarly, the occurrence of TR with zero area for heterogeneous capillary perfusion (Varying p_{cap}) entails the mean ratio μ_{R} is ill-defined in this case. An entry of # highlights that the statistics require more complex algorithms for quantitatively characterising all TR, due to non-uniform perfusion, as detailed in Section 2.8.2. For such cases, we have used Eq. (2.12) to compute trapping region areas noting that the capillaries with fluxes solely into the blood compartment automatically possess zero area trapping regions. The more complex prospect of trapping regions that share part of a boundary with a capillary possessing fluxes in both directions across its wall are not observed.

2.9.3 Quantitative correlations

2.9.3.1 The area correlation, $\mathcal{CC}$

Table 2.4 demonstrates a strong correlation between the areas of Voronoi polygons and trapping regions for all capillary distributions where homogeneous perfusion is considered. Generally, these data indicate that the highest area correlation ($\mathcal{CC}$) is seen in highly regular capillary distributions with uniform perfusion, with the lowest found in rarefied distributions. Although $\mathcal{CC}$ is high in all cases of capillary rarefaction, it is still slightly smaller compared to all other capillary distributions with uniform perfusion. In contrast, for the case of heterogeneous capillary perfusion, $\mathcal{CC}$ is substantially lower.

2.9.3.2 The normalized means μ_Δ, $\mu_\cap$, μ_R

These statistics have a trend correlated with heterogeneity, and are rather different for random and real capillary arrangements. The normalized mean of difference (μ_Δ) provides a measure of the degree of failure of Voronoi polygons to cover comparable areas to those of trapping regions, which increases with the degree of perturbation to capillary arrangements. Given uniform perfusion, the highest μ_Δ is observed in severe rarefaction.

The normalized mean of intersection ($\mu_\cap$) and the mean ratio (μ_R) describe how well Voronoi polygons capture functional capillary supply of trapping regions, with values of unity for cases of a perfect match. Both these statistics decrease linearly with measures of heterogeneity and, for homogeneous perfusion, are lowest in the case of severe rarefaction.

2.9.3.3 The normalised standard deviations σ_Δ, $\sigma_\cap$, σ_VP, σ_TR

The normalized standard deviations remain small across nearly homogeneous distributions and increase with greater heterogeneity of capillary distribution, the highest values corresponding to the highest degree of heterogeneity, i.e. severe rarefaction, at least in the absence of perfusion heterogeneity. The trend in σ_Δ illustrates that the spread of Voronoi polygon areas begins to differ extensively from that of the trapping regions for extreme cases of structural heterogeneity.

The measure $\sigma_\cap$ further scrutinises this relationship by considering areas of the Voronoi polygons that overlap with trapping regions. The greater magnitude with increasing heterogeneity suggests that even though Voronoi polygons might cover comparable areas with trapping regions, the 2D domains of capillary supply regions are increasingly different from trapping regions within the tissue domain, consistent with results in Figs. 2.8 and 2.10B.

The dispersion in oxygenation areas, as measured by σ_VP and σ_TR, remain very small for nearly homogeneous capillary distributions. However, both spread statistics begin to widen as structural heterogeneity is increased. In particular, the dispersion in Voronoi tessellation areas is found to be approximately double that of the trapping regions across all tissue heterogeneities, except in the case of perfect homogeneity where numerical error leads to a positive normalised standard deviation in trapping regions. Introducing functional heterogeneities (e.g., perfusion) has no effect on σ_VP:

only trapping regions are influenced by such changes as with a heterogeneous p_{cap} where $\sigma_{\text{TR}} = 0.5615$, highlighting an advantage of trapping regions.

2.10 Discussion and conclusions

Due to their practicality and ease of use, Voronoi polygons and Krogh cylinders are widely taken to represent capillary domains or supply areas in studies requiring an objective assessment of the capacity for oxygen delivery by diffusion (e.g. [49, 51, 62, 69, 92, 119, 155]). Krogh cylinders, however, are inadequate for this role since they lead to non-physiological tissue voids and overlaps. In contrast, a number of investigators [49, 96, 186] have observed that, for perfect structural symmetry and functional homogeneity, Voronoi polygons coincide with capillary supply regions. Whether this relationship is sufficiently accurate in less idealised and physiological scenarios is less clear. Hence, our present study considered the flux trapping region, which is a more general approximation for the capillary supply region, and examined the quality of Voronoi polygons in capturing capillary supply boundaries. We then consider when such polygons are appropriate to assess O_2 supply from capillary distributions within muscle tissue cross–sections.

It is clear that Voronoi polygons may exaggerate capillary supply areas. A qualitative understanding of this emerges from considering that wherever there is a local decrease in capillary density, the associated supply areas calculated via trapping regions can be compensated by non-nearest neighbour capillaries. In contrast, Voronoi polygon area distributions for capillary supply areas implicitly assume that only the nearest (contiguous) capillaries can supply oxygen: thus compensation is restricted to a small number of capillaries, hence overestimating the tissue regions they may supply.

Despite this, Voronoi polygons and trapping regions nonetheless have the same qualitative shapes and overall quantitative distributions for uniformly perfused, non-rarefied systems regardless of the degree of structural asymmetry (see Table 2.4 and Figs. 2.8–2.10), assuming the tissue is maintained above the level of saturating oxygen uptake. Then the mean ratio of the Voronoi polygon area to the trapping region area remains above 85% in the absence of noticeable capillary rarefaction. This remains true even for randomly distributed capillaries. These observations are also robust to variations in the adjustable parameters of the transport model, as illustrated in Section 2.6.4, where we consider the non-dimensional capillary permeability and

the dimensional capillary density. Thus, in the absence of extremes that are only associated with pathologies, our modelling predicts that Voronoi polygons provide a simple and accurate approximation of functional capillary supply under uniform perfusion, e.g. during maximal sustainable activity.

This is in contrast to Wang and Bassingthwaighte's modelling conclusions [186], due to the latter's consideration of unphysiologically low capillary densities to facilitate mathematical analysis, which presented artefacts associated with the boundary conditions. However, with an increase in computing power and a generic formalism, we have been able to consider more representative capillary distributions and larger domains, including the use of a region of interest sufficiently far from the domain perimeter to remove boundary artefacts. Furthermore, the trapping regions statistics are insensitive to substantial variations in all the modelling parameters, as detailed in Section 2.6.4, and thus share an attractive feature of Voronoi polygons of not requiring detailed parameter estimates.

However, increasing the degree of capillary rarefaction decreases the quality of Voronoi polygons as indices for the profile of tissue oxygenation. This is further validated by the rarefaction of a rat EDL muscle (Fig. 2.10 and Table 2.4), thus confirming the absence of methodological artefacts. In particular, rarefaction results in complex integral paths representing O_2 flux that cannot be accommodated within the purely geometrical construct of Voronoi polygons. This indicates that Voronoi polygons may be of limited use and inaccurate in assessing capillary supply areas for pathological situations associated with capillary rarefaction, such as hypertension [75], diabetes [29] and *vasculitides* [177], and perhaps even for muscle tissues that are undergoing cellular modifications, such as localised fibre hypertrophy, which may become in effect locally rarefied. We re-emphasise here that rarefaction is a local phenomenon. Thus, any change in global parameters such as capillary density may not necessarily affect the degree of tissue rarefaction. In particular, a reduction in capillary density and oxygen consumption effectively impacts a change in parameters to which trapping regions are insensitive assuming $p > p_{\text{critical}}$. This means that the appropriateness of Voronoi tessellations in this case is dependent on the level of heterogeneity in capillary distribution, which is usually signified by the normalised standard deviation of Voronoi tessellation areas.

Further note that histological rarefactions differ from functional ones. While the

physical removal of capillaries is captured by both trapping regions and Voronoi tessellations, a functional blockade of capillaries cannot be accommodated by Voronoi tessellations unless the non-functional capillaries are known *a priori*. Even in the latter case, the local O_2 feedback imposed by continuity of O_2 flux across capillary walls results in local minima at the walls of non-functional capillaries, whereas the removal of capillaries may not necessarily have the same effect. Due to this, trapping regions are anticipated to cover somewhat different areas in each of the above situations generating the discrepancy between the cases of rarefaction and non-uniform perfusion.

Additionally and in agreement with previous observations [49, 186], Voronoi polygons and trapping regions develop increasing differences as non-uniformity in capillary perfusion is introduced. In contrast, trapping regions analyses can in principle incorporate differential perfusion levels without violating the modelling assumptions, and therefore may be a useful tool in the presence of significant capillary functional heterogeneity. For instance, the influences of (1) large and differential variations in consumption rate for different muscle fibre types, (2) fibre type–dependent capillary density [53], (3) fibre–size variations, and (4) myoglobin facilitation and hypoxia may accentuate these differences and will form the subject of the next chapter.

Finally, the correlation between Voronoi polygon and trapping region areas is higher for the rat muscle cross–section compared to randomly distributed capillaries. This suggests the anatomical capillary distribution is tightly regulated to prevent random regions of capillary clustering and rarefaction. Hence, the correlations between Voronoi polygons and trapping regions may be more generally informative in physiological studies, likely reflecting local control of angiogenic foci on the lengthscale of fibre diameter, $50 - 100$ μm [9].

In summary, while the Voronoi polygon approximation to trapping regions depends on tissue heterogeneity, it is nonetheless representative for uniform perfusion and maximal oxygen uptake given the absence of rarefaction, while also exhibiting an insensitivity to model parameters. As such, measures of muscle capillary supply capacity based on Voronoi tessellations may be sensibly and reasonably used for normal tissue, though extremes in the underlying approximation of capillary supply area are slightly exaggerated. However, increases in heterogeneity associated with capillary rarefaction, even with maximal perfusion or perfusion heterogeneity, eventually

lead to a breakdown in the accuracy of Voronoi polygons. Hence, more sophisticated measures of capillary supply capacity should be used to study structural or functional dysregulation in pathological situations. Furthermore, flux trapping regions may provide a representation of capillary supply regions that is more robust to the introduction of heterogeneity compared to Voronoi tessellations, though an experimental validation has yet to be designed and performed.

Chapter 3

Oxygen Supply in Mixed Muscle

3.1 Summary

Developing effective therapeutic interventions for pathological conditions associated with abnormal O_2 transport to muscle fibres critically depends on the objective characterisation of capillarity. Local indices of capillary supply have the potential to identify the onset of fine–scale tissue pathologies and dysregulation. Detailed tissue geometry, such as muscle fibre size, has been incorporated into such measures by considering the distribution of the Voronoi polygons generated from planar capillary locations as a representation of capillary supply regions. Previously, our detailed simulations in Chapter 2 have predicted that this is generally accurate for muscle tissue with uniform O_2 uptake. In this chapter, we extend this modelling framework to heterogeneous muscle for the assessment of *capillary supply capacity* under maximal sustainable O_2 consumption. We demonstrate for muscle with heterogeneous fibre properties that VP theoretically provide a computationally simple but often accurate representation of trapping regions, which are predicted from biophysical transport models to represent the areas of tissue supplied by individual capillaries. However, this use of VP may become less accurate around large fibres, and at the interface of fibres of largely different oxidative capacities. In such cases, TR may provide a more robust representation of capillary supply regions. Additionally, given VP can only approximate O_2 delivery by capillaries, we show that their generally close relationship to TR suggests that (1) fibre type distribution may be tightly regulated to avoid large fibres with high oxidative capacities, (2) the anatomical fibre distribution is also tightly regulated to prevent large surface area of interaction between metabolically dissimilar fibres, and (3) in chronically hypoxic tissues capillary distribution is more

important in determining O_2 supply than the spatial heterogeneity of fibre demand.

3.2 Introduction

The objective assessment of anatomical capillary supply to striated muscle fibres is contingent on using methods that can accurately capture tissue capillarity while also unambiguously linking the local capillary distribution to the global supply. In the previous chapter, we demonstrated that Voronoi polygons generally give an accurate approximation of trapping regions within muscle tissues consuming O_2 uniformly at maximal capacity. Nonetheless, we also observed that the approximation accuracy may deteriorate with rising levels of capillary rarefaction, and may ultimately break down under significant perturbations to the uniformity of muscle PO_2. However, such complications under maximal functional supply require tissue pathology and hence we predicted that correlations between Voronoi polygons and supply regions may reflect local control of angiogenic foci on the lengthscale of a muscle fibre diameter, thus preventing random capillary rarefaction as observed by [9].

In contrast to the homogeneity in oxidative metabolism typically found in cardiac muscle tissue, skeletal muscle fibres often exhibit heterogeneous functional as well as structural characteristics. The O_2 transport properties associated with fibre microstructure and composition (e.g. myoglobin content and lipid stores), the metabolic demand for O_2, and the fibre size in animals are dependent on fibre type [46, 95, 111, 134, 194]. In particular, muscle fibres are classified into three main types, I, IIa, IIb with Type I generating energy predominantly from aerobic metabolism (i.e. oxidative phosphorylation), Type IIb from anaerobic glycolysis and Type IIa being an intermediate; thus the different fibre types have distinct O_2 demands due to metabolic differences. Additionally, capillary arrangements in skeletal muscle tissues have been observed to be regulated by fibre type and size [1, 193]. In particular, the heterogeneity of capillary spacing may be partly determined by the heterogeneity in fibre size [50, 53]. Furthermore, the influence of fibre heterogeneities has been explored in numerical simulations by Liu et al. [125], who concluded that changes in the fibre size distribution and O_2 uptake (MO_2) associated with different fibre types were particularly influential in the context of PO_2 heterogeneity within mixed muscles. Nevertheless, it is unknown whether a strong correlation between Voronoi polygons and capillary supply areas should hold in the presence of such heterogeneities. Hence, it is also unclear whether measures based on Voronoi polygons are appropriate for

mixed muscles in other physiological settings such as tissue hypoxia, given heterogeneous fibre–dependent properties (e.g. metabolic activity, geometry, O_2 diffusivity, and myoglobin content and facilitation).

Therefore, our objective is to extend the model developed in Chapter 2 for O_2 transport under maximal sustainable conditions in tissue, characterising when and where indices based on Voronoi polygons are likely to accurately assess O_2 supply from capillary distributions embedded in functionally heterogeneous tissue, e.g. skeletal muscle. As Voronoi polygons are generated with relative computational ease and require no parameter estimation, we additionally seek to assess their accuracy in terms of the less accessible trapping regions approach. We also investigate correlations between Voronoi polygons and trapping regions in an effort to characterise capillary supply in different physiological scenarios and to highlight possible regulatory mechanisms in skeletal muscles.

3.3 Methods

The cross section in Fig. 3.1A is a light microscopy image of rat hindlimb skeletal muscle, *m. extensor digitorum longus*, prepared via flash freezing in liquid nitrogen–cooled isopentane and cryostat sectioned at -20 °C with the capillary location identified using alkaline phosphatase staining [48].

We consider such a tissue cross–section, where capillary locations are represented by a single point, e.g. the centroid of each capillary in the image plane of the muscle cross–section. Given these cross sections we first of all want to estimate the *capillary supply regions*, that is the region of tissue supplied by each capillary and two theoretical predictions for these domains, in the form of Voronoi Polygons and Trapping Regions. These domains were introduced in previous chapters but we mathematically redefine them below for convenience, together with derivative measures. In particular, Voronoi polygons are simple to determine and based on geometry only, whereas trapping regions are ultimately found by solving the equations associated with the biophysical O_2 transport problem. Our objective therefore reduces to assessing whether the underlying biophysics, in the form of trapping regions predictions for the capillary supply regions, supports the use of simpler Voronoi polygons approximations, together with associated derivative indices, for characterising capillary supply regions under maximal sustainable conditions.

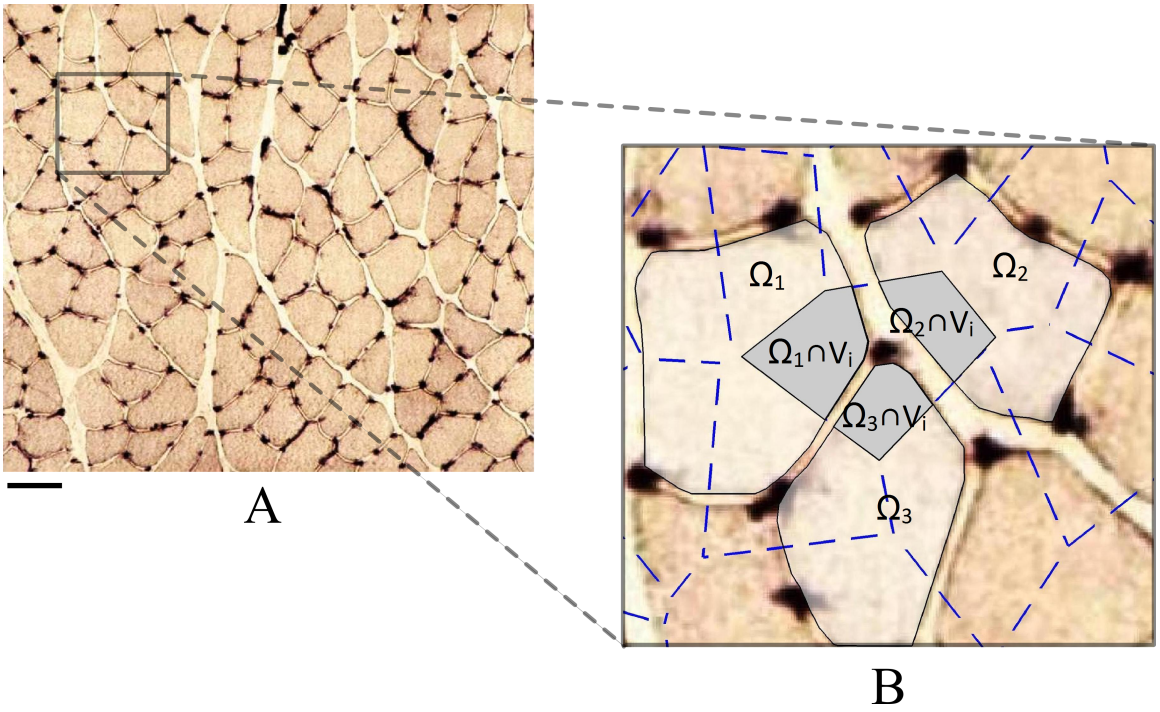

Figure 3.1: (A) Typical tissue cross–section of rat skeletal muscle (*m. extensor digitorum longus*) with capillary location identified by alkaline phosphatase staining. The *dark* structures are capillaries, the *lighter* objects are muscle fibres, and the *lightest* region is the interstitial space. Note the heterogeneity of intercapillary distances between adjacent vessels, in part reflecting heterogeneity of cell size in the host tissue [50, 53]. The scale bar corresponds to 50 μm. (B) An expanded region of the original image on which a Voronoi tessellation is superimposed by *dashed blue lines*. A central Voronoi polygon, V_i, is highlighted in *dark gray* and overlaps adjacent fibres denoted by Ω_1, Ω_2, and Ω_3 (*light gray*) with the overlapping regions $\Omega_1 \cap V_i$, $\Omega_2 \cap V_i$, and $\Omega_3 \cap V_i$ representing the fractional supply area of this Voronoi polygon to each fibre. The symbol $\cap$ denotes the intersection of or overlap between two regions.

3.3.1 Derivative indices

3.3.1.1 Voronoi polygons

Let N_c denote the number of capillaries, and $\mathbf{x}_i$ denote the position of the centroid of the i^{th} capillary with Ω representing the global domain. Recall that the Voronoi polygon containing the i^{th} capillary with centre $\mathbf{x}_i$ is the set

$$V_i = \left\{ \mathbf{x} \;\middle|\; \mathbf{x} \in \Omega;\ \|\mathbf{x} - \mathbf{x}_i\| \leq \|\mathbf{x} - \mathbf{x}_k\|,\ k \neq i \right\}, \tag{3.1}$$

with ∂V_i denoting the boundary of V_i as illustrated in Fig. 3.1B.

Recall from Chapter 1 that the derivative indices of the functional capillary supply for maximal muscle capacity are the local capillary–to–fibre ratio (LCFR) and the local capillary density (LCD; also known as the capillary fibre density, CFD). Letting Ω_j denote the region of the j^{th} fibre and $A(\cdot)$ denote the 2D Euclidean area measure, we recall that the LCFR and LCD of the j^{th} muscle fibre are defined with respect to VP as

$$LCFR_j^{VP} = \sum_i \frac{A(\Omega_j \cap V_i)}{A(V_i)}, \tag{3.2}$$

$$LCD_j^{VP} = \frac{1}{A(\Omega_j)} \sum_i \frac{A(\Omega_j \cap V_i)}{A(V_i)}, \tag{3.3}$$

respectively. As noted in Chapter 1, $LCFR_j^{VP}$ denotes the sum of the fractions of each VP area overlapping the j^{th} fibre (Fig. 3.1B), hence representing the fractional number of capillaries supplying the j^{th} muscle fibre with O_2. Similarly, LCD_j^{VP} is the number of capillaries supplying the j^{th} muscle fibre per unit fibre area.

3.3.1.2 Trapping regions

Given trapping regions $D_i \subseteq \Omega$, recall that the analogous derivative indices, $\mathcal{LCFR}_j^{TR}$ and $\mathcal{LCD}_j^{TR}$, are similar to those derived for Voronoi polygons with D_i replacing V_i

$$\mathcal{LCFR}_j^{TR} = \sum_i \frac{A(\Omega_j \cap D_i)}{A(D_i)}, \tag{3.4}$$

$$\mathcal{LCD}_j^{TR} = \frac{1}{A(\Omega_j)} \sum_i \frac{A(\Omega_j \cap D_i)}{A(D_i)}. \tag{3.5}$$

We remark here that, under maximal sustainable O_2 consumption, D_i represents the region of supply of each capillary according to the model used to determine tissue PO_2, p. When a VP is used to represent the region of capillary supply, the

validity of this assumption dictates the validity of the above capillary supply capacity indices. Thus, we are again interested in delimiting when the i^{th} VP, V_i, yields a good approximation to the i^{th} TR, D_i, but now in the context of heterogeneous skeletal muscle.

3.4 Domain geometry

3.4.1 Fibre geometric distributions

We use three domain geometries that are characterised by fibre size and shape: *Uniform*, *non-uniform*, and *histological*. The geometries are detailed below.

3.4.1.1 Uniform

The first geometry considered is synthetic uniform size distribution, SU, based on a total of ∼200 synthetic muscle fibres of hexagonal shape and uniform size with capillaries placed at fibre vertices (Fig. 3.2A). These fibres are generated from a Voronoi tessellation of the plane based on hexagonal array of nodes with prescribed side length and the number of capillaries is determined by the lengthscale, L, and capillary density, ρ, which are extracted from histological data and illustrated in Fig. 3.2. For the final domain illustrated in Fig. 3.2A, 151 muscle fibres are enclosed within a disc constituting the simulation domain, which is obtained by rescaling to the unit disc. We also consider a random local capillary rarefaction of SU, whereby 10% of the capillaries (about 21 in number) are removed at random, and denote the resulting geometry by SU_R (Fig. 3.2B). It should be noted here that no interstitial spaces are included in either of these geometries.

3.4.1.2 Non-uniform

The second geometry, synthetic non-uniform size distribution (SN), is based on a total of ∼200 polygonal muscle fibres of non-uniform size with capillaries placed at fibre vertices (Fig. 3.2C). These are generated from a Voronoi tessellation using nodes that have been placed on a random perturbation of the aforementioned hexagonal array. We employ Eq. (2.4) with $\beta = 1$ to perform this perturbation and note that the trends in our results are insensitive to such perturbations. The final domain geometry encloses 183 fibres of different sizes and shapes and, once more, no interstitial spaces are included in this geometry.

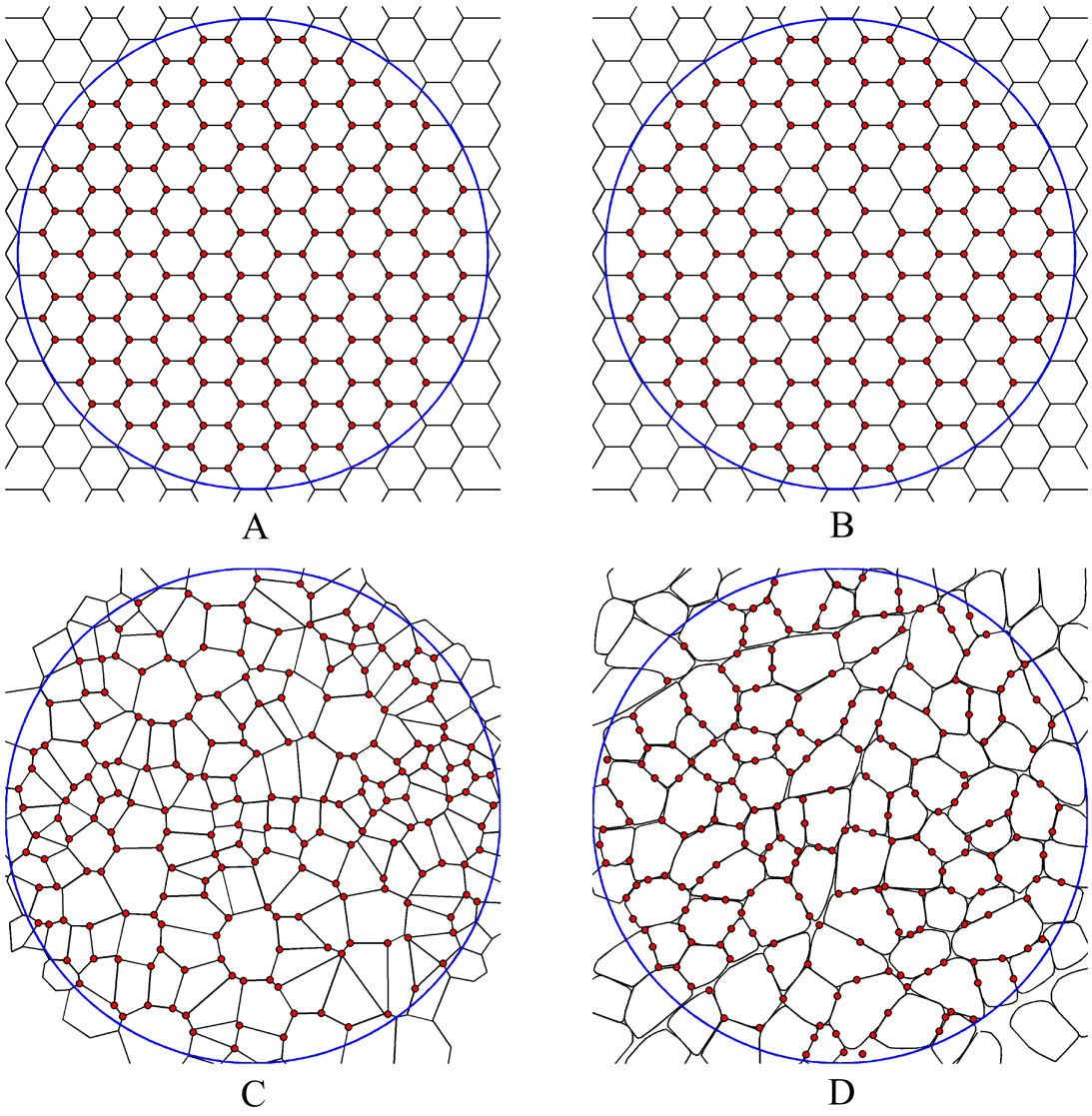

Figure 3.2: A view of modelling geometries. (A) Synthetic fibres of hexagonal shape and uniform size (SU) with capillaries placed on their vertices (symmetric capillary distribution). (B) The same fibre geometry as in (A) with 10% random capillary rarefaction irrespective of fibre type (SU_R). (C) Synthetic fibres of polygonal shape and non-uniform size with capillaries placed on fibre vertices (SN). Note that the fibre size non-uniformity reflects localised rarefactions around relatively large fibres. (D) A rat EDL muscle geometry (H). Traces of fibre cross–sections and capillary centroid locations were made from slides using a microscope drawing arm and their x, y coordinates were registered on a digitising tablet.

3.4.1.3 Histological

The third geometry is based on histological fibre size and type distribution (H), using a total of 114 muscle fibres extracted from a digitised image of a rat EDL (*m. extensor digitorum longus*) muscle cross–section (Fig. 3.2D). In this case, the final domain geometry is a disc enclosing 102 fibres and interstitial spaces.

3.4.2 Capillary distribution

Here we re-emphasise that, except for the case of a rarefied SU geometry, the spatial arrangement of capillaries is dictated by the geometrical distribution of fibre sizes, to reflect the experimental observations of [50, 53]. Three distinct capillary distribution result from the aforementioned fibre distributions: *symmetric*, *asymmetric*, and *real*. We describe each of these distributions below.

3.4.2.1 Symmetric

Since capillaries are placed at fibre vertices in the SU geometry, a symmetric capillary distribution is inherited from the symmetry of its fibre size distribution.

3.4.2.2 Asymmetric

The non-uniformity in fibre sizes gives rise to asymmetries in capillary distributions as exemplified by the SN fibre geometry. In addition, we obtain an asymmetrical capillary distribution from the SU geometry by selectively removing capillaries.

3.4.2.3 Real

Based on histological staining for capillaries, we obtain the capillary distribution of an image cross–section of a rat EDL muscle (see Fig. 3.2D).

3.4.3 Fibre type distribution and areal composition

The fibre type distribution in space is divided into three categories: random, size–based, and real. These are used selectively for the aforementioned geometries (Table 3.1).

	Fibre type distribution						
			Random			size–based	Real
Composition	0:0:100	25:0:75	50:0:50	75:0:25	100:0:0	50:0:50	9:37:54
Geometry	SU, SN	SU, SN	SU, SN, SU_R	SU, SN	SU, SN	SN	SU, SN, H

Table 3.1: The spatial distribution (random, size–based, real) and areal composition (Type I:IIa:IIb) of fibre types, for domain geometries: SU = synthetic uniform size, SU_R = rarefied SU, SN = synthetic non-uniform size, and H = histologic size.

3.4.3.1 Random

In the case of a *random* distribution of fibre types, Types I, IIa, and IIb are randomly assigned to fibres regardless of the underlying size distribution (e.g. Fig. 3.3A). Such random assignment is constrained by a predefined areal composition of fibre types (I:IIa:IIb). However, in our simulations, we often restrict ourselves to using only two fibre types (e.g. Types I & IIb) in order to have a control over potential fibre–fibre effects on supply regions.

3.4.3.2 size–based

In the *size–based* case, the spatial assignment of fibre types is based on (1) their increasing size in the following order I $\leq$ IIa $\leq$ IIb to reflect histological observations, and (2) a predefined areal composition (e.g. 50:0:50 and 9:37:54 as illustrated in Fig. 3.3B). We note here that, for the SU geometry, the uniformity in fibre sizes dictates a spatial randomness for all fibre–type assignments, hence the case of size–based SU geometry is identical to the random SU geometry.

3.4.3.3 Real

Based on histological staining of muscle fibres (Fig. 3.3C), we illustrate the *real* case where fibres are assigned the areal composition of a rat EDL muscle (9:37:54) with fibre–size ordering following the typically observed order I $\leq$ IIa $\leq$ IIb.

3.5 Model

An extension of our previous model of O_2 transport under maximal sustainable conditions (see Chapter 2) is developed to explore the validity of Voronoi polygons for

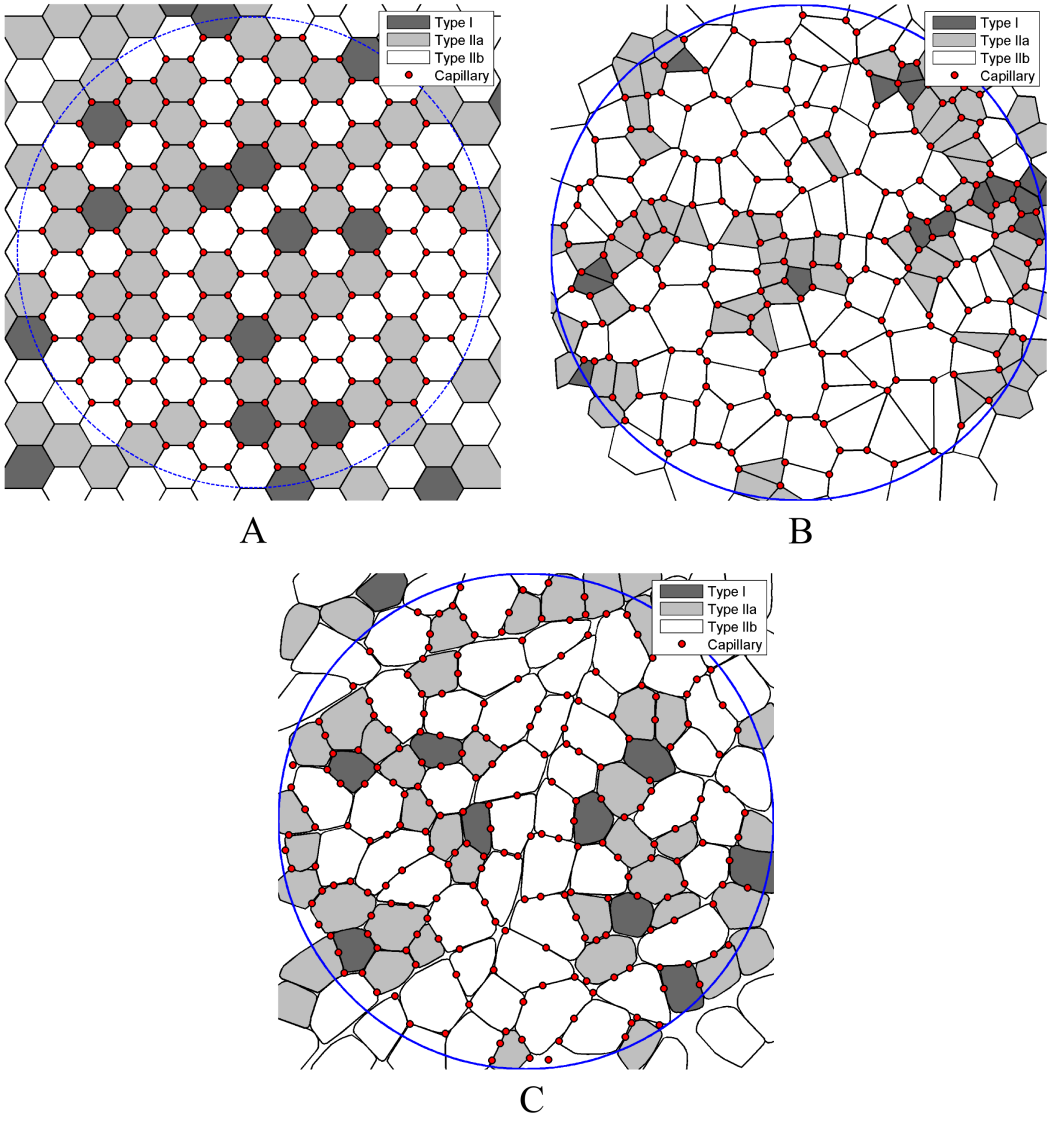

Figure 3.3: Examples of the fibre type distributions we use in our model. (A) A random distribution of a 9:37:54 (I:IIa:IIb) fibre–type composition. (B) A size–based distribution of 9:37:54 fibre type composition. (C) Fibre size and type distributions and fibre type composition (9:37:54) are obtained from histological sections of a rat EDL muscle with capillary locations identified via alkaline phosphotase staining and fibre types via succinate dehydrogenase and myosin ATPase staining.

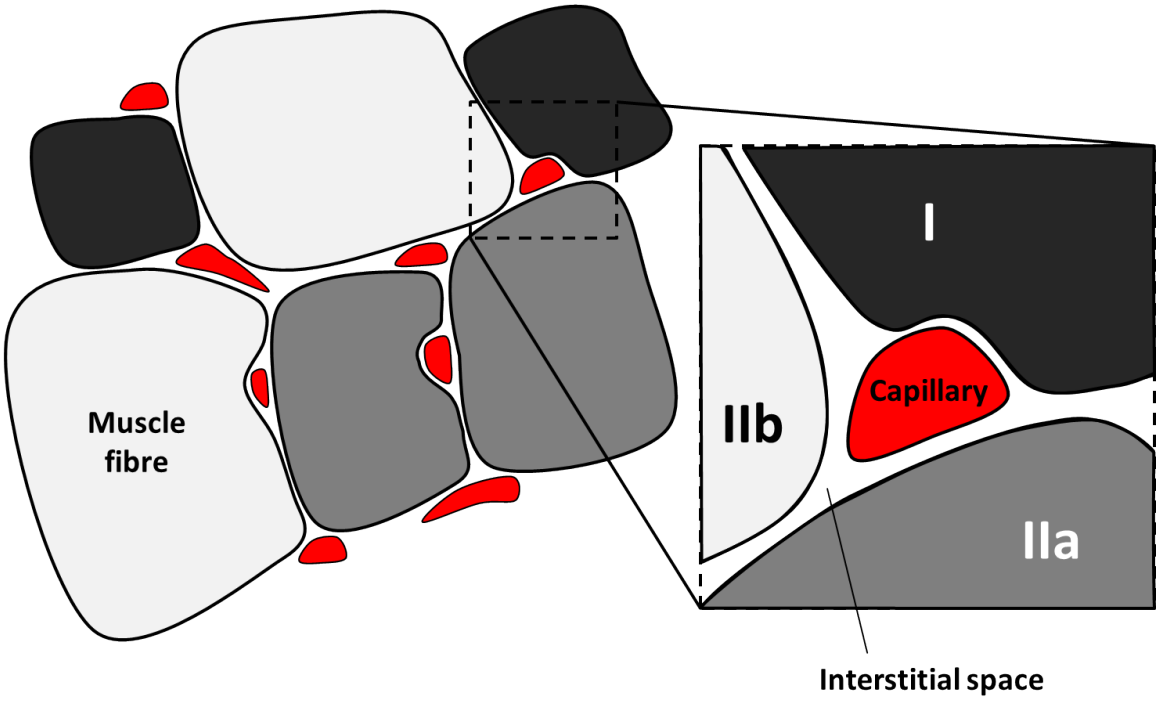

Figure 3.4: A diagram showing skeletal muscle fibres surrounded by capillaries.

use in morphometric analyses (see Chapter 1 for details) of mixed muscle tissues with heterogeneous metabolic activities and histological properties, as found in skeletal muscles. Therefore, we consider muscle tissues with either uniform or non-uniform functional characteristics, which allows an exploration general enough to cover both skeletal and cardiac muscles. A typical muscle is exemplified by the tissue cross–section presented in Fig. 3.1, where the lengthscale of a capillary cross–section is $2-4$ μm. In addition, we also incorporate facilitated diffusion and Michaelis–Menten kinetics of O_2 consumption into the transport equation to account for myoglobin–facilitated diffusion and to explore the consequences of tissue hypoxia.

3.5.1 Mathematical formulation of the model

Oxygen transport is explored in a two-dimensional domain representing a cross section of a skeletal or cardiac muscle tissue. In the section transversal to this domain, an array of capillaries of small circular cross–sectional shape supplies the tissue with O_2 through passive diffusion. Since the ratio of the characteristic intercapillary distance to capillary length is sufficiently small ($\mathcal{O}(10^{-2})$), tissue diffusion along the direction of the fibre axis can be neglected under maximal sustainable conditions and away from the arteriolar and venous ends of capillaries [63, 68, 189].

3.5.1.1 Equations

An extension of our previous model of O_2 steady–state diffusion in homogeneous tissue is used to explore further the trapping region analogue of Voronoi polygons under conditions of compartment–specific diffusion and uptake, myoglobin–facilitated diffusion, and O_2 consumption rate with Michaelis–Menten kinetics.

Assuming myoglobin freely diffuses in muscle fibres, the diffusional flux of free O_2 ($\mathbf{J}_{O_2}$) is further enhanced by an additional diffusive flux of myoglobin–bound O_2 ($\mathbf{J}_{MbO_2}$). Hence, the total diffusional flux of O_2 in muscle fibres becomes

$$\mathbf{J} = \mathbf{J}_{O_2} + \mathbf{J}_{MbO_2}.$$

To simplify this expression, we make use of the fractional saturation of myoglobin,

$$S_{Mb} = \frac{[MbO_2]}{[Mb] + [MbO_2]}, \tag{3.6}$$

where $[\cdot]$ denotes the concentration and

$$c_{Mb} = [Mb] + [MbO_2]$$

is the bulk myoglobin concentration in muscle fibres, which is taken to be constant. Hence, one can write

$$[MbO_2] = c_{Mb} S_{Mb}.$$

Using Fick's Law, we can then recast the total diffusional flux of O_2 in the form

$$\mathbf{J} = -\mathcal{D}_{O_2} \nabla [O_2] - \mathcal{D}_{Mb} c_{Mb} \nabla S_{Mb},$$

where $\mathcal{D}_{O_2}$ and $\mathcal{D}_{Mb}$ are the molecular diffusivities of free O_2 myoglobin, respectively.

In what follows we show that $S_{Mb} := S_{Mb}(p)$, where p is the local PO_2. Given the solubility of O_2 in muscle tissue is α, we can employ Henry's Law, $[O_2] = \alpha p$, to get

$$\mathbf{J} = -\left[\mathcal{D}_{O_2}\nabla(\alpha p) + \mathcal{D}_{Mb}c_{Mb}\left(\frac{dS_{Mb}}{dp}\nabla p\right)\right].$$

Such a derivation allows us to account for facilitated O_2 transport by exploiting a single partial differential equation. In particular, this equation describes O_2 diffusion in muscle tissue fibres and interstitial spaces via incorporating compartment–specific biophysical parameters, thus capturing the differences in O_2 diffusion resulting from the local heterogeneity in oxidative metabolism to be explored. In addition, intravascular transport is averaged out and incorporated via a boundary condition at capillary walls. For the purpose of exploring the appropriateness of Voronoi polygons, neglecting intravascular heterogeneities is appropriate as the primary assumption is that the tissue is under maximal sustainable (aerobic) activity.

Consequently, the steady–state transport of O_2 in each tissue compartment j can be described by p, which is governed by conservation of mass

$$\nabla \cdot \left[\mathcal{D}_j\nabla(\alpha_j p) + c_j^{Mb}\mathcal{D}_j^{Mb}\left(\frac{dS_{Mb}}{dp}\nabla p\right)\right] - \mathcal{M}_j(p) = 0, \tag{3.7}$$

where $\mathcal{D}_j$ and α_j are the molecular diffusivity and solubility of free O_2, c_j^{Mb} and $\mathcal{D}_j^{Mb}$ are the bulk myoglobin concentration and diffusivity, and $\mathcal{M}_j$ is the rate of O_2 consumption in muscle tissue compartment j. Here j denotes the following tissue compartments: *interstitial spaces* (j = IS) and *fibre types* I (j = Type I), IIa (j = Type IIa), and IIb (j = Type IIa). Note that α_j is constant below and thus $\nabla(\alpha_j p) = \alpha_j \nabla p$.

We further note that due to the near absence of myoglobin binding and consumption of free O_2 in interstitial spaces, the steady–state equation governing O_2

transport in this compartment is reduced to

$$\alpha_{\mathrm{IS}}\mathcal{D}_{\mathrm{IS}}\nabla^2 p = 0. \tag{3.8}$$

The domain geometry is obtained by considering a circular tissue cross–section and then rescaling to the unit disc, $\mathbb{D}^1$. After rescaling, the region enclosed by compartment j will be denoted by Ω_j with boundary $\partial\Omega_j$. Capillaries are assumed to possess an area, C_i, with a boundary, ∂C_i, though below we treat the capillaries as small circles with radius r_{cap}. Therefore, we seek to investigate PO_2 in a region of the unit disc that excludes the capillary *lumina*, $\Omega = \bigcup_j \Omega_j = \mathbb{D}^1 \setminus \bigcup_i C_i$.

3.5.1.2 Michaelis–Menten consumption

Given we also aim to explicitly study tissue hypoxia, we need to consider an O_2 consumption kinetics that is valid at very low PO_2 as our previous use of a constant O_2 consumption is only valid under the physiological assumption of saturated O_2 uptake. We address this by assuming that the rate of O_2 consumption by a tissue compartment (e.g. a muscle fibre) follows the Michaelis–Menten kinetics described by

$$\mathcal{M}_j(p) = \frac{\mathcal{M}_0^j p}{p + p_c}, \tag{3.9}$$

where $\mathcal{M}_0^j$ is the maximal consumption rate volume–averaged over tissue compartment j, and p_c is the tissue PO_2 value which reflects the partial pressure scale where fibre mitochondria are no longer able to extract O_2 at maximal rate. This drop in the mitochondrial O_2 consumption rate at very low local PO_2 values has been verified experimentally (see Fig. 3.5; [190]) and was recently explained [141] by the observation that the expression of *hypoxia inducible factor-1* (HIF-1) in hypoxic conditions actively downregulates mitochondrial O_2 consumption. Hence, such a non-linear dependence on PO_2 extends our modelling predictions to extremely low PO_2 values, thus allowing the exploration of tissue hypoxia. We note here that we have implicit assumed that mitochondria are homogeneously distributed within muscle fibres.

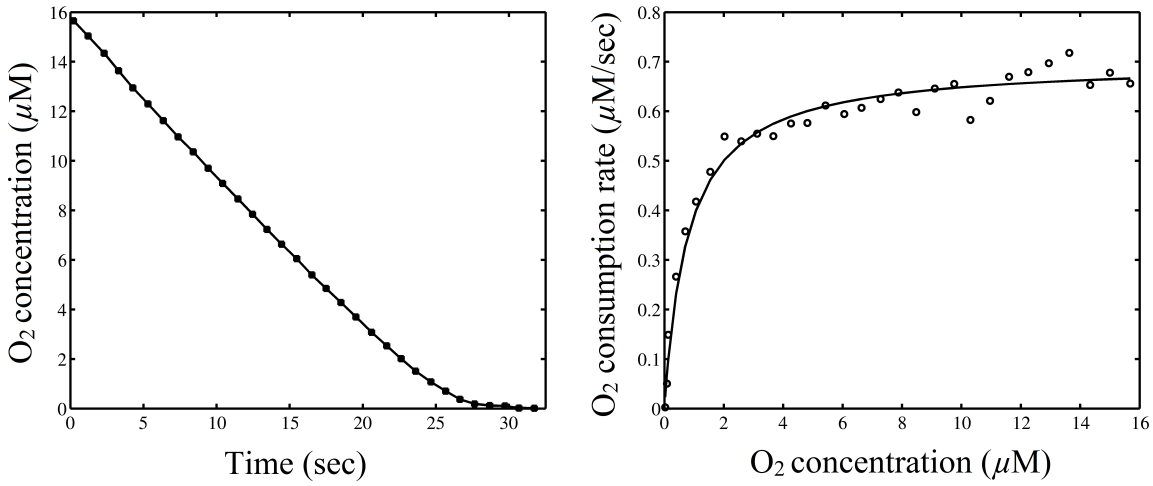

Figure 3.5: Left, the decrease in O_2 concentration, c, at pH 7.4 and in the presence of 0.5 mM ATP (adenosine triphosphate) during mitochondrial oxidative phosphorylation. Right, the rate of mitochondrial respiration (O_2 consumption, $\mathcal{M}$) as a function of c. This rate remains relatively constant for $c > 5$ μM. The best fit of the data was obtained from Michaelis–Menten kinetics $\mathcal{M} = V_m c/(c_{50}+c)$, where V_m is the consumption rate at full O_2 saturation, and c_{50} is the O_2 concentration at half–maximal consumption rate. Reproduced from [190] by permission of the publisher.

3.5.1.3 Myoglobin

In striated muscle an O_2 protein carrier, called myoglobin (Mb), is present in concentrations that vary significantly across a range of different tissues ($0-1$ mM; [192]). In particular, muscles with high oxidative metabolism exhibit a distinctive red colour owing to the large amounts of myoglobin present [134, 139]. In contrast, mixed and glycolytic muscles appear whiter, with the glycolytic ones having the least amount of myoglobin [134, 191].

Since myoglobin is an O_2 carrier, its concentration in muscle fibres can be used to estimate its O_2 binding capacity (i.e. O_2–bound concentration at full Mb saturation). For example, letting c_{Mb} be the value for the fibre concentration of myoglobin (in mM units), and assuming an O_2 solubility in fibre of 4×10^{-5} ml O_2/ml $\cdot$ mmHg with a mean PO_2 of 15 mmHg, the myoglobin capacity to bind O_2 at 37 °C and 1 atm is larger than the concentration of free O_2 by a factor of

$$\frac{[\mathrm{O_2}]_{\mathrm{Bound}}}{[\mathrm{O_2}]_{\mathrm{Free}}} = \frac{\left(25.45\ \frac{\text{ml O}_2}{\text{mM}\cdot\text{L}}\right)\times c_{\mathrm{Mb}}}{\left(4\times10^{-5}\frac{\text{ml O}_2}{\text{ml}\cdot\text{mmHg}}\right)\times\left(15\ \text{mmHg}\right)} \approx 42.42\ \text{mM}^{-1}\times c_{\mathrm{Mb}}.$$

Hence, fibres with more myoglobin will have more storage capacity of O_2 than those with lower myoglobin concentrations. In particular, given a muscle fibre consuming O_2 at a rate $\mathcal{M}_0$, a crude estimate for the time it takes this fibre to deplete its O_2–bound reserves when O_2 delivery is interrupted is

$$\frac{[O_2]_{\text{Bound}}}{\mathcal{M}_0} \approx \frac{0.02545 \ \frac{\text{ml } O_2}{\text{mM·ml}} \times c_{\text{Mb}}}{\mathcal{M}_0}.$$

Thus, for $c_{\text{Mb}} = 0.5$ mM and a range of uptake values representing resting to exercising conditions ($\mathcal{M}_0 = 2 - 20 \times 10^{-4}$ ml O_2/ml·sec), the O_2 depletion time is over a minute for a resting fibre and 6 seconds for an exercising one. Therefore, myoglobin can play an important role in storage of O_2 and enhancement of O_2 flux. However, this role is quite subtle and may only be fully appreciated in tissue regions where the scale of PO_2 is small (e.g. hypoxic tissue regions). Indeed, myoglobin remains fully saturated until local tissue PO_2 values fall well below 10 mmHg. This is better illustrated when we consider the kinetics of the MbO_2 reaction

$$\text{Mb} + \text{O}_2 \underset{k_{-1}}{\overset{k_{+1}}{\rightleftharpoons}} \text{MbO}_2.$$

Since that the Law of Mass Action gives the following relation at equilibrium

$$k_{-1}[\text{MbO}_2] = k_{+1}[\text{Mb}][\text{O}_2],$$

we can derive the Mb–saturation curve in terms of O_2 concentration by substituting the equilibrium relation above into Eq. (3.6) to get

$$S_{\text{Mb}} = \frac{K[\text{O}_2]}{1 + K[\text{O}_2]},$$

where $K = k_{+1}/k_{-1} = 1/[\text{O}_2]_{50}$. Here, $[\text{O}_2]_{50}$ is the O_2 concentration when myoglobin is half-saturated. Therefore, assuming a homogeneous distribution of myoglobin molecules within muscle fibres and rapid local kinetics of MbO_2 dissociation, the equilibrium O_2–saturation of Mb is governed by

$$S_{\mathrm{Mb}}(p) = \frac{p}{p + p_{50,\mathrm{Mb}}},$$

where $[O_2] = \alpha p$ (Henry's Law), and $p_{50,\mathrm{Mb}}$ is the tissue PO_2 at half Mb–saturation.

3.5.2 Boundary conditions

The exchange of O_2 between capillaries and the interstitial fluid or fibres occurs at their respective interfaces. Across the part of the capillary wall in contact with either the interstitial fluid or fibres, passive permeation of O_2 into the tissue is characterised by the boundary condition for the i^{th} capillary

$$\mathbf{n}_i \cdot (\alpha_j D_j \nabla p) = k(p_{\mathrm{cap}} - p), \qquad \partial C_i \cap \partial \Omega_j, \tag{3.10}$$

where $\mathbf{n}_i$ is the unit normal vector on the capillary wall pointing away from the tissue and into the capillary, k is the mass transfer coefficient, p_{cap} is the transversally–averaged intracapillary PO_2, and p is the partial pressure of O_2 at the external capillary wall. At the interstitium–fibre and fibre–fibre interfaces we assume continuity of O_2 flux and concentration

$$\mathbf{n}_{j_n} \cdot (\alpha_{j_n} \mathcal{D}_{j_n} \nabla p) = \mathbf{n}_{j_m} \cdot (\alpha_{j_m} D_{j_m} \nabla p), \qquad \partial \Omega_{j_n} \cap \partial \Omega_{j_m}, \tag{3.11}$$

$$\alpha_{j_n} p = \alpha_{j_m} p, \qquad \partial \Omega_{j_n} \cap \partial \Omega_{j_m}. \tag{3.12}$$

Additionally, a no–flux boundary condition is imposed at the outer boundary of the tissue, effectively the muscle fascicle, to signify no exchange across it

$$\mathbf{n}_j \cdot \Big(\alpha_j D_j \nabla p \Big) \Big|_{\partial \Omega} = 0. \tag{3.13}$$

As mentioned previously, perturbing the latter boundary condition is verified to induce no significant influence on the system behaviour away from the tissue domain boundary, thus justifying its use.

3.5.3 Non-dimensionalisation

To reduce the number of parameters, we non-dimensionalise the model as follows. Given that N_c capillaries in a tissue disc have an average capillary density ρ, the lengthscale, L, is taken to be equal to the diameter of the disc, which is given by $L = \sqrt{4N_c/\pi\rho}$. We use this along with p_{cap}, α_{I}, $\mathcal{D}_{\text{I}}$, c_{I}^{Mb}, $\mathcal{D}_{\text{I}}^{\text{Mb}}$, and $\mathcal{M}_0^{\text{I}}$ to non-dimensionalise our model by setting

$$
\begin{aligned}
&x = L\bar{x}, && p = p_{\text{cap}}\bar{p}, && p_c = p_{\text{cap}}\bar{p}_c, && p_{50,\text{Mb}} = p_{\text{cap}}\bar{p}_{50,\text{Mb}},\\
&\alpha_j = \alpha_{\text{I}}\bar{\alpha}_j, && \mathcal{D}_j = \mathcal{D}_{\text{I}}\bar{\mathcal{D}}_j, && c_j^{\text{Mb}} = c_{\text{I}}^{\text{Mb}}\bar{c}_j^{\text{Mb}}, && \mathcal{D}_j^{\text{Mb}} = \mathcal{D}_{\text{I}}^{\text{Mb}}\bar{\mathcal{D}}_j^{\text{Mb}},\\
&\mathcal{M}_0^j = \mathcal{M}_0^{\text{I}}\bar{\mathcal{M}}_0^j, && \theta_{\text{I}} = \frac{c_{\text{I}}^{\text{Mb}}\mathcal{D}_{\text{I}}^{\text{Mb}}}{\alpha_{\text{I}}\mathcal{D}_{\text{I}}p_{\text{cap}}}, && \mu_{\text{I}} = \frac{L^2\mathcal{M}_0^{\text{I}}}{\alpha_{\text{I}}\mathcal{D}_{\text{I}}p_{\text{cap}}}, && \kappa_{\text{I}} = \frac{Lk}{\alpha_{\text{I}}\mathcal{D}_{\text{I}}},
\end{aligned}
$$

where the bars denote non-dimensional variables and parameters. Here $\theta_{\text{I}}, \mu_{\text{I}}, \kappa_{\text{I}} > 0$ are the non-dimensionalised myoglobin content, metabolic O_2 demand, and mass transfer coefficient of fibre Type I. Dropping the bars, the non-dimensional model is reduced to

$$
\begin{aligned}
\nabla\cdot\left[\left((\alpha_j\mathcal{D}_j + c_j^{\text{Mb}}\mathcal{D}_j^{\text{Mb}}\theta_{\text{I}}\frac{dS_{\text{Mb}}}{dp}\right)\nabla p\right] - \mathcal{M}_0^j\mathcal{M}_{\text{I}}(p) &= 0, && \mathbf{x}\in\Omega_j, && \text{(3.14a)}\\
\mathbf{n}_i\cdot(\alpha_j\mathcal{D}_j\nabla p) &= \kappa_i(1-p), && \mathbf{x}\in\partial C_i\cap\partial\Omega_j, && \text{(3.14b)}\\
\mathbf{n}_{j_n}\cdot(\alpha_{j_n}\mathcal{D}_{j_n}\nabla p) &= \mathbf{n}_{j_m}\cdot(\alpha_{j_m}\mathcal{D}_{j_m}\nabla p), && \mathbf{x}\in\partial\Omega_{j_n}\cap\partial\Omega_{j_m}, && \text{(3.14c)}\\
\alpha_{j_n}p &= \alpha_{j_m}p, && \mathbf{x}\in\partial\Omega_{j_n}\cap\partial\Omega_{j_m}, && \text{(3.14d)}\\
\mathbf{n}_j\cdot\left(\alpha_j\mathcal{D}_j\nabla p\right)\Big|_{\partial\Omega} &= 0, && && \text{(3.14e)}\\
\mathcal{M}_{\text{I}}(p) &= \frac{\mu_{\text{I}}p}{p+p_c}, && && \text{(3.14f)}\\
S(p) &= \frac{p}{p+p_{50,\text{Mb}}}. && && \text{(3.14g)}
\end{aligned}
$$

3.6 Model parameters

The parameter values used in our model are given in Table 3.2. The lengthscale, L, is derived by assuming that capillaries in the circular simulation domain have a dimensional density of the rat EDL muscle cross–section in Fig. 3.2 ($\rho = 913.4$

Parameter	Symbol	Fibre type, j			Unit	Refs.
		I	IIa	IIb		
O_2 demand	$\mathcal{M}_0^j$	15.7	13.82	7.85	10^{-5}ml O_2/ml·s	[174, 193]
Mb concentration	c_j^{Mb}	10.2	4.98	1.55	10^{-3}ml O_2/ml	[134]
O_2 solubility	α_j	3.89×10^{-5}			ml O_2/ml·mmHg	[23, 127]
O_2 diffusivity	$\mathcal{D}_j$	2.41×10^{-5}			cm^2/s	[15, 57]
Mb diffusivity	$\mathcal{D}_j^{Mb}$	1.73×10^{-7}			cm^2/s	[111]
Mass transfer coefficient	k	4.00×10^{-6}			ml O_2/cm^2·mmHg·s	[54, 71]
Intracapillary PO_2	P_{cap}	20			mmHg	[55]
Mb half-saturation PO_2	$P_{50,\mathrm{Mb}}$	5.3			mmHg	[111]
PO_2 at half demand	P_c	0.5			mmHg	[91]
Capillary radius	r	$1.8 - 2.5 \times 10^{-4}$			cm	[58]
Capillary density	ρ	913.4			mm^{-2}	*
Number of capillaries	N_{cap}	$204 - 215$			unitless	*
Lengthscale	L	$5.33 - 5.47 \times 10^{-2}$			cm	
Transfer coefficient	κ_j	233.4			unitless	
O_2 demand	μ_j	25.05	22.05	12.53	unitless	

Table 3.2: Except for the capillary density and the number of capillaries, the parameter values in the upper part of the table, above the line, are based on experiments, while those in the lower part are derived values. The solubility and diffusivity of O_2 are constant across all compartments. Mb = myoglobin, * = estimated from our histological preparations (Fig. 3.2D).

mm^{-2}). For convenience, the diffusivity and solubility coefficients of O_2 in interstitial spaces are assumed to equal those of muscle fibres. Although interstitial diffusivity is typically taken to be similar to that of blood *plasma*, our simulations results are insensitive to such scalings as long as the scale of interstitial spaces does not exceed a few microns. We note here that such scales may not be valid under pathophysiological conditions and are a topic for further study (see Section 3.7 below).

3.7 Model limitations

For convenience, the compartment–dependent diffusive parameters (solubility and diffusivity) of our model were assumed to be uniform in our simulations, although actual values may not be. Parallel simulations based on non-uniform diffusive parameters have shown a general improvement in the correlation between Voronoi polygons and trapping regions, although not significant enough to alter any of the trends observed in our current results. Further, the current model geometries are limited in terms of intra-fibre resolution, but it can be extended to investigate finer micro-architecture

resolution such as the non-uniform mitochondrial distributions observed in oxidative fibres via aggregations under the *sarcolemma* [95, 129]. This can be modelled by allowing for intracellular uptake compartmentalisation whereby an oxidative fibre is composed of two metabolically distinct zones: a *subsarcolemmal* zone of higher uptake per unit volume and an *intermyofibrillar* region of lower uptake.

Other feasible extensions include the cases of *oedema* and *fibrosis*, where the interstitial parameters and scale become important and also the influence of arterioles and venules on O_2 supply regions, rather than focussing on regions of tissue where larger vessels are not present [168]. Finally, since our model predicts the behaviour of this system in the context of maximal capillary supply capacity where intravascular convection and intracellular axial diffusion are neglected, our results are currently restricted to 2D muscle cross–sections, but are in principle extendible to 3D image stacks. In particular, our model can be extended to allow for sub-maximal O_2 uptake and increased perfusion heterogeneities as well as geometrical details such as capillary cross bridges and tortuous or oblique capillaries.

3.8 Numerical solution

3.8.1 PO_2 flux lines

We seek to determine the areas of tissue where capillary PO_2 fluxes are restricted to a no-flux region surrounding each capillary, the *trapping regions*, which are generalisations of Krogh cylinders [120]. However, a direct way to accurately calculate O_2 supply region areas is not feasible due to the complexity of heterogeneous O_2 uptake. To proceed, we note that each such region of the muscle tissue is spanned by O_2 flux lines (or streamlines) that emerge from the enclosed capillary. Noting that Eq. (3.14) possesses a unique solution (see Appendix A), we use a finite element formulation to solve it for PO_2. The solution enables a derivation of O_2 streamlines via Eq. (2.10), and a subsequent determination of the TR geometries using the numerical methodologies outlined in the previous chapter and Appendix A.

3.9 Results

Since capillary interaction between neighbouring capillaries is excluded at the outer domain boundary by imposing a no-flux condition, we again consider generating

statistics for capillaries within a region of tissue where boundary artefacts are negligible, namely the region of interest (ROI; [46]). Recall that the ROI is a square box within the disc and concentric with it, which is used to sample capillaries for statistical consideration. The edges of this region are further from the edge of the domain than the intercapillary distance and the objective is to remove domain boundary artefacts, which can be confirmed *a posteriori*. The upper and left–hand sides of the square are identified as *inclusion lines*, whilst the lower and right-hand sides are, in contrast, *exclusion lines*. A capillary domain belongs to the ROI if it falls entirely within the box, or if it falls partly within the box and overlaps inclusion lines *only*. To ensure robust statistical measures we consider identical populations of capillaries. We emphasise that Voronoi polygons represent the capillary domains and, for definiteness, only Voronoi polygons are used to determine the inclusion criteria for the region of interest, even when the subject of study is the *trapping regions*.

In order to quantitatively assess the correlation between Voronoi polygons and capillary supply regions, as measured by trapping regions, we use statistical measures similar to those detailed in the previous chapter. These are defined in Table 2.1 and their numerical values are presented in Table 3.3 for various geometries and parameter regimes. Additionally, we present a comparison between VP and corresponding trapping regions (TR) in terms of the LCFR index (Eqs. (3.2) and (3.4)). This is shown as an average of the normalised difference of LCFR measures obtained from Voronoi polygons ($\mathrm{LCFR}^{\mathrm{VP}}$) and trapping regions ($\mathrm{LCFR}^{\mathrm{TR}}$)

$$LCFR_{\Delta} = \mathrm{mean}\left(\frac{|LCFR_i^{\mathrm{TR}} - LCFR_i^{\mathrm{VP}}|}{LCFR^{\mathrm{TR}}}\ \%\right). \tag{3.15}$$

3.9.1 Simulations and qualitative correlation

3.9.1.1 Spatial profile of PO_2

The range of PO_2 is an increasing function of fibre size heterogeneity as can be seen by comparing the spatial PO_2 distribution of different geometries (Fig. 3.6). In particular, the widest range and lowest PO_2 values for each parameter regime are found in the histologic geometry cases (Figs. 3.6G-I), with hypoxia being at the extreme (non-dimensional hypoxic threshold = 0.025). Cases of high scaling of

differential uptake show more heterogeneity in PO_2 distribution than normal cases even though the average tissue uptake is fixed (Figs. 3.6A vs. B, D vs. E, and G vs. H).

3.9.1.2 Voronoi polygons and trapping regions

Among all random fibre type distributions for the synthetic uniform fibre size distribution, SU, the most significant perturbations of trapping region boundaries, relative to those of the Voronoi polygons, are observed in the 50:0:50 ratio of type I, IIa and IIb fibres (Fig. 3.7A; other distributions are not shown here). Nonetheless, for such a symmetrical fibre geometry and capillary distribution, boundaries of TR are well approximated by those of VP (Figs. 3.7A, C), with only slight deviations near the interface of fibres of different metabolic demands. This is not the case for increased metabolic heterogeneities (Fig. 3.7B), where boundary deviations of TR are much more extensive in the presence of high differential scaling of fibre–dependent O_2 uptake (e.g. 10:1 for Type I vs. Type IIb). The opposite trend, of an increasing agreement between TR and VP, is observed when the tissue is hypoxic in the presence of a non-linear O_2 consumption rate and myoglobin facilitation of intracellular O_2 diffusion (e.g. Fig. 3.7C).

Although the aforementioned pattern holds for all other geometries, SN (Figs. 3.7D-F) and H (Figs. 3.7G-I), boundary deviations in these cases are relatively greater in extent than those observed in the SU geometry.

3.9.1.3 Variability in supply domain areas

Area frequency histograms of trapping regions in the SU geometry are generally highly peaked with slightly broader distributions than Voronoi polygons (Figs. 3.8A, C). This is no longer the case in the presence of additional functional heterogeneities. For example, a large differential scaling in fibre–dependent uptakes for the SU case is observed to give rise to fat tails with a distinctive left–skewed distribution (Fig. 3.8B). Nonetheless, under hypoxic conditions such distributions are narrowed and the extended tails are less extreme (Fig. 3.8C).

The frequency histogram distributions for other geometries, synthetic nonuniform (SN; Figs. 3.8D-F) and histologic (H; Figs. 3.8G-I), are broader, partly reflecting the non-uniform distribution of fibre sizes and the asymmetry in capillary arrangements. In the SN case, the size–based fibre type arrangements with normal differential

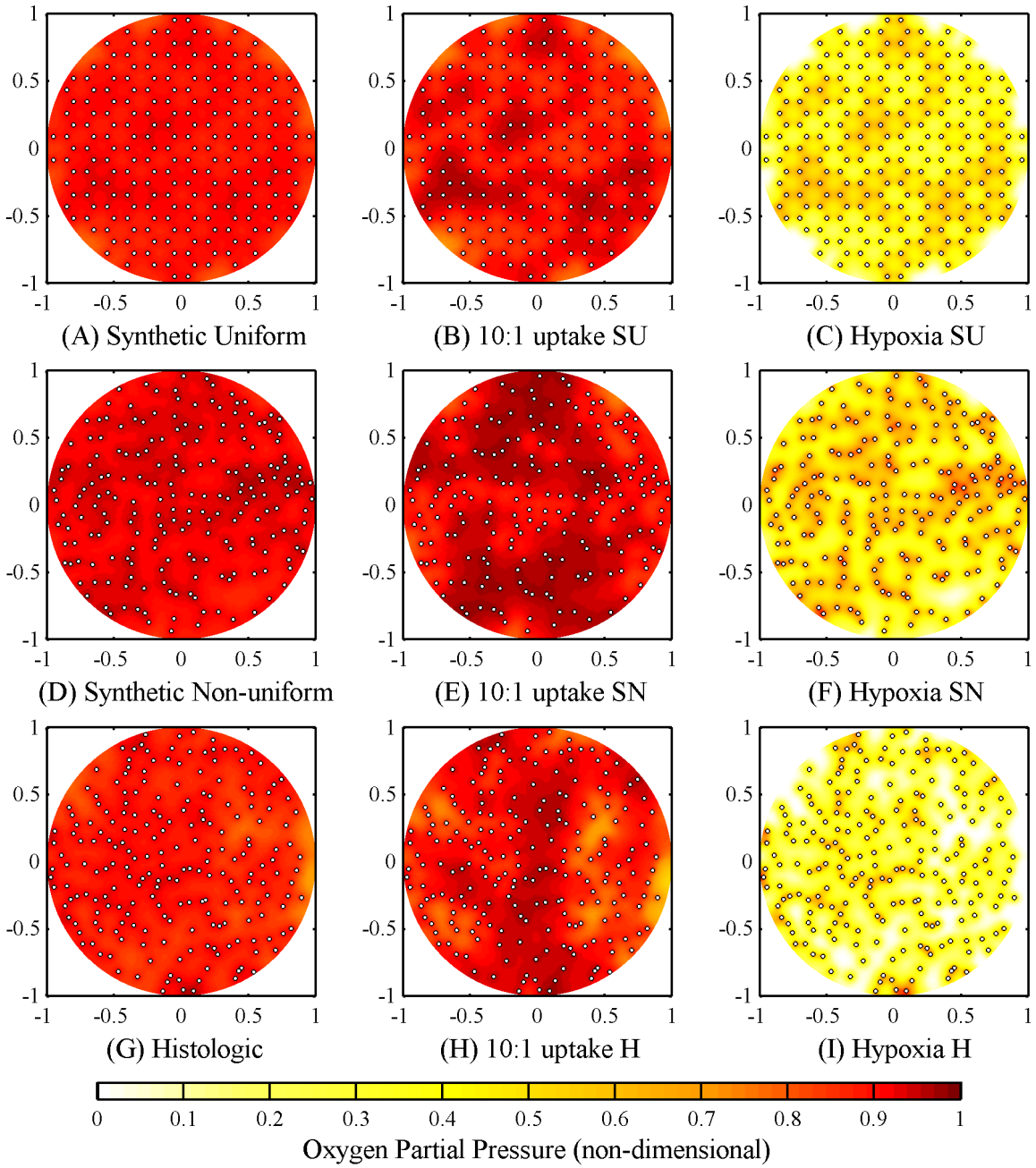

Figure 3.6: Spatial distribution of PO_2, with capillaries as small open circles. There are three geometry types (Row #1 = SU with a 50:0:50 Type I to IIb proportion; Row #2 = SN with a 50:0:50 size–based Type I to IIb proportion; Row #3 = H, with fibre types assigned by size according to the observed ratio 9:37:54 for types I, IIa, and IIb, where type I fibres constitute the smallest 9%). Plots (A, D, G) represent normal conditions. Plots (B, E, H) represent a 10-to-1 Type I:Type IIb differential uptake scaling keeping the same volume-averaged tissue uptake as in (A, D, G). Tissue hypoxia ($PO_2 < 0.5 - 1$ mmHg) is simulated in plots (C, F, I) via increasing the O_2 uptake of all fibres by a factor of eight (reducing capillary O_2 content gives similar results).

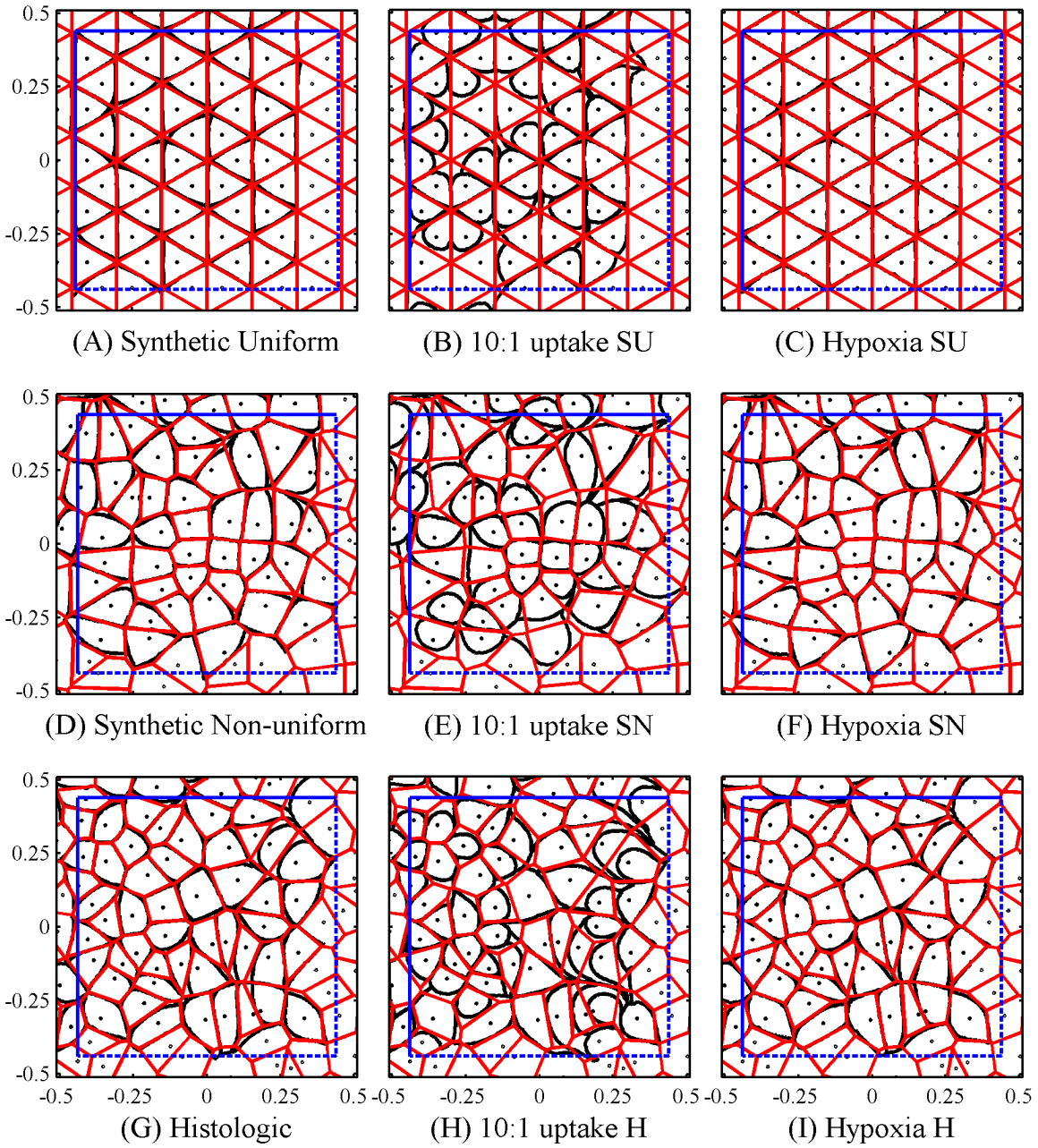

Figure 3.7: (A)-(I) Trapping region boundaries (black/dark colour) and Voronoi polygons (red/light colour) in the region of interest (blue/dark square: solid left/top edges and dashed right/bottom edges). The geometry and parameters in plots 3.7A-I are inherited from those used in Figs. 3.6A-I.

uptake (Figs. 3.8D, F) show TR distributions which are just as broad as those of VP, although the tails of the latter are slightly extended. Similar to SU, SN also exhibits the same left–skewed distribution when high differential scaling of uptake parameters is present (Fig. 3.8E), yet the tail is less extensive in this case. Moreover, the presence of hypoxic conditions shows a better histogram match with VP than the case of saturated O_2 uptake (Fig. 3.8D vs. Fig. 3.8F). These observations are also confirmed in the histologic geometry case (Figs. 3.8G-I).

3.9.1.4 Qualitative correlations

The spatial extent of TRs is described by VPs with a very good agreement for all fibre distributions considered with normal ratios of differential O_2 uptake (Figs. 3.7A, C, D, F, G, I) though the boundaries of TR are observed to deviate slightly from Voronoi polygons as the heterogeneity in fibre size is increased.

Similarly, given normal ratios of differential O_2 uptake, the area majority of histograms of VP coincide with those of TR (Figs. 3.8A, C, D, F, G, I), though VP distributions are more centralised than TR when fibre size is uniform. Nonetheless, as the heterogeneity in fibre size is increased, an extended tail emerges for the VP histograms (compare Figs. 3.8A, D, and G), whereas histograms of trapping regions remain relatively centralised, again as long as extensive uptake heterogeneities are not present. This confirms that Voronoi polygons can both underestimate and overestimate extremes of capillary supply areas, although our observations show this effect is not extensive for non-rarefied mixed muscles with realistic fibre–size distribution.

Distributions with non-uniform fibre sizes are naturally rarefied around relatively large fibres. In particular, in the case of fibre metabolic uptake varying inversely with fibre size, glycolytic fibres are effectively rarefied. Nonetheless, the area histograms of VP are seen to essentially coincide with those of TR (Figs. 3.8D, F, G, I).

However, with a large differential scaling of fibre–dependent O_2 uptakes, the VP boundaries show extensive differences from trapping regions (Figs. 3.7B, E, H), in addition to a more pronounced deviation in shape and distribution of TR areas (Figs. 3.8B, E, H). The influence of such fibre–uptake scaling on distant capillaries reveals that both non-neighbouring and nearest TR expand further in the direction

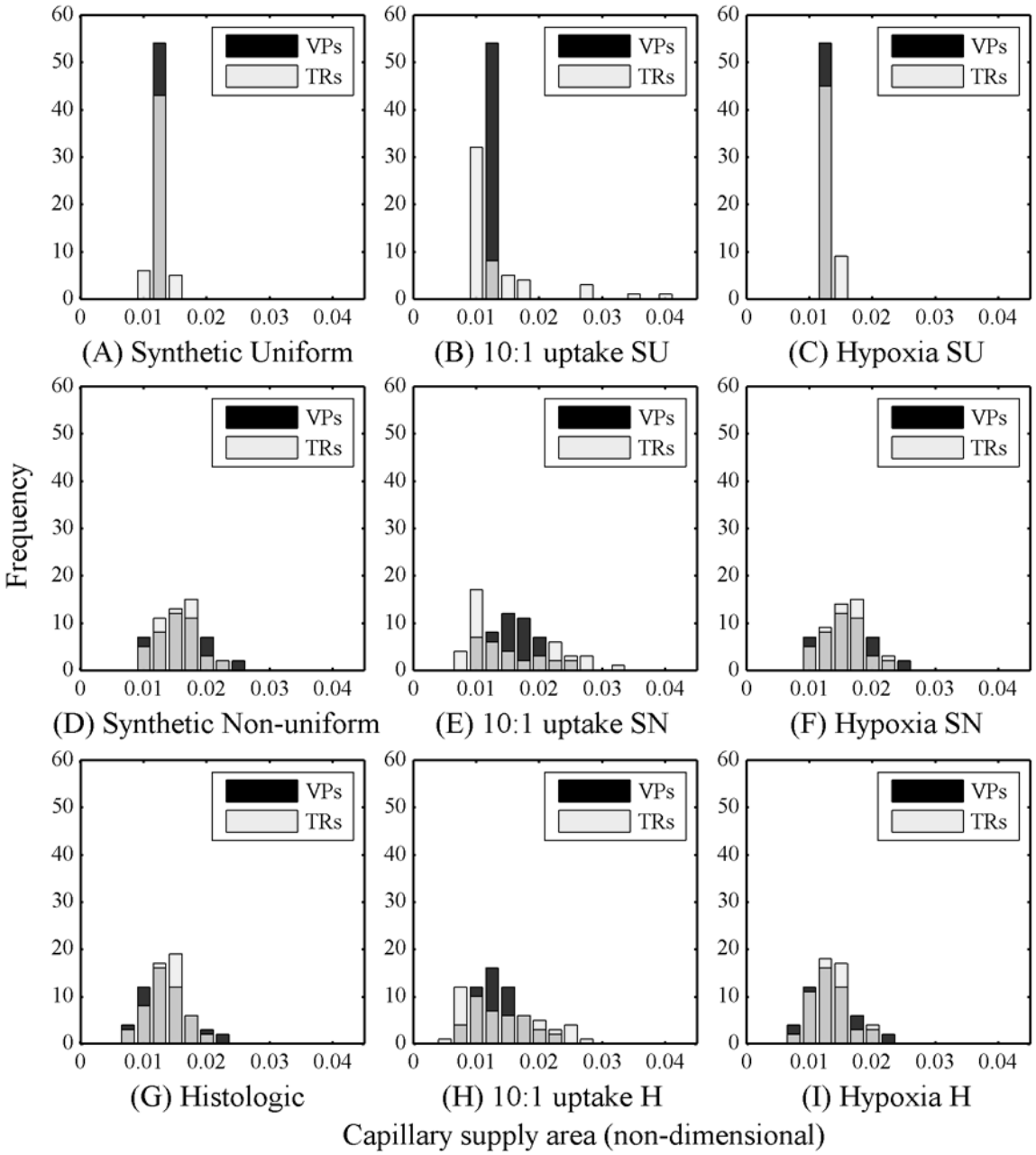

Figure 3.8: Frequency distributions of areas for Voronoi polygons and trapping regions within the region of interest. Histograms of the areas of Voronoi polygons are given by black/dark bars and trapping regions by light grey bars. Overlapping histograms are of intermediate shading. The horizontal axis represents tissue area fractions (supply area normalised by total tissue area) and the vertical axis shows frequency of occurrence, where the heights of the bars sum to the number of capillary domains included in region of interest. Again, the geometry and parameters in plots 3.8A-I are inherited from those used in Figs. 3.6A-I.

of more deprived fibres while, in contrast, VP are insensitive to such functional heterogeneities. Nonetheless, when the tissue is hypoxic all such differences in area frequency distributions are reduced and the correlation between boundaries of TR and VP is improved relative to the case of abundant O_2 and thus saturating uptake.

3.9.2 Data tabulation and quantitative correlation

3.9.2.1 The area correlation coefficient, $\mathcal{CC}$

The area correlation coefficient ($\mathcal{CC}$) is a measure of the linear dependence between the VP and TR areas (and is given by their covariance divided by both of their standard deviations). Table 3.3 demonstrates a decreased degree of correlation between the areas of VP and TR for random fibre type distributions. For such distributions, the trends in the data for random fibre types distributions are representative and shows that the highest $\mathcal{CC}$ is seen in the most metabolically homogeneous distributions, with lowest found in the mixed oxidative–glycolytic random arrangements (50% type I, 0% type IIa, and 50% type IIb), among which the randomly rarefied SU is lowest.

Except for extremely low correlations in high differential scaling of fibre uptakes, the data also indicate that the 50:0:50 size–based distributions have generally higher CC values than all randomly mixed distributions. Moreover, the area correlation of a real mixed distribution (9% type I, 37% type IIa, and 54% type IIb) is found to be greater than that of the 50:0:50 size–based cases, with hypoxia being the only exception where $\mathcal{CC}$ is found to be highest across all mixed fibre–type distributions. Additional simulations (not shown) show similar trends for the EDL muscle fibre distribution (H), although higher corresponding values are observed in this case.

3.9.2.2 The normalized means μ_Δ, $\mu_\cap$, μ_R, $LCFR_\Delta$

The *normalised mean of difference* (μ_Δ) provides a measure for the degree of failure of Voronoi polygons to cover comparable areas to those of trapping regions. This is observed to correlate with heterogeneities in fibre functional characteristics, fibre size, and capillary distributions.

For symmetrical capillary and fibre distributions (SU), this statistic increases with increased heterogeneity in fibre type composition with the 50:0:50 proportion of types I, IIa, IIb being the highest ($\mu_\Delta = 0.0679$), However, introducing fibre type IIa (9:37:54) leads to a slightly smaller value ($\mu_\Delta = 0.0473$). Further functional

heterogeneities, such as down–scaling the O_2 uptake of type IIb fibres by a factor of five, lead to a 332% increase in μ_Δ value ($\mu_\Delta = 0.3008$ vs. 0.0697). In contrast, a 10% random capillary rarefaction leads to a 78.6% increase in μ_Δ value ($\mu_\Delta = 0.1245$ vs. 0.0697), and a 50% reduction in capillary density increases μ_Δ by only 7.5% ($\mu_\Delta = 0.0749$ vs. 0.0697). However, when tissue PO_2 falls below $0.5 - 1$ mmHg (hypoxia) the areas covered by VP are generally improved by 35.6% with respect to areas of TR ($\mu_\Delta = 0.0449$ vs. 0.0697).

With fibre size heterogeneities introduced in the SN geometry, a comparison with the homogeneous fibre–type distribution in the SU geometry shows a marked increase in μ_Δ ($\mu_\Delta = 0.1209$ vs. 0.0077 in the 100:0:0 composition). As these two cases are of a similar non-mixed metabolic character (i.e. uniform fibre type), it is clear that such a deviation in mean normalised difference is a direct result of the heterogeneity in capillary spacing inherent in the SN geometry rather than a consequence of functional fibre heterogeneities, which are absent in this case. This implies that statistical values generated for a tissue with a uniform metabolic demand may serve as a baseline for exploring the functional effects of capillary asymmetries. For example, increasing the proportion of mixed fibre types influences μ_Δ less for distributions with non-uniform fibre size ($\mu_\Delta = 0.1600$ vs. 0.1206) than distributions with uniform fibre size ($\mu_\Delta = 0.0697$ vs. 0.0072), even in absolute terms.

Fibre size heterogeneities are also present in the H (histologic) geometry where, additionally, interstitial spaces add more to the spatial heterogeneity of capillaries. Given an EDL fibre–type composition (9:37:54), the H geometry shows higher μ_Δ values than those of the size–based SN and SU ($\mu_\Delta = 0.1129$ vs. 0.1048 and 0.0473, respectively). This likely reflects the heterogeneity in capillary spacing, which is highest in the H geometry (σ_{VP} is a measure of capillary heterogeneity). In contrast, despite the observation that high differential scaling of O_2 uptake increases μ_Δ for all geometries, we note that the histologic case has the lowest μ_Δ value ($\mu_\Delta = 0.2633$ vs. 0.3122 for SN and 0.3008 for SU). Noting that the effect of high differential uptake is expected to be more pronounced at the interface of dissimilar fibre types, the above change in μ_Δ trend is likely due the smaller interface in the histologic geometry which is reflected in the aggregation of similar fibre types.

The *normalised mean of intersection* ($\mu_\cap$) and the *mean ratio* (μ_R) describe how well Voronoi polygons capture the functional capillary supply of trapping regions, with values of unity for cases of a perfect match. Mean ratio values further infer whether,

			μ_Δ	σ_Δ	$\mu_\cap$	$\sigma_\cap$	μ_R	σ_{VP}	σ_{TR}	CC	$LCFR_\Delta$
Random	**0:0:100**	**SU**	0.0072	0.0073	0.9845	0.0028	0.9941	0	0.0073	*	0.19
		SN	0.1206	0.1455	0.8951	0.1800	1.0005	0.2528	0.1274	0.9307	6.44
	25:0:75	**SU**	0.0245	0.0291	0.9605	0.0339	1.0094	0	0.0301	*	3.46
		SN	0.1416	0.1794	0.8705	0.1697	1.0119	0.2528	0.1445	0.7381	9.05
	50:0:50	**SU**	0.0697	0.0882	0.9255	0.0382	1.0001	0	0.0882	*	4.60
		SU$_R$	0.1245	0.1612	0.8788	0.1065	1.0007	0.1983	0.1012	0.5901	7.41
		SN	0.1600	0.1955	0.8701	0.1671	1.0228	0.2528	0.1359	0.6770	8.18
	75:0:25	**SU**	0.0239	0.0285	0.9617	0.0329	1.0103	0	0.0285	*	3.10
		SN	0.1380	0.1680	0.8850	0.1763	1.0084	0.2528	0.1637	0.7662	6.93
	100:0:0	**SU**	0.0077	0.0078	0.9844	0.0030	0.9940	0	0.0078	*	0.23
		SN	0.1209	0.1448	0.8955	0.1805	1.0011	0.2528	0.1274	0.9340	6.43
Size based		**SN**	0.1115	0.1381	0.9084	0.1961	1.0103	0.2528	0.1886	0.8508	4.97
Real		**SU**	0.0473	0.0599	0.9447	0.0306	1.0042	0	0.0606	*	3.80
		SN	0.1048	0.1284	0.9114	0.1933	1.0025	0.2528	0.1757	0.8875	4.64
		H	0.1129	0.1451	0.8842	0.2136	0.9728	0.2854	0.1996	0.8692	3.41
Low CD		**SU**	0.0749	0.0931	0.9182	0.0408	1.0000	0	0.0931	*	4.93
		SN	0.1150	0.1422	0.9065	0.1959	1.0098	0.2528	0.1894	0.8380	4.89
		H	0.1186	0.1530	0.8782	0.2104	0.9710	0.2854	0.1972	0.8485	3.72
Uptake scale		**SU**	0.3008	0.4803	0.7615	0.0990	1.0833	0	0.4803	*	24.27
		SN	0.3122	0.3742	0.7700	0.2257	1.1529	0.2528	0.4362	0.5195	19.25
		H	0.2633	0.3118	0.7509	0.2626	1.0386	0.2854	0.4208	0.6723	17.95
MM		**SU**	0.0695	0.0867	0.9240	0.0383	1.0005	0	0.0867	*	4.47
		SN	0.1113	0.1376	0.9088	0.1970	1.0088	0.2528	0.1907	0.8502	4.96
		H	0.1131	0.1461	0.8846	0.2136	0.9733	0.2854	0.1995	0.8670	3.50
MM+Mb		**SU**	0.0689	0.0862	0.9244	0.0383	1.0004	0	0.0862	*	4.47
		SN	0.1113	0.1374	0.9088	0.1968	1.0085	0.2528	0.1900	0.8510	4.96
		H	0.1128	0.1454	0.8839	0.2134	0.9723	0.2854	0.1997	0.8681	3.46
Hypoxia		**SU**	0.0449	0.0551	0.9507	0.0244	0.9967	0	0.0551	*	2.96
		SN	0.0916	0.1128	0.9237	0.2058	1.0037	0.2528	0.1959	0.9082	3.83
		H	0.0894	0.1143	0.9112	0.2334	0.9793	0.2854	0.2132	0.9312	2.19

Table 3.3: Statistics determined from areas of VPs and TRs for the SU, SN, and H geometries. Fibre composition is denoted by I:IIa:IIb. Distinct parameter regime entries are denoted by *Low CD* (a 50% reduction in capillary density), *Uptake scale* (a I:IIa:IIb O_2 demand scaling of 1:0.88:0.1), *MM* (Michaelis–Menten kinetics), *MM+Mb* (MM & myoglobin–facilitated diffusion), and *Hypoxia* (MM+Mb in the presence of hypoxia, $PO_2 < 0.5 - 1$ mmHg). Hypoxia is achieved by increasing fibre uptake by a factor of eight. Unless otherwise specified, the entries for each row correspond to a random 50:0:50 for the SU geometry, a size–based 50:0:50 for the SN geometry, and a real 9:37:54 for the H geometry. * denotes cases where statistics are not applicable. The area correlation coefficient, $\mathcal{CC}$, is ill–defined for hexagonal arrays since all areas are the same, and hence their standard deviation is null. Nonetheless, it is clear that VP areas provide exceedingly good estimates of TR areas in this case. Note that the value of σ_{TR} under perfect symmetry reflects the scale of the boundary artefacts. See Eq. (3.15) for a definition of $LCFR_\Delta$.

on average, a VP is over- ($\mu_{\mathrm{R}} > 1$) or underestimating ($\mu_{\mathrm{R}} < 1$) the functional capillary supply.

The value of $\mu_{\cap}$ decreases with increased proportion of fibre types in SN and SU for random fibre type distributions, with SU distributions showing relatively higher values than SN. However, the decay of $\mu_{\cap}$ with respect to the proportion of mixed fibres is less in SN than SU. In addition, fibre distributions where a size–type correlation is enforced (size of Type I $\leq$ Type IIa $\leq$ Type IIb) show markedly higher $\mu_{\cap}$ values than randomly distributed fibre types of random size allocation ($\mu_{\cap} = 0.908$ vs. 0.87). In contrast, such values are significantly lower when differential scaling of fibre demand is present (e.g. $\mu_{\cap} = 0.77$ for SN). In addition, under the same conditions, an overestimate of functional capillary supply is evident (e.g. $\mu_R = 1.1529$ for SN). Conversely, when the tissue is hypoxic, there is a general improvement in the overlap of a Voronoi polygon with the corresponding trapping region ($\mu_{\cap} = 0.9084$ vs. 0.9237 for the SN 50:0:50 size–based distribution; $\mu_{\cap} = 0.9255$ vs. 0.9507 for the SU 50:0:50 distribution; $\mu_{\cap} = 0.8842$ vs. 0.9112 for the H distribution of EDL muscle).

Given that LCFR represents the number of capillary supply equivalents at maximum capacity, the mean of normalised difference of the LCFR indices, $LCFR_{\Delta}$, provides a measure of the degree of failure of VP–based capillary supply indices. As expected in the case of perfect capillary symmetry (SU) and uniform tissue uptake (100% Type I or Type IIb), this index is very small ($< 0.25\%$). However, even for this geometry, a random increase in the heterogeneity of fibre–type composition leads to a marked increase in $LCFR_{\Delta}$ value ($LCFR_{\Delta} = 0.23$ vs. 4.6). Similarly, the same trend is observed in the case of non-uniform fibre–size distribution, although the increase in $LCFR_{\Delta}$ is notably less ($LCFR_{\Delta} = 6.43$ vs. 8.18). Moreover, under normal differential uptake, the highest values of $LCFR_{\Delta}$ correspond to tissues with fibres of highly mixed types and random size (SU $= 3.1 - 4.6\%$ and SN $= 6.93 - 9.05\%$). Conversely, the case of size–based fibre type distributions shows a significant decrease in $LCFR_{\Delta}$, with lowest values observed in hypoxic tissues where O_2 consumption is adjusted significantly below maximum O_2 consumption ($\dot{\mathrm{V}}\mathrm{O}_{2,\mathrm{max}}$). It is interesting to note here that the SN geometry with a size–based fibre type distribution has a smaller value of $LCFR_{\Delta}$ than the rarefied SU geometry whose underlying capillary distribution is more symmetrical ($LCFR_{\Delta} = 4.97$ for SN vs. 7.41 for SU).

In all cases, introducing an extreme uptake heterogeneity, such as a high differential fibre O_2 uptake, leads to the highest discrepancy between VP–based and

TR-based LCFR, where values are largest for the SU case and smallest for the histological case.

3.9.2.3 The normalised standard deviations σ_Δ, $\sigma_\cap$, σ_{VP}, σ_{TR}

The normalised standard deviations increase with greater heterogeneity in fibre–type composition and size distribution. The highest values correspond to the greatest degree of functional heterogeneity, i.e. high differential scaling of different fibre type-specific O_2 uptake.

The *normalised standard deviation of difference* (σ_Δ) describes the difference between the spread of Voronoi polygon areas and that of trapping regions. This measure is found to follow the same trends as those of μ_Δ illustrating that the spread of VP areas begins to differ from that of TR for increased mixing of fibre types. In particular, random mixing of fibre types shows higher values of σ_Δ than size–based and real distributions.

The *normalised standard deviation of intersection* $\sigma_\cap$ extends the above correlations by considering the spread of VP areas that overlap with TR. This statistic tends monotonically toward the value of σ_{VP} as the O_2 demand and the capillary arrangement become increasingly homogeneous. Here σ_{VP} quantifies the asymmetry in the underlying capillary distribution, with increasing values corresponding to greater asymmetries. Also, the presence of size–based fibre–type distributions further shifts $\sigma_\cap$ in the direction of σ_{VP}, with hypoxic conditions showing the largest shift. This illustrates that the spread of the VP–TR overlap is reduced as the Voronoi polygons areas conform more to those of trapping regions when fibre type distributions are less random.

The dispersion in oxygenation supply areas, as measured by σ_{VP} and σ_{TR}, remains essentially zero for the SU geometry with uniform fibre–type composition ($\sigma_{\mathrm{VP}} = 0$, $\sigma_{\mathrm{TR}} = 0.0073$, where the value of σ_{TR} under perfect symmetry reflects the scale of the boundary artefacts). However, both spread statistics begin to widen as structural and functional heterogeneities are increased. In particular, despite the fact that there is no dispersion in VP areas in the SU geometry, the spread in TR areas is found to be increasingly positive across all mixed fibre composition. In the SN geometry, however, the spread in TR areas is generally smaller than that of VP areas, except for the case of an extreme functional heterogeneity (high differential

uptake). These observations indicate that TR are influenced by functional changes in the diffusive and metabolic properties, whereas VP are not, highlighting an advantage of trapping regions.

3.10 Discussion and conclusions

Techniques for the assessment of muscle capillary supply vary widely within the literature. Global methods are often used to analyse capillarisation where average values of structural composition or functional activity are taken to represent the whole tissue uniformly. However, such measures cannot capture the spatial heterogeneity in capillary supply generated by the local metabolic environment and variations in fibre size. In addition, the scale–dependency inherent in such indices may explain why data on capillarity is variable, if not conflicting [46]. On the other hand, the space–filling area–based method of capillary domains is used to avoid the spatial limitations of analyses based on global indices. In particular, space–filling methods have the advantage of capturing the local environment of capillaries by giving each a 2D domain representing its maximal supply area, and therefore take into account heterogeneities in O_2 supply and demand, while also allowing exploration of local influences of microvascular remodelling and regulation. In addition, the validity of using capillary domains (Voronoi polygons) to represent capillary supply areas was confirmed for general cases of muscle tissue with uniform O_2 uptake in the previous chapter. Whether this representation is sufficiently accurate to describe functionally heterogeneous tissues is not clear. Hence, our present study considered when capillary domains are appropriate to assess O_2 supply from capillary distributions embedded in functionally heterogeneous muscle tissues, e.g. skeletal muscle, by exploring their correlation with a biophysically based alternative, namely the trapping regions.

Voronoi polygons and trapping regions are observed to have the same qualitative shapes and overall quantitative distributions for all fibre distributions in a maximally perfused, non-rarefied, metabolically heterogeneous system regardless of the degree of structural asymmetry even for hypoxic tissues. This correlation is lowest in muscle with a highly heterogeneous fibre type composition, assuming the other conditions above are met. However, even in this case the normalised mean of the VP areas overlapping TR remains above 87%, provided that noticeable capillary rarefactions or significant heterogeneities in fibre–dependent O_2 uptake are absent. This remains true across all synthetic capillary and fibre distributions (type and size), and for those

extracted from an EDL muscle tissue cross–section. These observations are also robust to variations in the adjustable parameters of the transport model as detailed in the previous chapter. Therefore, in the absence of extremes that are only associated with pathologies, our modelling predicts that VP provide a computationally simple and accurate approximation of functional capillary supply for muscle tissue cross–sections of heterogeneous fibre types, which in turn theoretically validates the conclusions of modelling studies taking Voronoi polygons as a basis for morphometric analyses of maximal capillary supply in skeletal muscle tissues [1, 31–34, 48, 194].

A local increase in fibre area (local hypertrophy) lowers the accuracy of VP as it effectively leads to local capillary rarefaction, which is consistent with our previous predictions for homogeneous muscle tissue and also the numerical observations that fibre size influences PO_2 heterogeneity [125]. However, if such hypertrophies are localised to fibres with relatively low O_2 uptake (i.e. glycolytic fibres), a balance resulting between opposing PO_2 fluxes is observed as indicated for instance by the increase in $\mu_{\cap}$ and decrease in μ_{Δ} for size–based fibre type distribution. The overall accuracy of VP within the region of interest may then only change slightly, thus potentially retaining their validity in representing capillary supply areas. These observations suggest that the lower histological capillary supply to glycolytic fibres *in situ* is balanced by their reduced O_2 demand per unit volume. In turn, the high VP–TR correlation for rat EDL tissue perhaps suggests that the fibre type distribution may be tightly regulated to avoid large fibres with high oxidative capacities per fibre volume. Similarly, our findings also suggest that a local homogeneity in capillary supply is necessary when the specific O_2 demand of nearby fibres is relatively high, in agreement with the findings of [53].

The loss of capillaries via random capillary rarefactions, regardless of the local metabolic character, significantly decreases the correlation between VP and TR. In contrast, a global rarefaction via a reduction in mean capillary density only slightly perturbs the VP–TR correlation. A global reduction in capillary density increases diffusion distances and is effectively equivalent to an increase in the non-dimensionalised O_2 uptake of the biophysical model. Nonetheless, the effect of such increase in non-dimensional MO_2 on the VP–TR correlation is relatively small compared to that of random local rarefactions, and can be simply balanced by a parallel global decrease in O_2 consumption. This highlights the robustness of the estimates for the capillary supply regions for such parameter changes and entails that the correlation between

VP and TR is only weakly affected by global changes, in comparison to the influence of local rarefactions.

A common assumption is that the oxidative capacity or functional characteristics of different muscles depends on fibre type composition (i.e. proportion of Type I, IIa, and IIb). Also a random arrangement of fibre types can lead to significantly weaker correlations between VP and TR. This observation shows that, in addition to fibre type composition, oxidative capacity depends on the distribution of fibre types, in a close parallel with the relationship between functional capillary density and capillary distribution. Hence, the modelling observations are consistent with the hypothesis that to avoid peaks in O_2 demand, fibre type distribution may need to be tightly regulated to avoid large fibres with high oxidative capacities per fibre volume. This, in turn, reduces the heterogeneity and maximises the benefit from the smallest number of capillaries, thus minimising costs of maintenance.

Increasing the degree of differential O_2 uptake, the ratio of oxidative to glycolytic MO_2, has a significant impact on the accuracy of VP relative to TR for all tissue geometries. This effect is on the scale of a severe local rarefaction [3] and is expected to be far greater than the heterogeneities resulting from local fibre hypertrophies. This indicates that VP may be of limited use and inaccurate in assessing capillary supply areas for physiological situations associated with high degree of fibre differential uptake [60, 135, 184], such as altered patterns of fibre recruitment [76], and perhaps during muscle remodelling, such as an increase in mitochondrial volume densities [195]. However, aggregation of similar fibres as observed in histological cross–sections mitigates the impact of a high differential uptake on the accuracy of VP. In particular, grouping of the same fibre type in clusters provides a region of uniform uptake that is large enough to prevent PO_2 fluxes of interior capillaries from reaching remote fibres with high demands, thus acting as a local buffer to restrict capillary supply areas from remote supply. Capillaries near the periphery of a fibre cluster, however, are exposed to the oxidative–glycolytic interface and thus the direction of their O_2 fluxes will be forced into the oxidative side resulting in complex flux lines that cannot be accommodated within the pure geometrical construct of VP. Nonetheless, the overall effect has a low impact on the quality of VP in capturing capillary supply regions. The high correlations between VP and TR in rat EDL muscle therefore also suggest that the histological fibre distribution is also tightly regulated to prevent large surface area of interaction between metabolically dissimilar fibres.

Surprisingly, under conditions leading to tissue hypoxia VP appear to approximate O_2 supply regions to a better extent than under normal conditions. Indeed, under conditions of low oxygenation, myoglobin facilitated transport is additionally considered and the muscle tissue consumption is adjusted to very low values in accordance with Michaelis–Menten kinetics, thus decreasing PO_2 fluxes from remote capillaries and between fibres. Due to the PO_2 dependence of the Michaelis–Menten curve under such conditions, the local O_2 uptake of dissimilar fibres will become much more homogeneous, which in turn leads to substantial reduction in the extent of O_2 differential uptake. In addition, given that a VP distribution reflects the underlying distribution of capillaries, the observation that predictions of O_2 supply areas (TR) approach those of VP suggests that in chronically hypoxic tissues capillary distribution is more important than fibre demand for O_2.

The current data and modelling demonstrate that VP and TR tend to coincide with reasonable accuracy for a capillary bed dispersed in a mixed fibre population without high differential uptake, indicating that each region within such tissue is supplied by its nearest capillary. This in turn suggests a lack of redundant capillaries within such tissue, which is found in almost all human skeletal muscles. In other mammals, however, regional specialisations in function have led to clustering of more oxidative or more glycolytic populations of fibres. For example, in the rat *tibialis anterior* (TA) the outer cortex is almost all Type IIb fibres, whereas the inner core is a mix of Type I and Type IIa fibres, while the *soleus* is nearly all Type IIa fibres. Our data indicate that VP and TR are expected to coincide with higher degree of accuracy in the outer cortex of rat TA and soleus muscles than in the inner core of the TA muscle due to the latter's more abundant interfacial regions of dissimilar fibre types. This highlights that efficient capillary supply during the development of such muscles need not always be dominantly constrained to O_2 delivery, especially in the presence of relatively high differential uptake between fibre types as can occur during fibre remodelling [195].

In particular, since the VPs and TRs deviate in such muscle, not every capillary is simply supplying O_2 to the tissue closest to it. Hence, in this context there is supply inefficiency in that, in various locations, the structure of the tissue entails that distant capillaries compensate nearby capillaries, so that the latter are not fully utilised. This, in turn, suggests that the control of capillary distribution in mixed muscles can also be affected by other feedback regulators in addition to O_2 and also

muscle fibre type distribution and composition. In particular, developmentally the fibre types differentiate first and then the capillary bed expands along with innervation. In the case of remodelling of mature tissue the situation may be reversed. For example, improved resistance towards fatigue initiated by electrical stimulation preceded increased activity of oxidative enzymes and occurred concomitantly with increased capillary supply [19].

In summary, while the Voronoi polygon approximation to trapping regions depends on heterogeneity of fibre composition, it is nonetheless representative for maximal vascular capacity given the absence of capillary rarefaction and high differential uptake between fibres, while also exhibiting insensitivity to model parameters. Therefore, measures of muscle capillary supply capacity based on Voronoi polygons may be reasonably used for mixed muscle samples. However, increases in heterogeneity associated with differential uptake will eventually lower the accuracy of Voronoi polygons. Hence, more sophisticated measures of capillary supply capacity should be used to study structural or functional dysregulation in striated muscle tissues, when flux trapping regions may provide a more robust representation of capillary supply regions. In addition, the relationships between Voronoi polygons and trapping regions may be generally informative in studies exploring the regulatory mechanisms underlying the capillary and fibre distributions in skeletal muscles.

Chapter 4

Oxygen Supply to Mitochondrial Zones

4.1 Summary

Developing effective therapeutic interventions for pathological conditions associated with abnormal O_2 transport to muscle fibres critically depends on the objective characterisation of capillarity. Local indices of capillary supply have the potential to identify the onset of fine–scale tissue dysregulation and intracellular remodelling. Detailed tissue geometry, such as muscle fibre size, has been incorporated into such measures by considering the distribution of the Voronoi polygons generated from planar capillary locations as a representation of capillary supply regions. Previously, our detailed simulations in Chapters 2 and 3 have predicted that this is generally accurate for perfused muscle tissues with both homogeneous and heterogeneous fibre uptake of O_2. In this chapter, we extend this modelling framework to incorporate intracellular heterogeneities in O_2 demand, diffusivity, and geometry, for the assessment of *capillary supply capacity* under maximal sustainable O_2 consumption. This allows us to investigate theoretically the effect of such heterogeneities on the representation of VPs and on the distribution of PO_2 in muscle fibres under hypoxic tissue conditions.

We demonstrate for muscle fibres with heterogeneous fibre properties and mitochondrial clustering that VP theoretically provide a computationally simple but often accurate representation of trapping regions, which are predicted from biophysical transport models to represent the areas of tissue supplied by individual capillaries. However, this use of VP may become less accurate under extensive mitochondrial

aggregation beneath the sarcolemma. In such cases, subtle changes due to mitochondrial clustering may only be registered within a more robust representation of capillary supply regions, namely trapping regions. Thus we explore whether TR are better suited to investigate data from comparative studies of intracellular modifications. Additionally, both the observation that VP can only approximate O_2 delivery by capillaries, and that we generally find a close relationship to TR, suggest that the heterogeneity in capillary distribution is an important factor in regulating both the *inter*- and *intra*cellular heterogeneities of O_2 transport and uptake.

In addition, we show that intracellular heterogeneities may significantly affect PO_2 profile within myocytes when considered at the appropriate PO_2 scale (e.g. hypoxic threshold). Hence, we conclude that such heterogeneities may have a profound effect on cellular metabolism at the hypoxic threshold but the sensitivity we also observe entails that there are no detailed trends. Furthermore, previous models that neglect mitochondrial clustering when it is in fact extreme may be inaccurate, for example they may underestimate hypoxia in some fibre types, and more generally the concept that mitochondrial clustering should improve oxygenation does not hold universally. Additionally, we show that the decay in intracellular PO_2 is not always monotonic from the sarcolemma to the fibre centre, which is in contrast to the traditional view of tissue oxygenation based on the Krogh cylinder geometry.

4.2 Introduction

Understanding the link between global O_2 supply and local capillary distribution is crucial for assessing the efficacy of therapeutic interventions in pathological scenarios such as muscle ischaemia. Numerous morphometric methods have been used to quantitatively analyse the anatomical supply of capillaries to muscle fibres in an effort to assess the functional consequences of experimental interventions [1, 34, 47, 51, 97, 106, 175, 193–195]. Analyses of tissue structure that are based on morphometric methods can only reveal the maximal transport capacity of a system.

The majority of biophysical O_2 transport models base their geometrical framework, and ultimately O_2 supply indices, on estimates from global morphometric methods, where average values of structural composition and functional activity are taken to represent the tissue uniformly, e.g. mean intercapillary distance (ICD), capillary density (CD), capillary–to–fibre ratio (C:F), number of capillaries around a fibre

(NCAF), and O_2 uptake (MO_2). In particular, the majority of indices based on a single Krogh cylinder [120] use global values of either ICD or CD to estimate the radius of the cylinder. In addition, most biophysical models of concentric cylindrical geometries (a tissue cylinder surrounded by multiple capillaries) use global C:F or NCAF to estimate the number of capillaries that are distributed symmetrically around the central cylindrical fibre. However, capillary supply is likely spatially heterogeneous due to heterogeneities in the local capillary distribution [32], the local metabolic environment (e.g. local distribution of fibre type) [193], the local distribution of fibre size [1], and the local distribution of mitochondria [128, 142, 193]. Furthermore, not only are average indices inherently scale–dependent [46], but also Krogh cylinders inadequately partition the tissue space, leading to non-physiological tissue voids as well as overlapping Krogh cylinders.

To avoid the spatial limitations of global indices, further refinements sought to take into account areal (local) morphometric methods [97], such as those based on Voronoi polygons (capillary domains). Noting that *trapping regions* denote the prediction of capillary supply regions from biophysical models of O_2 transport and kinetics, we demonstrated in previous chapters that Voronoi polygons generally give an accurate approximation of trapping regions within striated muscle tissues at maximal aerobic capacity. Nonetheless, we also observed that the approximation accuracy may deteriorate with rising levels of capillary rarefaction, and may ultimately break down under significant perturbations to the uniformity of capillary PO_2 and fibre O_2 uptake (MO_2). However, such complications under maximal functional supply require either tissue pathology or intracellular remodelling. Hence we predicted that correlations between Voronoi polygons and supply regions may reflect local control of angiogenic foci on the lengthscale of an aerobic muscle fibre diameter, thus preventing random capillary rarefaction as observed by [9]. Additionally, we showed that the generally close relationship between Voronoi polygons and trapping regions may serve as a hypothesis generator by highlighting constraints on potential mechanisms for the regulation of fibre type and size distributions as well as emphasising the relative importance of heterogeneous metabolism and capillary distribution in determining capillary supply to mixed muscles.

4.2.1 The profile of intracellular oxygen tension and uptake

Contrary to the usual modelling assumption of intracellular spatial homogeneity of O_2 uptake, individual muscle fibres exhibit heterogeneous ultrastructural character-

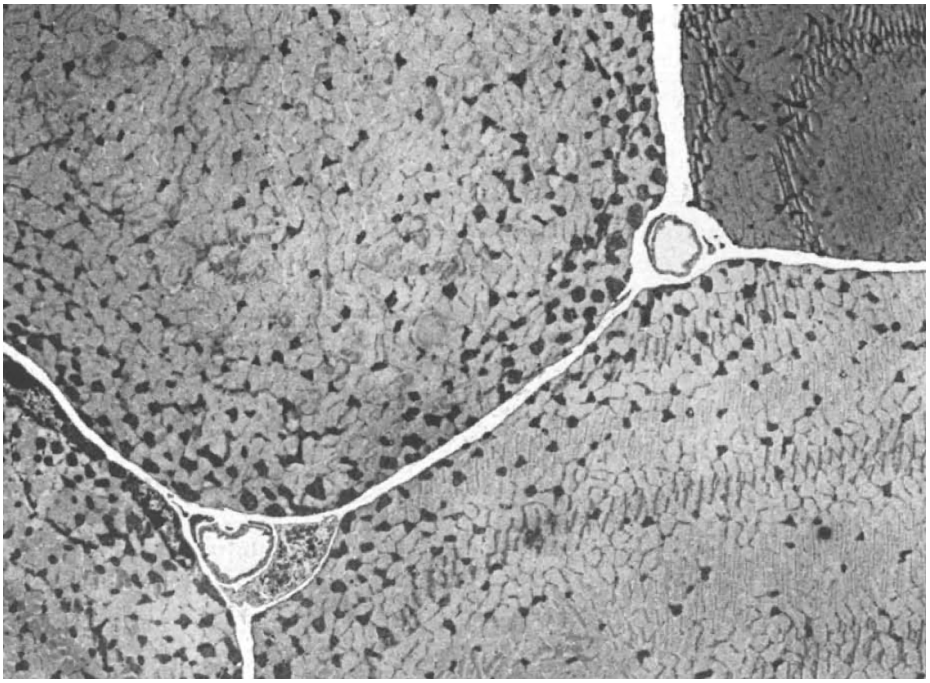

Figure 4.1: A typical spatial distribution of mitochondria within skeletal muscle fibres. Note the numerous mitochondria (*dark structures*) near the fibre membrane (i.e. sarcolemma). From [103], with permission.

istics. In particular, the transport properties associated with muscle fine structure and composition (e.g. fibre content and distribution of mitochondria, myoglobin, and lipids), are not uniform and may depend on fibre type [104, 115, 176, 193].

4.2.1.1 Mitochondria

In particular, mitochondria are the cellular power plants where most of the cell's supply of high energy molecules, e.g. adenosine triphosphate (ATP) [20], is aerobically generated at their inner membranes via the Krebs Cycle [6, 185]. Aerobic energy production within mitochondria is only possible if a continuous and sufficient supply of O_2 is present locally [185]. In particular, O_2 is almost exclusively consumed within mitochondria [100], thus making them the ultimate sites for O_2 consumption within muscle fibres (myocytes). In contrast, when O_2 supply is insufficient, the energy production is carried out in the absence of O_2 in the cytosol via a process called fermentation [6, 185]. This process of anaerobic generation of energy yields 13 times less ATP per metabolised glucose molecule than aerobic respiration, hence making fermentation less O_2–efficient [185].

Mitochondria have their own independent genome and are able to independently proliferate through repeated mitochondrial divisions, a process similar to bacterial binary fission [6]. While many think of mitochondria as ovoid structures with diameter around 1 μm, these organelles can actually undergo fusion, which if combined with repeated binary divisions can give rise to tubular mitochondrial networks [79].

In muscle fibres, mitochondria can be recruited to subcellular sites such as residing between myofibrils and/or clustering beneath the sarcolemma, particularly near capillaries [103, 104]. Given O_2 is exclusively consumed in these organelles, such distinctive arrangements of mitochondria imply that O_2 consumption must be spatially heterogeneous within muscle fibres. Since supply and demand heterogeneities at higher scales (see Chapters 2 and 3) affect tissue oxygenation, it is reasonable to consider that intracellular heterogeneities may constitute an additional local resistance to O_2 delivery to mitochondria, thus warranting a detailed mathematical framework to explore such heterogeneities. In fact, using endogenous enzymatic probes to localise relative metabolite concentrations, Jones [109] has experimentally demonstrated that heterogeneities in intracellular O_2 levels do exist under conditions of limited PO_2 and ATP. In addition, recent advances in myoglobin microspectrophotometry have led to the experimental finding of heterogeneous PO_2 levels in isolated cardiomyocytes [176].

4.2.1.2 Microgeometry

The intracellular distribution of mitochondria in muscle fibre cross–sections is typically non-uniform (Fig. 4.1). Electron transmission microscopy of individual muscle fibres typically shows two visually distinct mitochondrial zones within fibres [104, 115, 159]. The zone immediately underneath the sarcolemma, that is the cellular membrane of a muscle fibre, is referred to as the subsarcolemmal zone, or in abbreviation, ss; within this region it is common to observe aggregations of mitochondria as part of a decreasing gradient of mitochondrial density that is highest near the sarcolemma and capillaries and lowest at the fibre core [52, 159]. Toward the central region of the fibre a characteristically sparse mitochondrial distribution forms in what is referred to as an intermyofibrillar zone, imf [115, 159]. This central zone contains many chains of rod–like units of a muscle, called myofibrils, which are responsible for muscle contraction.

4.2.1.3 Functional role

The functional role of mitochondrial clusters is not yet understood. In particular, it is still unclear what role mitochondrial function (e.g. O_2 consumption and energy production) plays in such a spatial organisation. In addition, the regulatory factors causing mitochondria to exhibit such spatial patterns is still under debate. Nonetheless, there are currently two hypotheses seeking to explain the functional significance and the mechanisms leading to intracellular mitochondrial re-distribution to the subsarcolemal zone.

The "balance of demands" hypothesis

The physiological significance of fine scale mitochondrial distributions has always been hypothesised to reflect a functional balance between the mitochondrial demand for O_2 and the myofibrillar demand for ATP [104, 113, 114, 188]. In brief, if O_2 diffusion from capillaries is a limiting factor for mitochondrial metabolism, one would expect all mitochondria to aggregate in the subsarcolemmal zone, particularly beneath capillaries. This observation has always been crudely explained in terms of a reduction of diffusion distances between capillaries and mitochondria [77, 104, 113, 114, 188]. In contrast, if the diffusion of ATP from mitochondria to myofibrils was limiting for myofibrillar contractions, then one would expect all mitochondrial to uniformly aggregate in the intermyofibrillar zone. However, as noted by Hoppeller and Billeter [100], the actual observation is that not all mitochondria are clustered near the sarcolemma and capillaries, rather some mitochondria are clustered and some are scattered between myofibrils. This has led to the suggestion that the diffusion of both substrates is critical and a balance of demands may explain such an intermediate clustering [104].

In addition, there is experimental evidence indicating that mitochondrial distribution and clustering are important factors in determining the magnitude and location of intracellular O_2 gradients, with the cluster size being constrained by the magnitude of the PO_2 gradient needed for sustaining mitochondrial generation of ATP [109]. Such mitochondrial clusters are hypothesised to maintain steep gradients of high energy phosphate molecules by reducing their diffusion distances to the peripheral supply of O_2 [16, 109]. However, this latter hypothesis did not explain the potential mechanism by which O_2 gradients may influence the spatial distribution of mitochondria.

The "diffusional constraints" hypothesis

In a series of papers, a group of researchers [16, 80, 126, 138, 142–144] attempted to refine the aforementioned hypothesis in an effort to explain why and how mitochondria aggregate beneath the sarcolemma. It was suggested that large O_2 gradients (a theoretical marker for O_2 diffusion limitation) dictate the spatial dynamics of mitochondrial shifts towards the sarcolemma, particularly in large fibres of crustaceans and fishes [16, 80, 81, 108, 138].

With the aid of recent experimental advances unravelling the signalling pathways controlling the mitochondrial life–cycle, Pathi and co-workers [143] further suggested that mitochondrial sensitivity to local O_2 levels may cause greater mitochondrial degradation (death) within regions of low O_2 (e.g. fibre core) and proliferation (biogenesis) where O_2 levels are adequate (e.g. subsarcolemmal zone). Since intracellular O_2 and ATP transports are driven by diffusion, their diffusion constraints (e.g. O_2 and ATP supply, demand, and diffusion distance) will dictate the local O_2 concentrations within fibres. Therefore, it was suggested that the dynamics of mitochondrial spatial re-distribution might be dictated by the cellular need to prevent diffusional constraints. In a follow-up study [142], Pathi and co-workers further proposed a *selective removal* of mitochondria in response to low O_2 levels as the primary factor dictating the observed spatial heterogeneity of mitochondrial distribution in skeletal muscle fibres. This was suggested to result from spatially homogeneous signals for mitochondrial birth and spatially heterogeneous death that is dictated by the local PO_2 profile. The functional role of such birth–death dynamics was predicted to decrease the diffusional constraints of O_2 and ATP transport, hence emphasising the functional advantage of mitochondrial shifts.

4.2.1.4 Current theoretical models

A number of investigators have attempted to elucidate the above hypotheses using mathematical models. For example, reaction–diffusion models of multiple substrates (e.g. O_2, ADP, ATP, creatine phosphate) have been considered [128, 142–144]. In particular, Mainwood and Rakušan [128] considered O_2 transport from capillaries to clustered distributions of mitochondria exclusively near capillaries (mitochondria–free cell core) along with an additional mechanism for transporting high–energy molecules from mitochondria to the rest of the cell. They showed that the PO_2 drop from capillary to fibre centre is significantly smaller when clustering is considered with nearly

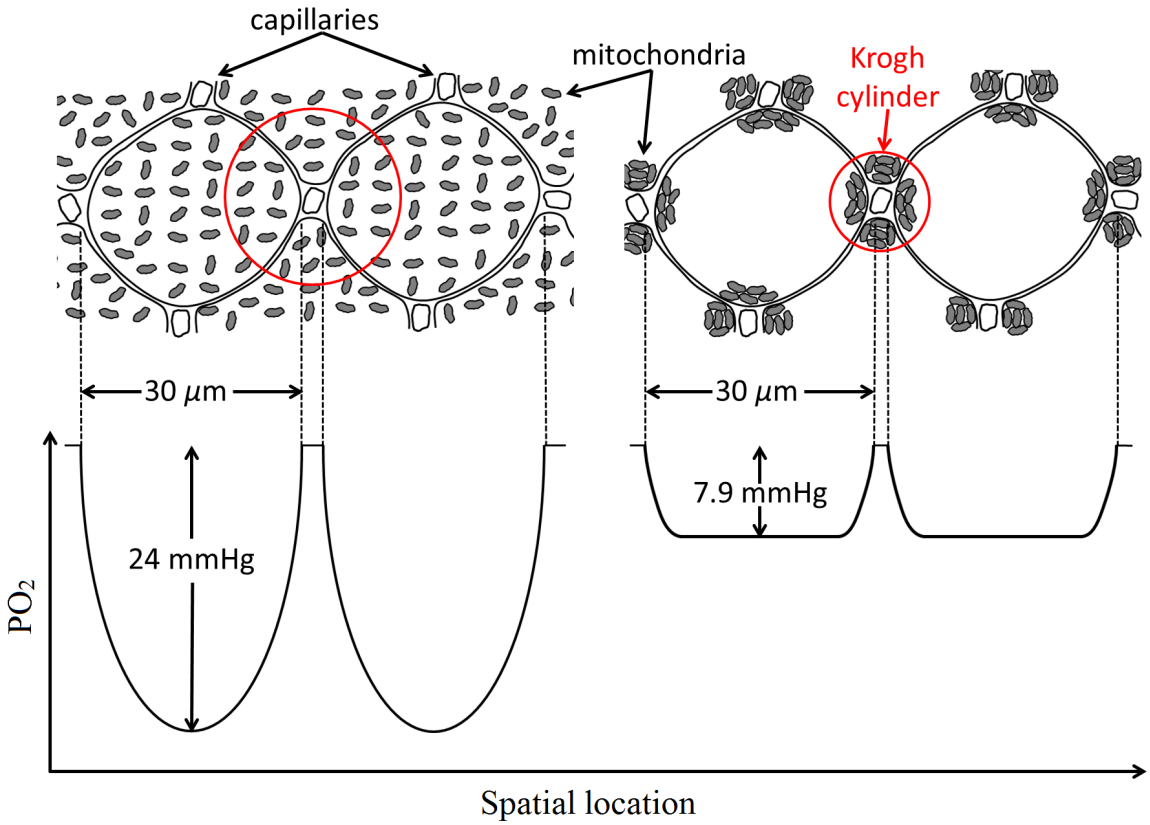

Figure 4.2: Effect of extreme mitochondrial aggregation near capillaries on intracellular PO_2 profile. (A) A typical Krogh model with homogeneous mitochondrial distribution. (B) Extreme mitochondrial clustering with all mitochondria aggregating around capillaries giving rise to mitochondria–free cell core. Note the consideration of a reduced Krogh cylinder in this case. Calculations are based on Eq. (1.1). Reproduced and modified from [128], with permission.

constant PO_2 profile across the fibre width (Fig. 4.2). This result, however, is heavily influenced by imposing a no–flux boundary condition at a distance much shorter than the original Krogh cylinder radius, which implies no O_2 exchange with the fibre core. Hence, it is not clear to what extent this clustering may affect intracellular PO_2 in more physiological scenarios. In addition, this study explored an extreme case of mitochondrial aggregation where all are directly beneath capillaries. However, mitochondria typically exhibit a combination of spatial aggregation near the sarcolemma and sparse distribution towards the fibre centre [100].

Considering a single–substrate transport (O_2), Groebe [77] used a mathematical model of steady–state transport of O_2 to a concentric tissue cylinder to show that clustering gives rise to shallower PO_2 gradients. Nonetheless, he concluded that this

effect is insignificant in terms of raising mean fibre PO_2, and ultimately recommended disregarding mitochondrial clustering in tissue O_2 transport models. This conclusion was based on predictions of a 2:1 subsarcolemmal–to–intermyofibrillar uptake ratio which corresponded to an equivalent amount of subsarcolemmal mitochondria that does not exceed 10% of the overall mitochondrial content of the fibre considered (see Fig. 4.7).

Pathi and colleagues [142–144] mathematically modelled the reaction and diffusion of key metabolic substrates (including O_2, ATP, and ADP). This model was coupled to a cellular–automata approach that describes the dynamic response of the mitochondrial life–cycle to spatial variations in the metabolic state of myocytes. These studies have demonstrated theoretical support of the hypothesis that mitochondrial clustering prevents diffusion constraints, thus emphasising the functional advantage of clustering in improving O_2 supply and reducing large intracellular gradients. In a single fibre, PO_2 profiles were found to be flatter in the fibre core when mitochondria clump beneath capillaries. Nevertheless, such explorations have only shown modest variations in intracellular O_2 levels, which is partly due to using a spatially–averaged PO_2 as an indicator of the oxygenation state of the fibre. Moreover, capillary O_2 supply was restricted to a single fibre with no-flux boundary conditions implying no interaction with adjacent fibres. Hence, these conclusions are based on the assumption that such mitochondrial clustering only affects the intracellular PO_2 of the fibre in question. However, it is well known that, in striated muscles, fibres are embedded in a tissue where other fibres of different shape, size, and metabolism neighbour each other. While mitochondrial aggregation in one fibre may flatten the PO_2 profile within it, it may have the opposite effect (steepen the PO_2 profile) on the neighbouring fibres if their anatomical details or metabolic properties are different or no proportional clustering exists within them.

It has also been observed that mitochondrial clustering is typical in aerobic, oxidative, fibres. Since such fibres have higher aerobic capacity than anaerobic, glycolytic, ones, it was suggested that clustering is a way to improve PO_2 levels in the high energy demanding aerobic fibres which are believed to have steeper PO_2 profiles (e.g. see [167]). The observation that aerobic fibres are typically smaller than glycolytic ones implies that diffusion distances are already small compared to the larger glycolytic fibres. Hence, it would make more theoretical sense to expect clustering to occur in glycolytic fibres if we were to assume that clustering reduces diffusion

distances. In fact, Kayar and co-workers [115] have reported that, in horse skeletal muscles, mitochondrial density was highest beneath the sarcolemma and sharply declines towards the fibre centre irrespective of fibre type. Also reports from histochemical studies in rodent hindlimb [193] have indicated that the ratio of O_2 consumption rate near the subsarcolemma to that in the fibre core is more or less the same for all fibre types. In addition, Boyle et al. [16] and Hardy et al. [80] have observed that mitochondrial clustering exclusively occurs in the glycolytic levator muscle of mature Blue Crab (*C. sapidus*). These muscles are used for power swimming and exhibit progressively larger fibres during the hypertrophic growth of blue crab (fibre diameter < 60 μm in juveniles and > 600 μm post–maturation). Such observations highlight that mitochondrial clustering (1) is not exclusive to aerobic fibres, and (2) can be an adaptive response to increased diffusion distances, increased intracellular O_2 demand, or decreased capillary O_2 supply [80, 167]. We remark here that the interplay between fibre size (hence, diffusion distance) and demand is better understood in terms of capillary supply regions, as demonstrated in Chapter 3.

As mentioned earlier, the current biophysical models of mitochondrial clustering show either a negligible elevation in overall fibre PO_2 [77, 95, 133, 142, 143] or a significant reduction in O_2 intracellular gradients [128]. Nevertheless, the functional role of such clustering in ameliorating O_2 transport limitations requires a re-assessment that takes into account (1) an accurate geometrical description of the transport medium, (2) accurate dimensions of mitochondrial zones, (3) a systematic derivation of relative intracellular O_2 uptake rates, and (4) appropriate boundary conditions.

4.2.1.5 Measuring mitochondrial distribution and the consequences for intracellular oxygen uptake

The planar distribution of mitochondria in myocytes is discrete due to the nature of individual mitochondria. This has led to the suggestion that O_2 consumption should be modelled as discrete O_2 sinks in the plane. However, Clark and Clark [24] and Clark et al. [25] have shown analytically that there is essentially continuity in PO_2 across mitochondrial membranes with practically no spikes in O_2 consumption (or, equivalently, sharp PO_2 drops) across these membranes (PO_2 drop $\sim 10^{-2}$ mmHg). This, in turn, suggested that, for uniformly distributed mitochondria, O_2 consumption in tissue is uniformly distributed within fibres (i.e. a continuum).

In modelling the discrete planar distribution of mitochondria in muscle fibres as

a continuum, it has always been assumed that the intracellular consumption of O_2 is spatially uniform within fibres. However, such models are highly accurate only when (1) the length scale of fibre diameter is much greater than that of inter–mitochondrial distances, and (2) the separation of mitochondria is uniform. In particular, recent advances in histological studies have revealed that such assumptions are supported by observations of the spatial distribution of oxidative enzyme activities within muscle fibres [136, 193].

Furthermore, under a given energy demand, the rate of local O_2 consumption within muscle fibres is assumed to be distributed in the same way as mitochondrial volume density, as demonstrated experimentally [99, 102, 184]. Mitochondrial volume densities can be determined experimentally by using stereological methods [44]. The distribution of O_2 consumption rates can also be determined from quantitative measurements of the kinetic activity of mitochondrial marker enzymes [14, 129, 184], such as succinate dehydrogenase (SDH) and citrate synthase (CS), which catalyse rate–limiting reactions within Krebs cycle [161]. Furthermore, the spatial distribution of enzymatic activities within muscle fibres can be determined from image analysis of the optical intensity of the enzymatic staining [21] (e.g. Fig. 4.3)

4.2.2 Aims and objectives

The influence of some of the aforementioned *micro*-heterogeneities has been explored both analytically and numerically in a single tissue cylinder with a concentric central capillary [77, 128, 133] or multiple capillaries around a concentric tissue cylinder [95, 142, 143]. However, there is still no theoretical consensus as to whether or not intracellular heterogeneities would significantly influence tissue and intracellular PO_2 levels.

Using a 2D Krogh cylinder model, Mainwood and Rakušan [128] showed that mitochondrial clustering around capillaries leads to a significant elevation in fibre PO_2, suggesting a significant sensitivity of diffusional O_2 transport to intracellular spatial heterogeneities in O_2 consumption. However, this conclusion was based on the assumption that mitochondrial clustering characterises a smaller Krogh cylinder radius which, in turn, infers limiting O_2 diffusion to an area near the capillary. The end result was an exaggerated level of tissue oxygenation.

In contrast, Groebe [77] and McGuire and Secomb [133] used a 3D model of

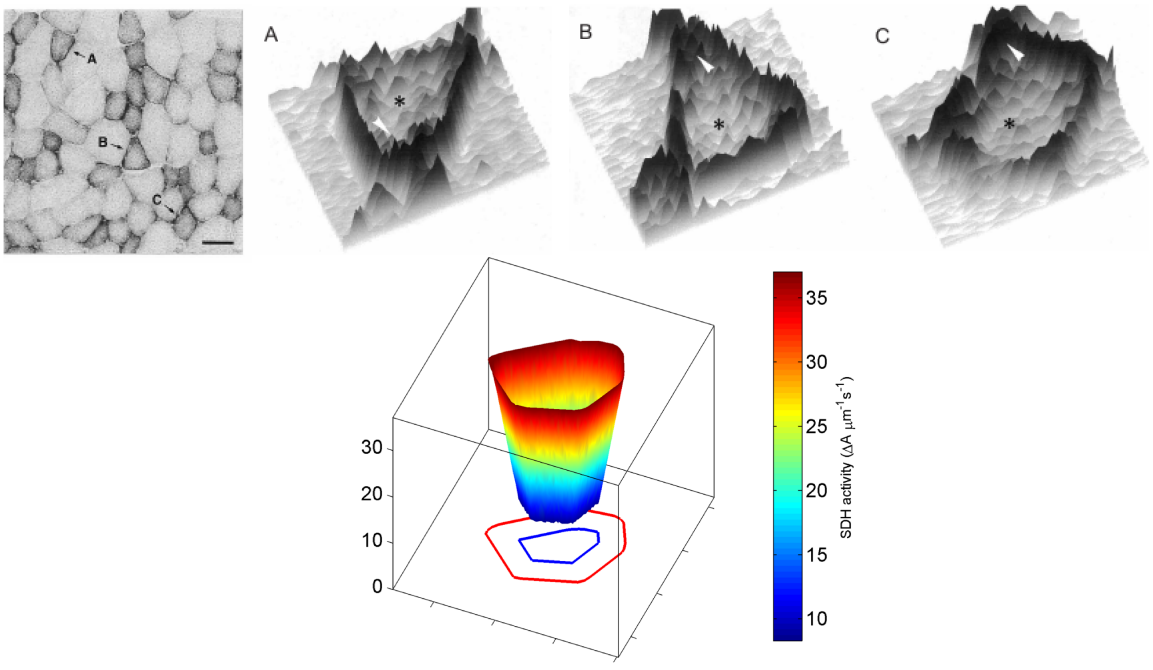

Figure 4.3: Stereographic patterns of SDH activity in the superficial region of the rat *plantaris* muscle (*top row*). Note the decreasing gradient of SDH activity from near the sarcolemma to the fibre centre. The scale bar is 50 μm. A continuum 3D representation of intracellular O_2 consumption profile as indicated by the relative SDH activity within the deep region of rat *plantaris* muscle (*bottom row*). Top images from [136], with permission. Data for bottom image from [193], with permission.

Krogh cylinder to examine the effects of heterogeneous mitochondrial distribution within muscle fibres and concluded that significant heterogeneity in intracellular O_2 uptake would only have a negligible effect on mean fibre PO_2. Additionally, using multiple capillaries around a central tissue cylinder, Hoofd and Egginton [95] investigated the role of O_2 diffusion limitations to fish myofibres in shaping their intracellular composition (e.g. lipid stores and mitochondrial distribution) via assessing the relative extent of intracellular fluxes of O_2. Similarly, they concluded that the intracellular, structural heterogeneities resulting from physiological adaptations following exercise or cold acclimatisation, particularly mitochondrial clustering, can only lead to a relatively modest elevation in intracellular PO_2 when compared to increasing the local capillary number.

It is noteworthy to mention that some of the models predicting a negligible effect in the presence of heterogeneous intracellular O_2 demand used a modest intracellular differential uptake (i.e. uptake near capillaries vs. uptake in the fibre core). This

reflects a common use of relative mitochondrial content per unit fibre area rather than per unit area of the local region within a fibre. Therefore, it is still unclear to what extent the intracellular spatial variation in O_2 demand actually affects the PO_2 profile within fibres when a representative measure of relative mitochondrial densities is used.

As mentioned above, Krogh cylinders are still widely used to predict PO_2 profiles in intracellularly heterogeneous fibres despite their inaccurate representation of capillary supply regions in heterogeneous muscles. In contrast, we have shown, in Chapters 2 and 3, that Voronoi polygons can accurately capture capillary supply regions in general. Nonetheless, it is still unknown whether a strong correlation between Voronoi polygons and capillary supply areas should hold in the presence of intracellular heterogeneities. Hence, it is unclear whether measures based on Voronoi polygons (e.g. local capillary–to–fibre ratio) are appropriate in other physiological settings such as tissue hypoxia given heterogeneous intracellular composition of muscle fibres. Therefore, our primary objective is to extend the model developed in Chapter 3 for O_2 transport under maximal sustainable conditions in tissue, characterising when and where indices based on Voronoi polygons are likely to accurately assess O_2 supply from capillaries embedded in functionally heterogeneous tissue (e.g. striated muscles) in the presence of mitochondrial and diffusion heterogeneities. Given Voronoi polygons are generated with relative computational ease and require no parameter estimation, we additionally seek to assess their accuracy in terms of the less accessible trapping regions approach. We also investigate correlations between Voronoi polygons and trapping regions to explore how such intracellular heterogeneities might affect the local capillary distribution.

4.3 Domain geometry

The domain geometries we consider here are similar to those in Chapter 3. Recall that these were characterised by different fibre size and shape: *synthetic uniform*, *synthetic non-uniform*, and *histological*.

4.3.1 Synthetic uniform

The first geometry considered is synthetic uniform size distribution, SU, based on a total of ∼200 synthetic muscle fibres of hexagonal shape and uniform size with capillaries placed at fibre vertices (Fig. 4.4A). Recall that these fibres were generated

from a Voronoi tessellation of the plane based on hexagonal array of nodes with prescribed side length and the number of capillaries is determined by the lengthscale, L, and capillary density, ρ, which are extracted from histological data. For the final domain illustrated in Fig. 4.4A, 151 fibres are enclosed within a disc constituting the simulation domain, which is obtained by rescaling to the unit disc. In contrast to Chapter 3, here the SU geometry includes a contiguous interstitial space of size $1-2$ μm. This is generated by shrinking fibres by a thickness of $0.5-1.0$ μm.

4.3.2 Synthetic non-uniform

The second geometry, synthetic non-uniform size distribution (SN), is based on a total of $\sim$200 polygonal muscle fibres of non-uniform size with capillaries placed at fibre vertices (Fig. 4.4B). Recall that these were generated from a Voronoi tessellation of nodes that have been placed on a random perturbation of the aforementioned hexagonal array. The final domain geometry encloses 183 fibres of different sizes and shapes with the addition of an interstitial space of size $1-2$ μm, which we generate by shrinking fibres by a thickness of $0.5-1.0$ μm.

4.3.3 Histological

The third geometry is based on histological fibre size and type distribution (H), with fibres extracted from digitised images of rat EDL (*m. extensor digitorum longus*) muscle cross sections (Fig. 4.4C, D). We denote these geometries by H1 and H2. The final domain geometry is a disc enclosing interstitial spaces and 102 fibres for H1, and 105 fibres for H2.

4.4 Fibre geometry

For all domain geometries each muscle fibre is partitioned into two concentric layers (defined below) with the outermost layer having a fixed thickness of 1-3 μm, regardless of the fibre size and shape (see Fig. 4.5). Here, the constraint on the thickness of the outer layer is based on experimental observations [115]. Consequently, layers of different fibres may have different areas unless the fibre distribution is synthetic uniform.

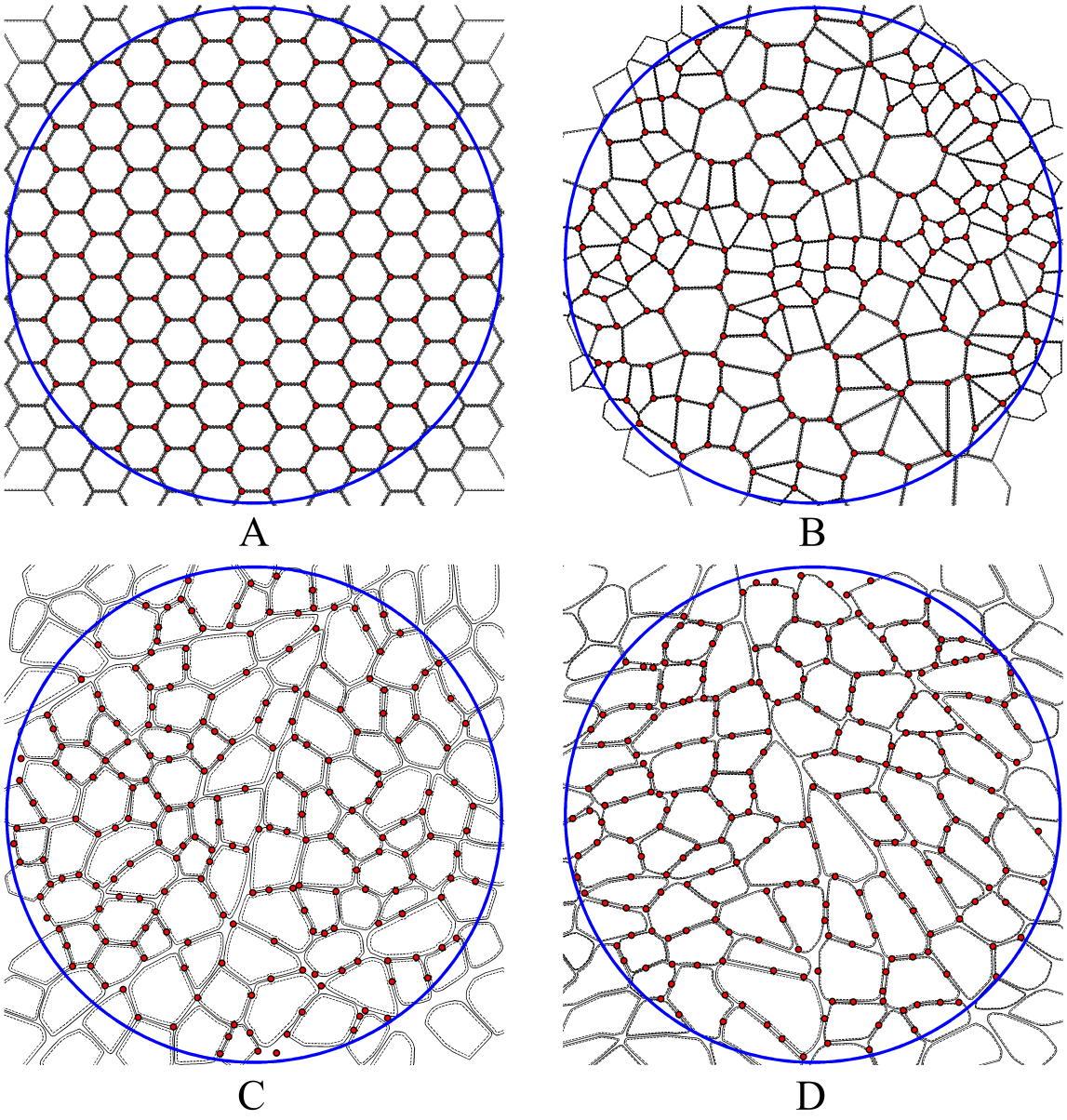

Figure 4.4: A view of modelling geometries. (A) Synthetic fibres of hexagonal shape and uniform size (SU) with capillaries placed on their vertices (symmetric capillary distribution). (B) Synthetic fibres of polygonal shape and non-uniform size with capillaries placed on fibre vertices (SN). (C-D) Rat EDL muscle geometries (H1 and H2). Traces of fibre cross–sections (*solid lines*) and capillary centroid locations (*red discs*) were made from slides using a microscope drawing arm and their x, y coordinates were registered on a digitising tablet. *Dashed lines* = the envelope of the peripheral myofibril edges within a fibre that delimits the intermyofibrillar zone (refer to Section 4.4 for more details).

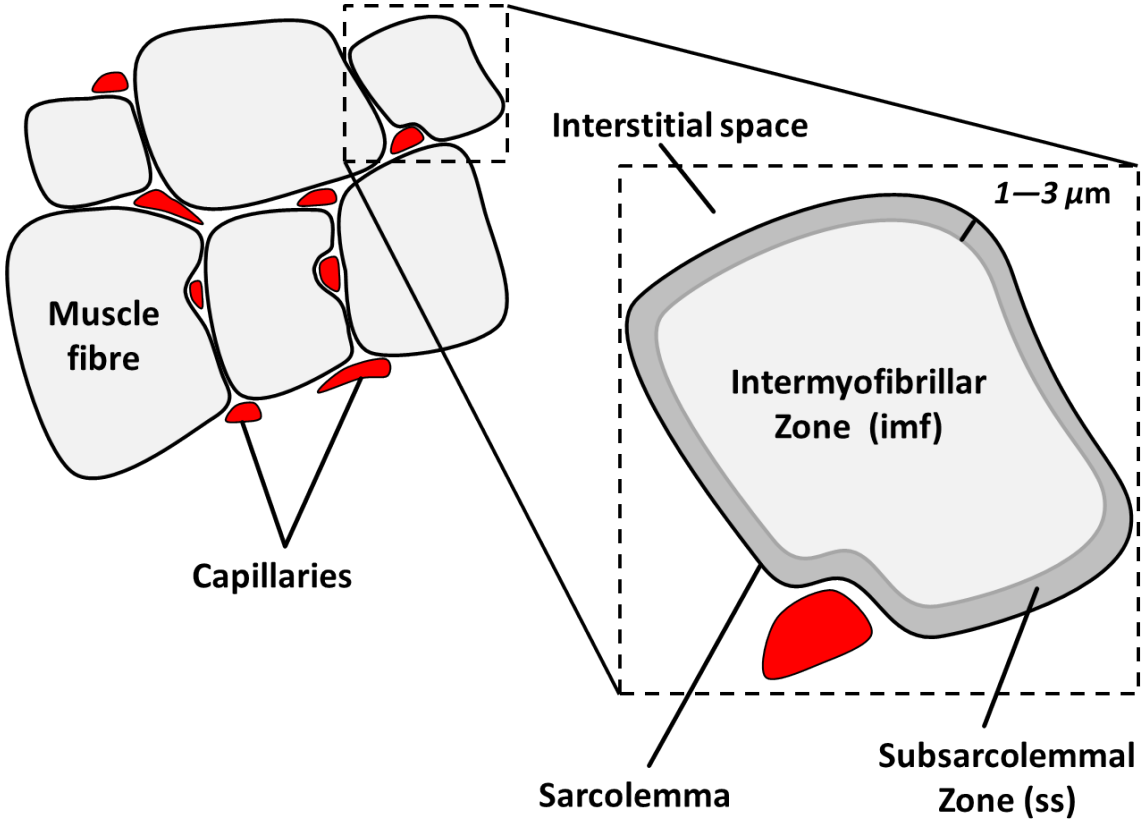

Figure 4.5: A cross–sectional view of muscle fibres. On the right is an expanded region of the left–hand image showing mitochondrial zones (intermyofibrillar zone in *light grey* colour; subsarcolemmal zone in *dark grey* shading).

4.4.1 Subsarcolemmal zone

The outer layer of a fibre is called the *subsarcolemmal zone*. We refine our definition of the subsarcolemmal zone to be the region beneath the sarcolemma that is external to the envelope of the peripheral myofibril edges. The *subsarcolemmal mitochondria* (ms) are the mitochondrial subpopulation enclosed within this zone. The distribution of these mitochondria is assumed to be uniform within this layer.

4.4.2 Intermyofibrillar zone

The inner layer of a fibre is called the *intermyofibrillar zone*. The intermyofibrillar zone is taken to be everything within the envelope of the peripheral myofibril edges. The *intermyofibrillar mitochondria* (mi) are the mitochondrial subpopulation enclosed within this zone. Similar to the other zone, the distribution of these mitochondria is assumed to be uniform within this layer.

4.4.3 Fibre–type distribution

Similar to Chapter 3, the fibre type distributions are divided into three categories: *random*, *size–based*, and *real*.

4.4.3.1 Random

In the case of a *random* distribution of fibre types, Types I, IIa, and IIb are randomly assigned to fibres regardless of the underlying size distribution (e.g. Fig. 4.6A). Such random assignment is constrained by a predefined areal composition of fibre types (I:IIa:IIb). Moreover, we only use the random fibre type distribution for the SU geometry with an areal composition similar to that of a rat EDL muscle cross section (9:37:54).

4.4.3.2 Size–based

In the case of a *size–based* distribution of fibre types, fibres of the SN geometry are assigned types based on a fibre–type areal composition of a rat EDL muscle cross–section (9:37:54), with fibre–size distribution following the typically observed order I $\leq$ IIa $\leq$ IIb.

4.4.3.3 Real

In the case of a *real* distribution of fibre types, fibres of the H1 and H2 geometries are assigned their histologically observed fibre–type distributions and compositions (9:37:54 and 10:42:48, respectively).

4.5 Mathematical formulation of the model

Here we extend our previous model of O_2 transport under maximal sustainable conditions (see Chapter 3) to explore the validity of Voronoi polygons for use in morphometric analyses of striated muscle tissues with micro-heterogeneous metabolic activities and anatomical properties. In addition, we seek to systematically quantify how such microscale heterogeneities may influence the intracellular O_2 profile.

We consider muscle tissues with either uniform or non-uniform functional characteristics, which allows a general exploration of striated muscles (skeletal and cardiac). A typical muscle is exemplified by the tissue cross–section presented in Fig. 3.1, where the lengthscale of a capillary cross–section is $2 - 4$ μm. In addition, we

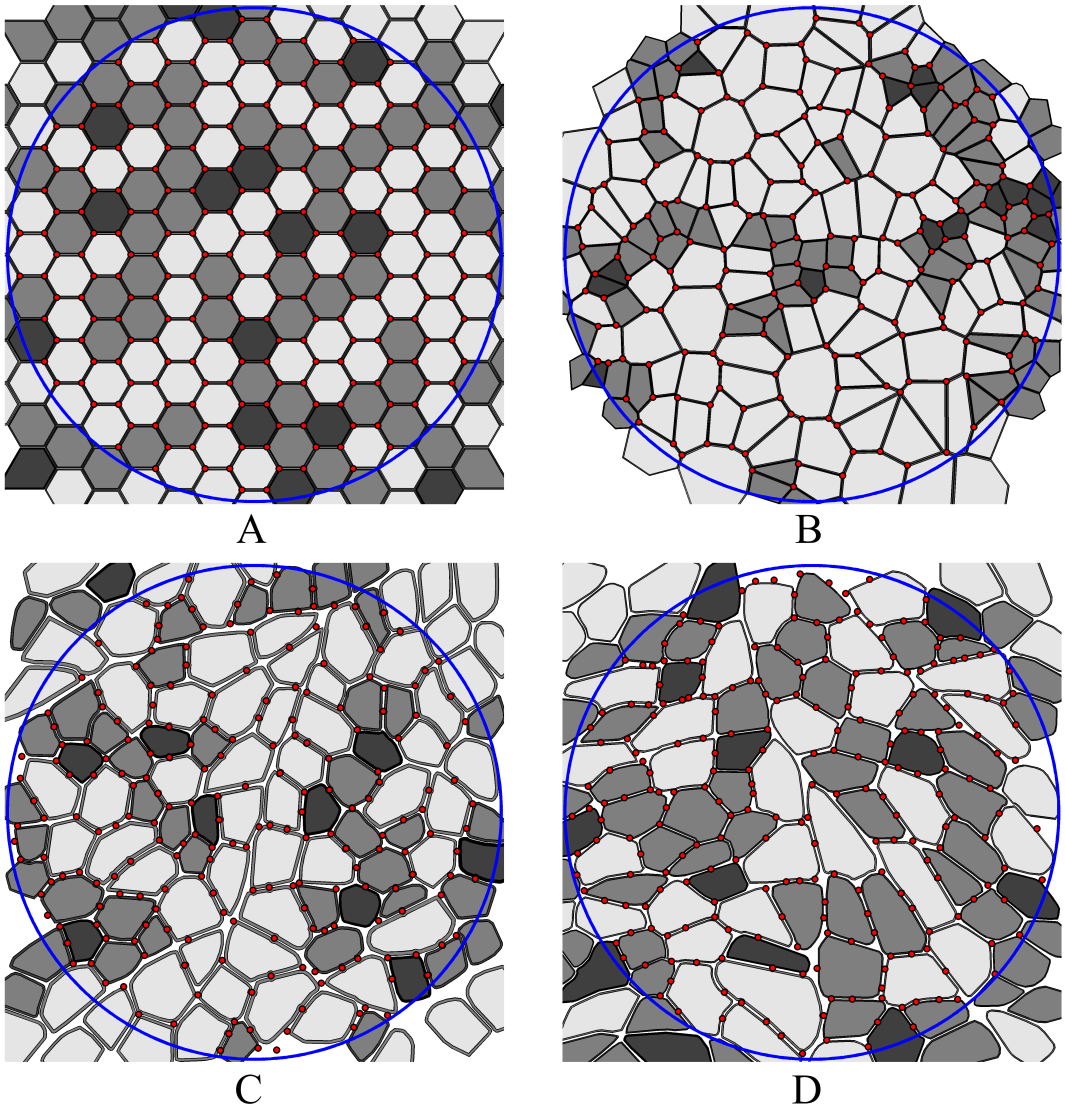

Figure 4.6: The fibre–type distributions used in our model. (A) A real distribution of a 9:37:54 (I:IIa:IIb) fibre–type composition. (B) A size–based distribution of 9:37:54 fibre–type composition. (C-D) Fibre size and type distributions and fibre type composition (9:37:54 and 10:42:48, respectively) are obtained from histological sections of a rat EDL muscle with capillary locations identified via alkaline phosphotase staining and fibre types via succinate dehydrogenase and myosin ATPase staining.

also incorporate facilitated diffusion and Michaelis–Menten kinetics of O_2 consumption, and a spatially heterogeneous O_2 demand into the transport equation to account for myoglobin–facilitated diffusion and to explore the consequences of tissue hypoxia under conditions of mitochondrial clustering.

4.5.1 Equations

We extend the O_2 transport model of Chapter 3 to explore the diffusive analogue of Voronoi polygons and the PO_2 distribution under conditions of heterogeneous intracellular uptake of O_2. The extended model still retains the same transport mechanisms as that of Chapter 3. In particular, we use a single partial differential equation to describe O_2 diffusion in muscle fibre zones and interstitial spaces. This is achieved by incorporating an additional interstitial compartment and distinct fibre sub-compartments, each with specific biophysical parameters, thus capturing the influence of the interstitial space and especially mitochondrial heterogeneity for O_2 transport and oxidative metabolism. In addition, the average transport of O_2 in the microvessels is incorporated via a Robin–type boundary condition at capillary walls. We emphasise here that neglecting intravascular heterogeneities is appropriate as the primary assumption is that the tissue is under maximal sustainable aerobic conditions.

Consequently, denoting each tissue compartment j and its subcompartment by j_l, the steady–state transport of O_2 in tissue can be described by the local oxygen partial pressure, which is governed by conservation of mass

$$\nabla \cdot \left[\mathcal{D}_{j_l} \nabla(\alpha_{j_l} p) + c_{j_l}^{\mathrm{Mb}} \mathcal{D}_{j_l}^{\mathrm{Mb}} \left(\frac{dS_{\mathrm{Mb}}}{dp} \nabla p \right) \right] - \mathcal{M}_{j_l}(p) = 0, \tag{4.1}$$

where $\mathcal{D}_{j_l}$ and α_{j_l} are the molecular diffusivity and solubility of free O_2, $c_{j_l}^{\mathrm{Mb}}$ and $\mathcal{D}_{j_l}^{\mathrm{Mb}}$ are the bulk myoglobin concentration and diffusivity, and $\mathcal{M}_{j_l}$ is the rate of O_2 consumption in muscle fibre subcompartment j_l. Here j denotes the following tissue compartments: *interstitial spaces* ($j = \mathrm{IS}$) and *fibre types I* ($j = \mathrm{I}$), *IIa* ($j = \mathrm{IIa}$), and *IIb* ($j = \mathrm{IIb}$). Moreover, noting that O_2 consumption is restricted to fibre subcompartments, l denotes the following fibre subcompartments: *intermyofibrillar zone* ($l = \mathrm{imf}$) and *subsarcolemmal zone* ($l = \mathrm{ss}$). Note that α_{j_l} is constant in each

subcompartment, and thus $\nabla(\alpha_{j_l} p) = \alpha_{j_l} \nabla p$.

Assuming the absence of myoglobin binding and consumption of free O_2 in interstitial spaces, the steady–state equation governing O_2 transport in this compartment is reduced to

$$a_{\mathrm{IS}} D_{\mathrm{IS}} \nabla^2 p = 0. \tag{4.2}$$

Similar to the previous chapters, the domain geometry is obtained by considering a circular tissue cross–section and then rescaling to the unit disc, $\mathbb{D}^1$. After rescaling, the region enclosed by compartment j will be denoted by Ω_j with boundary $\partial\Omega_j$. Each region enclosed by a subcompartmental zone will be denoted by Ω_{j_l} with boundary $\partial\Omega_{j_l}$. Note that, from Fig. 4.5, we have

$$\begin{aligned} \Omega_j &= \Omega_{j_{\mathrm{ss}}} \cup \Omega_{j_{\mathrm{imf}}}, \\ \partial\Omega_{j_{\mathrm{imf}}} &= \Omega_{j_{\mathrm{ss}}} \cap \Omega_{j_{\mathrm{imf}}}, \\ \partial\Omega_{j_{\mathrm{ss}}} &= \partial\Omega_{j_{\mathrm{imf}}} \cup \partial\Omega_j. \end{aligned}$$

In addition, capillaries are assumed to possess an area, C_i, with a boundary, ∂C_i, though below we treat the capillaries as small circles with radius r_{cap}. Therefore, we seek to investigate PO_2 in a region of the unit disc that excludes the capillary interior, $\Omega = \bigcup_j \Omega_j = \mathbb{D}^1 \setminus \bigcup_i C_i$.

4.5.1.1 Oxygen consumption

Within muscle tissue, the rate of O_2 consumption by a fibre sub-compartment j_l is assumed to follow the Michaelis–Menten kinetics described by

$$\mathcal{M}_{j_l}(p) = \frac{\mathcal{M}_0^{j_l} p}{p + p_c}, \tag{4.3}$$

where $\mathcal{M}_0^{j_l}$ is the maximal consumption rate volume–averaged over fibre subcompartment j_l, and p_c is the tissue PO_2 value which reflects the partial pressure scale where fibre mitochondria are no longer able to extract O_2 at maximal rate.

We remark here that although the mitochondrial distribution can be spatially heterogeneous within muscle fibres, we have nonetheless assumed that mitochondria is homogeneously distributed within each fibre subcompartment. These assumptions capture the continuum description illustrated in Fig. 4.5.

Let

$$V_V(l, j) = \frac{V(\Omega_{j_l})}{V(\Omega_j)}, \tag{4.4}$$

denote the volume fraction of subcompartment j_l with respect to the enclosing compartment j, and $V(\cdot)$ denote the Euclidean volume measure. We note here that for a cylindrical tissue, the volume fraction of a subcompartment is equal to its area fraction assuming uniformity in the direction of the fibre axis. For instance, the mitochondrial volume fraction of subsarcolemmal mitochondria relative to the volume of the subsarcolemmal compartment of muscle fibre j is given by

$$V_V(\mathrm{ms}_j, \mathrm{ss}) = \frac{V(\mathrm{ms}_j)}{V(\Omega_{j_{\mathrm{ss}}})}, \tag{4.5a}$$

where $\Omega_{j_{\mathrm{ss}}}$ is the subsarcolemmal zone of fibre j. Similarly, the mitochondrial volume fraction of the intermyofibrillar mitochondria relative to the volume of the intermyofibrillar compartment of muscle fibre j is given by

$$V_V(\mathrm{mi}_j, \mathrm{imf}) = \frac{V(\mathrm{mi}_j)}{V(\Omega_{j_{\mathrm{imf}}})}. \tag{4.5b}$$

Thus with an assumed fixed maximal rate of consumption per unit volume of mitochondria, denoted by $\mathcal{M}_0^{\text{mito}}$, the subcompartmental O_2 uptake rates per unit volume (and hence area, assuming uniformity in the direction of the fibre axis) are given by

$$\mathcal{M}_0^{j_{\text{ss}}} = V_V(\text{ms}_j, \text{ss})\mathcal{M}_0^{\text{mito}}, \tag{4.6a}$$
$$\mathcal{M}_0^{j_{\text{imf}}} = V_V(\text{mi}_j, \text{imf})\mathcal{M}_0^{\text{mito}}. \tag{4.6b}$$

Similarly, the mean uptake in muscle fibre j satisfies

$$\mathcal{M}_0^{j} = V_V(\text{mt}_j, j)\mathcal{M}_0^{\text{mito}}, \tag{4.6c}$$

where mt_j is the total mitochondrial population within the j^{th} fibre. Using this along with Eq. (4.5) and the identity $V(\text{mt}_j) = V(\text{ms}_j) + V(\text{mi}_j)$, and letting $q = V(\Omega_{j_{\text{ss}}})/V(\Omega_{j_{\text{imf}}})$, we derive the following relation

$$\begin{aligned} n = \frac{\mathcal{M}_0^{j_{\text{ss}}}}{\mathcal{M}_0^{j_{\text{imf}}}} &= \frac{V_V(\text{ms}_j, \text{ss})}{V_V(\text{mi}_j, \text{imf})}, \\ &= \left(\frac{V(\text{ms}_j)}{V(\text{mi}_j)}\right) \cdot \left(\frac{V(\Omega_{j_{\text{imf}}})}{V(\Omega_{j_{\text{ss}}})}\right), \\ &= \left(\frac{V(\text{mt}_j)}{V(\text{mi}_j)} - 1\right) \cdot \left(\frac{1}{q}\right), \\ &= \left(\frac{1}{\chi_{\text{mi}}^j} - 1\right) \cdot \left(\frac{1}{q}\right), \end{aligned} \tag{4.7}$$

where χ_{mi}^j is the fraction of mitochondria restricted to the intermyofibrillar zone of fibre j. Hence, given the relative subcompartmental uptake rates and volumes (i.e. n and q), we can estimate the mitochondrial fractions in the two zones by using

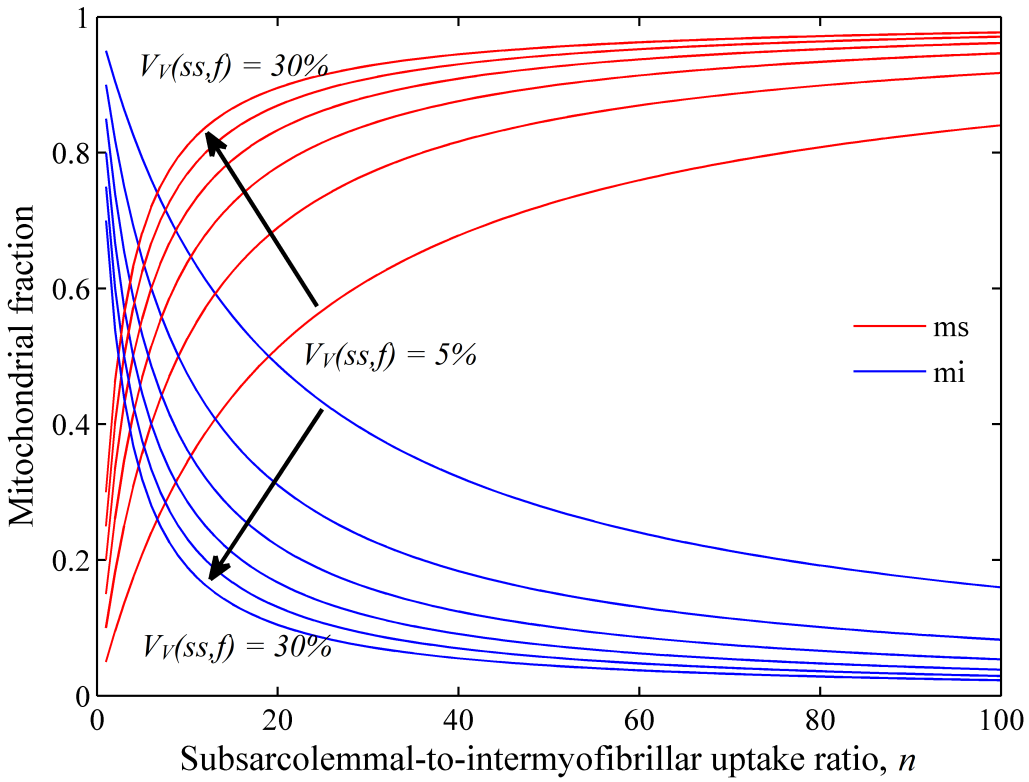

Figure 4.7: Variation of the relative O_2 uptake of mitochondrial zones (i.e. n) with respect to the fraction of mitochondria within each fibre subcomparment. The average fibre uptake is assumed to be fixed (i.e. fibre mitochondrial density is fixed). Here $q = V_v(ss, f)$ (refer to Eq. (4.7) for more details). $V_v(ss, f)$ increments by 5% for each subcompartment in the direction of the arrow.

$$\chi_{\text{ms}} = \frac{nq}{1+nq}, \tag{4.8}$$

$$\chi_{\text{mi}} = \frac{1}{1+nq}. \tag{4.9}$$

In Fig. 4.7 we demonstrate how variations in both mitochondrial fractions and the volume fraction of the subsarcolemmal zone affect the relative O_2 consumption rates in different fibre subcompartments, given a fixed average fibre uptake (hence, mitochondrial content). We remark here that this fixed fibre uptake is the volume average of the subcompartmental uptakes

$$\mathcal{M}_0^j = V_V(\mathrm{ss}, j) \cdot \mathcal{M}_0^{j_{\mathrm{ss}}} + V_V(\mathrm{imf}, j) \cdot \mathcal{M}_0^{j_{\mathrm{imf}}}, \tag{4.10a}$$

$$= \left(\frac{q}{1+q}\right) \cdot n\mathcal{M}_0^{j_{\mathrm{imf}}} + \left(\frac{1}{1+q}\right) \cdot \mathcal{M}_0^{j_{\mathrm{imf}}}, \tag{4.10b}$$

$$= \left(\frac{1+nq}{1+q}\right) \cdot \mathcal{M}_0^{j_{\mathrm{imf}}}. \tag{4.10c}$$

Given fixed $\mathcal{M}_0^j$ and q for each muscle fibre, we use Eqs. (4.7) and (4.10) in the results section to solve our model for a range of $\mathcal{M}_0^{j_{\mathrm{imf}}}$ by modifying n.

4.5.1.2 Myoglobin

Myoglobin is assumed to be homogeneously distributed within each subcompartment of muscle fibres with rapid local kinetics of Mb–O_2 dissociation. As noted in Chapter 3, this leads to the following equilibrium O_2–saturation relation

$$S_{\mathrm{Mb}}(p) = \frac{p}{p + p_{50,\mathrm{Mb}}},$$

where $p_{50,\mathrm{Mb}}$ is the tissue PO_2 when 50% of myoglobin molecules are saturated with O_2. We note here that heterogeneities in myoglobin distribution can be feasibly incorporated into our model by taking the subcompartmental parameters associated with myoglobin to be non-uniform (e.g. non-uniform $c_{j_l}^{\mathrm{Mb}}$ and $\mathcal{D}_{j_l}^{\mathrm{Mb}}$).

4.5.2 Boundary conditions

The exchange of O_2 between capillaries and the interstitial fluid or the subsarcolemmal zone of muscle fibres occurs at their respective interfaces. Across the part of the capillary wall in contact with either the interstitial fluid or the subsarcolemmal zone, passive transport of O_2 into tissue is characterised by the boundary condition for the i^{th} capillary

$$\mathbf{n}_i \cdot (\alpha_{\mathrm{IS}} D_{\mathrm{IS}} \nabla p) = k(p_{\mathrm{cap}} - p), \qquad \partial C_i \cap \partial\Omega_{\mathrm{IS}}, \tag{4.11a}$$

$$\mathbf{n}_i \cdot (a_{j_{\mathrm{ss}}} D_{j_{\mathrm{ss}}} \nabla p) = k(p_{\mathrm{cap}} - p), \qquad \partial C_i \cap \partial\Omega_{j_{\mathrm{ss}}}, \tag{4.11b}$$

where $\mathbf{n}_i$ is the unit normal vector on the capillary wall pointing away from the tissue and into the capillary, k is the mass transfer coefficient, p_{cap} is the transversally–averaged intracapillary PO_2, and p is the partial pressure of O_2 at the external capillary wall. Recalling from Henry's law that $[O_2] = \alpha p$, we assume continuity of O_2 flux and concentration at the interstitium–subsarcolemma, subsarcolemma–subsarcolemma (e.g. when edges of neighbouring fibres are indistinguishable), and subsarcolemma–intermyofibril interfaces

$$\mathbf{n}_{\text{IS}} \cdot (\alpha_{\text{IS}} \mathcal{D}_{\text{IS}} \nabla p) = \mathbf{n}_{j_{\text{ss}}} \cdot (\alpha_{j_{\text{ss}}} \mathcal{D}_{j_{\text{ss}}} \nabla p), \qquad \partial\Omega_{\text{IS}} \cap \partial\Omega_{j_{\text{ss}}}, \tag{4.11c}$$

$$\mathbf{n}_{j_{\text{ss}}} \cdot (\alpha_{j_{\text{ss}}} \mathcal{D}_{j_{\text{ss}}} \nabla p) = \mathbf{n}_{k_{\text{ss}}} \cdot (\alpha_{k_{\text{ss}}} \mathcal{D}_{k_{\text{ss}}} \nabla p), \qquad \partial\Omega_{j_{\text{ss}}} \cap \partial\Omega_{k_{\text{ss}}}, \tag{4.11d}$$

$$\mathbf{n}_{j_{\text{ss}}} \cdot (\alpha_{j_{\text{ss}}} \mathcal{D}_{j_{\text{ss}}} \nabla p) = \mathbf{n}_{j_{\text{imf}}} \cdot (\alpha_{j_{\text{imf}}} \mathcal{D}_{j_{\text{imf}}} \nabla p), \qquad \partial\Omega_{j_{\text{imf}}}, \tag{4.11e}$$

$$\alpha_{\text{IS}} p = \alpha_{j_{\text{ss}}} p, \qquad \partial\Omega_{\text{IS}} \cap \partial\Omega_{j_{\text{ss}}}, \tag{4.11f}$$

$$\alpha_{j_{\text{ss}}} p = \alpha_{k_{\text{ss}}} p, \qquad \partial\Omega_{j_{\text{ss}}} \cap \partial\Omega_{k_{\text{ss}}}, \tag{4.11g}$$

$$\alpha_{j_{\text{ss}}} p = \alpha_{j_{\text{imf}}} p, \qquad \partial\Omega_{j_{\text{imf}}}. \tag{4.11h}$$

Additionally, a no–flux boundary condition is imposed at the outer boundary of the tissue, effectively the muscle fascicle, to signify no exchange across it

$$\mathbf{n}_{j_l} \cdot \left(\alpha_{j_l} \mathcal{D}_{j_l} \nabla p \right) \Big|_{\partial\Omega} = 0. \tag{4.11i}$$

As detailed in Chapter 2, perturbing the latter boundary condition is verified to induce no significant influence on the system behaviour away from the tissue domain boundary, thus justifying its use.

4.5.3 Non-dimensionalisation

We reduce the number of parameters by non-dimensionalising the model as follows. Given that N_c capillaries in a tissue disc have an average capillary density ρ, the lengthscale, L, is taken to be equal to the diameter of the disc, which is given by $L = \sqrt{4N_c/\pi\rho}$. We use L along with $\mathcal{M}_0^{\text{I}}$, p_{cap},

$$\alpha_{\mathrm{I}^*} = \max_l \alpha_{\mathrm{I}_l},$$
$$\mathcal{D}_{\mathrm{I}^*} = \max_l \mathcal{D}_{\mathrm{I}_l},$$
$$c^{\mathrm{Mb}}_{\mathrm{I}^*} = \max_l c^{\mathrm{Mb}}_{\mathrm{I}_l},$$

and

$$\mathcal{D}^{\mathrm{Mb}}_{\mathrm{I}^*} = \max_l \mathcal{D}^{\mathrm{Mb}}_{\mathrm{I}_l},$$

to non-dimensionalise our model by setting

$$x = L\bar{x}, \qquad p = p_{\mathrm{cap}}\bar{p}, \qquad p_c = p_{\mathrm{cap}}\bar{p}_c, \qquad p_{50,\mathrm{Mb}} = p_{\mathrm{cap}}\bar{p}_{50,\mathrm{Mb}},$$
$$\alpha_{j_l} = \alpha_{\mathrm{I}^*}\bar{\alpha}_{j_l}, \qquad \mathcal{D}_{j_l} = \mathcal{D}_{\mathrm{I}^*}\bar{\mathcal{D}}_{j_l}, \qquad c^{\mathrm{Mb}}_{j_l} = c^{\mathrm{Mb}}_{\mathrm{I}^*}\bar{c}^{\mathrm{Mb}}_{j_l}, \qquad \mathcal{D}^{\mathrm{Mb}}_{j_l} = \mathcal{D}^{\mathrm{Mb}}_{\mathrm{I}^*}\bar{\mathcal{D}}^{\mathrm{Mb}}_{j_l},$$
$$\mathcal{M}^{j_l}_0 = \mathcal{M}^{\mathrm{I}}_0\bar{\mathcal{M}}^{j_l}_0, \qquad \theta_{\mathrm{I}^*} = \frac{c^{\mathrm{Mb}}_{\mathrm{I}^*}\mathcal{D}^{\mathrm{Mb}}_{\mathrm{I}^*}}{\alpha_{\mathrm{I}^*}\mathcal{D}_{\mathrm{I}^*}p_{\mathrm{cap}}}, \qquad \mu_{\mathrm{I}^*} = \frac{L^2\mathcal{M}^{\mathrm{I}}_0}{\alpha_{\mathrm{I}^*}\mathcal{D}_{\mathrm{I}^*}p_{\mathrm{cap}}}, \qquad \kappa_{\mathrm{I}^*} = \frac{Lk}{\alpha_{\mathrm{I}^*}\mathcal{D}_{\mathrm{I}^*}},$$

where the bars denote non-dimensional variables and parameters. Here $\theta_{\mathrm{I}}, \mu_{\mathrm{I}}, \kappa_{\mathrm{I}} > 0$ are the non-dimensionalised myoglobin content, metabolic O_2 demand, and mass transfer coefficient of fibre Type I. Dropping the bars, the non-dimensional model is reduced to

$$\nabla \cdot \left[\left((\alpha_{j_l}\mathcal{D}_{j_l} + c^{\mathrm{Mb}}_{j_l}\mathcal{D}^{\mathrm{Mb}}_{j_l}\theta_{\mathrm{I}^*}\frac{dS_{\mathrm{Mb}}}{dp}\right)\nabla p \right] - \mathcal{M}^{j_l}_0\mathcal{M}_{\mathrm{I}^*}(p) = 0, \qquad \mathbf{x} \in \Omega_{j_l}, \tag{4.12a}$$

with boundary conditions (1) dictating capillary exchange of O_2 with interstitial spaces and subsarcolemmal zones

$$\mathbf{n}_i \cdot (\alpha_{\mathrm{IS}}\mathcal{D}_{\mathrm{IS}}\nabla p) = \kappa_{\mathrm{I}^*}(1-p), \qquad \mathbf{x} \in \partial C_i \cap \partial\Omega_{\mathrm{IS}}, \tag{4.12b}$$

$$\mathbf{n}_i \cdot (\alpha_{j_{\rm ss}} \mathcal{D}_{j_{\rm ss}} \nabla p) = \kappa_{\rm I^*}(1-p), \qquad \mathbf{x} \in \partial C_i \cap \partial \Omega_{j_{\rm ss}}, \tag{4.12c}$$

(2) at interstitium–subsarcolemma interfaces

$$\mathbf{n}_{\rm IS} \cdot (\alpha_{\rm IS} \mathcal{D}_{\rm IS} \nabla p) = \mathbf{n}_{j_{\rm ss}} \cdot (\alpha_{j_{\rm ss}} \mathcal{D}_{j_{\rm ss}} \nabla p), \qquad \mathbf{x} \in \partial \Omega_{\rm IS} \cap \partial \Omega_{j_{\rm ss}}, \tag{4.12d}$$

$$\alpha_{\rm IS} p = \alpha_{j_{\rm ss}} p, \qquad \mathbf{x} \in \partial \Omega_{\rm IS} \cap \partial \Omega_{j_{\rm ss}}, \tag{4.12e}$$

(3) at fibre–fibre interfaces

$$\mathbf{n}_{j_{\rm ss}} \cdot (\alpha_{j_{\rm ss}} \mathcal{D}_{j_{\rm ss}} \nabla p) = \mathbf{n}_{k_{\rm ss}} \cdot (\alpha_{k_{\rm ss}} \mathcal{D}_{k_{\rm ss}} \nabla p), \qquad \mathbf{x} \in \partial \Omega_{j_{\rm ss}} \cap \partial \Omega_{k_{\rm ss}}, \tag{4.12f}$$

$$\alpha_{j_{\rm ss}} p = \alpha_{k_{\rm ss}} p, \qquad \mathbf{x} \in \partial \Omega_{j_{\rm ss}} \cap \partial \Omega_{k_{\rm ss}}, \tag{4.12g}$$

(4) at subsarcolemma–intermyofibril interfaces

$$\mathbf{n}_{j_{\rm ss}} \cdot (\alpha_{j_{\rm ss}} \mathcal{D}_{j_{\rm ss}} \nabla p) = \mathbf{n}_{j_{\rm imf}} \cdot (\alpha_{j_{\rm imf}} \mathcal{D}_{j_{\rm imf}} \nabla p), \qquad \mathbf{x} \in \partial \Omega_{j_{\rm imf}}, \tag{4.12h}$$

$$\alpha_{j_{\rm ss}} p = \alpha_{j_{\rm imf}} p, \qquad \mathbf{x} \in \partial \Omega_{j_{\rm imf}}, \tag{4.12i}$$

and (5) at the external tissue boundaries

$$\mathbf{n}_{j_l} \cdot \left(\alpha_{j_l} \mathcal{D}_{j_l} \nabla p \right) \Big|_{\partial \Omega} = 0, \tag{4.12j}$$

where

$$\mathcal{M}_{\mathrm{I}^*}(p) = \frac{\mu_{\mathrm{I}^*} p}{p + p_c}, \tag{4.12k}$$

$$S(p) = \frac{p}{p + p_{50,\mathrm{Mb}}}. \tag{4.12l}$$

4.6 Model parameters

The values for our model's biophysical parameters are listed in Table 4.1. Except for capillary density and number, all parameter values are obtained directly from the citations indicated in Table 4.1. Recall that, in our model, non-uniform diffusion refers to different O_2 diffusion coefficients in Type I, IIa and IIb fibres, whereas in the case of uniform diffusion distinct fibre types have the same O_2 diffusion coefficient. For cases of non-uniform diffusion we use the heterogeneous O_2 solubility and diffusivity parameters presented in Table 4.1, and refer to such cases by appending a '+' sign to the geometry under consideration (e.g. H1+). In contrast, for cases of uniform diffusion we use the values of O_2 solubility and diffusivity of fibre Type I for all fibre types, and denote such cases by SU, SN, H1 and H2. We also use the value of O_2 solubility in plasma [23] for the interstitial spaces. In addition, the O_2 diffusion coefficient in interstitial spaces is set equal to that of aqueous solution [8].

4.7 Model limitations

We use a spatial profile of maximal O_2 uptake ($\dot{V}O_{2,\max}$) that follows a step-function, with a constant high value near the sarcolemma and a lower value in the fibre core for non-uniform mitochondrial distributions. However, the experimentally observed profile of $VO_{2,\max}$ smoothly decays from the sarcolemma to the fibre core [193]. This can be accommodated in the current model by smoothing the O_2 uptake jump within fibres via the use of a hyperbolic tangent function with respect to a distance function that is specific to each fibre geometry.

We have also constrained the average uptake of each fibre in an effort to exclude any effects associated with changes to fibre aerobic capacity, thus permitting an unambiguous exploration of the influences of intracellular uptake heterogeneities. Nonetheless, this constraint can be feasibly relaxed to assess tissue oxygenation during concomitant changes to fibre aerobic capacity and the intracellular distribution of mitochondrial subpopulations (e.g. increase in both subsarcolemmal and intermyofibrillar mitochondrial volume densities with higher preference to subsarcolemmal

Parameter	Symbol	Compartment, j				Unit	Refs.
		I	IIa	IIb	IS		
O_2 demand	$\mathcal{M}_0^j$	15.7	13.82	7.85	0	10^{-5} ml O_2/ml·s	[174, 193]
O_2 solubility	α_j	3.89	3.89	3.89	2.8	10^{-5} ml O_2/ml·mmHg	[23, 127]
O_2 diffusivity	$\mathcal{D}_j$	2.41	1.39	0.81	2.4	10^{-5} cm^2/s	[8, 15, 57]
Mb concentration	c_j^{Mb}	10.2	4.98	1.55	0	10^{-3} ml O_2/ml	[134]
Mb diffusivity	$\mathcal{D}_j^{Mb}$	1.73×10^{-7}			#	cm^2/s	[111]
Mass transfer coefficient	k	4.00×10^{-6}				ml O_2/cm^2·mmHg·s	[54, 71]
$\mathcal{M}_0^{j_{ss}}/\mathcal{M}_0^{j_{imf}}$	n	$1-30$			#	unitless	[16, 115, 145, 193]
Intracapillary PO_2	P_{cap}	20				mmHg	[55]
Mb half-saturation PO_2	$P_{50,Mb}$	5.3				mmHg	[111]
PO_2 at half demand	P_c	0.5				mmHg	[91]
Capillary radius	r	$1.8-2.5\times10^{-4}$				cm	[58]
Capillary density	ρ	913.4				mm^{-2}	*
# of capillaries	N_{cap}	$204-248$				unitless	*
Lengthscale	L	$5.33-5.47\times10^{-2}$				cm	
Transfer coefficient	κ_j	233.4				unitless	
O_2 demand	μ_j	25.05	22.05	12.53	0	unitless	

Table 4.1: Except for the capillary density and the number of capillaries, the parameter values in the upper part of the table, above the line, are based on experiments, while those in the lower part are derived values. For cases of uniform diffusion, the fibre solubility and diffusivity are set to the values of fibre Type I. Hypoxia is achieved by increasing the O_2 demand of every fibre type by a factor of 12. We choose this factor such that the effective lengthscale of diffusion, $\sqrt{\alpha\mathcal{D}P_{cap}/\mathcal{M}_0}$, is much smaller than half the characteristic intercapillary distance. IS = interstitial spaces, # = not applicable, Mb = myoglobin, and * highlights parameters estimated from our histological preparations (Fig. 4.4C, D).

mitochondrial biogenesis), as observed in skeletal muscle fibres following repeated endurance training under both normal and low ambient O_2 levels [35, 36, 101]. In addition, although we have not investigated the potential effects that *oedema* and *fibrosis* might have on O_2 supply, it is still feasible to incorporate such pathologies in our current model given accurate histologic details and higher resolution biophysical parameters can be obtained.

4.8 Numerical solution

The general aim of this chapter is to investigate capillary O_2 supply to histologically representative tissues, e.g. mixed muscle. However, the complexity of histological geometries added to the nonlinearity of O_2 flux and tissue consumption does not permit a tractable analytical solution to our transport equations. Numerical schemes based on the method of finite elements are fairly standard for such geometrically

complex problems. In particular, subcellular geometries (e.g. mitochondrial zones) can be easily accommodated within such numerical frameworks.

We therefore determine the PO_2 distribution by solving Eqs. (4.12) via the use of the finite element scheme outlined in Appendix A. To capture subtle changes in intracellular PO_2 we concentrate the computation power on areas of large gradients of PO_2 (e.g. interstitium–fibre, subsarcolemma–intermyofibril, and capillary–tissue interfaces) via employing an adaptive meshing algorithm (see Appendix B).

We then seek to determine the trapping regions. However, a direct way to accurately calculate such regions is not feasible due to the complexity of the transport equations. Hence, we proceed by recalling from Chapters 2–3 that each such region of the muscle tissue is spanned by the O_2 flux lines of the enclosed capillary. Recall that these flux lines are derived from our numerical solution of PO_2 via Eq. (2.10). Subsequently, we determine the TR geometries using the numerical methodologies outlined in Chapter 2 and Appendix A.

4.8.1 Numerical accuracy

We assess the numerical accuracy of our method by first studying the steady–state transport problem over a two-zone Krogh cylinder, a central capillary with two concentric layers of tissue. The solution to this problem is detailed elsewhere [92]. Our numerical solution is compared to the analytical solution for a range of subcellular differential uptakes ($\mathcal{M}_0^{j_{\rm ss}}/\mathcal{M}_0^{j_{\rm imf}}$), with adaptive mesh refinements to ensure high accuracy where needed. We further assess the numerical accuracy by studying the trapping regions determined for a highly symmetrical geometry (synthetic uniform geometry) under conditions of uniform tissue uptake. Given that such symmetrical and uniform tissues have capillary supply regions that match Voronoi polygons under maximal sustainable conditions and spatially homogeneous perfusion, the mean deviation of trapping regions from Voronoi polygons can then quantify the scale of our numerical error.

4.9 Results

Our modelling equations were solved for a range of n values to consider a range of increases in mitochondrial redistribution to the peripheral region of muscle fibres (see

Table 4.1). Simulations were carried out to assess the effectiveness of Voronoi polygons in predicting the biophysical representation of capillary supply regions, namely trapping regions, as well as to study the distribution of oxygen partial pressure in muscle fibres. All simulations were performed with a parameter regime characterising tissue hypoxia, e.g. 12–fold increase in O_2 demand or a proportional decrease in capillary PO_2, as mitochondrial clustering is anticipated to have the greatest influence under such regimes.

4.9.1 PO_2 profile

The graphical results for our PO_2 simulations are presented in Figs. 4.8–4.15, with fibre and tissue PO_2 curves indicated in *black* colour and interstitial spaces in *magenta*. In addition, the results for the subsarcolemmal and intermyofibrillar fibre subcompartments are shown in *red* and *blue* colours, respectively.

4.9.1.1 Minimum PO_2

The minimum value of PO_2 exhibits a general sensitivity to the level of mitochondrial clustering, though no clear trend is observed in tissue or fibre types for modest clustering (e.g. compare curves for tissue and all subcompartments of all fibre types in Fig. 4.10 with Fig. 4.12; compare curves for all subcompartments of all fibre types in Fig. 4.14 with Fig. 4.12). Here by *modest* mitochondrial clustering we mean that the mitochondrial distribution within muscle fibres is approximately uniform (i.e. a perturbation from the homogeneous state; e.g. $n \leq 5$), hence we can infer the minimum levels of O_2 available to mitochondria from the minimum value of fibre PO_2 for relatively small n (e.g. consider the black or blue curves for very low n values).

In contrast, *extreme* mitochondrial clustering approximates the scenario where all fibre mitochondria are in the subsarcolemmal zone, hence we can infer the minimum levels of O_2 available to mitochondria from the minimum value of subsarcolemmal PO_2 for relatively large n (e.g. look at the red curve for $n \geq 80$). In particular, extreme mitochondrial clustering improves the minimum amount of O_2 available to fibre mitochondria markedly when compared to uniform mitochondrial distribution (compare with black curve at $n = 1$).

The minimum PO_2 value in tissue and individual fibres varies with increasing heterogeneity in mitochondrial distribution. Except for values at the scale of our

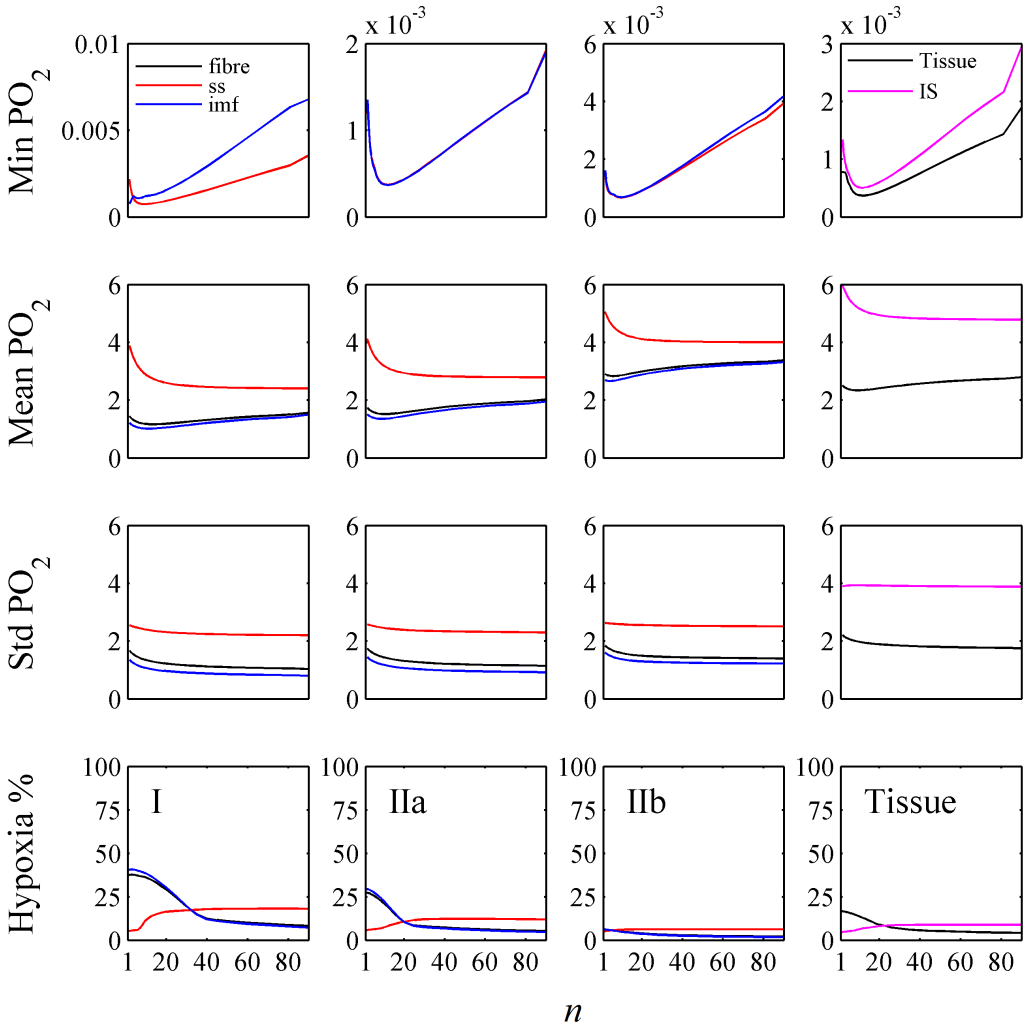

Figure 4.8: Oxygen profile statistics for the SU geometry with uniform diffusion parameters (SU). Oxygen tension is in mmHg units unless otherwise indicated. In this geometry, the spatial distribution of fibre types is *random* with an areal composition of 9:37:54 (i.e. Type I:IIa:IIb). Results for each fibre type are presented columnwise (see bottom row). n denotes the subsarcolemmal–to–intermyofibrillar uptake ratio (see Eq. (4.7)).

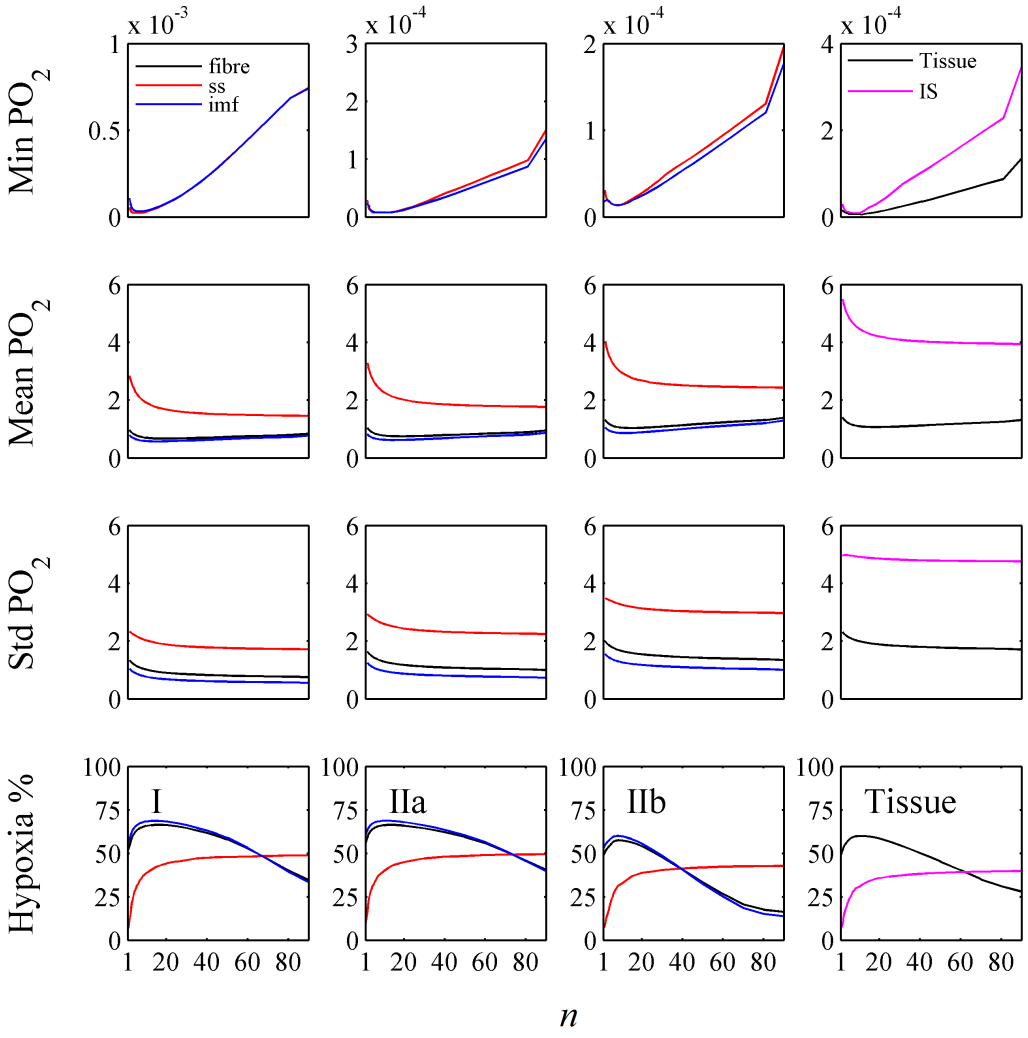

Figure 4.9: Oxygen profile statistics for the SU geometry with non-uniform diffusion parameters. Oxygen tension is in mmHg units unless otherwise indicated. See caption of Fig. 4.8 for more details about the SU geometry. n denotes the subsarcolemmal–to–intermyofibrillar uptake ratio (see Eq. (4.7)).

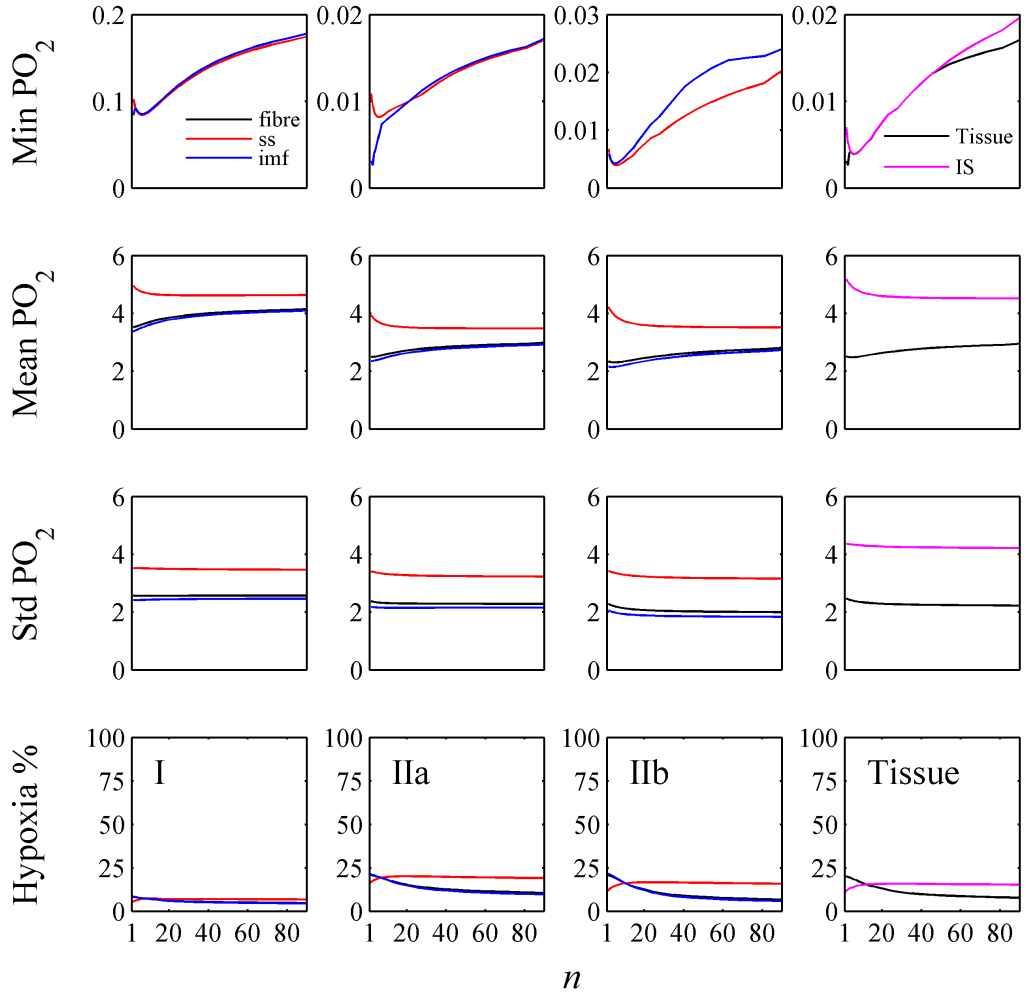

Figure 4.10: Oxygen profile statistics for the SN geometry with uniform diffusion parameters (SN). Oxygen tension is in mmHg units unless otherwise indicated. In this geometry, the spatial distribution of fibre types is *size–based* (I $\leq$ IIa $\leq$ IIb) with an areal composition of 9:37:54. Results for each fibre type are presented columnwise (see bottom row). n denotes the subsarcolemmal–to–intermyofibrillar uptake ratio (see Eq. (4.7)).

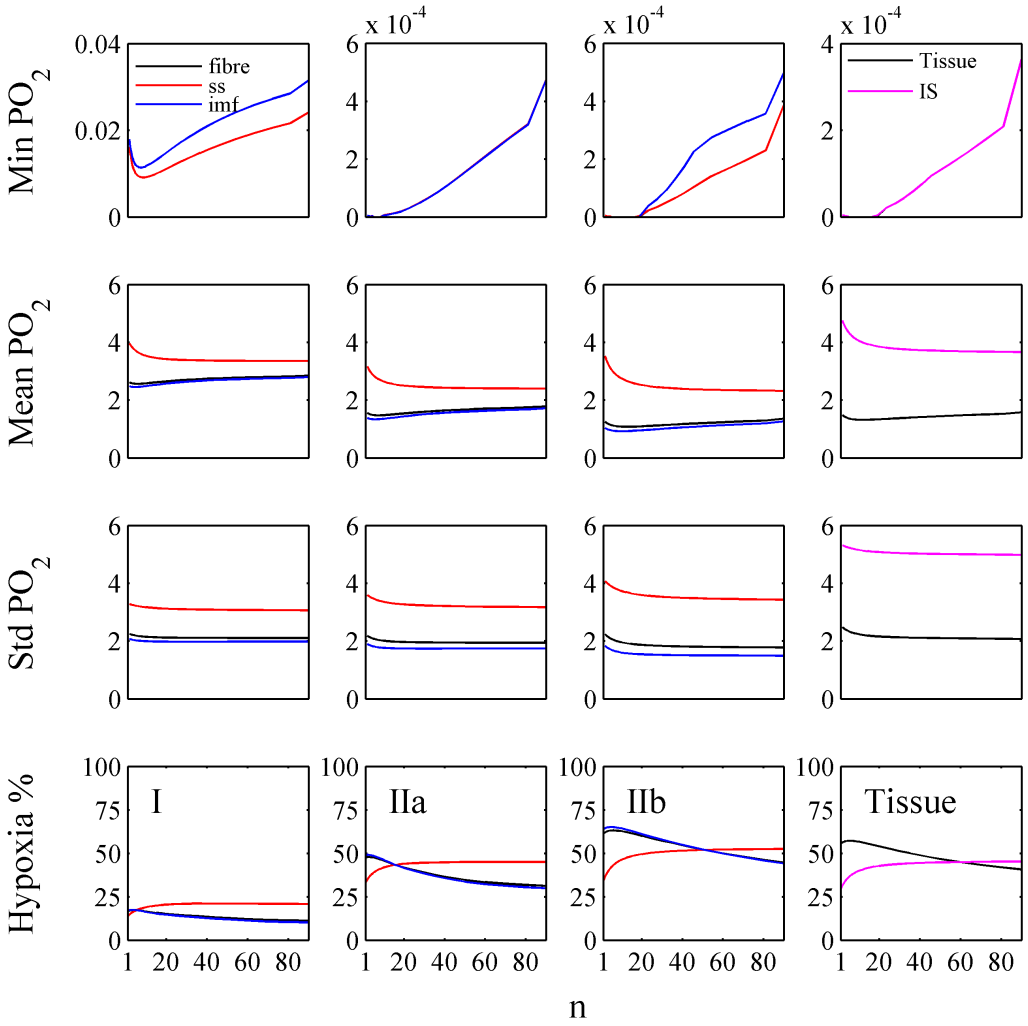

Figure 4.11: Oxygen profile statistics for the SN geometry with non-uniform diffusion parameters. Oxygen tension is in mmHg units unless otherwise indicated. See caption of Fig. 4.10 for more details about the SN geometry. n denotes the subsarcolemmal–to–intermyofibrillar uptake ratio (see Eq. (4.7)).

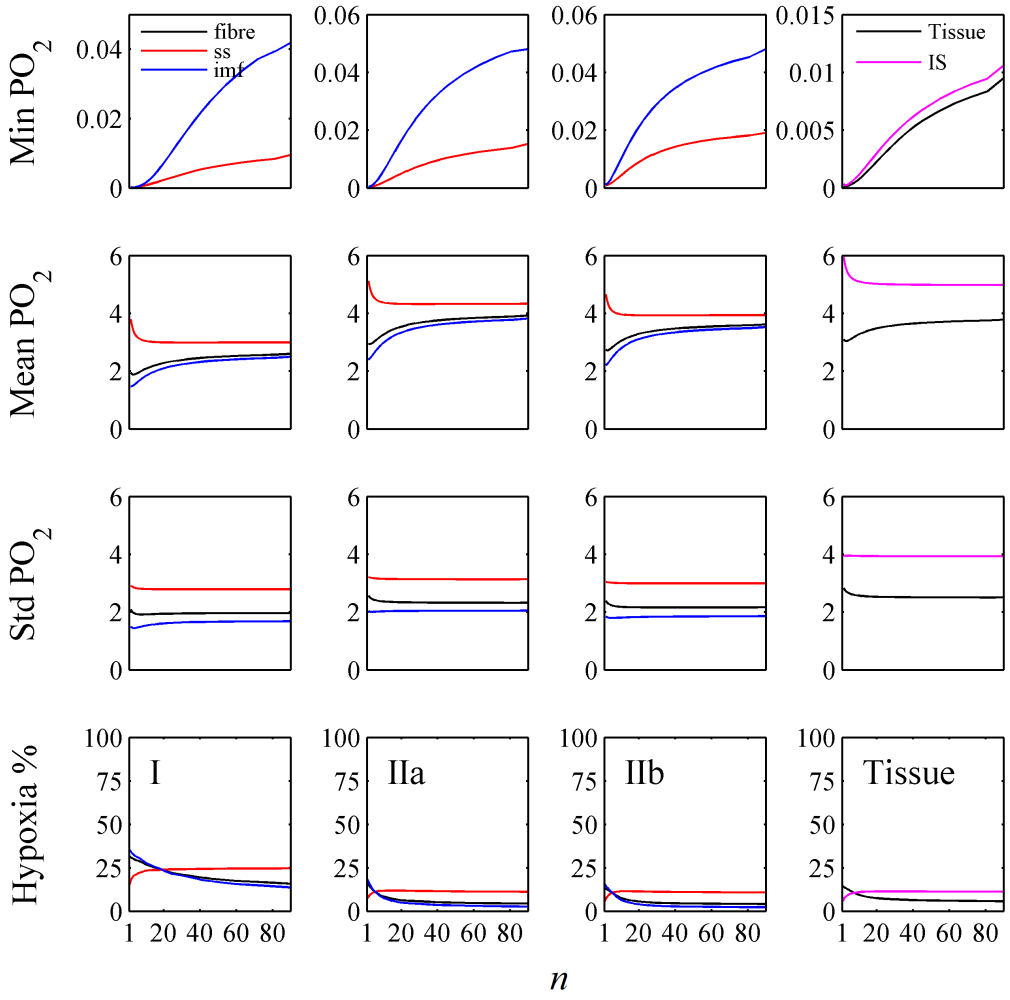

Figure 4.12: Oxygen profile statistics for the H1 geometry with uniform diffusion parameters. Oxygen tension is in mmHg units unless otherwise indicated. In this geometry, the spatial distribution of fibre types is *real* with an areal composition of 9:37:54. Results for each fibre type are presented columnwise (see bottom row). n denotes the subsarcolemmal–to–intermyofibrillar uptake ratio (see Eq. (4.7)).

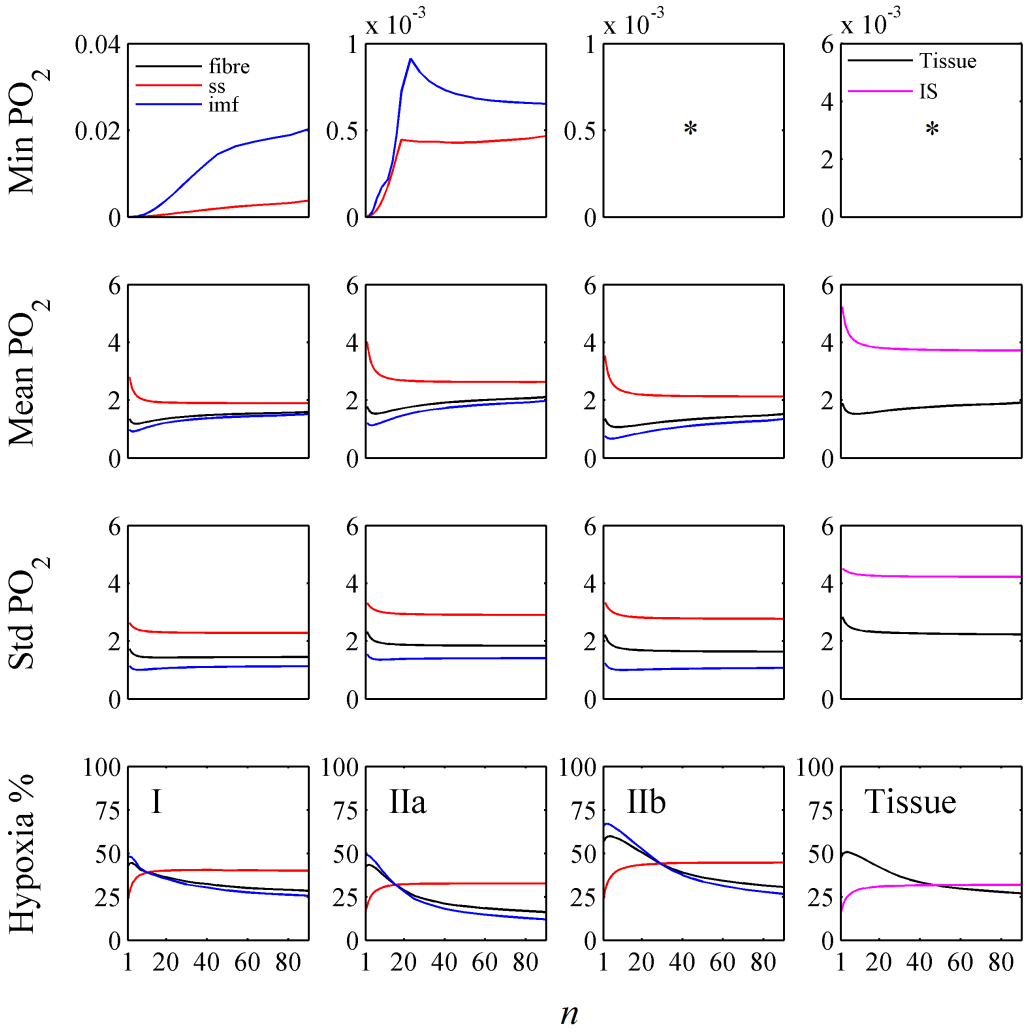

Figure 4.13: Oxygen profile statistics for the H1 geometry with non-uniform diffusion parameters. Oxygen tension is in mmHg units unless otherwise indicated. See caption of Fig. 4.12 for more details about the H1 geometry. n denotes the subsarcolemmal–to–intermyofibrillar uptake ratio (see Eq. (4.7)). $*$ = results vary at scales smaller than 10^{-6}.

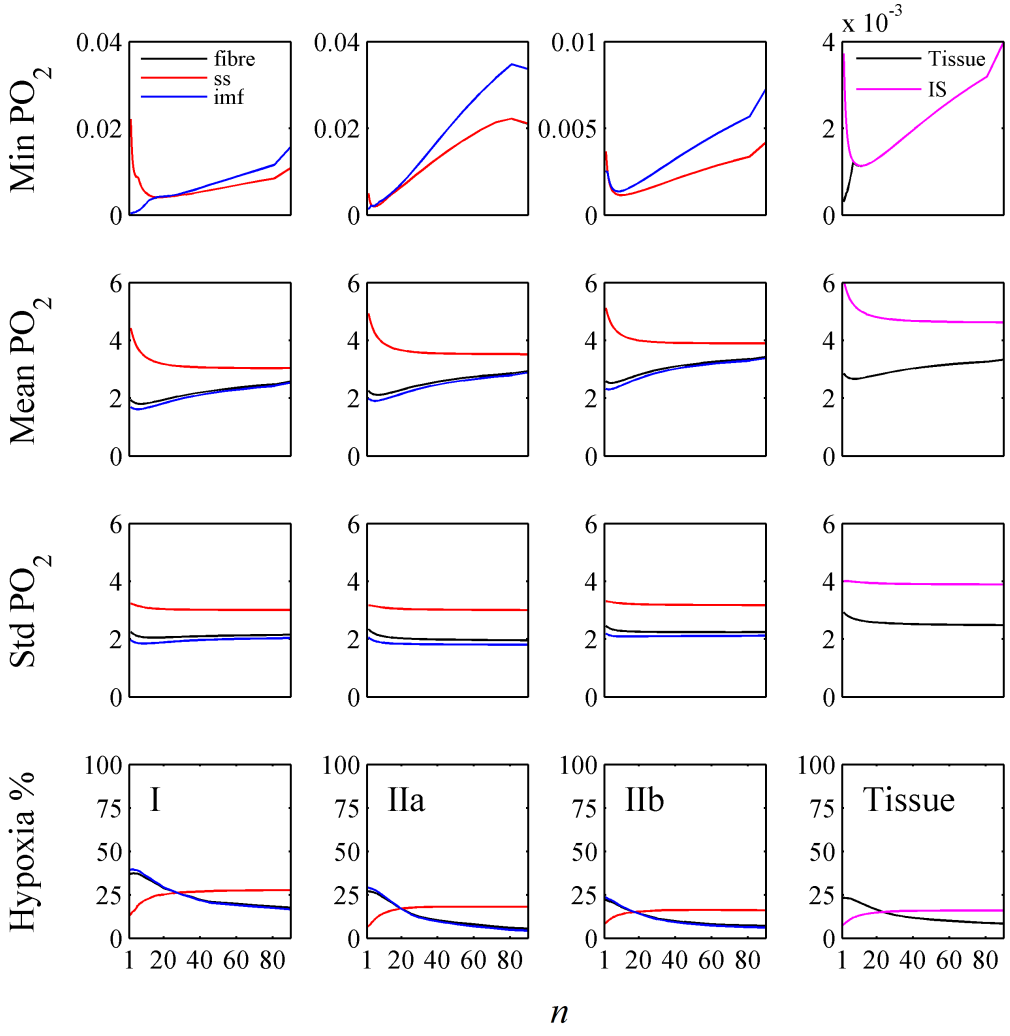

Figure 4.14: Oxygen profile statistics for the H2 geometry with uniform diffusion parameters. Oxygen tension is in mmHg units unless otherwise indicated. In this geometry, the spatial distribution of fibre types is *real* with an areal composition of 10:42:48. Results for each fibre type are presented columnwise (see bottom row). n denotes the subsarcolemmal–to–intermyofibrillar uptake ratio (see Eq. (4.7)).

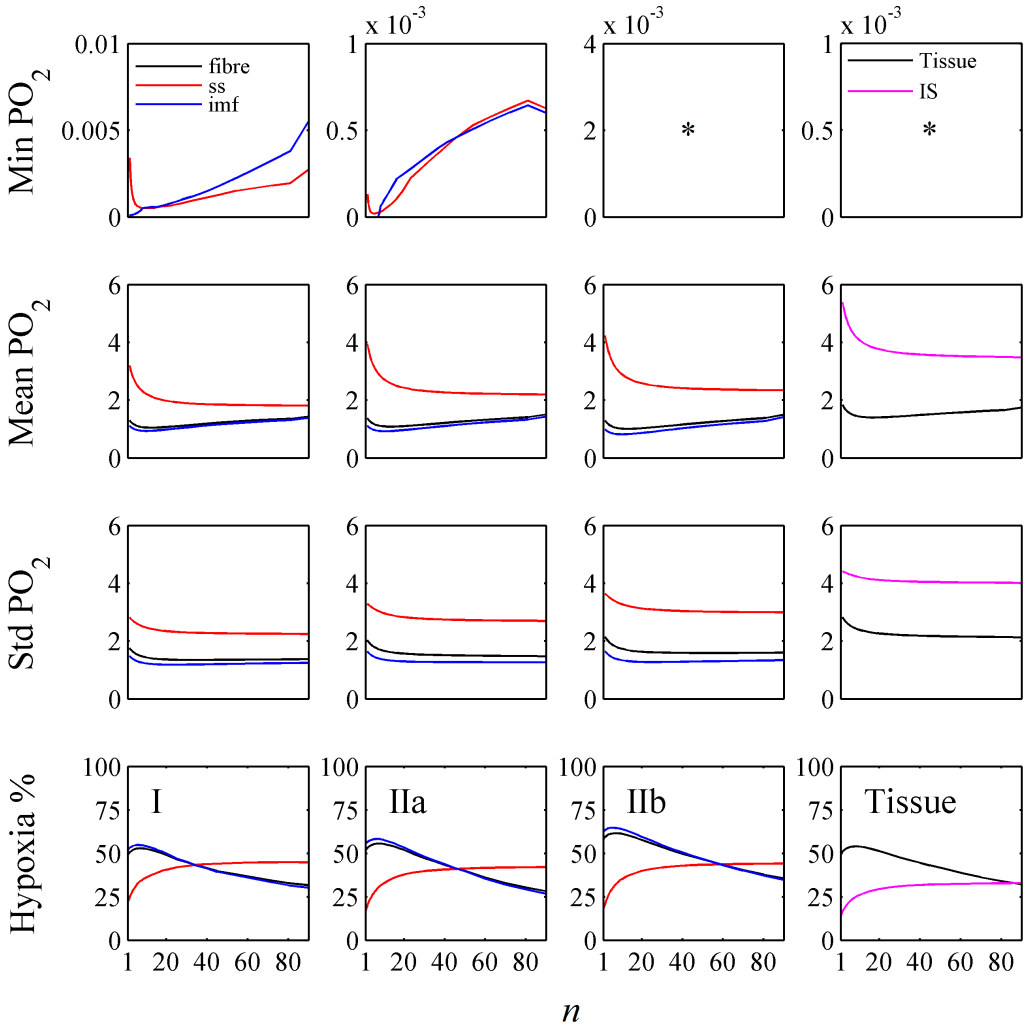

Figure 4.15: Oxygen profile statistics for the H2 geometry with non-uniform diffusion parameters. Oxygen tension is in mmHg units unless otherwise indicated. See caption of Fig. 4.14 for more details about the H2 geometry. n denotes the subsarcolemmal–to–intermyofibrillar uptake ratio (see Eq. (4.7)). $*$ = results vary at scales smaller than 10^{-6}.

numerical error, the minimum PO_2 value in tissue, individual fibres, and intermyofibrillar zones typically drops during initial subsarcolemmal aggregation of mitochondria until it reaches a point beyond which it increases (top row in Figs. 4.8–4.15). In certain cases, however, the improvement in tissue and/or fibre minimum PO_2 is monotonic (fibre Type I in Fig. 4.8; fibre Type IIa and tissue in Fig. 4.10; fibre Type IIa, IIb and tissue in Fig. 4.11; all fibres and tissue in Fig. 4.12; fibre Type I in Fig. 4.13; fibre Type I, IIa and tissue in Fig. 4.14; fibre Type I in Fig. 4.15). A similar trend is also generally observed in interstitial spaces. In contrast, the minimum PO_2 in the subsarcolemmal zone is monotonically decreasing for modest clustering of subsarcolemmal mitochondria, except for the H1 geometry case. In addition, in all cases, the minimum PO_2 for the whole fibre is closely approximated by the minimum PO_2 of the intermyofibrillar zone.

Furthermore, in all geometries and for all fibre types, the presence of heterogeneous diffusion parameters (O_2 diffusion coefficient and solubility) leads to a drop in the minimum value of PO_2 (first row in Figs. 4.8–4.15), with the extent of this drop varying with geometry and fibre type.

4.9.1.2 Mean PO_2

The mean PO_2 generally decreases monotonically in all subsarcolemmal zones and interstitial spaces as mitochondrial clustering increases (see red and magenta curves in the second row of Figs. 4.8–4.14). In particular, the extent of this decline is sensitive to the tissue geometry (e.g. compare Fig. 4.8 with 4.10), the fibre type (e.g. compare fibre Type I with IIb in Figs. 4.13 and 4.15), and the uniformity of diffusion parameters (e.g. compare fibre Type IIb in Fig. 4.8 with 4.9 and Fig. 4.12 with 4.13). Nonetheless, mean PO_2 in the subsarcolemmal zone is markedly greater than that of the fibre and the intermyofibrillar zone for all mitochondrial clustering levels. In particular, extreme mitochondrial aggregation near the sarcolemma (i.e. all mitochondria are effectively in the ss zone when $n \geq 80$) extensively improves the mean O_2 levels available to individual mitochondria in overall tissue and all fibre types (compare the mean subsarcolemmal PO_2 at $n = 80$ with that of the intermyofibrillar zone at $n = 1$ in Figs. 4.8–4.15).

The mean PO_2 value in tissue, individual fibres and intermyofibrillar zones is generally observed to vary with increasing the heterogeneity in mitochondrial distribution, although not as extensively as the minimum PO_2. This change in fibre and

	Mean tissue PO_2, mmHg		Coefficient of variation, %	
Geometry	**Uniform**	**non-uniform**	**VP area**	**Fibre area**
SU	2.502	1.398	0	0
SN	2.502	1.475	25.0	49.7
H1	3.095	1.892	26.6	45.2
H2	2.847	1.838	33.7	48.1

Table 4.2: Predicted mean tissue PO_2, in the absence of mitochondrial clustering (i.e. $n = 1$) and the presence of uniform and non-uniform diffusion parameters. We also estimated variability in the areas of Voronoi polygons and fibres for all considered geometries. The overall demand for O_2 is 2×10^{-3}ml O_2/ml·s, reflecting maximal tissue capacity. Coefficient of variation = (standard deviation/mean) $\times$ 100.

intermyofibrillar mean PO_2 is modest for some geometries and non-uniform diffusion parameters (Figs. 4.8–4.11, 4.13 and 4.15), and potentially non-existent in some fibre types (e.g. Type I and IIa in Fig. 4.9), but more prominent in other geometries and fibre types (e.g. Figs. 4.12 and 4.14). In detail, the mean PO_2 may drop during initial mitochondrial aggregation beneath the sarcolemma for certain geometries (e.g. tissue in Figs. 4.8, 4.9, 4.11, 4.13, 4.14 and 4.15) and for the intermyofibrillar zone of certain fibre types but not others (e.g. compare fibre Type I with IIb in Figs. 4.10 and 4.12). In addition, the relation between mean PO_2 values in different fibre types appears to vary with varying the geometry. For example, the average PO_2 value follows the relation IIb $\geq$ IIa $\geq$ I in the SU geometry, I $\geq$ IIa $\geq$ IIb in the SN and H2 geometries, and IIa $\geq$ IIb $\geq$ I in the H1 geometry.

We also find that in all geometries and for all fibre types, the presence of heterogeneous diffusion parameters (O_2 diffusion coefficient and solubility) leads to a drop in mean PO_2 values with and without mitochondrial clustering (Table 4.2; compare Fig. 4.8 with 4.9, Fig. 4.10 with 4.11, Fig. 4.12 with 4.13, and Fig. 4.14 with 4.15). The extent of this drop is also observed to vary with the geometry and the fibre type. In addition, despite increased capillary and fibre heterogeneities in the SN, H1 and H2 geometries, mean tissue PO_2 is either preserved or improved (e.g. see Table 4.2).

4.9.1.3 Standard deviation of PO_2

The standard deviation of PO_2 decreases steadily, to a limited extent, with increasing mitochondrial clustering in all tissue compartments (third row in Figs. 4.8-4.15). This trend remains the same for both uniform and non-uniform diffusion parameters, with

generally larger values for latter.

4.9.1.4 Hypoxic tissue fraction

The fractional area of tissue, fibre, and intermyofibrillar zone that is hypoxic generally drops with more mitochondrial clustering, except for the SU and H2 cases under conditions of non-uniform diffusion parameters (fourth row in Figs. 4.8-4.15). In particular, the extent and sharpness of this drop are found to vary with geometry and fibre type. In contrast, an increasing level of hypoxia is observed in interstitial spaces and the subsarcolemmal zone, with extensive changes observed during initial clustering. Additionally, in all cases, the addition of heterogeneous diffusion parameters increases hypoxia dramatically.

Furthermore, for modest mitochondrial clustering, we observe a sensitivity in the hypoxic fraction to the details of tissue geometry, fibre type and diffusion parameters. For example, while the hypoxic levels decrease in tissue and all fibre types (including the intermyofibrillar zone) in the H1 geometry under uniform diffusion (Fig. 4.12), they increase in the same compartments when diffusion is non-uniform (Fig. 4.13). In addition, when diffusion is non-uniform for the SN case (Fig. 4.11), hypoxia increases in tissue and fibre Type IIb (fibre and intermyofibrillar zone) but remains unchanged in fibre Types I and IIa . Similarly, for the H2 case (Fig. 4.14), hypoxia is reduced in fibre Type IIb yet it slightly increases in fibre Types I and IIa.

Extreme mitochondrial clustering typically ameliorates fibre and tissue hypoxia (e.g. Figs. 4.9, 4.10, 4.12–4.15), though in a few cases we note no change and even a detrimental effect for certain fibres (e.g. fibre Type IIb in 4.8 and fibre Type I in 4.11). In contrast, the level of hypoxia in the overall tissue and all fibre cores generally decreases under such extreme mitochondrial clustering. However, the details of this latter improvement are sensitive to tissue geometry, fibre types, and diffusion parameters (e.g. compare fibre Type IIb in Fig. 4.8 to that in Fig. 4.9; compare fibre Type I in Fig. 4.12 to that in Fig. 4.14).

4.9.2 Capillary supply regions

The results from our computations of trapping regions are presented in Figs. 4.16-4.17. These are based on an analysis of the statistical measures we detailed in previous chapters. Refer to Table 2.1 in Chapter 2 for a definition of these measures.

4.9.2.1 Difference in supply domain areas

Recall that the *normalised mean of difference* (μ_Δ) provides a measure for the degree of failure of Voronoi polygons (VP) to cover comparable areas to those of trapping regions (TR). Besides being affected by the distribution of fibre size, fibre type, and capillaries, this measure is observed to correlate with heterogeneities in intracellular mitochondrial distribution and diffusion parameters (O_2 diffusivity and solubility).

For all geometries, μ_Δ increases extensively with increased mitochondrial clustering, with the H1 and H2 geometries showing the highest values. In the presence of further intracellular heterogeneities, such as fibre–specific O_2 diffusivity and solubility, mitochondrial clustering has a lesser effect on μ_Δ, with the H1 and H2 geometries showing an initial decline in the value of μ_Δ.

In addition, the normalised standard deviation of difference (σ_Δ) is observed to follow similar trends to those of μ_Δ. Recalling that σ_Δ describes the difference between the spread of VP areas and that of TR, this illustrates that the spread of Voronoi polygon areas begins to differ from that of trapping regions as mitochondrial clustering is increased. Interestingly, additional non-uniformities in the diffusive characteristics of muscle fibres markedly reduce the spread of these areas.

4.9.2.2 Overlap of supply domains

Recall that the *normalised mean of intersection* ($\mu_\cap$) describes how well VP capture the functional capillary supply of TR, with values close to unity characterising a close match. $\mu_\cap$ is found to decrease extensively with increased proportion of subsarcolemmal mitochondria, with a steeper decay for the H1 and H2 geometries. However, mitochondrial clustering is observed to have a lesser effect on $\mu_\cap$ in the presence of non-uniform diffusive characteristics, with the H1 and H2 geometries showing a slight increase in $\mu_\cap$ for limited clustering.

Recalling that the *normalised standard deviation of intersection* ($\sigma_\cap$) extends the above correlations by considering the spread of VP areas that overlap with TR, we observe a somewhat constant spread for all mitochondrial clustering levels (except for the SU geometry case).

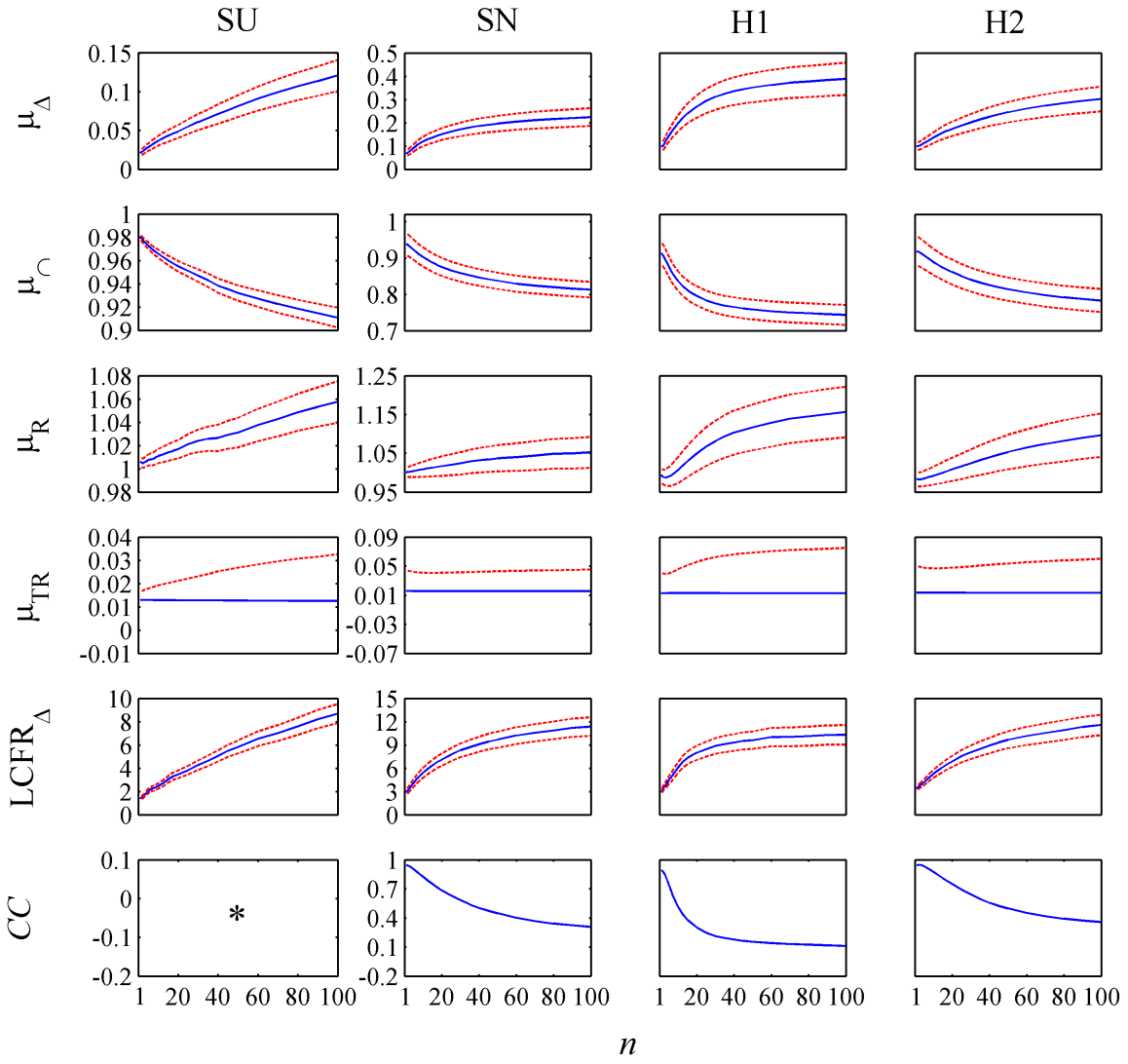

Figure 4.16: Domain variability for uniform diffusion parameters. The statistical differences between VP and TR are shown as a function of the subsarcolemmal–to–intermyofibrillar uptake ratio (i.e. n). Values for the ordinate are in *solid blue* colour. *Dashed red* colour denotes mean $\pm$ normalised standard error (e.g. $\mu_\Delta \pm \sigma_\Delta/\sqrt{M}$), where M is the number of Voronoi polygons in the sampled distribution. We recognise that when $\mu_{TR} - \sigma_{TR}/\sqrt{M} < 0$ the distribution is skewed, hence we do not present these curves in our results. The labels for the axes in H1 and H2 are inherited from SN. * = not applicable as $\mathcal{CC}$ is undefined for the SU geometry (division by $\sigma_{VP} = 0$). μ_{TR} = mean of TR areas. For a definition of the other measures refer to Table 2.1 and Eqs. (2.3) and (3.15).

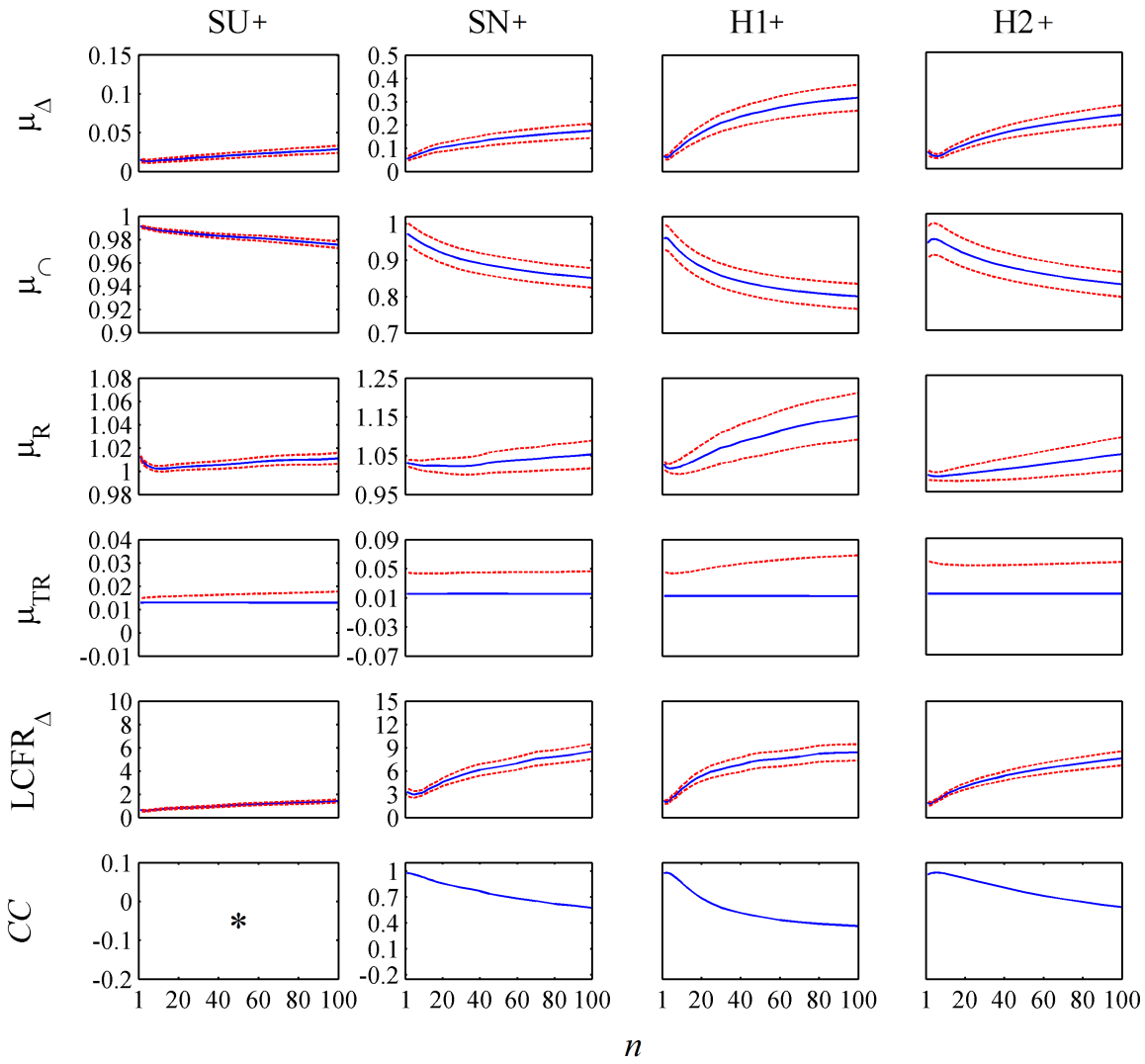

Figure 4.17: Domain variability for non-uniform diffusion parameters. The statistical differences between VP and TR are shown as a function of the subsarcolemmal–to–intermyofibrillar uptake ratio (i.e. n). A '+' sign signifies results for a parameter regime based on heterogeneous solubility and diffusivity. Refer to Fig. 4.16 for more details.

4.9.2.3 Ratio of supply domain areas

Similar to $\mu_{\cap}$, the *mean ratio* (μ_R) describes how well Voronoi polygons capture the functional capillary supply of trapping regions. Mean ratio values further infer whether, on average, a VP is over- ($\mu_R > 1$) or underestimating ($\mu_R < 1$) the functional capillary supply. For all geometries, VP overestimates TR on average, with increasing values and spread of overestimates as mitochondrial clustering is increased. However, these overestimates become weaker in the presence of non-uniform fibre diffusivity and solubility.

4.9.2.4 Trapping region areas

Regardless of the degree of mitochondrial clustering, the average area of trapping regions (μ_{TR}) is maintained. Nonetheless, the spread of the distribution of TR areas increases with higher levels of clustering. Although the same overall trend is maintained, the presence of non-uniform fibre diffusivity and solubility is observed to have a homogenising effect on TR areas (reduced spread), most notably in the SU geometry.

4.9.2.5 Difference in local capillary-to-fibre ratio

LCFR represents the number of capillary supply equivalents at maximum capacity. Hence, the *mean of normalised difference of the LCFR* indices, $LCFR_{\Delta}$, provides a measure of the degree of failure of VP–based capillary supply indices. We note here that $LCFR_{\Delta}$, along with the spread in its distribution, is observed to have the same trends as those of μ_{Δ} and σ_{Δ}.

4.9.2.6 Correlation coefficient of supply areas

The area correlation coefficient ($\mathcal{CC}$) is a measure of the linear dependence between the VP and TR areas (and is given by their covariance divided by both of their standard deviations). Except for the SU geometry where $\mathcal{CC}$ is not applicable, Figs. 4.16–4.17 demonstrate a monotonic decrease in the degree of correlation between the areas of VP and TR for increased mitochondrial clustering. This trend is maintained in the presence of heterogeneous fibre diffusivity and solubility, however the VP-TR correlation is generally improved for each level of clustering.

4.10 Discussion

There is still no theoretical consensus as to how mitochondrial clustering would influence capillary O_2 transport to muscle tissues. In particular, it is still unclear why the mitochondrial population in the subsarcolemmal zone exhibits a relatively increased volume density in respiring skeletal muscles [35, 59]. Currently, it is speculated that the short diffusion distances to capillaries from subsarcolemmal mitochondria would enhance the availability of O_2 for their respiration [115, 143], hence offering a metabolic advantage for aerobic muscle respiration when local O_2 supply is limiting [35, 143, 167]. Nevertheless, the majority of theoretical models of O_2 transport to muscles do not consider mitochondrial clustering, and the majority of those which do predict only modest changes to O_2 levels following mitochondrial clustering. In contrast, recent theoretical findings from single–fibre models have emphasised the role of intracellular O_2 gradients in dictating mitochondrial shifts [80, 142–144]. In particular, the functional advantage of mitochondrial clustering might be better manifested in conditions where O_2 supply is limited (e.g. hypoxia). Hence, a re-assessment of the influence of mitochondrial clustering on O_2 transport to tissue is required, at least in the case of hypoxia.

To this end, we have developed a mathematical model coupled with a geometrical framework based on intracellular geometries that are faithful to histological observations of spatially heterogeneous O_2 uptake layers as dictated by mitochondrial re-distribution toward the fibre periphery. Within this framework we can assess how the degree of mitochondrial aggregation near the sarcolemma, expressed in terms of relative uptake rates, may affect *intra*cellular O_2 levels and spatial distribution. Given this model is based on a histologic distribution of muscle fibre populations (possibly metabolically distinct) with embedded capillaries, we can further explore how such microscale re-arrangements in O_2 consumption may affect *inter*cellular as well as global tissue oxygenation. All previous modelling attempts were based on a single fibre with either a single central capillary or a number of concentric peripheral capillaries supplying the central fibre. Therefore, to our knowledge, this is the first attempt to explore O_2 transport in multi-capillary, multi-fibre system with heterogeneous intracellular demand. Given this framework is an extension of that of Chapter 3, a major aim is also to explore how mitochondrial clustering may affect the biophysical supply regions (trapping regions). In particular, the appropriateness and effectiveness of using capillary domains (Voronoi polygons) to represent such regions can be additionally investigated, giving an assessment of when and where they may

accurately characterise local capillary supply.

Minimum PO_2

Our results indicate that the minimum PO_2 is generally sensitive to the level of mitochondrial clustering, tissue geometry, fibre type and diffusion parameters, though we do not observe a clear trend in tissue or fibres for modest clustering. Interestingly, our results also reveal that, even under modest mitochondrial clustering, minimum PO_2 does not necessarily follow the traditional monotonic decay from the sarcolemma to the fibre core (e.g. see fibre Type I in Fig. 4.8, fibre Type IIb in Fig. 4.10, fibre Type I in Fig. 4.11, and fibre Types I, IIa, IIb in Fig. 4.12). Moreover, in contrast to modest clustering, the minimum amount of O_2 available to mitochondria is found to be markedly higher under extreme mitochondrial clustering. This finding is consistent with the first modelling study of O_2 transport in single muscle fibres with extensive mitochondrial clustering [128], though our predicted PO_2 improvement is not as extensive due to the presence of tissue, fibre and capillary heterogeneities.

Mean PO_2

Mean O_2 levels are found to be higher in the subsarcolemmal zone than in the fibre core owing to the proximity to O_2 sources, regardless of the degree of mitochondrial clustering. A modest mitochondrial redistribution towards the sarcolemma induces a differential influence on the mean amount of O_2 available for mitochondrial consumption. The details of such influence are observed to be sensitive to tissue geometry, fibre type and diffusion parameters. These findings suggest that if O_2 diffusion under conditions of limited supply (e.g. ambient hypoxia, hypoxaemia or tissue hypoxia) is a major factor in shaping the intracellular organisation of mitochondria, then we are unlikely to observe, *in vivo*, modest mitochondrial clustering within tissues or fibre types where a deterioration in O_2 levels is predicted. This may explain why glycolytic fibres in some mammalian mixed muscles (e.g. Type IIb) exhibit a uniform distribution of mitochondria with no mitochondrial clustering [193].

In contrast, extreme mitochondrial aggregation near the sarcolemma is generally found to improve the mean PO_2 available to individual mitochondria in all fibre types, and hence in the overall tissue. In addition, agreeing with previous experiments [176], such clustering generally improves mean PO_2 in the fibre core, with significant alleviation of hypoxia due to the extreme reduction of maximal O_2 uptake ($\mathcal{M}_0$)

in the fibre core as dictated by the weighted average of subcompartmental uptakes. Since a reduced maximal uptake will lead to a depressed O_2 consumption rate (MO_2), this suggests that an unconstrained clustering of subsarcolemmal mitochondria may ultimately suppress aerobic respiration (i.e. oxidative metabolism) within the fibre core, even when mean O_2 levels are improved. Furthermore, the predicted mean PO_2 for tissue and individual fibres exhibit a sensitivity to tissue geometry and fibre type (e.g. compare Fig. 4.11 with Fig. 4.12).

Hypoxic Fraction

Recall that the hypoxic fraction is obtained from dividing the hypoxic volume within a compartment (i.e. volume with $PO_2 < 0.5$ mmHg) by the total volume of this compartment. Hence, relatively low and high values of this index characterise improved and deteriorating O_2 levels, respectively.

In the presence of modest mitochondrial clustering, the fibre hypoxic fraction is observed to be sensitive to the tissue geometry, the distribution of fibre types and the diffusion parameters. In particular, such low levels of mitochondrial clustering may lead to improved, unchanged, and/or deteriorating levels of hypoxia in different fibre types and tissues. Interestingly, these observations are not captured by previous models of O_2 transport exploring mitochondrial clustering in single fibres [77, 95, 128, 133].

In addition, the observation that extreme mitochondrial clustering can have a detrimental effect for certain fibres suggests that such levels of clustering may sometimes be disadvantageous to muscle fibres. Nonetheless, such clustering is predicted to always lead to a reduced overall tissue hypoxia. Similarly, a general alleviation of hypoxia in fibre cores is predicted, though, as mentioned above, mitochondria are effectively absent under such extreme subsarcolemmal clustering, and there is sensitivity to geometry, fibre type and diffusion parameters. Also note that, in contrast to these observations, previous single fibre models always predict a general elevation, however modest, of intracellular PO_2 upon clustering [77, 95, 128, 142–144], suggesting that global tissue details (e.g. tissue geometry, and distributions of fibre size, type and diffusion parameters) are important for predicting intracellular O_2 levels. This, in turn, suggests that predictions based on models of O_2 transport in muscle tissue with uniformly distributed mitochondria may need a re-assessment (e.g. [13, 125]).

Testing Hypotheses

Generally, O_2 levels near the sarcolemma drop sharply with mitochondrial clustering, with a marked increase in hypoxia. Assuming mitochondrial death rate is spatially proportional to very low PO_2 (hypoxia) and their biogenesis is spatially homogeneous, as suggested by Pathi and colleagues [142], more mitochondrial loss near the sarcolemma and lesser death rates in the fibre core are to be expected as clustering is increased. This is of course not an indefinite scenario since the preservation of mitochondrial density in muscle fibres would sooner or later turn the direction of this death–birth around, ultimately balancing the spatial 'gradients' of hypoxia within myocytes. This suggests that a balance between outer and inner hypoxia (fibre core vs. periphery) should dictate an intermediate mitochondrial distribution. Indeed, exercise under hypoxic ambient conditions has been shown to increase mitochondrial density in both the subsarcolemmal and intermyofibrillar zones [36], with a preferential mitochondrial biogenesis underneath the sarcolemma for repeated endurance training [35]. For example, bar–headed geese, high-altitude hypoxia–adapted birds, have been demonstrated to have evolved for exercise in hypoxic conditions by enhancing both their aerobic capacity and local O_2 supply to recruited fibres, thus sustaining high metabolic rates for flight in severe ambient hypoxia [167]. This enhancement in O_2 supply was partly achieved by redistributing mitochondrial toward the subsarcolemmal zone. In addition, studies of concurrent endurance and strength exercise regiments have revealed that mitochondrial populations undergo differential changes throughout training, with a linear elevation in the mitochondrial density of the intermyofibrillar zone throughout training and a late, though preferential, increase in subsarcolemmal mitochondrial density [22].

Sensitivity & Implications

As discussed earlier, we found that in some mixed muscle cross–sections mitochondrial clustering improves O_2 levels and ameliorates hypoxia in some fibre types while in other sections it has the opposite effect. This finding might explain why in rat EDL muscle all mixed fibres exhibit mitochondrial clustering whereas in human EDL only Type I and IIa show clustering [193]. Given O_2 supply to muscle fibres is affected by fibre size and type distributions (see Chapter 3) and capillary distribution (see Chapter 2), this suggests that differences in the anatomical design of EDL across species may alter the expected trend of O_2 supply improvements following mitochondrial clustering.

The above observations alert that care must be taken when making physiological conclusions from theoretical models of O_2 transport in single muscle fibres. While such models give insight into why the redistribution of mitochondria towards the sarcolemma and closer to capillaries should improve O_2 transport, their limited geometrical detail may ultimately lead to exaggerated generalities. Indeed, single–fibre models assume that (1) supply of neighbouring capillaries is restricted to the fibre in question, (2) O_2 is not exchanged between nearby fibres (potentially of different oxidative capacities), (3) mitochondrial clustering underneath the sarcolemma does not influence the O_2 consumption kinetics of neighbouring fibres, (4) fibre type is uniform, (5) fibre size is uniform, and (6) capillary distribution is spatially symmetric. Given these assumptions, there is no way of predicting that mitochondrial clustering may become detrimental to some fibre types in mixed muscles, nor is there a way to assess why clustering differentially affects different muscles.

Voronoi Polygons

Aggregation of mitochondria underneath the sarcolemma is observed to generally lead to more complex O_2 diffusion paths, as exemplified by trapping regions, which in turn leads to larger deviations of trapping regions from Voronoi polygons. While such reductions in the effectiveness of Voronoi polygons accompany increasing levels of mitochondrial clustering, the approximation of VP remains appropriate for moderately low subsarcolemmal–to–intermyofibrillar uptake ratios (a proxy for mitochondrial clustering). Interestingly, the presence of heterogeneous diffusion improves this approximation markedly, even for high levels of clustering. Since the distribution of Voronoi polygons reflects the heterogeneity in anatomical supply, this observation suggests that the histological distribution of capillaries may be an important factor in regulating both the *inter*- and *intra*cellular heterogeneities of O_2 diffusivity to ensure the tissue is supplied by nearest capillaries, which supports previous experimental observations [95].

Theoretical assessments of oxygenation in skeletal muscles may benefit from estimating PO_2 in each fibre type to explore how local O_2 supply balances the underlying spatially–heterogeneous demand. In particular, clustering is observed to improve mean PO_2 markedly in some fibre types and less so in others. Hence, not only do models neglecting clustering risk underestimating global O_2 levels significantly in exercising conditions, during exposure to hypoxic conditions or in hypoxaemia, but they may also miss the dynamic balance between heterogeneous fibre demand

and local O_2 transport, though for typical physiological ranges ($n \leq 20$) the VP-TR difference between biophysical models with clustered and unclustered mitochondrial distributions is relatively small (Figs. 4.16–4.17). Nonetheless, the observed margin of error from neglecting clustering may lead to inaccurate correlations or trends concerning O_2 and its supply and demand [13, 125], especially if extreme mitochondrial clustering is present. In particular, based on derivative indices of Voronoi polygons, recent experiments found no significant correlation between fibre oxidative capacity (i.e. mitochondrial content) and capillary supply [193], though mitochondrial clustering was observed. Below we propose a derivative measure of VP that accounts for mitochondrial clustering.

Mitochondrial Density of Voronoi Polygons

Given the majority of striated muscles demonstrate at most moderate degrees of mitochondrial clustering in the subsarcolemma, Voronoi polygons may still accurately assess capillary supply under such circumstances. However, care should be taken as to account for the density (or count) of mitochondria within each Voronoi polygon if extreme clustering is present in the subsarcolemmal zone. This can be achieved by incorporating the mitochondrial density into measures of local capillary supply. An initial approach would be to estimate the mitochondrial density of a Voronoi polygon using

$$\rho_k^{\mathrm{mt}} = \frac{1}{A(V_k)} \sum_{j=1}^{N_{\mathrm{fibre}}} \sum_{n=1}^{N_{\mathrm{zone}}^j} \rho_{j_n}^{\mathrm{mt}} A(\Omega_{j_n} \cap V_k), \tag{4.13}$$

where $A(\cdot)$ is the planar area measure, V_k is the k^{th} Voronoi polygon, Ω_{j_n} is the n^{th} zone of the j^{th} muscle fibre overlapping Voronoi polygon k, N_{fibre} is the number of fibres overlapping the k^{th} Voronoi polygon, N_{zone}^j is the number of mitochondrial zones of fibre j that overlap the k^{th} Voronoi polygon, ρ_k^{mt} is the mitochondrial density of the k^{th} Voronoi polygon, and $\rho_{j_n}^{\mathrm{mt}}$ is the mitochondrial density of the n^{th} mitochondrial zone of fibre j. Despite its simplicity, this measure still retains the heterogeneities of local capillary supply, local fibre demand, and intracellular demand. Hence, correlating this measure with Voronoi polygon areas may potentially reveal

when local O_2 supply and cellular demand are balanced, even in the presence of intracellular consumption heterogeneities that are associated with mitochondrial spatial non-uniformity.

4.11 Conclusions

While the Voronoi polygon approximation to trapping regions depends on the heterogeneity of intracellular composition of muscle fibres, it is nonetheless representative for maximal sustainable aerobic capacity given the absence of extensive mitochondrial clustering. Therefore, measures of muscle capillary supply capacity based on Voronoi polygons may be reasonably used for mixed muscle samples with, at most, moderate levels of mitochondrial clustering in the subsarcolemmal zone. However, further increased re-distribution of mitochondria towards the sarcolemma will eventually lower the accuracy of Voronoi polygons, although not as extensively when the tissue diffusivity is heterogeneous. Nonetheless, in general, more sophisticated measures of capillary supply capacity should be used to study structural or functional dysregulation in striated muscle tissues, and flux trapping regions may provide a more robust representation of capillary supply regions. In addition, the improvement in the VP-TR approximation for heterogeneous diffusion parameters suggests tissue regulation of the intracellular substructure (e.g. lipid content) to ensure fibres are supplied by nearest capillaries.

Moreover, we found that the minimum subsarcolemmal PO_2 is not always greater than the minimum PO_2 in the fibre core, implying the decay in O_2 tension is not always monotonic from the sarcolemma to the fibre centre, which is in contrast to the traditional view of tissue oxygenation based on the Krogh cylinder geometry. In addition, we have predicted that diffusional O_2 transport (e.g. O_2 levels and kinetics) is sensitive to the level of intracellular heterogeneities in O_2 consumption (e.g. mitochondrial clustering) and the spatial uniformity of diffusion. Extreme clustering shows a general enhancement in overall tissue oxygenation, though no clear trend other than sensitivity is found for individual fibre types. In particular, the previous models of O_2 transport that do not consider mitochondrial clustering, when extreme, may be exaggerating the levels of hypoxia in mixed muscle tissues. Nonetheless, our predicted level of such improvements may be diminished in certain fibre types within the same muscle, with a potential for a complete deterioration of fibre O_2 levels, implying that these previous models may also potentially underestimate hypoxia in

some fibre types.

Similarly, modest clustering elevates hypoxia in some fibre types, but not in others, with details sensitive to fibre distribution, tissue geometry and diffusion parameters. Nonetheless, these observation offer examples of where increasing clustering does not improve oxygenation, which is in contrast to the long–held reasoning that mitochondrial clustering should improve oxygenation. Hence, a systematic re-appraisal of such reasoning is required. In particular, assessing the potential variations in O_2 levels and kinetics in mixed muscles in response to various adaptations or pathologies may benefit from theoretical models of O_2 transport to tissue that account for the observed inter- and intracellular heterogeneities in structural and functional characteristics. Such an integrative approach may refine previously generalised trends of O_2 enhancement and potentially explain why clustering is observed differentially across different muscles and fibre types.

Moreover, we remark here that for such theoretical investigations to be 'accurate' higher resolution data and parameters are required to better understand how supply and demand are balanced at fibre scales. Although the geometry at such small scales is available to some extent, the physiological literature still reports parameter values that are averaged over much larger scales than the intracellular one. Therefore, to understand the dynamic link between local supply and fibre demand more refined experimental procedures and high resolution parameters and histological analyses will be needed to advance the mathematical modelling front of O_2 transport.

Chapter 5

Applications

5.1 Statement of contribution

The image analysis, mathematical modelling, and modelling predictions detailed in this chapter were performed by Abdullah A. Alshammari and contributed to two interdisciplinary studies [84, 86]. We and our experimental collaborators interpreted these predictions and correlated them to certain aspects of their experimental measurements. Ultimately, we worked on manuscript writing to present these contributions in two co-authored papers: (1) a submitted paper to BBA General Subjects [86], and (2) a planned paper [84].

5.2 Summary

The cardiac muscle has a high demand for energy provision to meet its unremitting fibre contractions. In healthy myocardium, this energy is predominantly ($\sim 70\%$) derived from oxidation of free fatty acids (FFAs), with a lesser contribution from glucose [173]. The complete oxidation of a single lipid molecule (e.g. palmitate) ultimately yields ~ 106 ATP molecules, whereas glucose oxidation merely yields $\sim 30-36$ ATP molecules. However, glucose oxidation is much more efficient in terms of the amount of O_2 consumed to produce a single ATP [122], especially in the case of limiting local O_2 availability. In fact, metabolic substrate utilisation is a major determinant for the efficiency of muscular O_2 use. This highlights that capillary supply of oxygenated blood is important for the optimisation of myocardial ATP production, as substrate selection by the working heart may be dictated by the availability of O_2. This has implications on cardiac function and performance during increased activity and in

pathologies involving impaired O_2 transport and dysfunctional metabolism.

In this chapter, two examples are given to illustrate the important role that capillary O_2 supply may play in maintaining cardiac function and performance. In particular, we demonstrate how our O_2 transport models can be used to support hypothesis testing by examining how functional capillary supply of O_2 and myocardial demand are balanced, and correlating this balance with experimental observations of myocardial metabolism and mechanical performance.

More generally, this chapter illustrates how the models we have developed can be directly explored in experimental studies. To facilitate this, we have also designed a GUI interface to our models, allowing their use more readily by our physiological collaborators (see Fig. 5.1).

5.3 Mathematical methods

To better understand how experimental interventions and their subsequent metabolic modifications may affect tissue O_2 levels, we employ our previous modelling frameworks of O_2 transport in 2D tissue cross–sections, using digital images of tissue biopsies that are stained to capture histological details.

5.3.1 Mathematical model

Predictions of the spatial distribution of PO_2 are generated using a 2D circular region within a cross–section of heart muscle tissue. This is modelled as a homogeneous tissue composition, with an array of capillaries of circular cross–section diffusively supplying O_2 to the surrounding tissue with Michaelis–Menten consumption kinetics and additional facilitated diffusion via a haem-protein carrier, myoglobin (Mb).

At each capillary–tissue interface, the flux is proportional to the difference in PO_2 across this wall, whilst at the exterior boundary a no-flux condition is assumed, though sufficiently far into the sample area, the solution is insensitive to the details of this boundary condition. Thus the mathematical model is given by Eqs. (3.7) and (3.10)–(3.13) of Chapter 3, with uniform biophysical parameters—there is only one fibre type in the myocardium.

We solve these equations to determine tissue PO_2 using the finite element

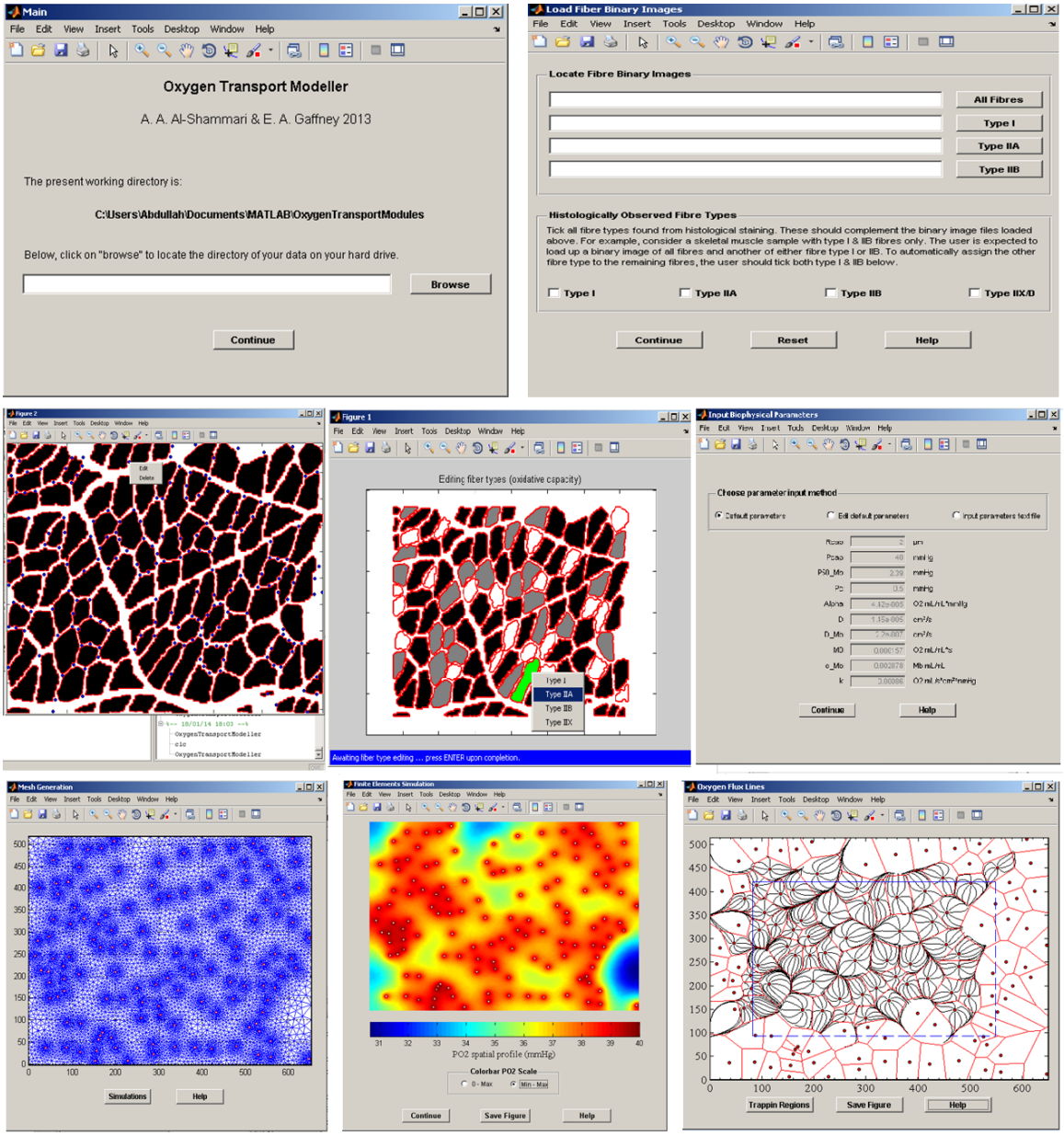

Figure 5.1: Snapshots of a Graphical User Interface we designed in Matlab [130] to facilitate a direct exploration of our O_2 transport models in experimental studies in addition to allowing its use in our physiological collaborator's laboratory. This GUI was designed by Abdullah A. Alshammari in Summer 2013, and is currently maintained by him. In addition, the GUI has been installed and is currently being used in Prof Stuart Egginton's laboratory at the University of Leeds.

method, implemented using Matlab [132] with a nonlinear solver based on Gauss-Newton iteration and adaptive meshing to resolve areas of rapid change in PO_2 (see Appendices A, B).

In addition, we assess the local supply of O_2 by estimating the supply area of capillaries via the Voronoi tessellation of digitised images. However, in cases of a capillary rarefaction, Voronoi polygons are replaced with biophysical supply regions (i.e. trapping regions), and can be directly calculated for homogeneous tissues, under saturated levels of mitochondrial O_2, using the equation

$$A_i = \frac{k}{\mathcal{M}_0} \oint_{\partial C_i} (p_{\text{cap}} - p)\, ds, \tag{5.1}$$

where A_i denotes the area of the i^{th} trapping region, C_i the boundary of the i^{th} capillary, and ds is the *anti-clockwise* parametrisation element around the capillary and the trapping region. Since the effect of nonlinear O_2 uptake and facilitated diffusion were shown to have a negligible effect on capillary supply regions in Chapter 3, this formula still accurately approximate the area of trapping regions, and this has been explicitly checked. In addition to capturing differences in local capillary supply, the computed supply areas are also used to give an estimate of the local variation in tissue capillary supply between control and experimental groups, hence allowing further assessments of the quality of the aforementioned interventions in improving O_2 supply.

We emphasise that these models were solved on a substantial number of extracted geometries, allowing the determination of statistical significance in the final results, generally emphasising the need to take the time necessary to design in the accommodation of substantial throughput into our modelling pipeline.

5.3.2 Statistical analyses

Data are presented as mean ± standard deviation (SD). Statistical analyses and hypothesis testing are carried out using one-way analysis of variance (ANOVA). Statistically significant differences are indicated in figures and tables using computed P-values of the appropriate statistical test.

5.4 On cardiac changes induced by maternal hypoxia

One of the most common insults to fetal development is associated with *in utero* maternal exposure to hypoxic environments (maternal hypoxia, MH). Although periods of transient tissue hypoxia are important for tissue development [123], particularly within the heart [28], chronic or severe hypoxia can have profound effects on the fetus, and these are dictated by the period during fetal development when hypoxia may occur [187].

For instance, chronic hypoxia *in utero* (CHU) during the second half of rat pregnancy increases the work performed by the heart (e.g. by increasing the developed pressure in the left ventricle) of the developing fetus to improve fetal oxygenation [85]. In particular, the rat fetus has an intact and functioning cardiovascular system by ten days of gestation and is therefore independent of maternal control [171]. During this period the rat heart is subject to significant hypertrophy (increasing cell size) and hyperplasia (increasing cell number) as a consequence of clonal expansion of cells [172] to meet the demands of the growing fetus and the limited supply of O_2 [56]. Surprisingly, previous experiments [85] demonstrate that this hypertrophy results in a decreased capillary density in the hearts of adult offspring despite maintenance of a normal–sized heart, therefore illustrating the impact of decreased global O_2 supply in adult offspring. Given the experimental observation of increased myocardial work following CHU [84], these changes suggest that a mismatch between metabolism and O_2 consumption may result in the developed heart—increased cardiac work coupled with a decreased capillary density indicating a reduction in the potential for diffusive exchange.

Furthermore, given the pivotal role that diffusive exchange for both O_2 and metabolic substrates plays in controlling myocardial metabolism [65, 86], a decreased capillary surface area for O_2 diffusion may favour the metabolism of glucose, over fatty acids, as a metabolic fuel for the myocardium.

To assess the role that capillary supply plays in such scenarios, our collaborators have conducted an experiment to investigate the mechanical and metabolic changes arising from CHU using the perfused 'working' heart of adult rat offspring [84, 85]. This allowed an experimental exploration of the effects of CHU–associated decreased capillary density on working heart metabolism as well as an investigation of the

substrate preference and mechanical performance of the CHU heart.

Metabolism in the CHU heart was found to be greater despite achieving lower cardiac output (less work) [84]. This strongly suggested that CHU may lead to intrinsic inefficiency in the myocardium manifested as mitochondrial inefficiency. Using the fact that the enzymatic activity of citrate synthase (CS), an enzyme catalysing the rate–limiting step in Krebs Cycle (conversion of acetyl-CoA to citrate at mitochondrial cristae), can be used to estimate mitochondrial density [121], our experimental collaborators noted that CHU decreased CS activity by 30% [84]. This implies either decreased mitochondrial density or decreased cristae density associated with individual mitochondria. Together these data raise a paradox: total metabolism and hence mitochondrial function is increased, yet the total mitochondrial metabolising capacity was decreased by CHU.

However, it is not feasible to track O_2 transport in these experiments. Thus we apply our methodologies in a comparative study of normal and CHU hearts, to highlight differences in O_2 supply/consumption and to test the hypothesis that mitochondrial inefficiency and decreased mitochondrial density in larger capillary supply areas compensate each other in maintaining O_2 supply, which is arguably counter–intuitive—it is not clear that reducing mitochondrial efficiency will improve oxygenation. Finally, we will explore the modelling predictions for consequences of this under conditions of hypoxic stress in the CHU heart.

5.4.1 Methods

The biological experiments, including metabolic, mechanical and histological analyses, were carried out by Dr David Hauton during his tenure at the University of Birmingham. Detailed experimental methods can be found elsewhere [83–85].

For the experimental tissue preparations (see Fig 5.1), vessels were quantified by experimental collaborators from digital images (magnification $\times 200$) and capillary locations were digitised by Abdullah A. Alshammari in Matlab [131] via processing the digital images of tissue cross–sections. Capillary densities were subsequently quantified by estimating the number of capillaries in each image.

The tissue sample geometries extracted from histological sections of tissue biopsies were incorporated into our mathematical model by A. A. Alshammari, together

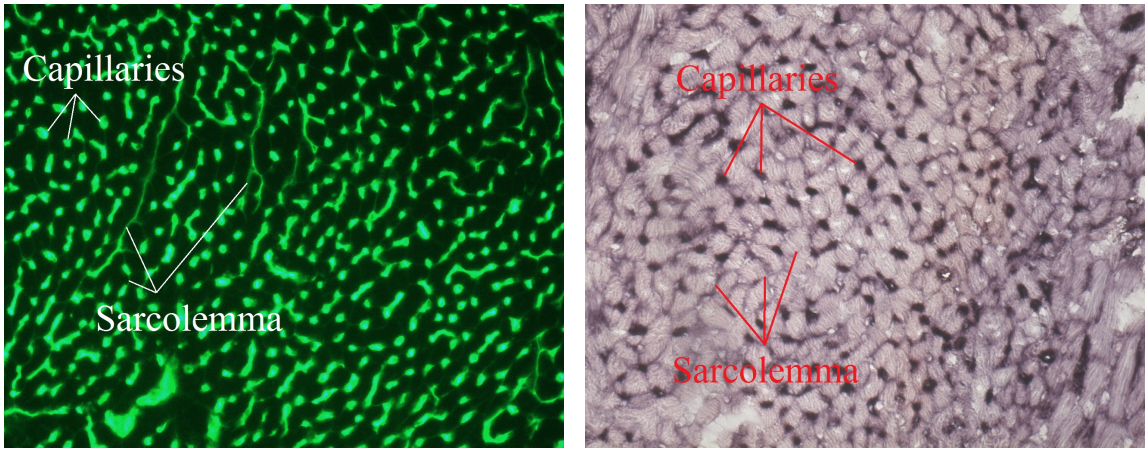

(A) Left ventricle (B) Right ventricle

Figure 5.2: Illustration of histochemical stains for 2D sections from mice myocardial biopsies. (A) A digital image of a left ventricle section after Lectin staining, with fibre boundaries (sarcolemma) and capillaries indicated in the image. (B) A digital image of a right ventricle section after alkalyne phosphotase staining, with capillaries as dark black structures. Sections are 10 μm thick. Prepared from excised samples by Abdullah A. Al-Shammari (November, 2012) in Prof Stuart Egginton's laboratory at the University of Birmingham.

with biophysical parameters that are estimated from a number of experiments (Table 5.1). The distribution of O_2 tension and consumption rate were computed numerically via using the numerical methodologies detailed in Appendix A. Areas of capillary supply regions were calculated using Voronoi tessellations of digitised images.

5.4.2 Results

Following digitisation of images, we solved our model equations for absolute values of O_2 demand that represent both moderate and maximal mitochondrial consumption rates in the myocardium [13]. Here moderate mitochondrial consumption is set at 50% of the maximal mitochondrial consumption and the latter is presented in Table 5.1. Further, two scenarios for relative O_2 demand in CHU hearts were considered in each of these parameter regimes: reduced and equal O_2 demands. The former relative demand was extrapolated from the decreased citrate synthase activity in CHU hearts as representative for decreased mitochondrial density (given the experimentally observed increase in mitochondrial metabolism), whereas the latter represents a hypothetical scenario where CHU hearts would maintain mitochondrial density similar to Control hearts.

Estimates of capillary supply in terms of capillary density and supply regions

Parameter	Symbol	Value	Unit	Refs.
O_2 demand	$\mathcal{M}_0$	3.77×10^{-3}	ml O_2/ml·s	[13]
Mb concentration	c_{Mb}	2.90×10^{-3}	ml O_2/ml	[13]
O_2 solubility	α	4.42×10^{-5}	ml O_2/ml·mmHg	[13]
O_2 diffusivity	$\mathcal{D}$	1.45×10^{-5}	cm^2/s	[13]
Mb diffusivity	$\mathcal{D}_{\mathrm{Mb}}$	2.20×10^{-7}	cm^2/s	[13]
Mass transfer coefficient	k	8.60×10^{-4}	ml O_2/cm^2·mmHg·s	[13]
Intracapillary PO_2	P_{cap}	40	mmHg	[55]
Mb half-saturation PO_2	$P_{50,\mathrm{Mb}}$	2.39	mmHg	[13]
PO_2 at half demand	P_{c}	0.5	mmHg	[91]
Capillary radius	r_{cap}	2	μm	[58]
Tissue dimensions				
MH samples		433×343	μm^2	*
Ischaemic samples		384×304	μm^2	*

Table 5.1: Biophysical parameter values for O_2 kinetics and diffusion in the myocardium of maternally hypoxic (MH) and ischaemic rats. Mb = myoglobin, * = estimated from our histological preparations.

are given in Table 5.2. Supply regions were estimated from the Voronoi tessellations of the capillaries captured in digital images. The use of Voronoi polygons in this case is justified by the low degree of heterogeneity in their areas, as represented by the heterogeneity index LogSD (standard deviation of the logarithm of supply areas). LogSD quantifies the spread in the logarithmic distribution of capillary supply areas.

The mean and cumulative frequency distributions of O_2 tension and consumption rate are presented in Fig. 5.3. Every data point on these curves is obtained by averaging over all control and CHU epicardial samples. In addition, we tabulate and present our predictions of O_2 tension and consumption rate in Table 5.3 and Figs. 5.3–5.4.

5.4.2.1 Oxygen supply indices

CHU led to a significant reduction in global supply capacity to the epicardium as manifested in decreasing capillary density by 20% ($P < 0.005$; Table 5.2). Consequently, local O_2 supply to CHU rat hearts was significantly affected. In particular, despite modestly increasing the heterogeneity of epicardial capillary distributions (11%; $P < 0.05$; Table 5.2), CHU significantly increased the area of the capillary supply regions (26.4%; $P < 0.01$; Table 5.2). In addition, the product of (1) the proportion of capillary densities from Control and CHU hearts and (2) the proportion of

Treatment	**Capillary supply area** (μm^2)	**LogSD**	**Capillary density** (capillaries/mm^2)
Control	572 ± 31	0.118 ± 0.009	1824 ± 77
CHU	723 ± 70††	0.131 ± 0.005†	1460 ± 126†††

Table 5.2: Estimates of O_2 supply indices in the epicardium of control and CHU rats. LogSD = standard deviation of the base–10 logarithm of capillary supply areas; this index characterises the extent of heterogeneity in O_2 supply areas in muscle cross–sections. Here the use of Voronoi polygons as representatives of capillary supply areas is valid given their accurate approximation of trapping regions. Data represents mean ± standard deviation (n = 6). Statistical significance is represented as: effects of CHU $^{\dagger}P < 0.05$, $^{\dagger\dagger}P < 0.01$, $^{\dagger\dagger\dagger}P < 0.005$.

Demand	**Animal**	**Oxygen profile**		**Consumption profile**	
		Mean PO_2 (mmHg)	**Hypoxia** (%)	**Mean MO_2** (mlO_2/100ml min)	**$MO_2 \leq \mathcal{M}_0/2$** (%)
Moderate					
	Control	19.56 ± 0.63	0.84 ± 0.55	9.54 ± 0.06	0.92 ± 0.58
	CHU	18.05 ± 1.87	1.47 ± 0.75†	7.72 ± 0.10††	1.60 ± 0.80†
	CHU^+	14.90 ± 1.77††	3.07 ± 1.84†	9.16 ± 0.20††	3.25 ± 1.90†
High					
	Control	7.86 ± 0.47	9.53 ± 1.60	18.87 ± 0.24	9.84 ± 1.70
	CHU	6.70 ± 1.33	13.31 ± 3.00†	14.85 ± 0.60††	13.66 ± 3.00†
	CHU^+	5.45 ± 1.07††	16.64 ± 5.59†	17.11 ± 0.87††	17.03 ± 5.63†

Table 5.3: Predictions of O_2 tension and consumption rate (MO_2) in the epicardium of adult rat offspring from control and CHU groups. Relative O_2 demands are extrapolated from the decreased citrate synthase activity in CHU hearts as representative of decreased mitochondrial density. O_2 demand for CHU^+ is equal to that of control, reflecting a hypothetical maintenance of mitochondrial density in CHU as meaasured by CS activity. $\mathcal{M}_0$ = high O_2 demand = 2 × moderate O_2 demand (see Table 5.1). Data represents mean ± standard deviation (n = 6). Statistical significance is represented as: effects of CHU $^{\dagger}P < 0.05$, $^{\dagger\dagger}P < 0.005$.

the corresponding capillary supply areas was found to be approximately 1 (unitless), an indication that changes in global O_2 supply match changes in local O_2 supply.

5.4.2.2 Oxygen kinetics

Extrapolating from the decreased citrate synthase activity in CHU hearts, CHU decreased the mean calculated tissue PO_2 by $8 - 15\%$, although not to the level of statistical significance (Table 5.3). In contrast, predictions of the corresponding mean

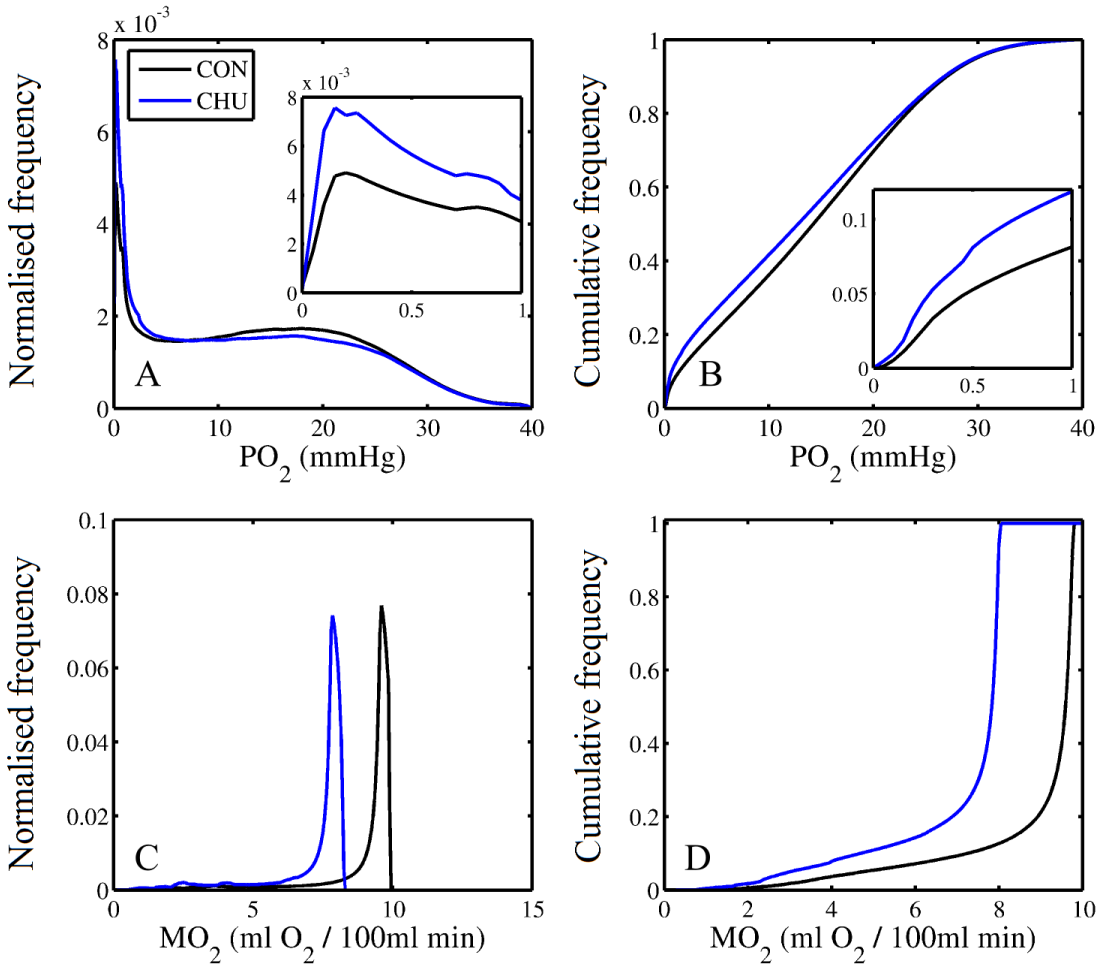

Figure 5.3: Predicted mean normalised frequency distributions for epicardial O_2 tension and consumption rate (MO_2) in control (CON) and CHU rats. Data represent moderate O_2 demand in epicardial tissue. Mitochondrial density in CHU reflects the experimentally–observed reduction in citrate synthase activity in CHU hearts.

tissue O_2 extraction indicate a significant decrease ($20-22\%$; $P < 0.005$; Table 5.3). Such reductions were also accompanied by both increased hypoxic tissue fraction ($40-75\%$; $P < 0.05$; Table 5.3) and increased tissue fractions uptaking O_2 at very low myocardial consumption rates ($39-74\%$ increase; $P < 0.05$; Table 5.3).

Plotting estimates of tissue PO_2 indicated that, despite the increased capillary supply areas in CHU hearts, the decreased O_2 consumption led to matching between the distributions for tissue PO_2 between control and CHU rats (Fig. 5.3A). Indeed, estimates of cumulative PO_2 indicated that only as PO_2 started to decline to very low levels was a greater proportion of the myocardium at a corresponding PO_2 to control tissue (Fig. 5.3B). Decreased citrate synthase activity led to decreased estimates for

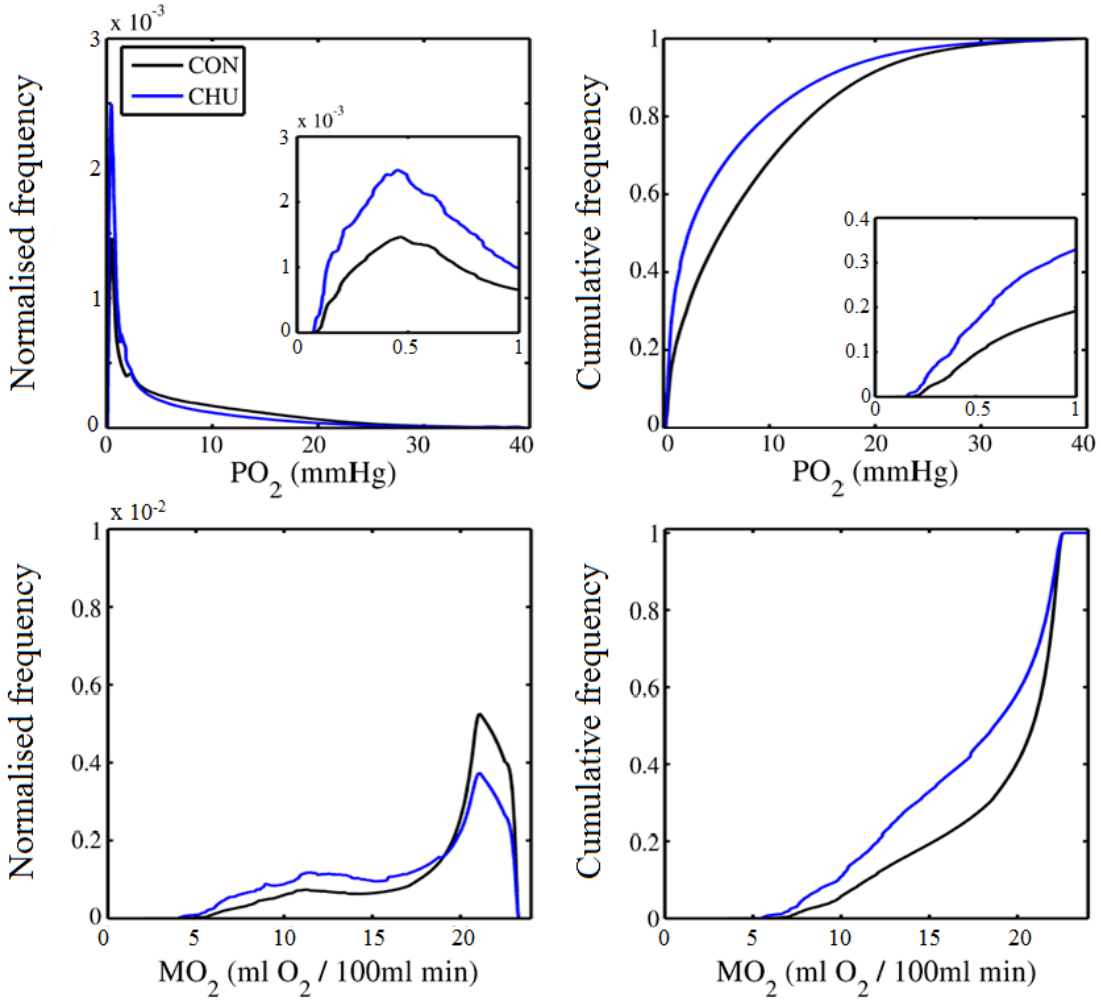

Figure 5.4: Predictions of the mean normalised frequency distributions of O_2 tension and consumption rate (MO_2) under maximal O_2 demand in epicardial tissues of control (CON) and CHU rats. Here CHU is assumed to maintain the same mitochondrial density as that in control hearts.

calculated O_2 consumption in CHU heart (Fig. 5.3C) such that at all calculated levels of O_2 consumption a greater proportion of the myocardium for CHU hearts was included in the cumulative distribution (Fig. 5.3D).

To estimate the effects of maintaining a normal mitochondrial density (O_2 demand) for hearts with an increased capillary supply area, calculations were repeated, estimating both moderate and maximal O_2 consumption. The increased supply area was found to significantly decrease the mean tissue PO_2 ($24-31\%$; $P < 0.005$; Table 5.3), and led to a $4-10\%$ decrease in mean tissue O_2 extraction in the CHU hearts ($P < 0.005$; Table 5.3). As a consequence, the hypoxic region within the myocardium

increased by $74 - 265\%$ for CHU hearts ($P < 0.05$; Table 5.3) accompanied by a $73 - 253\%$ increase in the area of myocardium with O_2 consumption rate (MO_2) $\leq 50\%$ $\mathcal{M}_0$ ($P < 0.05$; Table 5.3).

5.4.3 Discussion

One of the most common insults to fetal development is associated with maternal exposure to hypoxic environments. A severe episode of maternal hypoxia during late stages of pregnancy, such as late chronic hypoxia *in utero* (CHU), has been shown to alter cardiac performance in adult offspring [85]. Moreover, the experimental results indicated that CHU led to a decreased cardiac output in the isolated perfused heart, and revealed an alteration in a critical determinant for physical activity, namely the potential to deliver O_2 to respiring tissues. It was also found that this decrease is coupled with reductions in myocardial capillary density and total mitochondrial capacity despite an apparent increase in the overall metabolism of glucose and fatty acids undertaken by the CHU heart. These experimental observations suggest an inefficiency of mitochondria in CHU hearts (decreased cardiac output despite an increase in the overall metabolism), possibly as a consequence of proton leakage or oxidative stress. Here, we use mathematical modelling to explore how such mitochondrial inefficiency and increased supply regions may affect myocardial tissue O_2 level and consumption rate following CHU together with any consequences.

Impaired angiogenesis

The effect of CHU on angiogenesis may be explored via assessing changes in capillary domains, as these can accurately approximate *trapping regions*. Direct digitisation of capillary locations allowed a quantification of the local enlargement in O_2 supply areas which, in turn, partly reflects the extent of fibre hypertrophy [50, 53]. In particular, CHU led to a 27% enlargement in supply areas, suggesting an impeded angiogenesis (fewer capillaries per unit volume) associated with the hypertrophy of cardiomyocytes in adult CHU rats. Indeed, recent experiments report that maternal hypoxia in rats during early pregnancy led to a 30% decrease in the global fibre density, despite maintenance of normal adult heart size, suggesting fewer yet larger cardiomyocytes [83, 85]. Together, these findings are not inconsistent with the previous hypothesis that angiogenesis in CHU rat hearts may be impaired [85]; in particular our results demonstrate that increasing the region of tissue that must be supplied by a capillary does not induce angiogenesis in CHU rat hearts.

The CHU heart and O_2 stress

Our modelling results additionally indicate that CHU hearts exhibit reduced O_2 consumption rates coupled with an essentially normal mean PO_2 but, noting large samples were considered, increased extremes of the size of hypoxic regions within capillary supply regions ($\times$2.5; see Table 5.3 and Fig. 5.3A–D). Under oxidative stress these extremes become more pronounced. Thus while the CHU heart has similar oxygenation profiles to the normal heart under standard conditions, it is more susceptible to hypoxia. This can have the further effect of reducing mechanical efficiency by preventing contraction in larger myocardial regions further reducing pumping function under oxidative stress. Thus the CHU heart is theoretically predicted to be highly susceptible to extreme stress such as ischaemia–reperfusion injury, which is consistent with recent experimental observations [124, 196]. For example, hypothetical hearts with CHU capillary supply domains and normal mitochondrial densities exhibit these effects in a much more exaggerated manner. Hence reducing mitochondrial density whilst maintaining increased function is *predicted to reduce* hypoxia, a counter–intuitive observation.

5.4.4 Conclusions

In terms of an understanding of O_2 transport, our modelling studies provide support for hypotheses that angiogenesis does not respond to increased capillary O_2 supply regions of the CHU heart, but instead exhibits mitochondrial inefficiency compensation. However, this also increases sensitivity to extreme O_2 demand, generating the testable hypothesis that the CHU heart is particularly susceptible to hypoxia and thus, for example, ischaemia–reperfusion injuries.

5.5 Capillary supply in diabetic hearts

The selection of substrate for myocardial energy production may be dictated by the availability of O_2 and/or coronary flow [39]. For example, compromise to O_2 supply is accompanied by increased glucose reliance and decreased lipid oxidation in moderate cases [2], and elevated reliance on anaerobic energy production (glycolysis) in extreme cases [7]. Hence, capillary supply of oxygenated blood may be critically linked to the optimisation of myocardial ATP production. However, the relative importance of functional capillary supply or ability to switch between substrates to preserve cardiac performance is currently unclear, but may be critically important in conditions such

as diabetes that are characterised by a reduced metabolic flexibility (inability to utilise glucose) and microvascular disease (e.g. capillary rarefaction), which has the potential to impair the coronary capillary supply [147].

In an experimental study, our collaborators speculated that if microvascular units (an individual arteriole and its associated capillaries supplied downstream) are crucial for local provision of O_2 to the myocardium, then loss of functional capillaries by occlusion of individual arterioles would decrease output of the heart, and hence decreased total metabolism, without altering the balance between lipid and glucose metabolism for the remaining muscle fibres as no 'spillover' of O_2 into adjacent capillary supply regions may occur. Conversely, if diffusion of O_2 over wider distances supports metabolism in neighbouring fibres/capillary supply regions then metabolism will be altered to improve the efficiency of ATP production through 'metabolic flexibility', at least if perfusion levels are kept fixed, as with maximal perfusion. This response involves switching of substrate use if the prevailing O_2 supply is limited and would be exemplified by a decrease in fatty acid oxidation and increased reliance on glucose metabolism.

Our experimental collaborators have conducted several laboratory experiments [86] in an effort to investigate the relationship between functional capillary supply and myocardial selection of energy substrates (lipids and glucose) as well as to correlate these variables to the mechanical performance and metabolism in isolated, normal and diabetic perfused working rat hearts. The role of functional capillary supply was established by variable infusion of polystyrene microspheres (mean diameter 15.0 ± 0.2 μm) into the coronary circulation blocking arterioles and thus mimicking capillary rarefaction due to microvascular disease (e.g. diabetes and hypertension). The random blockade of coronary arterioles by microspheres led to an acute loss of functional capillary supply in both normal and diabetic working hearts. The mechanical performance and metabolism decreased following progressive arteriolar occlusions with microspheres in the perfused, working heart for both control and diabetic rats [86].

Their subsequent experimental data was uniformly consistent with substrate switching; however the requirements of O_2 transport in the hypothesis that substrate switching is due to O_2 supply is beyond the resolution of their oxygenation measurements. Hence, as part of this study, our modelling objective was to assess whether the experimental compromise of the coronary vasculature was sufficient to induce

tissue hypoxia and reduce tissue O_2 consumption, and to assess whether the tissue subsequently allowed compensation from other arterioles once an arteriole becomes blocked, and whether our biophysical understanding of O_2 transport is consistent with the hypothesised mechanism of substrate switching.

5.5.1 Methods

Cardiac mechanics, metabolism, and tissue histology were analysed experimentally by Dr David Hauton and Dr James Winter at the University of Birmingham. For completeness, we briefly describe the tissue preparation procedure carried out by our collaborators. Detailed experimental methods can be found elsewhere [86].

The resulting images of both total and patent capillary supply (e.g. Fig. 5.5) were digitised by Dr David Hauton, and followed by image segmentation and finite element computations performed by A. A. Alshammari in conjunction with estimates of the diffusivity of O_2 from capillaries to the surrounding myocardium to predict tissue PO_2 and MO_2. The tissue sample geometries extracted from histological sections of tissue biopsies were incorporated into our mathematical model, together with relevant biophysical parameters (Table 5.1). The spatial distribution of O_2 tension and consumption rate were computed numerically by using the numerical methodologies detailed in Appendix A.

The capillary density was quantified as the number of capillary profiles per mm^2 of cross–sectional area. The shortest distance between adjacent capillaries was calculated by Delaunay triangulation, producing a value for the total influence of all nearest neighbours (NN), and giving an assessment of the variance in capillary supply in control and experimental groups. Areas of capillary supply regions were calculated using Voronoi tessellations of digitised images. The coefficient of variation (CV) was calculated for O_2 supply areas and NN distances as standard deviation/mean $\times 100$. The logarithmic standard deviation (LogSD) was additionally calculated as standard deviation of the base–10 logarithm of supply areas.

5.5.2 Results

Arteriolar occlusion decreased the density of patent (perfused) capillaries by 38% (Fig. 5.5A and Table 5.4) coupled with a 64% increase in capillary supply area (Fig. 5.5B and Table 5.4; also compare Figs. 5.6A and B) and a 19% increase

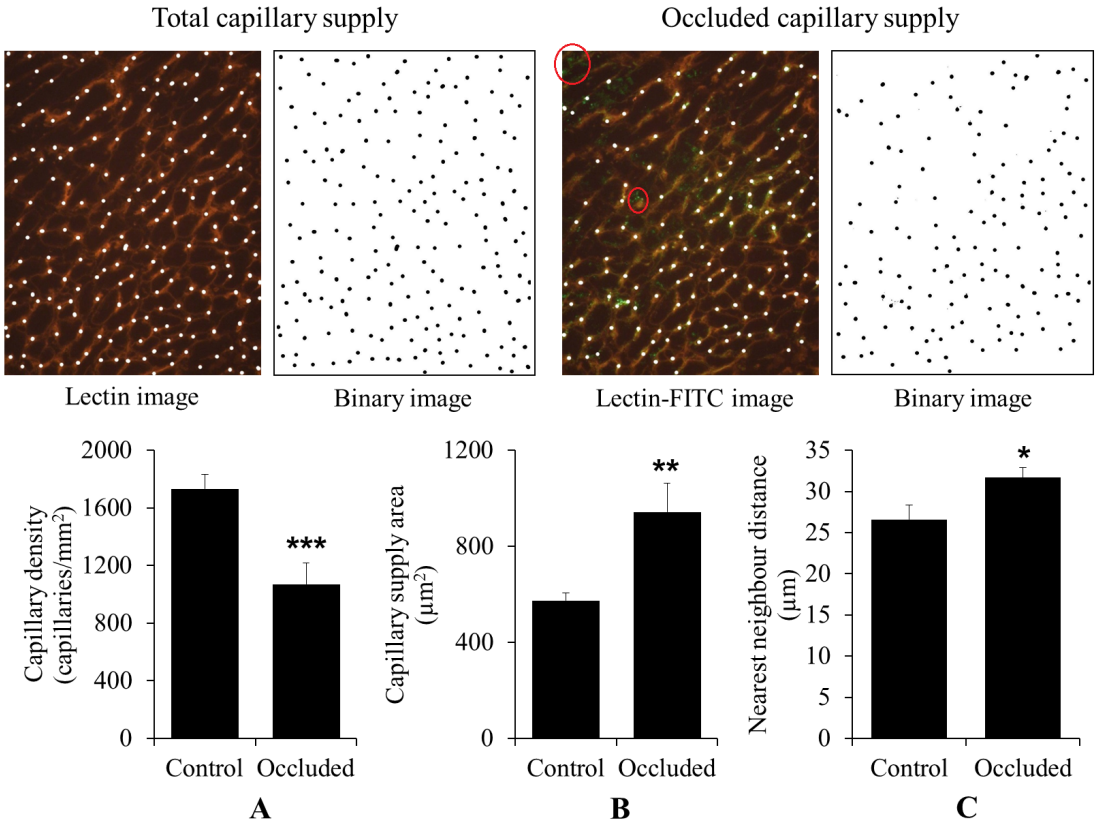

Figure 5.5: Histological estimates of total capillary supply and patent capillaries within the occluded sample following infusion of microspheres. Total capillary supply was estimated by rhodamine–labelled lectin–staining of capillaries and capillaries were identified digitally with *white discs*. Patent capillaries following microsphere infusion were estimated by inclusion of FITC–labelled dextran (green colour; e.g. see areas within the *oval red circles*) to highlight only those capillaries possessing flow. Images represent 384 μm $\times$ 304 μm of myocardium. Data represents mean $\pm$ standard deviation ($n = 3$). Statistical significance is indicated as: effect of microsphere infusion $^{*}P < 0.05$, $^{**}P < 0.01$, $^{***}P < 0.005$.

Treatment	**Capillary supply area** (μm^2)	**CV** (%)	**LogSD**	**Capillary density** (capillaries/mm^2)
Control	574 ± 31	27.33 ± 2.92	0.121 ± 0.014	1733 ± 101
Occluded	$942 \pm 129^{\dagger}$	$47.50 \pm 3.32^{\dagger\dagger}$	$0.182 \pm 0.012^{\dagger\dagger}$	$1069 \pm 148^{\dagger\dagger}$

Table 5.4: Estimates of O_2 supply indices in randomly selected samples from the epicardium before and after occlusion. CV = coefficient of variation in supply areas (standard deviation normalised by the mean $\times 100$). LogSD = standard deviation of the base-10 logarithm of capillary supply areas. Here CV and LogSD characterise the extent of heterogeneity in O_2 supply areas within the myocardium. Data represent mean $\pm$ standard deviation (n = 3). Statistical significance represented as: effects of microspheres occlusion $^{\dagger}P < 0.01$, $^{\dagger\dagger}P < 0.005$.

in the distance to the nearest capillary neighbour (Fig. 5.5C and Table 5.5). In addition, the heterogeneity in nearest neighbour distances increased by 60% following microsphere infusion (Table 5.5). Consequently, supply areas became significantly more heterogeneous (see CV and LogSD in Table 5.4 and Figs. 5.5A, B).

Under conditions of moderate mitochondrial O_2 demand ($\mathcal{M}_0/2$; see Table 5.1), arteriolar occlusion decreased the mean epicardial PO_2 by 43% (Table 5.6) and quadrupled the heterogeneity in O_2 distribution (CV = 4.1% vs. 15.5%). In particular, occlusion generated significant regional hypoxia in the myocardium (hypoxic fraction = 0.18% vs. 16.44%; Table 5.6), thus demonstrating a largely depressed O_2 consumption rate ($MO_2 \leq 50\%\ \mathcal{M}_0/2$). This, in turn, led to an 18% decline in myocyte O_2 uptake, coupled with increased heterogeneity in the spatial distribution of O_2 uptake (CV = 0.4% vs. 7.4%; Table 5.6).

Under conditions of high mitochondrial O_2 demand ($\mathcal{M}_0$; see Table 5.1), random arteriolar occlusion decreased the mean epicardial PO_2 by 46% (Table 5.6), doubled the heterogeneity in O_2 distribution (CV = 11% vs. 23%; also compare Figs. 5.6C and D), and induced elevated regional hypoxia (260%; Table 5.6; also compare Figs. 5.6C and D). Consequently, the mean O_2 consumption rate of the epicardium was reduced by 34%, with significant heterogeneities in the spatial distribution of O_2 uptake (CV = 3.4% vs. 12.3%; Table 5.6; also compare Figs. 5.6E and F). This was also accompanied by 260% increase in the fraction of tissue area consuming O_2 at a very low rate (below half maximal uptake; compare Figs. 5.6A and B).

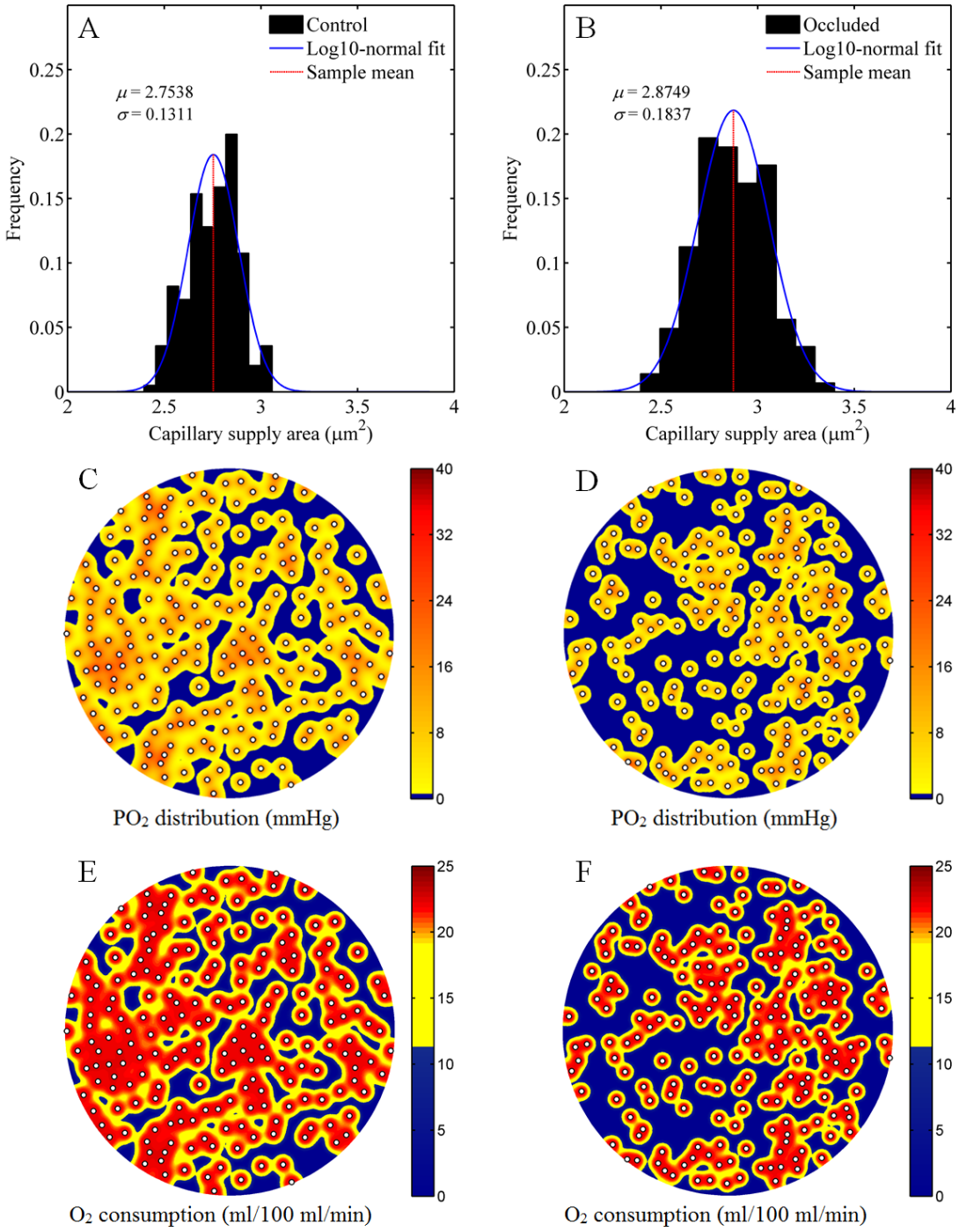

Figure 5.6: Distribution of capillary supply areas, PO_2, and O_2 consumption in control and occluded rat myocardia (single sample). (A, B) Estimated distribution of capillary supply areas. (C, D) Predicted spatial distribution of tissue PO_2. (E, F) Predicted spatial distribution of tissue O_2 consumption rate. Note the increased heterogeneity in capillary supply, tissue PO_2, and tissue uptake across sections of myocardium before (A, C, E) and after (B, D, F) arteriolar occlusion of control perfused working rat hearts.

Treatment	**Nearest neighbour distance** μm	**CV** (%)
Control	26.63 ± 1.71	14.15 ± 0.57
Occluded	$31.73 \pm 1.18^{\dagger}$	$22.70 \pm 4.01^{\dagger}$

Table 5.5: Heterogeneity of capillary supply in randomly selected samples from the epicardium before and after occlusion. CV = coefficient of variation in the distance to the nearest neighbouring capillary (standard deviation normalised by the mean $\times 100$). Here CV characterises the extent of heterogeneity in the spatial distribution of capillaries within the myocardium. Data represent mean $\pm$ standard deviation (n = 3). Statistical significance represented as: effects of microspheres occlusion $^{\dagger}P < 0.05$.

Demand	**Treatment**	**Oxygen profile**		**Consumption profile**	
		Mean PO_2 (mmHg)	**Hypoxia** (%)	**Mean MO_2** (mlO_2/100ml min)	**$MO_2 \leq \mathcal{M}_0/2$** (%)
Moderate					
	Control	11.92 ± 0.49	0.18 ± 0.21	10.87 ± 0.04	0.18 ± 0.21
	Occluded	$6.84 \pm 1.06^{\dagger\dagger}$	$16.44 \pm 6.35^{\dagger}$	$8.87 \pm 0.66^{\dagger}$	$16.44 \pm 6.35^{\dagger}$
High					
	Control	6.82 ± 0.73	18.08 ± 2.76	17.25 ± 0.58	18.08 ± 2.76
	Occluded	$3.71 \pm 0.85^{\dagger}$	$47.00 \pm 6.54^{\dagger\dagger}$	$11.39 \pm 1.40^{\dagger\dagger}$	$47.00 \pm 6.54^{\dagger\dagger}$

Table 5.6: Predictions of O_2 tension and consumption rate in randomly selected samples from the epicardium before and after occlusion. $\mathcal{M}_0$ = high O_2 demand = 2 $\times$ moderate O_2 demand (see Table 5.1). Data represents mean $\pm$ standard deviation (n = 3). Statistical significance represented as: microspheres occlusion $^{\dagger}P < 0.01$, $^{\dagger\dagger}P < 0.005$.

5.5.3 Discussion

Following microsphere occlusion a decrease in the regularity of functional capillary spacing was noted, with increases in capillary supply areas similar to that for patients with ischaemic cardiomyopathy [112]. This heterogeneity of capillary supply was predicted to leave regions of poorly–oxygenated myocardium which may become non-contractile contributing to a decrease in mechanical performance and increased internal work for the heart. Indeed, our modelling predictions fulfils one of the objectives by demonstrating that the observed decrease in cardiac work following arteriolar occlusion is indeed coupled with a theoretical prediction of an increase in both the size of the regional hypoxia and a reduction in O_2 consumption. Furthermore, our second objective of assessing the prospect of inter-arteriole compensation of O_2 transport is fulfilled by noting that the prediction of a substantial increase in the size and heterogeneity of capillary supply regions. Thus our modelling supports the hypothesis that

substrate switching is due to O_2 transport and declining myocardial PO_2.

5.5.4 Conclusions

The cardiac muscle demonstrates the capacity to switch between substrates, from palmitate to glucose, to maximise O_2 efficiency and sustain cardiac work under O_2 stress, with the latter confirmed by modelling studies. We note that the importance of this study is the deduction that the diabetic heart, with its lack of metabolic plasticity, lacks the compensation mechanism for microvascular disease exhibited by the normal heart, which will be the subject of further studies exploring the diabetic heart response to O_2 stress, again with modelling to assess microscale O_2 transport.

Chapter 6

Discussion

Maintaining intracellular oxygen tension above a hypoxic threshold is crucial for aerobic energy production in striated muscles. In normally respiring muscle tissues a functional capillary bed supplies an adequate amount of oxygen to the surrounding fibres. In contrast, in ischaemic muscles the local capillary supply of oxygen may fall short in meeting the metabolic demand of the respiring cells. Such a mismatch between capillary supply and local cellular demand is a stimulus for microvascular remodelling (*angiogenesis*) where new capillaries grow from a pre-existing capillary bed [106]. This is believed to be an adaptive response to restore normal oxygen flux from individual capillaries to neighbouring fibres by decreasing oxygen diffusion distances.

6.1 The biological problem

Our current understanding of interventions to enhance functional capillary supply of oxygen in ischaemic muscles is far from complete. The discrepancies in data on capillary supply reported in numerous experimental studies suggest that this may be partly due to the current characterisation of tissue oxygenation levels [46]. For example, quantitative classifications based on measures of gross capillary supply—such as mean capillary density (CD), capillary–to–fibre ratio (C:F), or intercapillary distance (ICD)—may characterise a global tissue ischaemia [46], but cannot account for local dysfunction associated with the underlying capillary distribution. In particular, recent experimental findings have demonstrated an inherent sensitivity of such measures to scalings in fibre cross–sectional area [1, 106], thus highlighting a need for the development of an area–based quantitative classification of capillary supply

to better inform studies assessing regulation of angiogenesis for the enhancement of intracellular oxygenation in ischaemic striated muscles [49, 51]. Progress in this area can potentially improve our current understanding of the limits to peripheral oxygen transport in striated muscle tissues. In particular, a histological framework incorporating the influence of the surrounding tissue in analyses of capillary supply of oxygen will enable an exploration of the supply–demand balance at the scale of a single capillary.

6.2 Current theoretical framework

The current experimental quantitative analyses of local capillary supply are based on the incorporation of detailed tissue geometry and functional characteristics, e.g. muscle fibre size and oxidative capacity, into indices of capillary supply, e.g. local capillary-to-fibre ratio (LCFR) and local capillary density (LCD). Based on the planar distribution of capillary domains, the basic physiological premise underlying these analyses is that Voronoi polygons (VP) represent the tissue domain maximally perfused by individual capillaries [51]. By identifying vessel locations in a plane perpendicular to muscle fibre orientation, each Voronoi polygon represents the area of supply of its enclosed capillary [46]. Such an unambiguous identification of the supply area of a capillary quantifies the relative diffusive stress an individual capillary may experience, with larger areas reflecting more diffusive stress and very small areas inferring capillary supply redundancy. Part of the convenience in using such geometrical constructs is that they (a) allow calculation of scale-independent measures of local capillary supply, (b) allow robust estimation of gross capillary supply measures, (c) require no detailed parameter estimation, and (d) are generated with extreme computational ease.

6.2.1 Limitations

Although Voronoi polygons have proven to be useful in describing oxygenation for homogeneous muscles [1, 96], it was unclear, prior to this work, how well they may capture capillary supply areas in the presence of structural and metabolic heterogeneities [53, 96]. In particular, it was unclear how these Voronoi polygons should be adjusted to accommodate the heterogeneities extracted from images of 2D section from cardiac and skeletal muscle biopsies. Indeed, there is yet to be a theoretical framework that can systematically generalise this histological framework to normal and pathologic physiological states, whilst retaining *all* of advantages (a)–(d) above.

6.3 Dissertation objectives

In this dissertation, we have aimed to investigate these limitations by exploring the transport of oxygen in cardiac and skeletal muscle 2D sections by developing mathematical and computational frameworks that can account for the anatomical and histological details of 2D tissue sections. In particular, we have sought to build a theoretical framework of oxygen diffusion that generalises the current anatomical framework of Voronoi polygons given the complex geometries of, and functional variability in, histological tissue sections. More generally, we have aimed to develop indices and research tools to allow objective assessment and improvement of the current measures of local tissue oxygenation and ultimately metabolite transport given muscle tissue cross–sections. This must include making these tools accessible rather than requiring specialist mathematical modellers for their implementation.

It has been of particular interest to explicitly assess the validity of using Voronoi polygons to characterise the transport of oxygen by comparing them to a more realistic alternative, trapping regions, which capture the biophysics of oxygen diffusion from capillaries into tissue while also accounting for the intricate anatomical and histological details of striated muscles. This has allowed us to characterise when and where current indices of local capillary supply (e.g. LCFR and LCD) are in fact likely to be an accurate representation of the underlying transport processes, and thus genuinely provided insight into levels of oxygenation given tissue heterogeneities.

To this end, we have aimed to develop and apply general transport models describing oxygen transport in 2D sections from cardiac and skeletal muscle biopsies, build a finite element computational framework, predict spatial distributions of oxygen tension and consumption rates in muscle tissue sections and, subsequently, compute a more realistic alternative to Voronoi polygons, namely the flux trapping regions, on 2D muscle sections. The resulting finite element framework has been designed to work at various scales taking into account cellular structure for the physiological phenomenon of interest.

6.4 Conclusions

6.4.1 Chapter 2

In Chapter 2 we developed a theoretical model describing oxygen transport from capillaries to uniform muscle tissues (e.g. cardiac muscle). A finite element computational framework was designed to capture the complex histological geometries

extracted from 2D sections from cardiac muscle biopsies and to solve the transport equations over such geometries. This allowed for a systematic exploration of the influence of capillary distribution heterogeneities on tissue oxygen levels. In addition, a further computational framework was developed to compute the underlying regions of capillary supply of oxygen, thus allowing qualitative and quantitative assessments of the quality of Voronoi polygons in approximating such biophysical regions of supply.

Our results indicate Voronoi polygons provide a generally accurate representation of trapping regions for uniform tissues with uniform perfusion and maximal oxygen uptake. However, this representation deteriorates with increasing levels of heterogeneity, and ultimately breaks down in severe cases of capillary heterogeneity (e.g. capillary rarefaction and extreme non-uniformity in the perfusion of neighbouring capillaries). In such cases, trapping regions can provide more robust measures of capillary capacity to study structural or functional dysregulation in pathological situations (e.g. ischaemic hearts). In addition, the increased differences between Voronoi polygons and trapping regions may be informative in studies assessing the local control of the angiogenic response in the myocardium.

6.4.2 Chapter 3

In Chapter 3 we explored the potential influence of heterogeneities in the surrounding tissue by accounting for the spatial anisotropies in the oxidative capacity and diffusivity of muscle fibres as well as the heterogeneity in fibre size and shape, as observed in skeletal muscles. In addition, we extended our equations to explore the effects of diffusion through the interstitium, facilitated–diffusion by myoglobin, and Michaelis–Menten kinetics of tissue oxygen consumption. Computationally, this was achieved by extending our finite element framework to capture the histological details of muscle fibre size and shape based on 2D sections from skeletal muscle biopsies.

We found that the Voronoi polygons approximation to trapping regions is generally accurate, thus inferring that measures of muscle capillary supply capacity based on Voronoi polygons may be reasonably used for mixed muscle samples. However, the increase in heterogeneity associated with differential uptake is found to lower the accuracy of Voronoi polygons. In such cases, flux trapping regions may provide a more robust representation of capillary supply regions, thus providing more appropriate measures of capillary supply capacity for studies assessing the structural and

functional dysregulation in mixed, striated muscle tissues. Interestingly, the relationships between Voronoi polygons and trapping regions may once more highlight potential regulatory mechanisms underlying the capillary and fibre distributions in skeletal muscles, hence providing a tool for generating testable biological hypotheses.

6.4.3 Chapter 4

In Chapter 4 we explored the influence of the spatial heterogeneity in mitochondrial distributions within striated muscle fibres, as observed in histologic tissue sections. This was achieved by extending the equations from Chapter 3 to take into account mitochondrial clustering underneath the fibre membrane and the intercellular anisotropy underlying the diffusive parameters, and ultimately assess fibre and tissue oxygenation as well as the accuracy of current capillary supply indices. In addition, our finite element framework was extended to resolve the microscale details inherent in the anatomy of mitochondrial clusters.

For maximal tissue and vascular capacity, our results indicate that Voronoi polygons provide a generally accurate representation of trapping regions, with additional improvements noted when heterogeneous diffusion coefficients are considered. However, extensive re-distribution of mitochondria towards the fibre membrane will eventually lower the accuracy of Voronoi polygons, further suggesting that measures of functional capillary based on flux trapping regions may better inform studies of structural and functional remodelling in striated muscle fibres.

In addition, fibre and tissue oxygen levels and kinetics are found to be sensitive to the level of mitochondrial clustering, with increased clustering showing a general enhancement in tissue oxygenation. However, this enhancement does not hold absolutely. Instead, it is observed to vary depending on the underlying heterogeneity of the tissue, with some cases showing diminished oxygen levels rather than enhanced. This finding may serve to explain the experimental observation that mitochondrial clustering may differentially occur across different muscles and fibre types.

6.4.4 Chapter 5

In Chapter 5 we demonstrated the potential of the models derived in Chapter 2–4 by predicting oxygen tension and consumption distributions in sections from myocardial

tissue biopsies of rats with either impaired angiogenesis or impaired arteriolar perfusion. In particular, we showed how our modelling frameworks may be used to process large biological data sets of 2D sections from muscle tissue biopsies, with quantitative predictions assisting in the interpretation of experimental measurements of cardiac performance and metabolism. More generally, this demonstrates how our modelling can become a genuine and systematically exploited tool in the study of transport and microvascular regulation within muscle.

6.4.5 Main findings

Here we summarise the main findings of this work:

1. Measures of maximal capillary supply capacity that are based on Voronoi polygons may be sensibly and reasonably used for normal tissue, though extremes in the underlying approximation of supply areas are slightly exaggerated.

2. Flux trapping regions may provide a representation of capillary supply regions that is more robust to tissue and vascular heterogeneities compared to Voronoi polygons, though computationally costly (> 12 sec/TR vs. 10^{-5} sec/VP; based on an AMD Phenom II X4 925/2.8GHz processor and a 3.8GB RAM).

3. The *normalised standard deviation* of VPs (σ_{VP}) correlates well with the degree of appropriateness of VPs, with values > 0.40 indicating very low VP quality.

4. The correlation between area frequency distributions of Voronoi polygons and trapping regions may be useful in physiological studies seeking to explore the location and extent of the local control of the angiogenesis process.

5. Flux trapping regions may permit a more accurate analysis of the local remodelling process in striated muscle tissues following experimental and therapeutic interventions.

6. Flux trapping regions may be used to study structural and functional dysregulation in pathological situations such as ischaemia, and intracellular remodelling of mitochondria.

6.5 Future work

This work is open for further theoretical extensions and biological explorations and applications. Below we briefly describe some of these directions.

6.5.1 Modelling directions

6.5.1.1 Current scales

At current scales (i.e. $400-1000\ \mu$m), fairly straightforward extensions to our models can be pursued as potential avenues for addressing the following questions:

- How may non-uniformities in the spatial distribution of discrete mitochondria within all fibre subcompartments influence tissue PO_2, MO_2 (O_2 uptake or consumption rate), hypoxia, and capillary supply regions?
- How would partial capillary permeability due to blockade by epithelial nuclei affect oxygen transport and capillary supply regions?
- What influences would temporal changes in tissue oxygen demand and capillary oxygen content (e.g. simulated RBC fluctuations) have on our previous predictions?
- Can metabolic products be studied in essentially the same framework?
- How may coupling the transport of metabolic and energy substrates affect oxygen kinetics and distribution within myocytes?

6.5.1.2 Multiscale frameworks

Our current modelling frameworks permit extensions to and investigations of larger domain sizes (e.g. at the scale of $2-5$ mm) which, in turn, would allow their application to be extended to larger datasets of biological imaging. Ultimately, such investigations should aim to take into account complex geometries, such as capillary anastomoses, the heterogeneities of three spatial dimensions and macroscale domains. In particular, given these scales permit the exploration of sub-maximal conditions, a question arises as to whether or not exploring oxygen transport in large 2D sections (or stacks of sections) can effectively capture the underlying distribution of capillary supply areas in muscles. It is also possible to construct representative domains based on tissue imaging allowing the oxygen transport equations to be solved, at least in principle. Furthermore, multi-photon imaging of tumour angiogenesis–capillary–networks reveals a level of resolution in capillary locations and perfusion [Prof Helen Byrne, Private Communication] that suggests such data can be generated. Hence, tumour imaging modalities might be utilised to provide the means of generating data

for the first 3D studies in striated muscles. However the geometrical complexity at this stage is prohibitive, highlighting the need to seek modelling simplifications to enable further progress and to utilise many biological imaging datasets. In particular, our current approach is ideal for developing multiscale mathematical and computational techniques to enable the efficient consideration of larger systems. Hence, one modelling direction is to explore simplifications, in particular investigating the use of homogenisation techniques. Within biomathematics, this approach has been extremely successful in cardiac electrophysiology, reducing the complexity of cardiac microgeometry to the bidomain equations [87, 116]. Such homogenisation studies can be validated using the fundamental 2D finite element codes developed for this dissertation via simulations on intermediate domain sizes. The resulting modelling framework will allow, in future studies, the investigation of more complex geometries and larger domains. At the simplest level, these homogenisation studies will require asymptotic analyses utilising the large difference between the macroscopic length scale, over which the system exhibits at least a statistical regularity, and the cellular length scale, over which there is extensive and complex heterogeneity plus the numerical simulation of the resulting homogenised equations.

6.5.2 Experiments

6.5.2.1 Model validation

Given the current technical limitations in measuring PO_2 in muscle fibres [150, 152], validating our models may, instead, be achieved by testing our biological predictions from capillary supply regions and hypoxia levels. In particular, we have demonstrated in Chapter 5 how predictions of the relative levels of myocardial hypoxia matched the experimentally–measured relative change in glucose and lipid metabolism in partially ischaemic myocardium. In addition, our predicted distributions of capillary supply domains (VP and TR) can be used to predict the potential location of regions of capillary growth in 2D sections from muscles following stimulation or overload [9].

6.5.2.2 Model applications

Our current models may inform experimental studies requiring an assessment of oxygen levels in muscle tissue cross–sections following experimental disruptions to the path of oxygen delivery. Here we give some examples of ongoing and future experimental studies requiring processing of large biological datasets of 2D muscle sections:

1. improving capillary supply in ischaemic muscles;
2. assessing the role of functional capillary supply of oxygen in *fetal hypoxia*;
3. assessing the role of rarefied capillary supply of oxygen in the co-morbidities associated with *chronic heart failure*;
4. assessing the role of capillary rarefaction in diabetic hearts;
5. assessing the role of capillary supply in myocardial metabolic flexibility.

Thus the implementation of GUI-led modelling codes within collaborators' laboratories to allow physiologists to process data on-site is a further future direction, given the variety and extent of the applications for this modelling framework.

Appendix A

Computational Aspects

A full analytical solution to our model problem is intractable due to the complexity of the domain geometry under consideration, the flux–jump condition at capillary walls, and the non-linearities of oxygen consumption kinetics and myoglobin facilitation flux. Other researchers have sought the following alternatives to analytical investigations:

1. The use of capillaries as point sources, thus removing the element of feedback imposed on capillary–wall flux (see [26, 93, 94, 98, 154, 186])
2. Asymptotic expansions in the limit of a small capillary diameter (see [179]).
3. Simple, highly regular, geometries of capillary distributions.

In the case of taking capillaries as a set of discrete oxygen point sources, the PO_2 field in the tissue is represented as a superposition of fields resulting from those sources. As such, a fundamental hypothesis is the radial symmetry of PO_2 in the vicinity of capillaries. We will show in the results section that this is not generally true and local feedback must dictate local levels of O_2. In addition, given a fixed capillary radius, note that point–source approximations are only valid when the intercapillary distance is sufficiently large. However, there are certain cases where capillary arrangements lead to relatively small intercapillary distances (e.g. highly clustered distributions), thus challenging the previous assumption. There are also issues when choosing appropriate boundary conditions at the external domain boundary (e.g. non-unique solutions in [94, 98]). Moreover, as revealed by Titcombe and Ward

[179], the accuracy of point–source approximations is questionable for a typical tissue cross–section scale.

Asymptotic solutions based on both the actual geometry of capillary boundaries and capillary interactions, will simplify when circular geometry is considered (see [179]). Nonetheless, the convergence rate of these approximations is still quite slow.

Regular capillary geometries are found in certain tissues (e.g., myocardium). However, in most cases, realistic capillary distributions are far from regular. Hence, analytical methods based on regular capillary distributions are of insufficient generality, thus will fail to answer many physiological questions.

A.1 Finite element solution

The goals of our study require the prediction of oxygen tension and consumption levels and to accurately investigate trapping regions for various anatomical and functional heterogeneities. In order to address the scales of our problem in such a way as to account for capillary distributions, fibre distribution, and local capillary feedback, we introduce a weak formulation for the finite element method, which we base upon the geometry of real tissue cross–section images. This computational framework is then implemented in Matlab [132] to solve our model equations.

Consider the following general PDE

$$\nabla \cdot \Big(c(p) \nabla p \Big) = M(p), \qquad x \in \Omega, \tag{A.1a}$$

$$\mathbf{n}_i \cdot \Big(c(p) \nabla p \Big) = k_i \left(p_{\mathrm{cap}_i} - p \right), \qquad x \in \partial C_i, \tag{A.1b}$$

$$\mathbf{n} \cdot \Big(c(p) \nabla p \Big) = 0, \qquad \|\mathbf{x}\| = 1, \tag{A.1c}$$

where c and M are non-negative bounded nonlinear functions of space and p, $\Omega \subset \mathbb{R}^2$ is a compact domain (e.g. unit disc), ∂C_i is the i^{th} capillary boundary, $k_i \in \mathbb{R}$ is a finite non-negative permeability, $p_{\mathrm{cap}_i} \in \mathbb{R}$ is the volume–averaged oxygen tension of the i^{th} capillary, $\mathbf{n}_i$ is the unit normal pointing inward to ∂C_i, and $\mathbf{n}$ is the unit normal pointing outward to Ω on its external boundary.

Within the framework of finite elements, one is able to resolve intricate details of local PO_2 gradients as well as the overall geometry of tissue cross–sections with high accuracy. We solve the equations using the finite element method (see Reddy [160]). The mesh used was generated by the PDE toolbox provided by Matlab [132]. Adaptive meshing was used to improve the accuracy of the computed solution around capillaries to resolve areas of rapid changes in PO_2.

A.1.1 Weak formulation

Here we will give an overview of a weak formulation of Eq. (A.1a), as required for the use of finite element methods. If p is a *classical* solution of Eq. (A.1), then for any *test function* $q \in \mathrm{C}^1(\bar{\Omega})$ integration by parts (Green's first identity) yields

$$\int_\Omega \Big(c(p)\nabla p\Big) \cdot \nabla q \, d\mathbf{x} - \sum_{i=1}^{N_c} \oint_{\partial C_i} \mathbf{n}_i \cdot \Big(c(p)\nabla p\Big) q \, ds = -\int_\Omega q M(p) \, d\mathbf{x}$$

for all $q \in \mathrm{C}^1(\bar{\Omega})$. Using the boundary conditions, Eqs. (A.1b)–(A.1c), we obtain

$$\int_\Omega \Big(c(p)\nabla p\Big) \cdot \nabla q \, d\mathbf{x} - \sum_{i=1}^{N_c} \oint_{\partial C_i} k_i p q \, ds = -\int_\Omega q M(p) \, d\mathbf{x} - \sum_{i=1}^{N_c} \oint_{\partial C_i} k_i p_{\mathrm{cap}_i} q \, ds.$$

Let $\mathcal{H}^1(\Omega)$ be the Sobolev space of functions u with the property $u,\ \nabla u \in L^2(\Omega)$. Then $\mathrm{C}^1(\bar{\Omega})$ is dense in $\mathcal{H}^1(\Omega)$ and, for $p \in \mathcal{H}^1(\Omega)$, both sides are continuous with respect to $q \in \mathcal{H}^1(\Omega)$. Hence, this identity can be extended to $q \in \mathcal{H}^1(\Omega)$. Thus a well–posed weak formulation [61, 89] is to find $p \in \mathcal{H}^1(\Omega)$ such that

$$a(p,q) = l(q), \tag{A.2a}$$

$$a(p,q) = \int_\Omega \Big(c(p)\nabla p\Big) \cdot \nabla q \, d\mathbf{x} - \sum_{i=1}^{N_c} \oint_{\partial C_i} k_i p q \, ds, \tag{A.2b}$$

$$l(q) = -\int_{\Omega} qM(p)\,d\mathbf{x} - \sum_{i=1}^{N_c} \oint_{\partial C_i} k_i p_{\mathrm{cap}_i} q\,ds. \tag{A.2c}$$

for all $p, q \in \mathcal{H}^1(\Omega)$. By the *trace theorem*, the operators $a(\cdot,\cdot)$ and $l(\cdot)$ are bounded [61, 89]. Moreover, $a(\cdot,\cdot)$ is V-coercive as a consequence of a generalised Poincaré inequality [61, 89]. Therefore, by the Lax-Milgram lemma, the initial problem possesses a unique weak solution $p \in \mathcal{H}^1(\Omega)$.

A.1.2 Finite element discretisation

To discretise Eqs. (A.1), we first choose a set of orthonormal linear basis functions $\{\phi_1, \ldots, \phi_n\}$ where $\phi_j \in \mathcal{H}^1(\bar{\Omega})$. Then, we expand the solution p in this basis

$$p = \sum_k P_k \phi_k,$$

where $P = (P_1, \ldots, P_n)$ is a vector of unknown coefficients. Substituting for p in Eq. (A.2), and taking $q = \phi_j$, we obtain

$$\begin{aligned}\sum_{k=1} \Bigg[\int_{\Omega} \Big(c(P)\nabla\phi_k\Big) \cdot \nabla\phi_j\,d\mathbf{x} - \sum_{i=1}^{N_c} \oint_{\partial C_i} k_i \phi_j \phi_k\,ds \Bigg] P_k, \\ + \Bigg[\int_{\Omega} \phi_j M(P)\,d\mathbf{x} + \sum_{i=1}^{N_c} \oint_{\partial C_i} k_i p_{\mathrm{cap}_i} \phi_j\,ds \Bigg] \\ = 0,\end{aligned}$$

for all j. In turn, this equation can be contracted into the following matrix equation

$$(\mathbf{K} + \mathbf{Q})\,P - (F + G) = 0, \tag{A.3}$$

where

$$
\begin{aligned}
K_{jk} &= \int_{\Omega} \Big(c(P) \nabla \phi_k \Big) \cdot \nabla \phi_j \, d\mathbf{x}, \\
Q_{jk} &= \sum_{i=1}^{N_c} \oint_{\partial C_i} k_i \phi_j \phi_k \, ds, \\
F_j &= \int_{\Omega} \phi_j M(P) \, d\mathbf{x}, \\
G_j &= \sum_{i=1}^{N_c} \oint_{\partial C_i} k_i p_{\mathrm{cap}_i} \phi_j \, ds.
\end{aligned}
$$

Due to the nonlinearity of c and M, matrix $\mathbf{K}$ and vector F are nonlinear, thus yielding a system of nonlinear equations. The "Partial Differential Equations Toolbox" in Matlab [132] has many useful built-in algorithms that can handle this system along with its complex domain geometry (see Appendix B). In brief, given data structures representing the PDE problem and its geometry, Matlab generates an initial triangular mesh, discretises the problem over this mesh, assembles the system in Eq. (A.3), and subsequently solves the system adaptively (if need be) using an iterative procedure which is based on a damped Newton–Gauss iteration with an Armijo–Goldstein line–search strategy in order to improve convergence by optimising the dampening coefficient. This yields the numerical solution of our model oxygen tension, i.e. vector P. The finite element solution is then post–processed to compute the distribution of oxygen consumption and PO_2 gradient. Subsequently, the latter enables a further numerical study of PO_2 streamlines and the enclosing trapping regions.

A.2 Streamlines

Central to our understanding and numerical computation of oxygen trapping regions is the concept of a *streamline*.

A.2.1 Nature of streamlines

A streamline for a vector field is a curve, the direction of which coincides at each point with the direction of the vector field; that is, at all locations it is tangent to the vector field.

We consider the streamlines associated with ∇p and recall that streamlines are trajectories (integral paths) of

$$\frac{d\mathbf{x}}{ds} = -\nabla p \tag{A.4}$$

for all $\mathbf{x} = (x, y)$ in the physical domain, with s parametrising the integral path. This is a vector field that vanishes exactly at the critical points of p. A stationary point is a constant trajectory of the flow associated with the vector field. That is, when $\nabla p = \mathbf{0}$, we have a stationary point in the phase plane diagram associated with Eq. (A.4) which is equivalently a critical point of p. Given the above is a gradient dynamical system, and by Clairaut's theorem, the Jacobian matrix must be symmetric and thus diagonalisable by a two–dimensional set of orthogonal eigenvectors

$$\mathcal{J} = \frac{\partial^2 p}{\partial x_i \partial x_j} = -\begin{pmatrix} p_{xx} & p_{xy} \\ p_{yx} & p_{yy} \end{pmatrix} = -\text{Hessian}(p).$$

Being symmetric, all eigenvalues of this system are real. In particular, a *nondegenerate* (hyperbolic) stationary point of this system is either a sink (local minimum for p), a source (local maximum for p), or a saddle [78]. Note here that the Jacobian matrix is exactly the Hessian matrix of p. Moreover, any hyperbolic minimum must be asymptotically stable [78, 90].

A particularly important property of this system is that its saddle points, among all other hyperbolic stationary points, satisfy the Hartman–Grobman theorem [27].

Theorem (Hartman–Grobman)**.** *Let $f : \mathbb{R}^n \to \mathbb{R}^n$ be a C^1 map with $f(\mathbf{x}_0) = \mathbf{0}$, where $\mathbf{x}_0$ is a hyperbolic stationary point. Then, there exists a neighbourhood U of $\mathbf{x}_0$ and a homeomorphism $h : U \to \mathbb{R}^n$ such that the flow of f is topologically conjugate by h to the flow of its linearisation and $h(\mathbf{x}_0) = 0$.*

Equipped with this theorem, we can topologically classify the dynamics in a neighbourhood of hyperbolic stationary points based on the existence of a conjugacy of the local dynamics with the linearised system at the same points.

To study the behaviour of streamlines of this two–dimensional system on the plane, the Poincaré–Bendixson theorem gives a classification of every possible type of trajectory. However, prior to proceeding with this we make the following observation: A gradient dynamical system cannot possess periodic orbits besides its stationary points. For suppose there exists a periodic orbit with period τ. Then, after one circuit around this orbit we obtain

$$0 = p(\tau) - p(0) = \int_0^\tau \frac{dp}{ds} ds = \int_0^\tau \nabla p \cdot \frac{d\mathbf{x}}{ds} ds = -\int_0^\tau ||\nabla p||^2 ds < 0$$

unless $\frac{d\mathbf{x}}{ds} = 0$ in which case the trajectory is a stationary point (not a closed orbit). Hence, no such orbits exist. Moreover, any α-limit or ω-limit point of a streamline must be a stationary point of Eq. (A.4) [90].

From Eq. (A.4), we know that streamlines are tangent to PO_2 flux, and thus cannot cross no-flux boundaries (trapping regions and domain boundary). Thus, a streamline whose initial position is sufficiently close to a capillary cannot escape that capillary's trapping region (Fig. A.1). In particular, a streamline starting on a trapping region boundary will follow that boundary down to a partial pressure minimum, which can be either a saddle or a sink. This monotonic behaviour of p on streamlines follows from the following property:

$$\frac{dp}{ds} = \frac{\partial p}{\partial x}\frac{dx}{ds} + \frac{\partial p}{\partial y}\frac{dy}{ds}$$

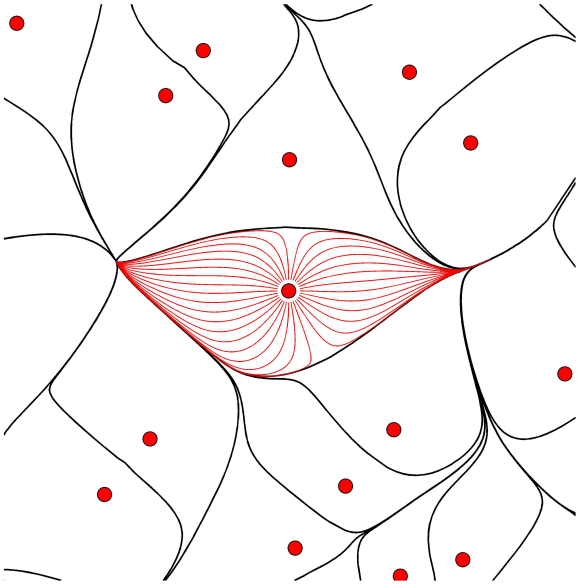

Figure A.1: PO_2 flux lines (red) generated for each capillary (disc) by numerically solving $\frac{d\mathbf{x}}{ds} = -\nabla p$ with trapping regions delimited (black), where s parameterises the flux lines.

$$
\begin{aligned}
&= \nabla p \cdot \frac{d\mathbf{x}}{ds} \\
&= -\nabla p \cdot \nabla p \\
&= -||\nabla p|| \\
&\leq 0.
\end{aligned}
$$

In addition to being bounded due to a global no-flux imposed on tissue domain, trapping regions are clearly closed, and thus compact. Since in every model of oxygen transport microvessels are taken to be the only source of oxygen [69], the Poincaré–Bendixson theorem [90] guarantees that a streamline within a trapping region must approach its ω-limit set, which, in this case, can only be a closed loop composed of a finite number of fixed points together with homoclinic or heteroclinic connections [78]. Homoclinic connections cannot exist in a gradient dynamical system; see Guckenheimer [78] for a general proof. For instance, in the context of our model, consider a homoclinic connection (e.g. of saddle points) surrounding a capillary. An application of the Poincaré-Bendixson theorem demonstrates the presence of a limit cycle within the region delimited by this homoclinic connection, which leads to a contradiction as we have already shown these cannot exist. A trapping region, therefore, can be characterised by an area of the muscle cross–section reached by streamlines from a given

capillary whereby its boundaries are delineated by heteroclinic connections between stationary points of Eq. (A.4).

A.2.2 Computation of streamlines

Central to our study is the estimation of oxygen streamlines from our finite element solution. Below we detail how such streamlines can be estimated numerically.

A.2.2.1 Heun's method

The integral paths representing oxygen streamlines are computed by numerically solving Eq. (A.4) by Heun's method. This is a second–order Runge–Kutta method whereby Euler's method is called to predict the value half-way through a step and then the trapezoidal method corrects this value. That is, given the initial value problem $\frac{d\mathbf{x}}{ds} = f\left(s, \mathbf{x}(s)\right)$, $\mathbf{x}(s_0) = \mathbf{x}_0$, we proceed numerically from step i to step $i+1$ as follows

$$\tilde{\mathbf{x}}_{i+1} = \mathbf{x}_i + hf(s_i, \mathbf{x}_i), \tag{A.5}$$

$$\mathbf{x}_{i+1} = \mathbf{x}_i + \frac{h}{2}\left(f(s_i, \mathbf{x}_i) + f(s_{i+1}, \tilde{\mathbf{x}}_i)\right). \tag{A.6}$$

A.2.2.2 Interpolation

Using this ODE solver, the numerical computation of the streamlines of the above mentioned gradient dynamical system requires two numerical evaluations of ∇p per time–step. We use the C^1 linear interpolation for scattered data described in [73] to provide approximate values of ∇p, which we compute using finite elements.

A.3 Computation of trapping regions

Here we detail the computational algorithms developed to numerically estimate the boundaries of trapping regions from our finite element solution.

Knowing that a trapping region is delimited by unstable manifolds connecting saddles to sinks of Eq. (A.4), an algorithm is implemented to estimate the unstable manifold through each saddle point which is based on the Hartman–Grobman theorem

for hyperbolic equilibrium points of dynamical systems [27].

In the process of estimating unstable manifolds we need to compute the oxygen streamlines which are very close to saddle points. Hence, the first step in this algorithm is to numerically estimate the stationary points of our dynamical system.

A.3.1 Stationary points

Given the finite element solution, we wish to locate points satisfying $\nabla p = (f, g)^T = \mathbf{0}$. To estimate these, we use the following algorithm:

1. Take an FEM triangle. Note that refining the FEM will refine the accuracy of this algorithm.
2. If there is a mix of signs of f at the nodes of this triangle, the nullclines of f must cross two edges of this FEM triangle.
3. Find all such triangles.
4. Repeat this for g.
5. Record all elements appearing in both lists because the nullclines of both f and g pass through these elements.
6. If both nullclines pass within a small epsilon of a vertex (we chose $\epsilon = 10^{-40}$), record a zero of (f, g) at this vertex.
7. Else, if the nullclines intersect away from the vertices, we can find two points on each nullcline by considering where the nullclines intersect the edges of the element. We proceed by finding the intersection within the element by approximating the nullclines by straight lines within the elements and finding where they cross (and confirming the crossing is within the element). Then record a zero of (f, g) at this intersection point.

A.3.2 Saddle points

Based on the sign of p_{xx}, p_{xy}, and p_{yy} we can distinguish saddle points from sinks. We note that our system does not possess degenerate stationary points. Nonetheless, we further solve the system around stationary points and examine the behaviour of the resulting trajectories. If, for each such point, all trajectories end at the same point (within a specified tolerance), the fixed point in question is a sink. This provides a way to collect all saddle points of the above dynamical system.

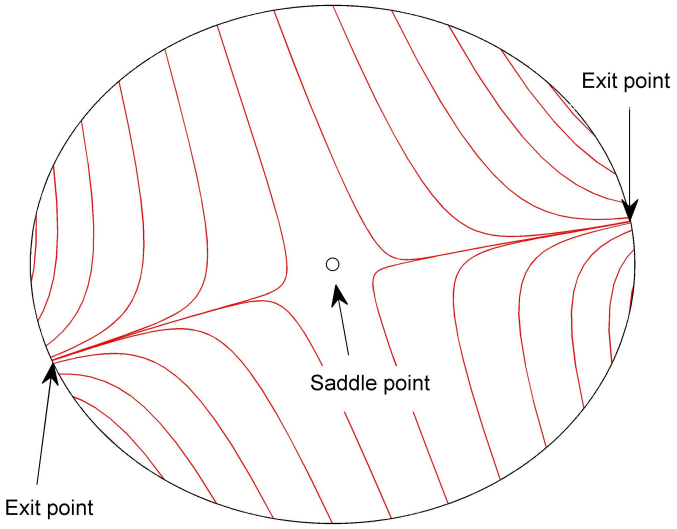

Figure A.2: A typical behaviour of streamlines in the vicinity of saddle points. Streamlines are plotted in red and their initial conditions are chosen to be equiangular on the $\frac{\epsilon}{2}$-circle.

A.3.3 Boundaries of trapping regions

Since each trapping region is composed of a collection of trajectories connecting saddles to sinks, we need to compute these and patch them together for each capillary. Doing this requires tackling one saddle point at a time. Then, from the Hartman–Grobman theorem, we know that streamlines typically exit a small neighbourhood of a saddle point from two locations which are angularly π apart (see Fig. A.2). Hence, one can estimate an unstable manifold by estimating exit points, computing integral paths starting at each exit point, and connecting exit points by a line segment of small length.

To compute a single segment of the trapping region, we proceed with the following algorithm

1. Pick a saddle point.
2. Draw an $\frac{\epsilon}{2}$-circle around it, where ϵ is sufficiently small.
3. Pick an initial angular position at this circle, preferably $\theta_0 = 0$.
4. Compute an initial streamline $\mathbf{x}_0(s)$ which takes θ_0 as its initial condition, and record the angle of its exit point with respect to the saddle point, ϕ_0.

5. Pick the next angular position $\theta_1 = \theta_0 + \Delta\theta$, where $\Delta\theta$ is chosen to be appropriately small and divides 2π evenly.

6. Compute the next streamline $\mathbf{x}_1(s)$ which takes θ_1 as its initial condition, and record the angle of its exit point with respect to the saddle point, ϕ_1.

7. If the angular difference, $\Delta\phi_1 = \phi_1 - \phi_0$, is smaller than some chosen tolerance, repeat steps $5 - 6$ with $\theta_i = \theta_0 + i \times \Delta\theta$ and $\Delta\phi_i = \phi_i - \phi_{i-1}$.

8. If not, exit the loop and record the last two exit points, ϕ_{end-1} and ϕ_{end}.

9. Call the ODE solver to generate integral paths starting from these exit points, generated by calculating the trajectories associated with θ_i and θ_{i+1}. By the previous algorithm these will exit the $\frac{\epsilon}{2}$-circle, within numerical error of the unstable manifold.

10. Finally, connect these two integral paths through the $\frac{\epsilon}{2}$-circle by a line segment of length ϵ.

With this algorithm, we are able to generate a trapping region segment that approximates the unstable manifold of a saddle point. Doing this for all saddle points, we end up with a collection of trapping region segments which, together, tessellate the entire domain.

A.3.4 Delimiting trapping regions

Segments of trapping region boundaries are indexed according to the order in which saddle points are indexed. Due to the ambiguity arising from asking which of these segments corresponds to which trapping region, and thus which capillary, we resort to converting our final tessellated plot to an image (see Fig. A.3). This image has a square shape with a white background colour in addition to segments of trapping regions and domain boundary in black. Moreover, the domain enclosed has a boundary that fits the image square perfectly. The following are algorithms for tracing out all trapping regions in this image.

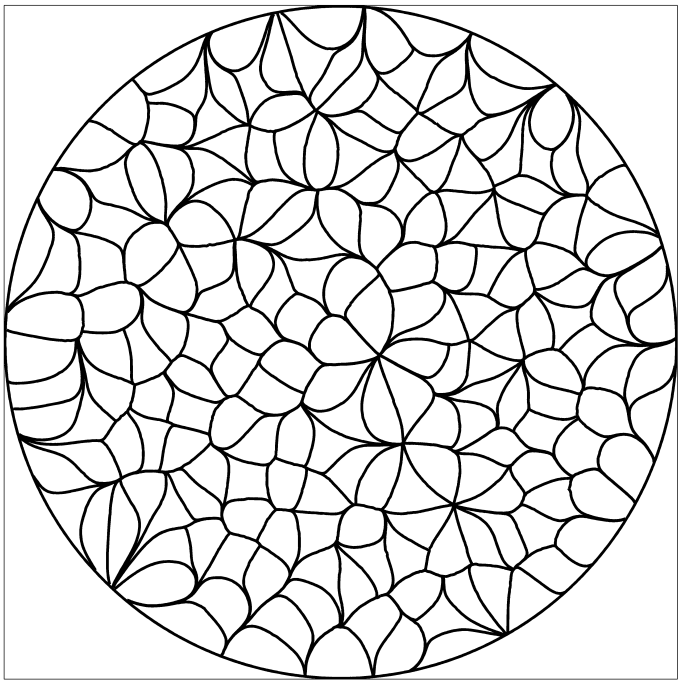

Figure A.3: A typical image setup that we use to segment the trapping regions tessellating the unit disc. Note that, for illustration purposes, we have removed the capillaries.

Regions:

1. Convert the image to a binary matrix with 0's for black pixels and 1's for white pixels. Note that, given the above image setup, this matrix must have a white upper leftmost pixel.

2. Start a loop at the $(1, 1)$ location of this binary matrix, which we just showed to be always a 1.

3. If this element is a 1, replace this number with a label j ($j = 1, 2, 3, \ldots$) signifying the j^{th} region, and proceed clockwise to the next element.

4. If the next element is a 1, assign the same label to it and proceed similarly.

5. If not, skip over this element by marching in a clockwise fashion around the current element's nearest neighbours until hitting a 1.

6. Keep doing this until collecting a whole set of connected elements that have the same label.

7. Now look for a white element that has not been labelled previously and do the same procedure to it, although this time assign it a different label, preferably $j+1$.

8. Carry this algorithm on until all 1's have been assigned a label.

Boundaries:

1. Exclude all regions that are external to the unit disc by checking whether or not they contain a capillary.

2. Loop over the remaining labelled regions.

3. From region j, pick an arbitrary element and march rightward until you hit a 0. Record the location of this element.

4. March to hit the next 0 by cycling around nearest neighbours. This element must be connected to both the previous 0 and an element with label j.

5. Continue circling around the perimeter of region j until hitting the initial 0 that was found previously. At this point we will have obtained a vector of the locations of boundary elements of the region j.

6. Do this procedure to the remaining regions.

7. Convert matrix locations to the coordinate system of the original unit disc.

The polygonal boundaries of trapping regions can now be used to determine which trapping region belongs to which capillary. In addition to this, computing trapping regions areas becomes straightforward. Note that, for algorithmic ease, conversion to an image and tracing boundaries of trapping regions were carried out by the Image Processing Toolbox in Matlab [131], which provides efficient built-in algorithms for the above segmentation based on trapping regions.

Appendix B

MATLAB PDE Toolbox

The computational framework of our biophysical models is based on a finite element formulation in Matlab, using the "Partial Differential Equations Toolbox" [132]. This toolbox is designed to solve generic partial differential equations (PDE) over 2D complex geometries using finite elements methods. In particular, it houses numerous command-line tools and functions that can handle all stages of setting up and solving the modelling equations: Pre-processing, solving, post-processing, and graphical presentation. In addition, the toolbox has a built-in meshing library enclosing routines with capabilities for manual, automatic and adaptive refinements. These features are integrated in a convenient fashion through the use of simple data structures. We devote this appendix to detailing the aforementioned features.

B.1 The general PDE to be solved

Our PDE of interest has the following general mathematical form

$$-\nabla \cdot \Big(c(\mathbf{x}, p, \nabla p)\nabla p \Big) + a(\mathbf{x}, p, \nabla p)p \;\; = f(\mathbf{x}, p, \nabla p), \quad \mathbf{x} \in \Omega, \tag{B.1}$$

where c, a, f are scalar real–valued functions of space and the unknown oxygen tension p and its gradient ∇p, with $\Omega \subset \mathbb{R}^2$ being the bounded domain over which the solution is desired. We remark here that the negative sign in the left–hand side

is a Matlab convention (compare with Eq. (A.1a) in Appendix A).

Our boundary conditions are generally Robin–type

$$\mathbf{n} \cdot \Big(c(\mathbf{x}, p, \nabla p) \nabla p \Big) + q(\mathbf{x}, p) p = g(\mathbf{x}, p), \qquad \mathbf{x} \in \partial\Omega, \tag{B.2}$$

where $\mathbf{n}$ is the outward unit normal vector, and q and g are scalar real–valued functions of space and oxygen tension.

B.2 Pre-processing

The model geometry and equations need to be defined prior to meshing and solving. The PDE Toolbox is designed to handle a specific format of data structures to comprehend the description of the model geometry and equations.

B.2.1 Constructive solid geometry model

We begin by translating our model geometries into three simple data structures that make up Matlab's Constructive Solid Geometry model (CSG): a Geometry Description matrix (GD), a set formula (SF), and a name space (NS).

B.2.1.1 Geometry description matrix, GD

This matrix describes the geometry objects present in our model 2D domain. These are restricted to circles, polygons, rectangles, and ellipses. Each column in GD corresponds to an object, with the first row specifying the object type (circle = 1, polygon = 2, rectangle = 3, and ellipse = 4). For more details about how each object is represented in GD see [132].

B.2.1.2 Set formula, SF

This is a formula (in string format) that corresponds to a user–defined set operations of the 2D objects in GD, with individual set variables corresponding to each geometry object (defined in NS below). The set operations are restricted to union, intersection, and set difference. As an example, in our models capillary discs are excluded from the modelling domain by setting SF = '$\Omega - (C_1 + \cdots + C_{N_c})$'.

B.2.1.3 Name space, NS

The set variable names are defined in NS (in character format), thus linking the columns of the geometry description matrix to the entries of the set formula.

B.2.2 Decomposed geometry matrix, DL

The next step is to decompose the constructive solid geometry model to a set of disjoint 'minimal' regions whose boundaries can be composed of border line segments from neighbouring other minimal regions (e.g. fibre–fibre or fibre–interstitium) or boundary line segments from neighbouring external boundaries (e.g. fibre–capillary, interstitium–capillary, fibre–domain, or interstitium–domain).

The built-in function DECSG [132] decomposes the CSG model by applying the set formula to the columns of GD, outputting a matrix DL describing the relationship between minimal regions and their line segments. This data structure is a pre-requisite for the built-in meshing routines. We remark here that the computation of DL *via* the DECSG algorithm is currently not efficient, especially in the presence of quadratic geometrical objects (i.e. circles and ellipses). We remark here that this algorithm should be avoided when dealing with complex geometries (e.g. skeletal muscles) due to the computational overhead it incurs. Instead, one may find it rewarding to manually construct DL by writing a customised routine to handle the desired geometries.

B.2.3 Boundary conditions matrix, B

Each column in the boundary condition matrix corresponds to a column in DL (a line segment). This matrix can be easily customised by the user. For example, if one wishes to impose a no-flux condition on certain segments from a capillary boundary with the remaining segments following a Robin–type, all is needed is the location of these segments within B (the column index). For details about the format of B see [132].

B.2.4 Mesh generation

Matlab has a built-in library for mesh generation with convenient capabilities (1) to fully access the data structures and (2) to refine desired sets of triangular elements.

B.2.4.1 INITMESH

This built-in function generates an initial mesh based on the information supplied by DL. The generated mesh is described by three data structures (matrices): mesh points (P), the edges connecting mesh points (E), and the triangular elements made up by edge connections (T). Each minimal region is triangulated into a subdomain with border and/or boundary segments broken up into edges. The mesh matrices are fully accessible by the user, and the mesh information of subdomains can be extracted quite easily. This is very convenient as in our model we desire information about the triangulation making up individual fibres and interstitial spaces (subdomains).

B.2.4.2 REFINEMESH

As the name implies, this built-in algorithm generates further mesh refinements given a predefined mesh and a decomposed geometry matrix (DL). These refinements can be chosen to be globally uniform or locally non-uniform by the user. In addition, one can resolve regions of interest by supplying triangle or subdomain indices. For example, in our model of mitochondrial clustering we desire to resolve the mesh near the subsarcolemmal layer (see Chapter 4). This can be achieved by extracting the indices of both the triangular elements making up the subsarcolemmal layer and those in direct contact with the subsarcolemmal elements. In turn, the quality of the mesh can be conveniently assessed *a posteriori* using other useful built-in functions such as PDEJMPS. We note here that, at any stage during mesh generation, the user can visualise the triangular mesh using PDEMESH.

B.2.5 Equation coefficients

As mentioned previously, minimal regions corresponding to muscle fibres and interstitia are triangulated into subdomains. Part of pre-processing the mesh data is concerned with linking subdomains to the coefficients of the model equations (e.g. Eq. (B.1)). These coefficients can be defined on each subdomain or triangular element *via* customised user-defined functions. Additionally, they can be defined in terms of a Matlab 'string form', with entries positioned in accordance with their subdomain indices.

B.3 Solving

Matlab has a number of built-in functions designed for solving linear and nonlinear elliptic problems having the form of Eq. (B.1), of which we emphasise two below: PDENONLIN and ADAPTMESH.

B.3.1 PDENONLIN

PDENONLIN is a nonlinear elliptic PDE solver with an algorithm based on a damped Gauss–Newton iteration coupled to an Armijo–Goldstein line–search strategy to improve convergence. It takes as input a boundary condition matrix, mesh data, PDE coefficients which may depend on x, y, p, ∇p, and adjustable iteration parameters. Internally, PDENONLIN assembles the matrices and vectors of system (A.3) by calling another useful built-in function, ASSEMBPDE. Additionally, the user has the option of using either one of three methods for approximating the Jacobian of the nonlinear system. For details about these methods or the PDENONLIN algorithm see [132].

B.3.2 ADAPTMESH

This algorithm generates a sequence of solutions *via* repeated calls to PDENONLIN with successive localised refinements. At each stage of the refinement triangular elements are selected for further refinement based on their contribution to an estimated error. This feedback loop is controlled by a set of user–defined termination criteria (e.g. a bound on the maximum allowable number of elements). For our model simulations, we optimise the criteria for selecting 'bad' triangular elements and for terminating refinements in such a way as to incur the lowest possible computational cost while maintaining solution accuracy at a desired level.

B.4 Post-processing

Given the full accessibility to our computed solution vector and mesh data, the numerical PO_2 can be further processed to (1) compute the oxygen consumption rate (MO_2), (2) visualise the predicted spatial distributions of oxygen tension and consumption, (3) generate statistical estimates for PO_2 and MO_2 distributions, (4) compute PO_2 gradients. The following built-in functions are generally useful, and may be used for accomplishing the aforementioned tasks: PDEPLOT, PDEGRAD, PDEINTRP, PDESDP, PDESDT, and PDETRG.

Bibliography

[1] S. K. Ahmed, S. Egginton, P. M. Jakeman, A. F. Mannion, and H. F. Ross. Is human skeletal muscle capillary supply modelled according to fibre size or fibre type? *Experimental Physiology*, **82**(1):231–4, 1997.

[2] A Akki, K. Smith, and A. M. L. Seymour. Compensated cardiac hypertrophy is characterised by a decline in palmitate oxidation. *Molecular and Cellular Biochemistry*, **311**(1-2):215–224, 2008.

[3] A. A. Al-Shammari, E. A. Gaffney, and S. Egginton. Re-evaluating the use of Voronoi Tessellations in the assessment of oxygen supply from capillaries in muscle. *Bulletin of Mathematical Biology*, **74**(9):2204–31, 2012.

[4] A. A. Al-Shammari, E. A. Gaffney, and S. Egginton. Modelling capillary oxygen supply capacity in mixed muscles: Capillary domains revisited. *Journal of Theoretical Biology*, **356**:47–61, 2014.

[5] A. A. Al-Shammari, E. A. Gaffney, and S. Egginton. Modelling oxygen capillary supply to striated muscle tissues. In A. R. Ansari, editor, *Advances in Applied Mathematics*, **87** of *Springer Proceedings in Mathematics & Statistics*, pages 13–21, Switzerland, 2014. Springer.

[6] B. Alberts, D. Bray, K. Hopkin, A. Johnson, J. Lewis, M. Raff, K. Roberts, and P. Walter. *Essential Cell Biology*. Garland Science, 2013.

[7] M. F. Allard, R. B. Wambolt, S. L. Longnus, M. Grist, C. P. Lydell, H. L. Parsons, B. Rodrigues, J. L. Hall, W. C. Stanley, and G. P. Bondy. Hypertrophied rat hearts are less responsive to the metabolic and functional effects of insulin. *American Journal of Physiology–Endocrinology and Metabolism*, **279**(3):E487–E493, 2000.

[8] P. L. ALTMAN AND D. K. DITTMER. *Respiration and Circulation*, pages 139–154. Biological Handbooks. Federation of American Societies for Experimental Biology, Bethesda, MD, 1971.

[9] I. BADR, M. D. BROWN, S. EGGINTON, O. HUDLICKÁ, M. MILKIEWICZ, AND J. VERHAEG. Differences in local environment determine the site of physiological angiogenesis in rat skeletal muscle. *Experimental Physiology*, **88**(5):565–568, 2003.

[10] S. BATRA AND K. RAKUŠAN. Geometry of capillary networks in volume overloaded rat-heart. *Microvascular Research*, **42**(1):39–50, 1991.

[11] D. A. BEARD. Computational framework for generating transport models from databases of microvascular anatomy. *Annals of Biomedical Engineering*, **29**(10):837–843, 2001.

[12] D. A. BEARD AND J. B. BASSINGTHWAIGHTE. Modeling advection and diffusion of oxygen in complex vascular networks. *Annals of Biomedical Engineering*, **29**(4):298–310, 2001.

[13] D. A. BEARD, K. A. SCHENKMAN, AND E. O. FEIGL. Myocardial oxygenation in isolated hearts predicted by an anatomically realistic microvascular transport model. *American Journal of Physiology–Heart and Circulatory Physiology*, **285**(5):H1826–H1836, 2003.

[14] G. J. BELL, T. P. MARTIN, E. I. ILYINA-KAKUEVA, V. S. OGANOV, AND V. R. EDGERTON. Altered distribution of mitochondria in rat soleus muscle fibers after spaceflight. *Journal of Applied Physiology*, **73**(2):493–7, 1992.

[15] T. B. BENTLEY, H. MENG, AND R. N. PITTMAN. Temperature-dependence of oxygen diffusion and consumption in mammalian striated muscle. *American Journal of Physiology*, **264**(6):H1825–H1830, 1993.

[16] K. L. BOYLE, R. M. DILLAMAN, AND S. T. KINSEY. Mitochondrial distribution and glycogen dynamics suggest diffusion constraints in muscle fibers of the blue crab, Callinectes sapidus. *Journal of Experimental Zoology Part A: Comparative Experimental Biology*, **297**(1):1–16, 2003.

[17] R. G. BOYLE AND S. TRAVERS. Hypoxia: targeting the tumour. *Anti-Cancer Agents in Medicinal Chemistry*, **6**(4):281–286, 2006.

[18] J. M. BROWN. Tumor hypoxia in cancer therapy. In H. SIES AND B. BRÜNE, editor, *Oxygen Biology and Hypoxia*, **435** of *Methods in Enzymology*, pages 297–322. Academic Press, 2007.

[19] M. D. BROWN, M. A. COTTER, O. HUDLICKÁ, AND G. VRBOVÁ. The effects of different patterns of muscle activity on capillary density, mechanical properties and structure of slow and fast rabbit muscles. *Pflügers Archiv*, **361**(3):241–250, 1976.

[20] N. A. CAMPBELL, B. WILLIAMSON, AND R. J. HEYDEN. *Biology: Exploring Life*. Pearson Prentice Hall, 2006.

[21] K. R. CASTLEMAN, L. A. CHUI, T. P. MARTIN, AND V. R. EDGERTON. Quantitative muscle biopsy analysis. *Monographs in Clinical Cytology*, **9**:101–16, 1984.

[22] P. D. CHILIBECK, D. G. SYROTUIK, AND G. J. BELL. The effect of concurrent endurance and strength training on quantitative estimates of subsarcolemmal and intermyofibrillar mitochondria. *International Journal of Sports Medicine*, **23**(1):33–39, 2002.

[23] C. CHRISTOFORIDES, L. H. LAASBERG, AND J. HEDLEY-WHYTE. Effect of temperature on solubility of O_2 in human plasma. *Journal of Applied Physiology*, **26**(1):56–60, 1969.

[24] A. CLARK AND P. A. CLARK. Local oxygen gradients near isolated mitochondria. *Biophysical Journal*, **48**(6):931–8, 1985.

[25] A. CLARK, P. A. CLARK, R. J. CONNETT, T. E. GAYESKI, AND C. R. HONIG. How large is the drop in PO_2 between cytosol and mitochondrion? *The American Journal of Physiology*, **252**(6 Pt 1):C583–7, 1987.

[26] P. A. CLARK, S. P. KENNEDY, AND A. JR CLARK. Buffering of muscle tissue PO_2 levels by the superposition of the oxygen field from many capillaries. In K. RAKUŠAN, G. P. BIRO, T. K. GOLDSTICK, AND Z. TUREK, editors, *Oxygen Transport to Tissue XI*, **248** of *Advances in Experimental Medicine and Biology*, pages 165–174. Plenum Press, 1989.

[27] E. A. CODDINGTON AND N. LEVINSON. *Theory of Ordinary Differential Equations*. R.E. Krieger, Malabar, Fla, 1984.

[28] V. COMPERNOLLE, K. BRUSSELMANS, D. FRANCO, A. MOORMAN, M. DEWERCHIN, D. COLLEN, AND P. CARMELIET. Cardia bifida, defective heart development and abnormal neural crest migration in embryos lacking hypoxia-inducible factor-1α. *Cardiovascular Research*, **60**(3):569–579, 2003.

[29] B. COSYNS, S. DROOGMANS, S. HERNOT, C. DEGAILLIER, C. GARBAR, C. WEYTJENS, B. ROOSENS, D. SCHOORS, T. LAHOUTTE, P. R. FRANKEN, AND G. VAN CAMP. Effect of streptozotocin-induced diabetes on myocardial blood flow reserve assessed by myocardial contrast echocardiography in rats. *Cardiovascular Diabetology*, page 26.

[30] P. L. DA LUZ, J. M. CAVANILLES, S. MICHAELS, M. H. WEIL, AND H. SHUBIN. Oxygen delivery, anoxic metabolism and hemoglobin-oxygen affinity (P_{50}) in patients with acute myocardial infarction and shock. *The American Journal of Cardiology*, **36**(2):148–154, 1975.

[31] H. DEGENS, R. K. ANDERSON, AND S. E. ALWAY. Capillarization in skeletal muscle of rats with cardiac hypertrophy. *Medicine and Science in Sports and Exercise*, **34**(2):258–66, 2002.

[32] H. DEGENS, D. DEVECI, A. BOTTO-VAN BEMDEN, L. J. C. HOOFD, AND S. EGGINTON. Maintenance of heterogeneity of capillary spacing is essential for adequate oxygenation in the soleus muscle of the growing rat. *Microcirculation*, **13**(6):467–476, 2006.

[33] H. DEGENS, S. N. KOŞAR, M. T. E. HOPMAN, AND A. DE HAAN. The time course of denervation-induced changes is similar in soleus muscles of adult and old rats. *Applied Physiology, Nutrition, and Metabolism*, **33**(2):299–308, 2008.

[34] H. DEGENS, Z. TUREK, L. J. HOOFD, M. A. VAN'T HOF, AND R. A. BINKHORST. The relationship between capillarisation and fibre types during compensatory hypertrophy of the plantaris muscle in the rat. *Journal of Anatomy*, pages 455–63.

[35] D. DESPLANCHES, M. AMAMI, S. DUPRÉ-AUCOUTURIER, P. VALDIVIESO, S. SCHMUTZ, M. MUELLER, H. HOPPELER, R. KREIS, AND M. FLÜCK. Hypoxia refines plasticity of mitochondrial respiration to repeated muscle work. *European Journal of Applied Physiology*, **114**(2):405–417, 2014.

[36] DESPLANCHES, D. AND HOPPELER, H. AND LINOSSIER, M. T. AND DENIS, C. AND CLAASSEN, H. AND DORMOIS, D. AND LACOUR, J. R. AND GEYSSANT, A. Effects of training in normoxia and normobaric hypoxia on human muscle ultrastructure. *Pflügers Archiv*, **425**(3-4):263–267, 1993.

[37] D. DEVECI AND S. EGGINTON. Muscle ischaemia in rats may be relieved by overload-induced angiogenesis. *Experimental Physiology*, **87**(4):479–488, 2002.

[38] C. W. DIGIOVANNI, A. PATEL, R. CALFEE, AND F. NICKISCH. Osteonecrosis in the foot. *Journal of the American Academy of Orthopaedic Surgeons*, **15**(4):208–227, 2007.

[39] M. A. DIJKMAN, J. W. HESLINGA, P. SIPKEMA, AND N. WESTERHOF. Perfusion-induced changes in cardiac O_2 consumption and contractility are based on different mechanisms. *American Journal of Physiology–Heart and Circulatory Physiology*, **40**(3):H984, 1996.

[40] M. DONG. *Influence of aging on oxygen transport in the microcirculation of skeletal muscle*. PhD thesis, Virginia Commonwealth University, 1997.

[41] B. D. DUSCHA, W. E. KRAUS, S. J. KETEYIAN, M. J. SULLIVAN, H. J. GREEN, F. H. SCHACHAT, A. M. PIPPEN, C. A. BRAWNER, J. M. BLANK, AND B. H. ANNEX. Capillary density of skeletal muscleA contributing mechanism for exercise intolerance in class II–III chronic heart failure independent of other peripheral alterations. *Journal of the American College of Cardiology*, **33**(7):1956–1963, 1999.

[42] B. D. DUSCHA, P. C. SCHULZE, J. L. ROBBINS, AND D. E. FORMAN. Implications of chronic heart failure on peripheral vasculature and skeletal muscle before and after exercise training. *Heart Failure Reviews*, **13**(1):21–37, 2008.

[43] T. EBINA, N. HOSHI, M. KOBAYASHI, K. KAWAMURA, H. NANJO, A. SUGITA, T. SUGIYAMA, H. MASUDA, AND C. P. XU. Physiological angiogenesis in electrically stimulated skeletal muscle in rabbits: characterization of capillary sprouting by ultrastructural 3-D reconstruction study. *Pathology International*, **52**(11):702–712, 2002.

[44] S. EGGINTON. Metamorphosis of the American eel, Anguilla rostrata Le Seur: II. Structural reorganisation of the locomotory musculature. *Journal of Experimental Zoology*, **238**(3):297–309, 1986.

[45] S. EGGINTON. Morphometric analysis of tissue capillary supply. In *Vertebrate Gas Exchange*, pages 73–141. Springer, 1990.

[46] S. EGGINTON. Numerical and areal density estimates of fibre type composition in a skeletal muscle (rat extensor digitorum longus). *Journal of Anatomy*, **168**:73–80, 1990.

[47] S. EGGINTON. Temperature and angiogenesis: the possible role of mechanical factors in capillary growth. *Comparative Biochemistry and Physiology. Part A, Molecular & Integrative Physiology*, **132**(4):773–787, 2002.

[48] S. EGGINTON, J. FAIRNEY, AND J. BRATCHER. Differential effects of cold exposure on muscle fibre composition and capillary supply in hibernator and non-hibernator rodents. *Experimental Physiology*, **86**(5):629–39, 2001.

[49] S. EGGINTON AND E. A. GAFFNEY. Tissue capillary supply–it's quality not quantity that counts! *Experimental Physiology*, **95**(10):971–979, 2010.

[50] S. EGGINTON AND H. F. ROSS. Quantifying capillary distribution in four dimensions. In K. RAKUŠAN, G. P. BIRO, T. K. GOLDSTICK, AND Z. TUREK, editors, *Oxygen Transport to Tissue XI*, **248** of *Advances in Experimental Medicine and Biology*, pages 271–280. Plenum Press, 1989.

[51] S. EGGINTON AND H. F. ROSS. Planar analysis of tissue capillary supply. In S. EGGINTON AND H. F. ROSS, editors, *Oxygen Transport in Biological Systems: Modelling of Pathways from Environment to Cell*, **51** of *Society for Experimental Biology Seminar Series*, pages 165–195. Cambridge University Press, 1992.

[52] S. EGGINTON AND B. D. SIDELL. Thermal acclimation induces adaptive changes in subcellular structure of fish skeletal muscle. *The American Journal of Physiology*, **256**(1 Pt 2):R1–9, 1989.

[53] S. EGGINTON, Z. TUREK, AND L. J. HOOFD. Differing patterns of capillary distribution in fish and mammalian skeletal muscle. *Respiration Physiology*, **74**(3):383–96, 1988.

[54] C. D. EGGLETON, T. K. ROY, AND A. S. POPEL. Predictions of capillary oxygen transport in the presence of fluorocarbon additives. *The American Journal of Physiology*, **275**(6 Pt 2):H2250–7, 1998.

[55] C. D. EGGLETON, A. VADAPALLI, T. K. ROY, AND A. S. POPEL. Calculations of intracapillary oxygen tension distributions in muscle. *Mathematical Biosciences*, **167**(2):123–143, 2000.

[56] S. K. ELLINGTON. In vitro analysis of glucose metabolism and embryonic growth in postimplantation rat embryos. *Development*, **100**(3):431–439, 1987.

[57] M. L. ELLSWORTH AND R. N. PITTMAN. Heterogeneity of oxygen diffusion through hamster striated muscles. *The American Journal of Physiology*, **246**(2 Pt 2):H161–7, 1984.

[58] M. L. ELLSWORTH, A. S. POPEL, AND R. N. PITTMAN. Assessment and impact of heterogeneities of convective oxygen transport parameters in capillaries of striated muscle: Experimental and theoretical. *Microvascular Research*, **35**(3):341–362, 1988.

[59] P. A. ELUSTONDO, A. E. WHITE, M. E. HUGHES, K. BREBNER, E. PAVLOV, AND D. A. KANE. Physical and functional association of lactate dehydrogenase (LDH) with skeletal muscle mitochondria. *Journal of Biological Chemistry*, **288**(35):25309–25317, 2013.

[60] G. ELZINGA AND W. J. VAN DER LAARSE. Oxygen consumption of single muscle fibres of Rana temporaria and Xenopus laevis at 20 degrees C. *The Journal of Physiology*, **399**(1):405–418, 1988.

[61] L.C. EVANS. *Partial Differential Equations*. Graduate studies in mathematics. American Mathematical Society, 2010.

[62] J. E. FLETCHER. Mathematical modeling of the microcirculation. *Mathematical Biosciences*, **38**(3-4):159–202, 1978.

[63] J. E. FLETCHER. On facilitated oxygen diffusion in muscle tissues. *Biophysical Journal*, **29**(3):437–58, 1980.

[64] J. E. FLETCHER AND R. W. SCHUBERT. Axial diffusion and wall permeability effects in perfused capillary-tissue structures. *Biosystems*, **20**(2):153–174, 1987.

[65] J. E. GALGANI, C. MORO, AND E. RAVUSSIN. Metabolic flexibility and insulin resistance. *American Journal of Physiology–Endocrinology and Metabolism*, **295**(5):E1009–E1017, 2008.

[66] A. W. GARDNER AND A. AFAQ. Management of lower extremity peripheral arterial disease. *Journal of Cardiopulmonary Rehabilitation and Prevention*, **28**(6):349, 2008.

[67] J. D. GARDNER AND R. W. SCHUBERT. Evaluation of myoglobin function in the presence of axial diffusion. In E. M. NEMOTO AND J. C. LAMANNA, editors, *Oxygen Transport to Tissue XVIII*, **411** of *Advances in Experimental Medicine and Biology*, pages 157–169. Plenum Press, 1997.

[68] T. E. J. GAYESKI AND C. R. HONIG. Intracellular PO_2 in long axis of individual fibers in working dog gracilis muscle. *American Journal of Physiology*, **254**(6):H1179–H1186, 1988.

[69] D. GOLDMAN. Theoretical models of microvascular oxygen transport to tissue. *Microcirculation*, **15**(8):795–811, 2008.

[70] D. GOLDMAN, R. M. BATEMAN, AND C. G. ELLIS. Effect of decreased O_2 supply on skeletal muscle oxygenation and O_2 consumption during sepsis: role of heterogeneous capillary spacing and blood flow. *American Journal of Physiology*, **290**(6):H2277–85, 2006.

[71] D. GOLDMAN AND A. S. POPEL. A computational study of the effect of capillary network anastomoses and tortuosity on oxygen transport. *Journal of Theoretical Biology*, **206**(2):181–194, 2000.

[72] GONZALEZ–FERNANDEZ, J. M. AND ATTA, S. E. Concentration of oxygen around capillaries in polygonal regions of supply. *Mathematical Biosciences*, **13**(1-2):55–69, 1972.

[73] T. N. T. GOODMAN AND H. B. SAID. A C-1 Triangular Interpolant Suitable for Scattered Data Interpolation. *Communications in Applied Numerical Methods*, **7**(6):479–485, 1991.

[74] H. R. GOSKER, E. F. M. WOUTERS, G. J. VAN DER VUSSE, AND A. M. W. J. SCHOLS. Skeletal muscle dysfunction in chronic obstructive pulmonary disease and chronic heart failure: underlying mechanisms and therapy perspectives. *The American Journal of Clinical Nutrition*, **71**(5):1033–1047, 2000.

[75] A. S. GREENE, P. J. TONELLATO, Z. ZHANG, J. H. LOMBARD, AND A. W. COWLEY JR. Effect of microvascular rarefaction on tissue oxygen delivery in hypertension. *The American Journal of Physiology*, **262**(5 Pt 2):H1486–93, 1992.

[76] C. M. GREGORY AND C. S. BICKEL. Recruitment patterns in human skeletal muscle during electrical stimulation. *Physical Therapy*, **85**(4):358–64, 2005.

[77] K. GROEBE. Factors important in modelling oxygen supply to red muscle. In S. EGGINTON AND H. F. ROSS, editors, *Oxygen Transport in Biological Systems: Modelling of Pathways from Environment to Cell*, **51** of *Society for Experimental Biology Seminar Series*, pages 231–252. Cambridge University Press, 1992.

[78] J. GUCKENHEIMER AND P. J. HOLMES. *Nonlinear Oscillations, Dynamical Systems, and Bifurcations of Vector Fields*, **42** of *Applied Mathematical Sciences*. Springer-Verlag, New York; London, 1997.

[79] K. G. HALES. Mitochondrial fusion and division. *Nature Education*, **3**(9):12, 2010.

[80] K. M. HARDY, R. M. DILLAMAN, B. R. LOCKE, AND S. T. KINSEY. A skeletal muscle model of extreme hypertrophic growth reveals the influence of diffusion on cellular design. *American Journal of Physiology–Regulatory, Integrative and Comparative Physiology*, **296**(6):R1855–67, 2009.

[81] K. M. HARDY, S. C. LEMA, AND S. T. KINSEY. The metabolic demands of swimming behavior influence the evolution of skeletal muscle fiber design in the brachyuran crab family portunidae. *Marine Biology*, **157**(2):221–236, 2010.

[82] D. HARGREAVES, S. EGGINTON, AND O. HUDLICKÁ. Changes in capillary perfusion induced by different patterns of activity in rat skeletal muscle. *Microvascular Research*, **40**(1):14–28, 1990.

[83] D. HAUTON. Hypoxia in early pregnancy induces cardiac dysfunction in adult offspring of rattus norvegicus, a non-hypoxia-adapted species. *Comparative Biochemistry and Physiology Part A: Molecular & Integrative Physiology*, **163**(3–4):278 – 285, 2012.

[84] D. HAUTON, A. A. AL-SHAMMARI, E. A. GAFFNEY, AND S. EGGINTON. Maternal hypoxia decreases capillary supply and increases metabolic inefficiency leading to mismatch between oxygen supply and demand. *PLoS ONE*, 2014 (Submitted).

[85] D. HAUTON AND V. OUSLEY. Prenatal hypoxia induces increased cardiac contractility on a background of decreased capillary density. *BMC Cardiovascular Disorders*, **9**(1):1–14, 2009.

[86] D. HAUTON, J. WINTER, A. A. AL-SHAMMARI, E. A. GAFFNEY, R. D. EVANS, AND S. EGGINTON. Changes to both cardiac metabolism and performance accompany acute reductions in functional capillary supply. *BBA General Subjects*, 2014 (Submitted).

[87] C. S. HENRIQUEZ. Simulating the electrical behavior of cardiac tissue using the bidomain model. *Critical Reviews in Biomedical Engineering*, **21**(1):1–77, 1992.

[88] M. I. HERON AND K. RAKUŠAN. Geometry of coronary capillaries in hyperthyroid and hypothyroid rat heart. *The American Journal of Physiology*, **267**(3 Pt 2):H1024–31, 1994.

[89] M. HINZE, R. PINNAU, M. ULBRICH, AND S. ULBRICH. *Optimization with PDE Constraints*, **23** of *Mathematical Modelling: Theory and Applications*. Springer, New York, 2008.

[90] M. W. HIRSCH AND S. SMALE. *Differential Equations, Dynamical Systems, and Linear Algebra*. Academic Press, New York, 1974.

[91] C. R. HONIG AND T. E. GAYESKI. Correlation of O_2 transport on the micro and macro scale. *International Journal of Microcirculation, Clinical and Experimental*, **1**(4):367–380, 1982.

[92] L. HOOFD. Updating the krogh model: Assumptions and extensions. In S. EGGINTON AND H. F. ROSS, editors, *Oxygen Transport in Biological Systems: Modelling of Pathways from Environment to Cell*, **51** of *Society for Experimental Biology Seminar Series*, pages 197–229. Cambridge University Press, 1992.

[93] L. HOOFD. Calculation of oxygen pressures in tissue with anisotropic capillary orientation. I. Two-dimensional analytical solution for arbitrary capillary characteristics. *Mathematical Biosciences*, **129**(1):1–23, 1995.

[94] L. HOOFD. Calculation of oxygen pressures in tissue with anisotropic capillary orientation. II. Coupling of two-dimensional planes. *Mathematical Biosciences*, **129**(1):25–39, 1995.

[95] L. HOOFD AND S. EGGINTON. The possible role of intracellular lipid in determining oxygen delivery to fish skeletal muscle. *Respiration Physiology*, **107**(2):191–202, 1997.

[96] L. HOOFD, J. OLDERS, AND Z. TUREK. Oxygen pressures calculated in a tissue volume with parallel capillaries. In J. PIIPER, T. K. GOLDSTICK, AND M. MEYER, editors, *Oxygen Transport to Tissue XII*, **277** of *Advances in Experimental Medicine and Biology*, pages 21–9. Plenum Press, 1990.

[97] L. HOOFD, Z. TUREK, K. KUBAT, B. E. RINGNALDA, AND S. KAZDA. Variability of intercapillary distance estimated on histological sections of rat heart. In F. KREUZER, S. M. CAIN, Z. TUREK, AND T. K. GOLDSTICK, editors, *Oxygen Transport to Tissue VII*, **191** of *Advances in Experimental Medicine and Biology*, pages 239–247. Plenum Press, 1985.

[98] L. HOOFD, Z. TUREK, AND J. OLDERS. Calculation of oxygen pressures and fluxes in a flat plane perpendicular to any capillary distribution. In K. RAKUŠAN, G. P. BIRO, T. K. GOLDSTICK, AND Z. TUREK, editors, *Oxygen Transport to Tissue XI*, **248** of *Advances in Experimental Medicine and Biology*, pages 187–196. Plenum Press, 1989.

[99] H. HOPPELER. The different relationship of VO_2max to muscle mitochondria in humans and quadrupedal animals. *Respiration Physiology*, **80**(2-3):137–45, 1990.

[100] H. HOPPELER AND R. BILLETER. Conditions for oxygen and substrate transport in muscles in exercising mammals. *The Journal of Experimental Biology*, **160**:263–83, 1991.

[101] H. HOPPELER, H. HOWALD, K. CONLEY, S. L. LINDSTEDT, H. CLAASSEN, P. VOCK, AND E. R. WEIBEL. Endurance training in humans: aerobic capacity and structure of skeletal muscle. *Journal of Applied Physiology*, **59**(2):320 – 327, 1985.

[102] H. HOPPELER, O. HUDLICKÁ, AND E. UHLMANN. Relationship between mitochondria and oxygen consumption in isolated cat muscles. *The Journal of Physiology*, **385**:661–75, 1987.

[103] H. HOPPELER, O. MATHIEU, R. KRAUER, H CLAASSEN, R. B. ARMSTRONG, AND E. R. WEIBEL. Design of the mammalian respiratory system. vi. distribution of mitochondria and capillaries in various muscles. *Respiration Physiology*, **44**(1):87 – 111, 1981.

[104] H. HOPPELER, O. MATHIEU-COSTELLO, AND S. R. KAYAR. Mitochondria and microvascular design. In R. G. CRYSTAL, J. B. WEST, P. J. BARNES, N. S. CHERNIACK, AND E. R. WEIBEL, editors, *The Lung: Scientific Foundations*, pages 1467–1477. Raven Press, New York, 1991.

[105] R. HSU AND T. W. SECOMB. A Green's function method for analysis of oxygen delivery to tissue by microvascular networks. *Mathematical Biosciences*, **96**(1):61 – 78, 1989.

[106] O. HUDLICKÁ, M. BROWN, AND S. EGGINTON. Angiogenesis in skeletal and cardiac muscle. *Physiological Reviews*, **72**(2):369–417, 1992.

[107] J. A. HUDSON AND D. B. CATER. An analysis of factors affecting tissue oxygen tension. *Proceedings of the Royal Society of London, Series B. Biological Sciences*, **161**(983):247–274, 1964.

[108] A. G. JIMENEZ, B. R. LOCKE, AND S. T. KINSEY. The influence of oxygen and high–energy phosphate diffusion on metabolic scaling in three species of tail–flipping crustaceans. *The Journal of Experimental Biology*, **211**(20):3214–3225, 2008.

[109] D. P. JONES. Intracellular diffusion gradients of O_2 and ATP. *American Journal of Physiology*, **250**(5 Pt 1):C663–75, 1986.

[110] A. CLARK JR., W. J. FEDERSPIEL, P. A. A. CLARK, AND G. R. COKELET. Oxygen delivery from red cells. *Biophysical Journal*, **47**(2 I):171–181, 1985.

[111] K. D. JÜRGENS, T. PETERS, AND G. GROS. Diffusivity of myoglobin in intact skeletal muscle cells. *Proceedings of the National Academy of Sciences of the United States of America*, **91**(9):3829–33, 1994.

[112] R. KARCH, F. NEUMANN, R. ULLRICH, J. NEUMULLER, B. K. PODESSER, M. NEUMANN, AND W. SCHREINER. The spatial pattern of coronary capillaries in patients with dilated, ischemic, or inflammatory cardiomyopathy. *Cardiovascular Pathology*, **14**(3):135–144, 2005.

[113] S. R. KAYAR AND N. BANCHERO. Volume density and distribution of mitochondria in myocardial growth and hypertrophy. *Respiration Physiology*, **70**(3):275–86, 1987.

[114] S. R. KAYAR, H. CLAASSEN, H. HOPPELER, AND E. R. WEIBER. Mitochondrial distribution in relation to changes in muscle metabolism in rat soleus. *Respiration Physiology*, **64**(1):1–11, 1986.

[115] S. R. KAYAR, H. HOPPELER, B. ESSEN-GUSTAVSSON, AND K. SCHWERZMANN. The similarity of mitochondrial distribution in equine skeletal muscles of differing oxidative capacity. *The Journal of Experimental Biology*, **137**:253–63, 1988.

[116] J. P. KEENER AND A. V. PANFILOV. The effects of geometry and fibre orientation on propagation and extracellular potentials in myocardium. *Computational Biology of the Heart*, pages 235–258, 1997.

[117] B. KLITZMAN, A. S. POPEL, AND B. R. DULING. Oxygen transport in resting and contracting hamster cremaster muscles: experimental and theoretical microvascular studies. *Microvascular Research*, **25**(1):108–131, 1983.

[118] T. KOYAMA AND A. TAKA. Renal vasoconstriction in rats causes a decrease in capillary density and an increase in alkaline phosphatase expression in cardiac capillary nets. In E. TAKAHASHI AND D. F. BRULEY, editors, *Oxygen Transport to Tissue XXXI*, **662** of *Advances in Experimental Medicine and Biology*, pages 83–88. Plenum Press, 2010.

[119] F. KREUZER. Oxygen supply to tissues: the Krogh model and its assumptions. *Experientia*, **38**(12):1415–1426, 1982.

[120] A. KROGH. The number and distribution of capillaries in muscles with calculations of the oxygen pressure head necessary for supplying the tissue. *The Journal of Physiology*, **52**(6):409–415, 1919.

[121] S. LARSEN, J. NIELSEN, C. N. HANSEN, L. B. NIELSEN, F. WIBRAND, N. STRIDE, H. D. SCHRODER, R. BOUSHEL, J. W. HELGE, F. DELA, AND M. HEY-MOGENSEN. Biomarkers of mitochondrial content in skeletal muscle of healthy young human subjects. *The Journal of Physiology*, **590**(14):3349–3360, 2012.

[122] L. LEE, R. CAMPBELL, M. SCHEUERMANN-FREESTONE, R. TAYLOR, P. GUNARUWAN, L. WILLIAMS, H. ASHRAFIAN, J. HOROWITZ, A. G. FRASER, K. CLARKE, AND M. FRENNEAUX. Metabolic modulation with perhexiline in chronic heart failur: a randomized, controlled trial of short-term use of a novel treatment. *Circulation*, **112**:3280–3288, 2005.

[123] Y. M. LEE, C. H. JEONG, S. Y. KOO, M. J. SON, H. S. SONG, S. K. BAE, J. A. RALEIGH, H. Y. CHUNG, M. A. YOO, AND K. W. KIM. Determination of hypoxic region by hypoxia marker in developing mouse embryos in vivo: A possible signal for vessel development. *Developmental Dynamics*, **220**(2):175–186, 2001.

[124] G. LI, Y. XIAO, J. L. ESTRELLA, C. A. DUCSAY, R. D. GILBERT, AND L. ZHANG. Effect of fetal hypoxia on heart susceptibility to ischemia and reperfusion injury in the adult rat. *Journal of the Society for Gynecologic Investigation*, **10**(5):265–274, 2003.

[125] G. LIU, F. MAC GABHANN, AND A. S. POPEL. Effects of fiber type and size on the heterogeneity of oxygen distribution in exercising skeletal muscle. *PLoS ONE*, **7**(9):e44375, 2012.

[126] B. R. LOCKE AND S. T. KINSEY. Diffusional constraints on energy metabolism in skeletal muscle. *Journal of Theoretical Biology*, **254**(2):417–429, 2008.

[127] M. MAHLER, C. LOUY, E. HOMSHER, AND A. PESKOFF. Reappraisal of diffusion, solubility, and consumption of oxygen in frog skeletal muscle, with applications to muscle energy balance. *The Journal of General Physiology*, **86**(1):105–134, 1985.

[128] G. W. MAINWOOD AND K. RAKUŠAN. A model for intracellular energy transport. *Canadian Journal of Physiology and Pharmacology*, **60**(1):98–102, 1982.

[129] T. P. MARTIN AND V. R. EDGERTON. Intrafibre distribution of succinate dehydrogenase in cat tibialis anterior motor units. *Canadian Journal of Physiology and Pharmacology*, **70**(7):970–6, 1992.

[130] MATHWORKS. *Creating Graphical User Interfaces (R2012a). MATLAB.* The Mathworks, Inc, Natick, MA, 2012.

[131] MATHWORKS. *Image Processing Toolbox User's Guide (R2012a). MATLAB.* The Mathworks, Inc, Natick, MA, 2012.

[132] MATHWORKS. *Partial Differential Equations Toolbox User's Guide (R2012a). MATLAB.* The Mathworks, Inc, Natick, MA, 2012.

[133] B. J. MCGUIRE AND T. W. SECOMB. A theoretical model for oxygen transport in skeletal muscle under conditions of high oxygen demand. *Journal of Applied Physiology*, **91**(5):2255–2265, 2001.

[134] H. MENG, T. B. BENTLEY, AND R. N. PITTMAN. Myoglobin content of hamster skeletal muscles. *Journal of Applied Physiology*, **74**(5):2194–2197, 1993.

[135] T. NAKATANI, T. NAKASHIMA, T. KITA, C. HIROFUJI, K. ITOH, M. ITOH, AND A. ISHIHARA. Succinate dehydrogenase activities of fibers in the rat extensor digitorum longus, soleus, and cardiac muscles. *Archives of Histology and Cytology*, **62**(4):393–9, 1999.

[136] T. NAKATANI, T. NAKASHIMA, T. KITA, C. HIROFUJI, K. ITOH, M. ITOH, AND A. ISHIHARA. Cell size and oxidative enzyme activity of different types of fibers in different regions of the rat plantaris and tibialis anterior muscles. *The Japanese Journal of Physiology*, **50**(4):413–8, 2000.

[137] D. J. NUSZ, D. C. WHITE, Q. DAI, A. M. PIPPEN, M. A. THOMPSON, G. B. WALTON, C. J. PARSA, W. J. KOCH, AND B. H. ANNEX. Vascular rarefaction in peripheral skeletal muscle after experimental heart failure. *American Journal of Physiology–Heart and Circulatory Physiology*, **285**(4):H1554–H1562, 2003.

[138] A. C. NYACK, B. R. LOCKE, A. VALENCIA, R. M. DILLAMAN, AND S. T. KINSEY. Scaling of postcontractile phosphocreatine recovery in fish white muscle: effect of intracellular diffusion. *American Journal of Physiology–Regulatory, Integrative and Comparative Physiology*, **292**(5):R2077–R2088, 2007.

[139] G. A. ORDWAY AND D. J. GARRY. Myoglobin: an essential hemoprotein in striated muscle. *Journal of Experimental Biology*, **207**(20):3441–3446, 2004.

[140] J. PALIS AND S. SMALE. Structural stability theorems. In S. S. CHEIN AND S. SMALE, editors, *Proceedings of Symposia in Pure Mathematics*, **14**, Providence, Rhode Island, 1970. American Mathematical Society.

[141] I. PAPANDREOU, R. A. CAIRNS, L. FONTANA, A. L. LIM, AND N. C. DENKO. HIF-1 mediates adaptation to hypoxia by actively downregulating mitochondrial oxygen consumption. *Cell Metabolism*, **3**(3):187–197, 2006.

[142] B. PATHI, S. T. KINSEY, M. E. HOWDESHELL, C. PRIESTER, R. S. MCNEILL, AND B. R. LOCKE. The formation and functional consequences of heterogeneous mitochondrial distributions in skeletal muscle. *The Journal of Experimental Biology*, **215**(Pt 11):1871–83, 2012.

[143] B. PATHI, S. T. KINSEY, AND B. R. LOCKE. Influence of reaction and diffusion on spatial organization of mitochondria and effectiveness factors in skeletal muscle cell design. *Biotechnology and Bioengineering*, **108**(8):1912–24, 2011.

[144] B. PATHI, S. T. KINSEY, AND B. R. LOCKE. Oxygen control of intracellular distribution of mitochondria in muscle fibers. *Biotechnology and Bioengineering*, **110**(9):2513–2524, 2013.

[145] M. PHILIPPI AND A. H. SILLAU. Oxidative capacity distribution in skeletal muscle fibers of the rat. *Journal of Experimental Biology*, **189**(1):1–11, 1994.

[146] J. PIIPER AND P. SCHEID. Diffusion limitation of O_2 supply to tissue in homogeneous and heterogeneous models. *Respiration Physiology*, **85**(1):127–136, 1991.

[147] O. P. PITKÄNEN, P. NUUTILA, O. T. RAITAKARI, T. RÖNNEMAA, P. J. KOSKINEN, H. IIDA, T. J. LEHTIMÄKI, H. K. LAINE, T. TAKALA, J. S. A. VIIKARI, AND J. KNUUTI. Coronary flow reserve is reduced in young men with iddm. *Diabetes*, **47**(2):248–254, 1998.

[148] R. N. PITTMAN. Oxygen supply to contracting skeletal muscle at the microcirculatory level: diffusion vs. convection. *Acta Physiologica Scandinavica*, **168**(4):593–602, 2000.

[149] R. N. PITTMAN. Oxygen transport and exchange in the microcirculation. *Microcirculation*, **12**(1):59–70, 2005.

[150] R. N. PITTMAN. Oxygen gradients in the microcirculation. *Acta Physiologica*, **202**(3):311–322, 2011.

[151] R. N. PITTMAN. Regulation of tissue oxygenation. In *Colloquium Series on Integrated Systems Physiology: From Molecule to Function*, **3**, pages 1–100. Morgan & Claypool Life Sciences, 2011.

[152] R. N. PITTMAN. Oxygen transport in the microcirculation and its regulation. *Microcirculation*, **20**(2):117–137, 2013.

[153] D. C. POOLE AND L. F. FERREIRA. Oxygen exchange in muscle of young and old rats: muscle–vascular–pulmonary coupling. *Experimental Physiology*, **92**(2):341–346, 2007.

[154] A. S. POPEL. Analysis of capillary-tissue diffusion in multicapillary systems. *Mathematical Biosciences*, **39**(3-4):187–211, 1978.

[155] A. S. POPEL. Theory of oxygen transport to tissue. *Critical Reviews in Biomedical Engineering*, **17**(3):257–321, 1989.

[156] A. S. POPEL, C. K. CHARNY, AND A. S. DVINSKY. Effect of heterogeneous oxygen delivery on the oxygen distribution in skeletal-muscle. *Mathematical Biosciences*, **81**(1):91–113, 1986.

[157] M. E. RAICHLE. The pathophysiology of brain ischemia. *Annals of Neurology*, **13**(1):2–10, 1983.

[158] K. RAKUŠAN, M. F. FLANAGAN, T. GEVA, J. SOUTHERN, AND R. VANPRAAGH. Morphometry of human coronary capillaries during normal growth and the effect of age in left-ventricular pressure-overload hypertrophy. *Circulation*, **86**(1):38–46, 1992.

[159] K. RAKUŠAN AND R. J. TOMANEK. Distribution of mitochondria in normal and hypertrophic myocytes from the rat heart. *Journal of Molecular and Cellular Cardiology*, **18**(3):299–305, 1986.

[160] J. N. REDDY. *An Introduction to the Finite Element Method*. McGraw-Hill, 1993.

[161] H. REICHMANN AND D. WILDENAUER. Quantitative succinate dehydrogenase analysis in normal and ragged-red muscle fibers. *Histochemistry*, **96**(3):251–3, 1991.

[162] R. S. RICHARDSON, S. C. NEWCOMER, AND E. A. NOYSZEWSKI. Skeletal muscle intracellular PO_2 assessed by myoglobin desaturation: response to graded exercise. *Journal of Applied Physiology*, **91**(6):2679–2685, 2001.

[163] R. S. RICHARDSON, E. A. NOYSZEWSKI, K. F. KENDRICK, J. S. LEIGH, AND P. D. WAGNER. Myoglobin O_2 desaturation during exercise. Evidence of limited O_2 transport. *Journal of Clinical Investigation*, **96**(4):1916–1926, 1995.

[164] E. P. SALATHÉ. Mathematical modeling of oxygen transport in skeletal muscle. *Mathematical Biosciences*, **58**(2):171–184, 1982.

[165] E. P. SALATHÉ. A mathematical method for determining oxygen distribution in skeletal muscle with multiple capillaries and axial diffusion. *Proceedings of the Royal Society A, Mathematical Physical and Engineering Sciences*, **461**(2056):975–1004, 2005.

[166] P. T. SCHUMACKER, N. CHANDEL, AND A. G. N. AGUSTI. Oxygen conformance of cellular respiration in hepatocytes. *American Journal of Physiology*, **265**(4):L395–L402, 1993.

[167] G. R. SCOTT, S. EGGINTON, J. G. RICHARDS, AND W. K. MILSOM. Evolution of muscle phenotype for extreme high altitude flight in the bar–headed goose. *Proceedings of the Royal Society B*, **276**(1673):3645–53, 2009.

[168] T. W. SECOMB AND R. HSU. Simulation of O_2 transport in skeletal muscle: diffusive exchange between arterioles and capillaries. *American Journal of Physiology*, **267**:H1214–H1214, 1994.

[169] T. W. SECOMB, R. HSU, E. Y. H. PARK, AND M. W. DEWHIRST. Green's function methods for analysis of oxygen delivery to tissue by microvascular networks. *Annals of Biomedical Engineering*, **32**(11):1519–1529, 2004.

[170] M. SHARAN AND S. SELVAKUMAR. The effects of chemical kinetics on oxygen delivery to tissue. *Mathematical Biosciences*, **108**(2):253–277, 1992.

[171] T. H. SHEPARD, L. A. MUFFLEY, AND L. THAYER SMITH. Ultrastructural study of mitochondria and their cristae in embryonic rats and primate (N. nemistrina). *The Anatomical Record*, **252**(3):383–392, 1998.

[172] S. SIEDNER, M. KRÜGER, M. SCHROETER, D. METZLER, W. ROELL, B. K. FLEISCHMANN, J. HESCHELER, G. PFITZER, AND R. STEHLE. Developmental changes in contractility and sarcomeric proteins from the early embryonic to the adult stage in the mouse heart. *The Journal of Physiology*, **548**(2):493–505, 2003.

[173] W. C. STANLEY, F. A. RECCHIA, AND G. D. LOPASCHUK. Myocardial substrate metabolism in the normal and failing heart. *Physiological Reviews*, **85**(3):1093–1129, 2005.

[174] S. M. SULLIVAN AND R. N. PITTMAN. In vitro O_2 uptake and histochemical fiber type of resting hamster muscles. *Journal of Applied Physiology*, **57**(1):246–253, 1984.

[175] J. SUZUKI, T. KOBAYASHI, T. URUMA, AND T. KOYAMA. Strength training with partial ischaemia stimulates microvascular remodelling in rat calf muscles. *European Journal of Applied Physiology*, **82**(3):215–22, 2000.

[176] E. TAKAHASHI, K. SATO, H. ENDOH, Z. L. XU, AND K. DOI. Direct observation of radial intracellular gradients in a single cardiomyocyte of the rat. *American Journal of Physiology–Heart and Circulatory Physiology*, **275**(1):H225–H233, 1998.

[177] S. G. THACKER, C. C. BERTHIER, D. MATTINZOLI, M. P. RASTALDI, M. K., AND M. J. KAPLAN. The detrimental effects of IFN-α on vasculogenesis in lupus are mediated by repression of Il-1 pathways: potential role in atherogenesis and renal vascular rarefaction. *Journal of Immunology*, **185**(7):445–4469, 2010.

[178] G. THEWS. Die Sauerstoffdiffusion im Gehirn. *Pflüger's Archiv für die gesamte Physiologie des Menschen und der Tiere*, **271**(2):197–226, 1960.

[179] M. S. TITCOMBE AND M. J. WARD. An asymptotic study of oxygen transport from multiple capillaries to skeletal muscle tissue. *SIAM Journal on Applied Mathematics*, **60**(5):1767–1788, 2000.

[180] R. J. TOMANEK, M. R. AYDELOTTE, AND C. A. BUTTERS. Late onset renal hypertension in old rats alters myocardial microvessels. *The American Journal of Physiology*, **259**(6 Pt 2):H1681–7, 1990.

[181] Z. TUREK, L. HOOFD, S. BATRA, AND K. RAKUŠAN. The effect of realistic geometry of capillary networks on tissue PO_2 in hypertrophied rat heart. In W. ERDMANN AND D. F. BRULEY, editors, *Oxygen Transport to Tissue XIV*, **317** of *Advances in Experimental Medicine and Biology*, pages 567–572. Plenum Press, 1992.

[182] Z. TUREK, L. HOOFD, AND K. RAKUŠAN. Myocardial capillaries and tissue oxygenation. *The Canadian Journal of Cardiology*, **2**:98–103, 1986.

[183] Z. TUREK, L. HOOFD, AND K. RAKUŠAN. A comparison of the methods for assessment of the heterogeneity of myocardial capillary spacing. In I. A. SILVER, A. P. SILVER, T. K. GOLDSTICK, AND Z. TUREK, editors, *Oxygen Transport to Tissue IX*, **215** of *Advances in Experimental Medicine and Biology*, pages 13–19. Plenum Press, 1987.

[184] W. J. VAN DER LAARSE, P. C. DIEGENBACH, AND G. ELZINGA. Maximum rate of oxygen consumption and quantitative histochemistry of succinate dehydrogenase in single muscle fibres of Xenopus laevis. *Journal of Muscle Research and Cell Motility*, **10**(3):221–8, 1989.

[185] D. VOET, J. G. VOET, AND C. W. PRATT. Fundamentals of biochemistry. *John Willey & Sons, Inc*, 2006.

[186] C. Y. WANG AND J. B. BASSINGTHWAIGHTE. Capillary supply regions. *Mathematical Biosciences*, **173**(2):103–14, 2001.

[187] W. S. WEBSTER AND D. ABELA. The effect of hypoxia in development. *Birth Defects Research Part C: Embryo Today*, **81**(3):215–228, 2007.

[188] E. R. WEIBEL. *The Pathway for Oxygen.* Harvard University Press, Cambridge, MA, 1984.

[189] J. P. WHITELEY, D. J. GAVAGHAN, AND C. E. W. HAHN. Mathematical modelling of oxygen transport to tissue. *Journal of Mathematical Biology*, **44**(6):503–522, 2002.

[190] D. F. WILSON, W. L. RUMSEY, T. J. GREEN, AND J. M. VANDERKOOI. The oxygen dependence of mitochondrial oxidative phosphorylation measured by a new optical method for measuring oxygen concentration. *The Journal of Biological Chemistry*, **263**(6):2712–18, 1988.

[191] B. A. WITTENBERG AND J. B. WITTENBERG. Transport of oxygen in muscle. *Annual Review of Physiology*, **51**(1):857–878, 1989.

[192] J. B. WITTENBERG AND B. A. WITTENBERG. Myoglobin function reassessed. *Journal of Experimental Biology*, **206**(12):2011–2020, 2003.

[193] R. C. I. WÜST, S. L. GIBBINGS, AND H. DEGENS. Fiber capillary supply related to fiber size and oxidative capacity in human and rat skeletal muscle. In P. LISS, P. HANSELL, D. F. BRULEY, AND D. K. HARRISON, editors, *Oxygen Transport to Tissue XXX*, **645** of *Advances in Experimental Medicine and Biology*, pages 75–80. Plenum Press, 2009.

[194] R. C. I. WÜST, R. T. JASPERS, A. F. VAN HEIJST, M. T. E. HOPMAN, L. J. C. HOOFD, W. J. VAN DER LAARSE, AND H. DEGENS. Region-specific adaptations in determinants of rat skeletal muscle oxygenation to chronic hypoxia. *American Journal of Physiology–Heart and Circulatory Physiology*, **297**(1):H364–74, 2009.

[195] R. C. I. WÜST, D. S. MYERS, R. STONES, D. BENOIST, P. A. ROBINSON, J. P. BOYLE, C. PEERS, E. WHITE, AND H. B. ROSSITER. Regional skeletal muscle remodeling and mitochondrial dysfunction in right ventricular heart failure. *American Journal of Physiology–Heart and Circulatory Physiology*, **302**(2):H402–11, 2012.

[196] Y. XU, S. J. WILLIAMS, D. OBRIEN, AND S. T. DAVIDGE. Hypoxia or nutrient restriction during pregnancy in rats leads to progressive cardiac remodeling and impairs postischemic recovery in adult male offspring. *The FASEB Journal*, **20**(8):1251–1253, 2006.

Glossary

$\dot{V}O_{2,max}$	Maximal rate of oxygen consumption (oxygen demand).
PO_2	Oxygen partial pressure (or tension).
C:F	Capillary–to–fibre ratio. The ratio of the total number of capillaries to the total number of fibres in a muscle tissue cross–section.
CD	Planar capillary density. The number of capillaries per mm^2 of tissue cross–section.
CFD	Capillary–fibre density. This is another acronym used by physiologists to refer to LCD.
DOM	Capillary domain. A region enclosing a capillary within a muscle tissue cross–section and is closer to it than all other capillaries.
ICD	Intercapillary distance. The mean (or minimum) of the distances to adjacent capillaries.
imf	Intermyofibrillar zone. A region within muscle fibres that engulfs all myofibrils but does not overlap the subsarcolemmal zone.
IS	Interstitial spaces.
LCD	Local capillary density. It is defined as the LCFR normalised by individual fibre areas.
LCFR	Local capillary-to-fibre ratio. The cumulative sum of the fractions of all capillary domains overlapping a fibre.
MO_2	Rate of oxygen consumption.
mi	The mitochondrial subpopulation present in the intermyofibrillar zone of a muscle fibre.
ms	The mitochondrial subpopulation present in the subsarcolemmal zone of a muscle fibre.
mt	Total mitochondrial population of a muscle fibre.
myocyte	A muscle cell/fibre.

NCAF	Number of capillaries around a fibre.
sarcolemma	The cellular membrane of muscle fibres.
ss	Subsarcolemmal zone. A region within muscle fibres that extends directly underneath the sarcolemma but does not overlap myofibrils.
TR	Trapping region. The smallest 2D biophysical region enclosing a capillary with a zero substrate flux at its boundary.
Type I	Slow oxidative muscle fibres (or SO). These are aerobic fibres.
Type IIa	Fast oxidative muscle fibres (or FO). These are partly aerobic fibres.
Type IIa	Fast glycolytic muscle fibres (or FG). These are anaerobic muscle fibres.
VP	Voronoi polygon. The boundary of a 2D region enclosing a node and is closer to it than all other nodes.